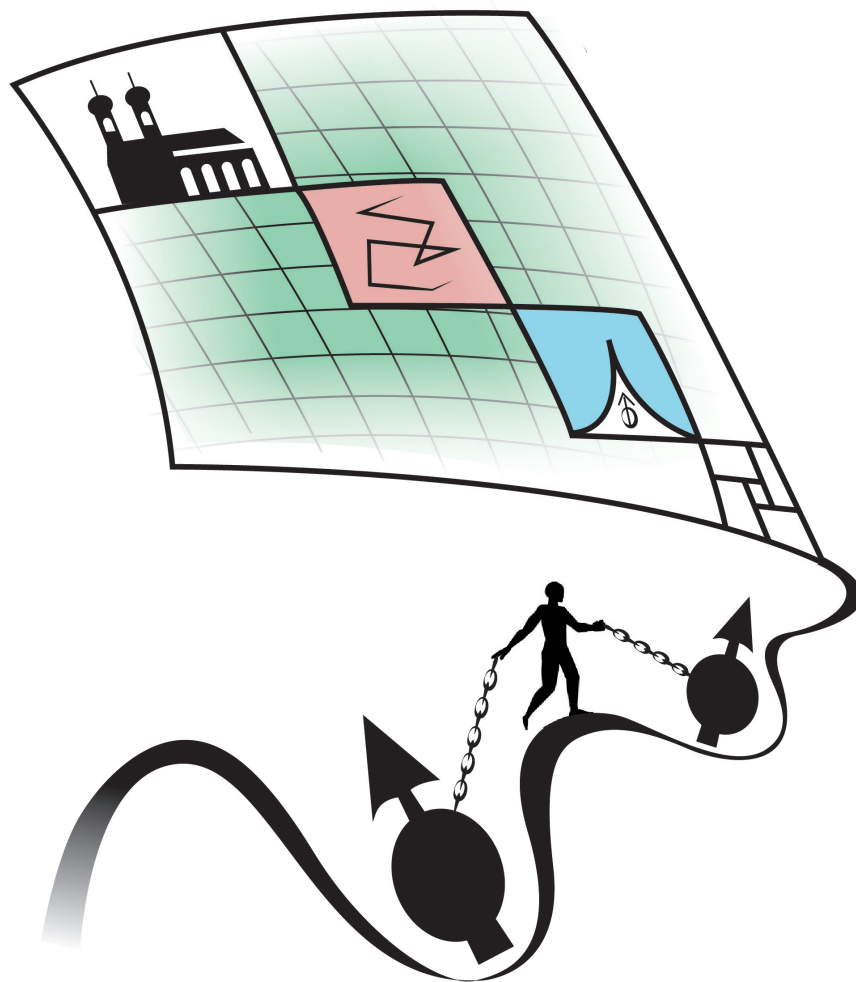


THE ROLE OF UNCONVENTIONAL SYMMETRIES IN THE DYNAMICS OF MANY-BODY SYSTEMS

Dissertation

Pablo Sala de Torres-Solanot



Chair of Theoretical Solid-State Physics
Department of Physics
Technical University of Munich

The front picture was originally designed by the author with the help of Eleazer Johan Canda Orozco. The professional artist María Carretero Jiménez composed and drew the final version.

TECHNISCHE UNIVERSITÄT MÜNCHEN

FAKULTÄT FÜR PHYSIK

**The role of unconventional symmetries in the
dynamics of many-body systems**

Pablo Sala de Torres-Solanot

Vollständiger Abdruck der von der Fakultät für Physik der Technischen
Universität München zur Erlangung des akademischen Grades eines
Doktors der Naturwissenschaften (Dr. rer. nat.)
genehmigten Dissertation.

Vorsitzender: Prof. Dr. Alexander Holleitner

Prüfer der Dissertation:

1. Prof. Dr. Frank Pollmann
2. Prof. Dr. Johannes Knolle

Die Dissertation wurde am 21.06.2022 bei der Technischen Universität München
eingereicht und durch die Fakultät für Physik am 19.07.2022 angenommen

Abstract

Symmetries are essential to classify equilibrium phases of matter and to explain how such global thermal equilibrium is attained. In this thesis, we explore the role that certain *unconventional* symmetries play in the dynamics of classical and quantum many-body systems. To begin with, we show that the conservation of a charge and its associated dipole moment leads to a provable *fragmentation of the Hilbert space* into exponentially many disconnected sectors. In turn, this can translate into non-vanishing bulk correlators and the existence of localized modes at the boundaries of the system among other possible unexpected phenomena. In general, we find that this conservation leads to novel universal hydrodynamic behavior, which can coexist with initial states that avoid thermalization, hence providing examples of weak ergodicity breaking. We achieve this by combining simple minimal models of interacting degrees of freedom compatible with these symmetries, and extensive numerical methods.

We then explore the experimental realization of these models, and investigate the far-from-equilibrium behavior of certain closed quantum many-body systems where such models become a good approximation. This happens in the presence of a strong tilted field that couples to the center of mass coordinate. We use our previous insights to interpret the experimental results, where the system is observed to remain localized at the accessible time scales. This is possible due to the flourishing development of new experimental platforms, which thanks to an extraordinary level of control over the system, allow us to address fundamental questions in the realms of statistical and quantum mechanics.

Encouraged by these results, we conclude by revisiting the notion of symmetry, approaching it from a broader perspective. In particular, we inquire about what spatially-modulated symmetries a system can have, providing a novel approach to constructing some of them. These appear as non-trivial solutions of linear recurrence relations, including multipole and subsystem symmetries, but also new types of unconventional ones. We show that these can take the form of lines and surfaces of conserved momenta, or be localized at the edges of the system.

Kurzfassung

Symmetrien sind essenziell, um Gleichgewichtsphasen der Materie zu klassifizieren und zu erklären, wie sich ein solches globales thermisches Gleichgewicht einstellt. In dieser Arbeit wird untersucht, welche Rolle bestimmte unkonventionelle Symmetrien für die Dynamik klassischer und quantenmechanischer Vielteilchensysteme spielen. Zunächst wird aufgezeigt, wie die Erhaltung des Dipolmoments zu einer nachweislichen Fragmentierung des Hilbert-Raumes in exponentiell viele nicht zusammenhängende Sektoren führt. Dies wiederum kann zu nicht verschwindenden Bulk-Korrelatoren und der Existenz von lokalisierten Moden an den Rändern des Systems führen, neben anderen möglichen unerwarteten Phänomenen. Im Allgemeinen stellt sich heraus, dass diese Erhaltungsgröße zu einem neuartigen universellen hydrodynamischen Verhalten führt, das mit Anfangszuständen koexistieren kann, die eine Thermalisierung vermeiden und somit Beispiele für ein schwaches Brechen von Ergodizität liefern. Dies wird erreicht durch die Kombination von einfachen Minimalmodellen wechselwirkender Freiheitsgrade, die mit diesen Symmetrien kompatibel sind, mit umfangreichen numerischen Methoden.

Anschließend werden experimentelle Realisierungen dieser Modelle erforscht, indem das Verhalten fern vom Gleichgewicht bestimmter geschlossener Quanten-Vielteilchensysteme untersucht wird, für die solche Modelle eine gute Näherung darstellen. Dies geschieht durch ein starkes, lineares Potential, das an den Massenmittelpunkt koppelt. Mithilfe der bisherigen Erkenntnisse können die experimentellen Ergebnisse interpretiert werden, wobei beobachtet wurde, dass das System auf den erreichbaren Zeitskalen lokalisiert bleibt. Dies ist durch die florierende Entwicklung neuer experimenteller Plattformen möglich, die es dank eines außergewöhnlichen Maßes an Kontrolle über das System erlauben, grundlegende Fragen im Bereich der statistischen Physik und Quantenmechanik zu beantworten.

Ermutigt durch diese Ergebnisse, wird abschließend der Begriff der Symmetrie neu aufgegriffen und aus einer breiteren Perspektive betrachtet. Insbesondere wird untersucht, welche räumlich modulierten Symmetrien ein System haben kann, wobei ein neuartiger Ansatz für die Konstruktion einiger dieser Symmetrien dargelegt wird. Diese erscheinen als nicht-triviale Lösungen linearer Rekursionsgleichung, einschließlich Multipol- und Subsystemsymmetrien, aber auch neuer Arten unkonventioneller Symmetrien. Es wird gezeigt, dass diese die Form von Linien und Flächen mit konservierten Impulsen annehmen können oder am Rand des Systems lokalisiert sind.

Publications

Most parts of this thesis have been published in a peer-reviewed journal or uploaded to the open access repository arXiv. The corresponding chapters are extended versions of these publications, which include a discussion of relevant previous and contemporaneous works by other authors. Chapter 1 gives a brief review of the underlying concepts used in the writing of this thesis. Chapter 2 is based on

- **Pablo Sala**, Tibor Rakovszky, Ruben Verresen, Michael Knap and Frank Pollmann: “Ergodicity breaking arising from Hilbert Space Fragmentation in dipole-conserving Hamiltonians”
Physical Review X, 10(1), 2020 [1].

Chapter 3 is based on

- Tibor Rakovszky*, **Pablo Sala***, Ruben Verresen, Michael Knap and Frank Pollmann: “Statistical localization: From strong fragmentation to strong edge modes”
Physical Review B, 101(12), 2020 [Editor’s suggestion] [2].

Chapter 4 is mainly based on

- Sebastian Scherg, Thomas Kohlert, **Pablo Sala**, Frank Pollmann, Bharath Hebbe Madhusudhana, Immanuel Bloch and Monika Aidelsburger: “Observing non-ergodicity due to kinetic constraints in tilted Fermi-Hubbard chains”
Nature Communications, 12(1), 2021 [3],

and on

- Thomas Kohlert, Sebastian Scherg, **Pablo Sala**, Frank Pollmann, Bharath Hebbe Madhusudhana, Immanuel Bloch and Monika Aidelsburger: “Experimental realization of fragmented models in tilted Fermi-Hubbard chains”
arXiv:2106.15586 [Submitted to Physical Review Letters] [4].

Chapter 5 discusses the one-dimensional systems introduced in

- **Pablo Sala***, Julius Lehmann*, Tibor Rakovszky and Frank Pollmann: “Dynamics in systems with modulated symmetries”
arXiv:2110.08302 [Submitted to Physical Review Letters] [5],

and in

- Johannes Feldmeier, **Pablo Sala**, Giuseppe De Tomasi, Frank Pollmann and Michael Knap: “Anomalous diffusion in dipole- and higher-moment-conserving systems”
Physical Review Letters, 125(24), 2020 [6],

the latter appearing as a particular case of the first. For this reference, the author introduced the higher-moment conserving models and contributed to derive the analytical results presented in the publication, apart from actively contributing to the writing of the manuscript.

* indicates equal contribution.

Chapter 6 is partly based on Ref. [5] and also presents new unpublished results for conserved quantities that are localized at the boundary of two (or higher) -dimensional systems.

The author has also worked on lattice gauge theories and on many-body localization (MBL). The content of these works have not been included in the thesis, but their main results are summarized here. In

- **Pablo Sala***, Tao Shi*, Stefan Kühn, Mari Carmen Bañuls, Eugene Demler and Ignacio Cirac: “Variational study of U(1) and SU(2) lattice gauge theories with Gaussian states in 1 + 1 dimensions”
Physical Review D, 98(3), 2018,

we introduced a method that allows to efficiently investigate the static and dynamic properties of both Abelian (e.g., quantum electrodynamics) and non-Abelian (e.g., quantum chromodynamics) lattice gauge models in 1 + 1 dimensions. The main idea is to first apply transformations that disentangle the bosonic and fermionic degrees of freedom, followed by transformations that convert Gaussian states in suitable ansätze for variational calculations. Moreover, we proposed a Hamiltonian formulation suitable for both the design of future quantum simulators as well as for other numerical methods.

In

- Giuseppe De Tomasi, Daniel Hetterich, **Pablo Sala** and Frank Pollmann: “Dynamics of strongly interacting systems: From Fock-space fragmentation to many-body localization”
Physical Review B, 100(21), 2019 [7],

we studied the effect of Hilbert space fragmentation on the many-body-localization (MBL) transition. We identified sectors that can be mapped to the single-particle Anderson localization problem on the Fock-space with correlated disorder, and provide evidence for an MBL transition between states that can be considered thermal within the block and localized ones. On the one hand, we show that such constraints reduce the amount of disorder required to localize the system and on the other, shed light into the transport properties when approaching the transition point from the ergodic side at strong disorder.

In addition, the author started working on two research projects that are still ongoing. The first of those addresses the role of modulated symmetries (as introduced in Chapter 5) at low-temperature, considering for that a generalization of the well-studied Bose-Hubbard model in one dimension. The second, aims to shed light on the low-temperature physics of certain magnetic systems for which there is no consensus on the nature of its ground state. We are formulating an effective description where the role of quantum fluctuations is encoded in external charges on a lattice gauge theory description.

The author has made significant contributions to all of these works, including the development of ideas, analytical calculations, the implementation of numerical algorithms and data acquisition, the interpretation of results and an active writing of the manuscripts.

Acknowledgements

I feel I could cover just as many pages thanking all those people that have accompanied me during all these years. Our common experiences have positively influenced my understanding of life and physics.

First of all, I would like to thank my supervisor Frank Pollmann. He has been an inspiration to me, not only in the physics domain but also personally. He has transmitted to me his passion for research, allowing me to explore my own ideas, and giving me advice when he found me dispersed. He has shared his incredible physics intuition and taught me that a basic question can lead to the deepest understanding.

I would also like to thank my other mentor Michael Knap, for our many discussions about physics and his guidance during these last years. He has been always available when I needed his advice, and I have enjoyed and benefited from his close and extraordinary collaboration with Frank.

The works discussed in this thesis are the result of the many fruitful discussions and common effort of the many out-standing physicists I have had the pleasure to collaborate with: Monika Aidelsburger, Mari Carmen Bañuls, Immanuel Bloch, Ignacio Cirac, Giuseppe De Tomasi, Eugene Demler, Johannes Feldmeier, Bharath Hebhe Madhusudhana, Daniel Hetterich, Michael Knap, Thomas Kohlert, Stefan Kühn, Julius Lehmann, Olexey Motrunich, Frank Pollmann, Tibor Rakovszky, Tao Shi, Sebastian Scherg, Ari Turner, Ruben Verresen and Yizhi You. I have also been really fortunate to attend the Boulder and Les Houches summer schools on ‘Quantum Information’ and ‘Dynamics and Disorder in Quantum Many Body Systems’ respectively. Their lecturers and attendees have strongly and positively influenced my research career. I want to thank you all for sharing your time and expertise with me, which I hope I managed to depict in this thesis.

The very stimulating and friendly environment in the condensed matter theory group at TUM has also been a powerful stimulus. I have enjoyed sharing time together with Adam, Alex, Clemens, Daniel, Elizabeth, Giuseppe, Izabella, Johannes Hauschild and Johannes Feldmeier, Josef, Julian, Kevin, Leo, Markus, Raúl, Ruben, Sergej, Sheng-Hsuan, Umberto and Tibor, with whom I had the fortune to share an office and continue working together. I have also been very lucky to get to know Melissa and Yahui, who have devoted a great enthusiasm to their master theses and I with whom I have enjoyed many discussions in the last year. I have very much enjoyed chilling out together while playing table tennis at the physics department and walking along the Isar with many of you. I have a special thank you to Johannes Hauschild for his infinite patience in answering as many questions as I had about Tenpy, and also to Kevin, Markus, and Sheng-Hsuan for helping me to deal with the cluster, and to Daniel, for teaching me how to properly use Inkscape.

My immense gratitude to Giuseppe De Tomasi, Adrián Franco, Jad Halimeh, Sebastian Scherg and Tibor Rakovszky for reading different parts of the thesis. And in particular to my supervisor Frank Pollmann, for going over early versions of the thesis; and to Miguel Ángel García-March, who completely read a final version. Thank you all for your very valuable comments and our many insightful discussions. I hope we can start and continue working together in the future. I also want to thank Philip Zechmann for translating the abstract into German.

I also want to thank Prof. Armando Pérez and also Dr. Miguel Ángel García-March, who have hosted me in Valencia for two months, generously making me part of their groups and ongoing research, and investing their time in me. You made me feel very welcome.

All these years would not have been possible without the continuous support and love that I have received from my friends, some of them I had the fortune to meet in Munich, and specially from my family and my amazing partner. Gracias mamá, gracias papá, gracias Johan y gracias también a mis hermanos Ricardo y Mamen. Thank you all for being my fuel during all these years and being always available to spend some time together, in the up but also the down moments. This thesis is dedicated to you.

Contents

Abstract	i
Kurzfassung	ii
Publications	iii
Acknowledgements	v
Contents	vii
Introduction	1
1. Dynamics of closed quantum many-body systems	4
1.1. Thermalization in closed quantum systems	5
1.1.1. The eigenstate thermalization hypothesis	7
1.1.2. Random matrix theory	10
1.1.3. Emerging classical hydrodynamics	11
1.2. Dynamical probes of interest	12
1.2.1. Thermal correlations and Mazur's bound	13
1.2.2. Bipartite entanglement entropy	13
1.3. Many body localization and weak-ergodicity breaking	14
1.4. Simulating quantum many-body dynamics	16
1.4.1. Numerical methods and canonical typicality	16
1.4.2. Experiments with ultracold atoms	17
I. Hilbert space fragmentation	19
2. Ergodicity breaking arising from Hilbert space fragmentation in dipole-conserving Hamiltonians	21
2.1. Model and symmetries	22
2.2. Hamiltonian H_3	23
2.2.1. Lack of thermalization	23
2.2.2. Hilbert space fragmentation	24
2.2.3. Saturation value of $C_0^z(t)$	28
2.3. Combined Hamiltonian $H_3 + H_4$	29
2.3.1. Thermalization for $H_3 + H_4$	29
2.3.2. Constructing frozen states	30
2.3.3. Strong versus weak fragmentation	33
2.4. Comparison to random unitary circuits	36
2.5. Summary and discussion	37
3. Statistical localization: From strong fragmentation to strong edge modes	39
3.1. Illustrative example of SLIOMs: $t - J_z$ model	40
3.1.1. Definition of the model	41
3.1.2. Statistically localized integrals of motion	43

3.1.3.	Bulk vs boundary SLIOMs and their relationship to thermalization	47
3.1.4.	Experimental realization	54
3.2.	Dipole-conserving Hamiltonian H_3	55
3.2.1.	Mapping to bond spins and defects	56
3.2.2.	Labeling of connected sectors: Non-local conserved quantities	58
3.2.3.	Implications for dynamics	61
3.2.4.	Largest sectors and SPT order	64
3.3.	Embedded PXP dynamics: Relation to quantum many-body scars	66
3.4.	Summary of results	68
3.5.	Discussion and outlook	68
3.5.1.	Hilbert space fragmentation and commutant algebras	68
3.5.2.	Reducibility in classical kinetically constrained systems	69
3.5.3.	Non-local conserved quantities and ETH	70
3.5.4.	Future directions	70
 II. Experimental realization in tilted interacting systems		72
 4. The tilted Fermi-Hubbard model: An experimental platform for constrained systems		74
4.1.	Single particle dynamics in a tilted field	75
4.2.	Tilted Fermi-Hubbard model	77
4.2.1.	Choice of gauge: From a tilted to a driven lattice	79
4.2.2.	Dynamical symmetry: Attractive versus repulsive interactions	79
4.3.	Perturbative construction of effective constrained Hamiltonians	80
4.3.1.	Resonant regime $ U \simeq 2\Delta$	81
4.3.2.	Strong tilt regime: dipole conservation	85
4.3.3.	Role of the Schrieffer-Wolff transformation	88
4.4.	Numerical results and perturbative picture	89
4.4.1.	Higher order contributions and relevant on-site interactions in the dipole-conserving regime	89
4.4.2.	Real-time evolution of the imbalance and the entanglement entropy at resonance	91
4.5.	Experimental results	93
4.5.1.	Harmonic confinement	94
4.5.2.	Many-body dynamics at short time scales	95
4.5.3.	Non-ergodic behavior at late times	97
4.6.	Conclusions and discussion	100
 III. Spatially-modulated symmetries		102
 5. New families of modulated symmetries in 1D		104
5.1.	Cellular automaton dynamics	104
5.2.	Models and symmetries	105
5.2.1.	Dipole conservation	106
5.2.2.	Quasi-periodic modulation	106
5.2.3.	Exponentially localized	106
5.3.	General construction and analogous quantum models	107
5.3.1.	General parametrization of size-3 gates	107
5.3.2.	Longer-range gates	108
5.3.3.	Quantum Hamiltonians and strong zero modes	109

5.3.4.	Dipole and higher-moment conserving systems	110
5.4.	Hydrodynamics for multipole-conserving systems	112
5.4.1.	Generalized Fick’s law	112
5.4.2.	Quantum model with dipole conservation	115
5.4.3.	Numerical results with cellular automaton dynamics	117
5.5.	General “hydrodynamic” approach with modulated symmetries: Quasi-periodic symmetries	119
5.6.	Exponentially-localized symmetries and Mazur’s bound	121
5.7.	Discussion and outlook	122
6.	Modulated symmetries in 2D	125
6.1.	The discrete Laplacian model	126
6.1.1.	Solving the recurrence relation	128
6.1.2.	Finite boundary correlations and Mazur’s bound	130
6.2.	Subsystem symmetries in momentum space	134
6.2.1.	Symmetries in real space	136
6.2.2.	Hydrodynamic description: Long-time scaling of correlations	140
6.2.3.	Generalization and extension to higher dimensions	141
6.3.	Conclusions and outlook	143
7.	Conclusions and outlook	145
7.1.	Part I: Hilbert space fragmentation	145
7.2.	Part II: Experimental realization in tilted interacting systems	147
7.3.	Part III: Modulated symmetries in 2D	149
A.	Additional results for dipole-conserving chains	154
A.1.	Largest charge and dipole symmetry sector	155
A.2.	Finite-size scaling of the autocorrelator	157
A.3.	Operator spreading of $S_0^z(t)$	158
B.	More in-depth look into SLIOMs	161
B.1.	A more refined definition of SLIOMs	161
B.2.	Averaging over ensembles of random states	164
B.2.1.	Haar average and variance	164
B.2.2.	Fixed U(1) symmetry sectors	165
B.2.3.	Computation of the average number of defects	166
B.3.	Finite-size scaling of Fig. 3.4	166
B.4.	Spatially resolved autocorrelations at long times	167
B.5.	$t - J_z$ model with closed boundaries	167
B.6.	Saturation value of the entanglement entropy	168
C.	Effective description in the strong interacting limit	170
D.	Implementation of cellular automaton dynamics and Mazur bound	172
D.1.	Details on the implementation of cellular automaton dynamics	172
D.2.	Scaling analysis of the generalized diffusion equation	174
D.3.	Non-negativity of autocorrelations	175
E.	Survey of results for spatially-modulated symmetries	176
E.1.	Further examples of systems with periodically modulated symmetries	176
E.2.	General theory for the decay of autocorrelations in 2D	179
E.2.1.	General considerations	179

Contents

E.2.2. Applications to models in Fig. 6.6a 182
E.3. Counting the number of independent modulated symmetries 182

Bibliography **184**

Introduction

Recent and present-day experimental developments in the coherent control and manipulation of quantum many-body systems are enabling physicists to explore their far-from-equilibrium dynamics [8–10]. The possibility of manipulating these systems directly in the lab has attracted the attention of researchers working on many different areas. These include physicists working on condensed matter, quantum information, and statistical physics, but also on high energy physics [11, 12] and quantum gravity [13, 14]. In particular, a long-standing question that can benefit from these achievements is when and how a statistical description can emerge from the evolution of an isolated quantum system [15–23]. This physical process is known as *quantum thermalization* and our experience tells us that it generally occurs. In fact, rather than resorting to the memory-consuming many-body wave function, we often can understand our observations in terms of few thermodynamic quantities.

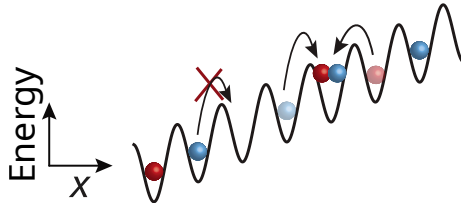
This fundamental question that was already addressed in the early days of quantum mechanics [24] (see Ref. [25] for an English translation), has now regained great interest driven not only by the thriving experimental advances in the recent years, but also due to a better understanding of the role of quantum entanglement [26–28] and the concomitant development of analytical and numerical methods. To this day, a widespread, though not unanimously accepted explanation is known by the *eigenstate thermalization hypothesis* (ETH) [21, 29–31]. According to this, every energy eigenstate of a Hamiltonian that exhibits thermalization essentially behaves like a thermal Gibbs ensemble [32] as far as the expectation values of *physical* observables are concerned. Nevertheless, the ETH is a conjecture that to this day lacks a rigorous proof and in general, a proper understanding that can be applied to any physical system. Although guided by pioneering analytical works [29, 30], we so far mostly rely on a great body of numerical evidence [21, 31, 33].

Given the generality of quantum thermalization and the apparent success of the ETH, looking for systems that defy them has the potential to give us important insights on how to move forward. Imagine discovering a scenario where, after piercing an inflated balloon (say one isolated from its environment by a vacuum chamber) [31] the air molecules do not uniformly distribute across the chamber, but rather remain localized at their initial locations. The most prominent example of such non-thermal behavior that violates the ETH is known as a *many-body localized phase* (MBL). It appears in the presence of a strong disorder potential, even for an interacting system [34–37]. This direct challenge to our understanding of the applicability of statistical physics has since then inspired many basic questions: How relevant is disorder to avoid quantum thermalization? Under what general conditions can a system fail to thermalize? Can we identify mechanisms leading neither to complete localization nor to full thermal behavior? The attempt to answer these has driven the search for MBL-like physics in disorder-free models [38, 39], the study of slow thermalization in systems with glassy behavior [40, 41], and the appearance of *quantum many-body scars* [42–48], namely, non-thermal eigenstates in otherwise thermalizing systems. Overall, the lesson to be learned is that symmetries — and their associated conserved quantities [49] — together with kinetic constraints, play a fundamental role in searching for behaviors that departs from standard quantum thermalization. In fact, this is also the case in the MBL phase, characterized by the existence of extensively many local

conserved quantities, which retain memory of the initial conditions [50, 51].

Concurrently to these recent discoveries and partly motivated by the same goals [52], the search for more robust quantum memories even at room temperature [53], led to the theoretical discovery of so-called *fractonic* systems (see reviews Refs. [54, 55]). These are characterized by their large ground-state degeneracy, but more relevant to us, by the restricted mobility of their fundamental excitations, so-called *fractons* [53, 56]. Only when bringing many of these excitations together, the resulting compound object is able to freely move, hence the name fracton. This suggests that it might be possible to prepare certain initial configurations for which the system evades thermalization. The key reason underlying this unusual property is once again symmetries, and in particular, the conservation of unconventional quantities which exhibit non-trivial spatial dependence. On the one hand, early works [52, 56–59] considered models with discrete subsystem symmetries, which would act along planes of a three-dimensional system. However, it was later realized that such mobility constraints can be also linked to the conservation of the center of mass (or equivalently, the dipole moment) of an already conserved quantity, which results in the localization of isolated charged excitations [60–66]. In view of these discoveries, and aiming to obtain new insights about quantum thermalization, the constrained behavior of fractonic systems provides a promising playground to elucidate the role of symmetries in the non-equilibrium dynamics [52, 67, 67–69].

However, how can we experimentally realize these systems? and if so, what is their fate at long times? It turns out that some of these quantities, like the dipole moment, are approximately conserved in certain scenarios. These include the quantum Hall effect in the Tao-Thouless limit, namely in the thin torus limit [70–74]; and, more experimentally relevant, interacting systems that are confined in an optical lattice and subject to a linear potential or *tilt*. This scenario is shown in the following figure:



When the energy difference between two consecutive wells of the lattice is very large, tunneling either up or down the tilt requires too much energy. Hence, a single particle remains localized around its initial location [75]. However, in the presence of interactions, two particles can coordinate themselves to simultaneously hop down and up the tilt, then preserving the center of mass of the system. Hence, while formerly appearing as of merely academic interest, understanding the behavior of systems which exactly realize such symmetries is important to address experimentally accessible scenarios. In fact, this directly relates to the suggestion that an interacting system in the presence of such a strong tilt and a weak harmonic potential, will give rise to a localized interacting phase reminiscent of MBL, which has been dubbed *Stark MBL* [76, 77].

The main goal of this thesis is to address these questions, understand the role that unconventional symmetries and kinetic constraints play on the dynamics of many-body systems, and provide a generalization of such symmetries to even richer spatial structures. The thesis is organized as follows:

In Chapter 1 we introduce the main concepts that are used throughout the thesis. The main focus is discussing what it means for an isolated quantum many-body system to thermalize and when it happens. We introduce the eigenstate thermalization hypothesis (ETH) as a plausible explanation, paying special attention to the role of initial states, observables and conservation laws. As exceptions to the general thermalizing rule, we discuss many-body localization, integrable systems and quantum many-body scars, and conclude the chapter with a short introduction to numerical methods, as well as to the use of ultracold atoms as a perfect arena to simulate isolated quantum many-body systems.

The rest of the thesis is then divided into three main parts. In Part I we consider simple one-dimensional toy models to investigate the phenomenon of Hilbert space fragmentation and its consequences. In Chapter 2, we first show that dipole-moment conservation alone is not sufficient to yield spatial localization, and that while any finite-range dipole-conserving system with a finite local Hilbert space dimension is exponentially fragmented, localization only occurs together with strong fragmentation. Then in Chapter 3, we introduce the statistically localized integrals of motion (SLIOM). We use them to prove several properties of the system, which include observable fluctuations on eigenstates, finite boundary magnetization at infinite times and string-order at finite energy density, among other results. In particular, we use them to completely label the fragmented structure of the strongly fragmented model discussed in Chapter 2.

Part II, which contains Chapter 4, deals with the experimental relevance of these results in actual physical scenarios. We start by introducing the tilted one-dimensional Fermi-Hubbard model in the strong tilt regime as a suitable platform to realize dipole-conserving and other kinetically constrained models. We derive several effective Hamiltonians, including a dipole-conserving one, and study their dynamics when preparing specific initial states that can be experimentally prepared. We then use this understanding to develop a perturbative explanation of the localized behavior that is observed, and which connects to the physics of Stark many-body localization.

In Part III, we extend the notions of dipole and subsystem symmetries to more general spatially-modulated ones, interpreting their spatial modulations as solutions of linear recurrence relations. We then study their effect on the late-time dynamics, providing a general analytical prediction for the decay of certain correlation functions, which we confirm using a stochastic block cellular automaton evolution. We first study one-dimensional systems in Chapter 5, and later on extend our results to higher dimensions in Chapter 6.

Finally in Chapter 7, we summarize the main results of this thesis, highlighting open questions and unsettled debates, as well as pointing towards interesting research directions.

1. Dynamics of closed quantum many-body systems

There is no line of argument proceeding from the laws of microscopic mechanics to macroscopic phenomena that is generally regarded by physicists as convincing in all respects.

Edwin Thompson Jaynes from *Information theory and statistical mechanics* [78].

In this chapter we focus on the dynamics of closed quantum systems — those that are isolated from their environment to a high degree — and the emergence of thermal behavior. Providing a complete review of the current knowledge (which includes extensive literature on many related topics, unsettled discussions and developments in the field) is certainly a daunting task. Hence, we focus only on those concepts directly related to the ideas that are discussed in this thesis, and refer the reader to the excellent reviews that already exist for a broader and more detailed presentation. Apart from specific references that will be provided along the way, I found particularly useful the following reviews, as an introduction to the field of quantum thermalization:

- (i) The review by Luca D’Alessio, Yariv Kafri, Anatoli Polkovnikov and Marcos Rigol [21] is a good starting point. It starts discussing “classical” thermalization, reviewing the ergodic hypothesis, typicality arguments and classical chaos; and states the main obstacles that one already encounters there and the main differences when investigating quantum systems. It also briefly motivates the eigenstate thermalization hypothesis (ETH) using random matrix theory (RMT) and von Neumann’s quantum ergodic theorem [24], and states the main existing conjectures in the realm of quantum thermalization. Moreover, it collects an extensive survey of numerical results which helps to understand the key concepts but also show our current limitations.
- (ii) Ref. [79] by the authors Takashi Mori, Tatsuhiko N. Ikeda, Eriko Kaminishi and Masahito Ueda, is also a detailed review. Its historical introduction dating back to Boltzmann and his H -theorem to current experimental advances in isolated quantum systems, complements the former review. It provides a more theoretical analysis which gives additional insights spelling out certain assumptions and details. It distinguishes between microscopic (sometimes called subspace) and macroscopic thermalization, reviewing von Neumann’s ergodic theorem on the way and introducing the concepts of (canonical) typicality and effective dimension when discussing equilibration. Moreover, it briefly discusses existing approaches to estimate equilibration time scales as well as the quantum recurrence theorem, and it also covers in detail the concept of prethermalization.
- (iii) The review by Christian Gogolin and Jens Eisert [22] focuses on mathematical rigorous results including: equilibration time scales (providing an extended discussion which partially covers that in Ref. [79]), a brief discussion of the role of Lieb-Robinson bounds and a quantum maximum entropy principle which relates to the classical formulation by Jaynes [78]. This reference also provides an alternative approach to the

problem of quantum thermalization, which restricts the family of initial states considered and is independent of the ETH. This rather long reference was preceded by Ref. [80] by the same authors together with Mathis Friesdorf. This is a short review summarizing the main accomplishments and open questions, which gives a general motivation and overview before reading Ref. [22].

- (iv) Moreover, I was also really fortunate to attend the 2019 Les Houches summer school on “Dynamics and disorder in quantum many body systems far from equilibrium”, whose lectures I used to write this introduction.

We remark that we do not attempt to provide a rigorous presentation of the results, but rather a physical intuition of the physics at hand, explicitly stating which questions remain to be answered.

1.1. Thermalization in closed quantum systems

In particular, our concern are *isolated quantum many-body* systems initially prepared in a highly-excited state. *Isolated* means that our system does not interact with its environment, as if it was placed in a vacuum chamber and isolated from all possible forms of background radiation. Hence “probability is conserved”. It is also *many-body*, meaning that the system is formed by a large number N of interacting degrees of freedom, whose state is described by the many-body pure state $|\psi_0\rangle$. These could be of fermionic or bosonic nature, or (artificial) spin degrees of freedom where the local Hilbert space is isomorphic to \mathbb{C}^{2S+1} , with S either a half- or an integer. Moreover, although not strictly necessary, we assume these particles lie on the nodes of a lattice (of volume V) in one or higher spatial dimensions. Such models are motivated by experimental setups and extremely amenable for theoretical studies. Being quantum (and isolated), its evolution is governed by a time-independent Hamiltonian \hat{H} via the Schrödinger equation $i\hbar\frac{d}{dt}|\psi(t)\rangle = \hat{H}|\psi(t)\rangle$, namely $|\psi(t)\rangle = e^{-i\hat{H}t/\hbar}|\psi_0\rangle$ ¹ (in the following we set $\hbar = 1$). In this section we want to understand under which circumstances a (generic) quantum system can thermalize, that is: “relax to states in which the values of macroscopic quantities are stationary, universal with respect widely different initial conditions, and predictable using statistical mechanics” [31].

At first glance, this is clearly at odds with the unitary dynamics and hence with the time-reversibility of the dynamics (see discussions in the previously mentioned reviews for a discussion about this topic, which dates back to the foundations of statistical mechanics). Let us assume \hat{H} has a discrete spectrum $\hat{H}|E_n\rangle = E_n|E_n\rangle$ with the eigenevalue E_n corresponding to the eigenstate $|E_n\rangle$. Then, the time-evolved state

$$|\psi(t)\rangle = \sum_n c_n e^{-iE_n t} |E_n\rangle \quad (1.1)$$

is completely specified by the dynamical phases $e^{-iE_n t}$ and the overlaps $c_n = \langle n|\psi_0\rangle$, whose distribution is preserved under time evolution. Notice that as $|\psi_0\rangle$, the time-evolving state also remains a pure state at all times. Hence, the global state of the system $|\psi(t)\rangle\langle\psi(t)|$ (with a finite energy density $\langle\psi(t)|\hat{H}|\psi(t)\rangle/V$) will never agree with an equilibrium thermal density matrix defined as

$$\hat{\rho}_{\text{th}}(\beta, \mu, \dots) = \frac{1}{Z(\beta, \mu, \dots)} \exp\left(-\beta(\hat{H} - \sum_k \mu_k \hat{Q}_k + \dots)\right), \quad (1.2)$$

¹Assuming the fact that the many-body wave function is pure is a theoretical idealization, since no experiments nowadays can prepare a state with full fidelity. Hence, in general the system will be in a mixed state, evolving under the von Neumann’s equation $i\hbar\partial_t\hat{\rho} = [\hat{H}, \hat{\rho}]$.

with $\beta = 1/(k_B T)$ the inverse temperature and $Z(\beta, \mu, \dots)$, an ensemble partition function. This thermal state includes all *extensive* conserved quantities \hat{Q}_k , meaning those which can be written as an *extensive* sum of local terms: $\hat{Q}_k = \sum_{j \in V} \hat{q}_j$. These include the total energy and particle number. However, it does not include the (exponentially many in N) non-local conserved quantities given by projections on energy eigenstates $|E_n\rangle\langle E_n|$. This condition ensures the equivalence among different ensembles (in the thermodynamic limit), since the relative fluctuations in \hat{Q}_k are sub-extensive, that is scaling as N^ν , with $\nu < 1$. Therefore, unlike $|\psi_0\rangle$, $\hat{\rho}_{\text{th}}$ is completely specified by a finite number of intensive parameters corresponding to the inverse temperature β and other possible Lagrange multipliers μ_k .

However, *quantum thermalization* rather refers to the “success of the system acting as its own bath, that is, as a *bath* for its subsystems, bringing them to a thermal state” [81] effectively forgetting about the initial state. The key role of this bath is to become maximally entangled to the subsystem, with which it can then interchange some conserved quantities. Given a global Hilbert space \mathcal{H} , quantum thermalization deals with the long-time behavior of observables on subsystems \mathcal{H}_A , which only involve a subextensive number of degrees of freedom, i.e., $\dim(\mathcal{H}_A)/\dim(\mathcal{H}_{A^c}) \rightarrow 0$ where A^c is its orthogonal complement. These for example, include spatially local subsystems with subextensive volume V_A , i.e., $V_A/V \rightarrow 0$ in the thermodynamic limit, but also observables that are local in some other basis, like e.g., momenta distributions; or correlations among two spatially distant locations; or simply extensive conserved quantities which involve the linear combinations of spatially localized observables. In the literature, such observables are sometimes dubbed *few-body*. Hence, when restricting to few-body observables, the expectation value $\langle \psi(t) | \hat{O} | \psi(t) \rangle = \text{tr}[\rho_A(t) \hat{O}]$ can be evaluated on the reduced density matrix $\rho_A(t) = \text{tr}_{A^c}[|\psi(t)\rangle\langle\psi(t)|]$ on region A , which generically will no longer be a pure state.

A system is said to have *thermalized* if for all such subsystems A it holds that

$$\lim_{t \rightarrow \infty} \lim_{V \rightarrow \infty} \text{tr}[\hat{\rho}_A(t) \hat{O}] \rightarrow \text{tr}[\hat{\rho}_{\text{th}}(\beta, \dots) \hat{O}] \equiv \langle \hat{O} \rangle_{\text{th}}, \quad (1.3)$$

for all observables \hat{O} with support on A on any compatible ensemble. We highlight that the order of limits is important, as thermalization can only be sharply defined in the thermodynamic limit. As it will become clear later on, for a finite system there will always be finite-size effects and hence the system will not be close to a thermal density matrix. Here the intensive parameters associated to the conserved quantities are fixed by the initial state $|\psi_0\rangle$ via

$$\begin{cases} \langle \psi_0 | \hat{H} | \psi_0 \rangle = \text{tr}[\hat{\rho}_{\text{th}}(\beta, \mu_k) \hat{H}] & \text{fixes } \beta, \\ \langle \psi_0 | \hat{Q}_k | \psi_0 \rangle = \text{tr}[\hat{\rho}_{\text{th}}(\beta, \mu_k) \hat{Q}_k] & \text{fixes } \mu_k \forall k. \end{cases} \quad (1.4)$$

This definition of thermalization implies that the system was indeed successful acting as its own bath, spreading the information about $|\psi_0\rangle$ (whose conditions need to be yet specified) and “hiding” it in long-range correlations that are unreachable via the few-body observables. In fact, everything we need in order to predict the long-time value of local observables is a finite number of intensive parameters, instead of the exponentially many complex coefficients c_n ! Notice that defining thermalization via Eq. (1.3) is saying that we demand $\hat{\rho}_A(t)$ to converge to the thermal density matrix

$$\lim_{t \rightarrow \infty} \lim_{V \rightarrow \infty} \hat{\rho}_A(t) \rightarrow \text{tr}_{A^c}[\hat{\rho}_{\text{th}}(\beta, \dots)] \quad (1.5)$$

in the weak-sense, hence capturing many different physical scenarios which assume nothing about the strength of interactions among degrees of freedom in A and A^c . In particular,

decomposing $\hat{H} = \hat{H}_A + \hat{H}_{A^c} + \hat{H}_{A|A^c}$, we are not assuming that $\hat{H}_{A|A^c}$ is in some sense small when compared to \hat{H}_A, \hat{H}_{A^c} , which would imply that $\text{tr}_{A^c}[\hat{\rho}_{th}(\beta)] \approx \exp(-\beta\hat{H}_A)/Z(\beta)$. Nevertheless, we still need to understand whether this definition makes physical sense and discuss the difficulties that arise.

Let us consider the time evolution of one of these few-body observables \hat{O}

$$\begin{aligned} O(t) &\equiv \langle \psi(t) | \hat{O} | \psi(t) \rangle = \sum_{n,m} c_n^* c_m e^{i(E_n - E_m)t} O_{nm} \\ &= \sum_n |c_n|^2 O_{nn} + \underbrace{\sum_{n,m \neq n} c_n^* c_m e^{i(E_n - E_m)t} O_{nm}}_{=O_{\text{osc}}(t)}, \end{aligned} \quad (1.6)$$

where $O_{nm} = \langle n | \hat{O} | m \rangle$. Notice that if \hat{O} is a conserved quantity, i.e., $[\hat{O}, \hat{H}] = 0$, then $O_{\text{osc}}(t) = 0$. Its time-average value is given by

$$\bar{O} \equiv \lim_{T \rightarrow \infty} \frac{1}{T} \int_0^T dt O(t) = \sum_n |c_n|^2 O_{nn}, \quad (1.7)$$

assuming the generic situation of no (extensive) degeneracies of the many-body spectrum, i.e., that $E_n = E_m$ only when $n = m$ (more comments about this later on). Equivalently, the saturation value \bar{O} can be understood as the expectation value of \hat{O} evaluated on the time-average density matrix $\hat{\rho}_{\text{DE}} = \sum_n |c_n|^2 |E_n\rangle\langle E_n|$ which is known as *diagonal ensemble* density matrix.

We say that an observable \hat{O} has *equilibrated* if after some finite relaxation time τ_R , the instantaneous value $O(t)$ coincides with the time-average value \bar{O} for *almost all* times. If in addition the system thermalizes, then by Eq. (1.3), the stationary value agrees with the thermal prediction $\bar{O} = \langle \hat{O} \rangle_{\text{th}}$. Comparing this with Eqs. (1.6) and (1.7), some clear difficulties arise: (i) Thermalization requires that temporal fluctuations around \bar{O} are small and in particular, suppressed in system size; (ii) Eq. (1.6) suggests that the system can only relax after all dynamical phases $e^{iE_n t}$ have *dephased*, i.e., the possibly fine-tuned configuration of phases in the initial state $|\psi_0\rangle$ becomes completely erased. Naively, this would occur at the Heisenberg time $\tau_H \sim 2\pi\hbar/\delta$ where δ is the minimum energy difference $\delta = \min_{n,m} |E_n - E_m|$ between the involved energy eigenvalues. However, since the dimension of the Hilbert space scales exponentially with N , and the width of the spectrum of \hat{H} only linearly, this implies that $\delta \sim e^{-\text{const} \times N}$, and hence $\tau_H \sim e^{\text{const} \times N}$. Nevertheless, this predicts an extremely long time for the system to relax, which matches neither with experimental nor numerical observations. (iii) We need to explain how $\bar{O} = \langle \hat{O} \rangle_{\text{th}}$ can hold even though the conserved probabilities $|c_n|^2$ are fixed by a particular initial state. Finally, we notice that genuine equilibration is impossible in finite systems due to the (quantum) recurrence theorem — the fact that for sufficiently long-times the system will end up being extremely close to the initial condition $|\psi(t)\rangle \simeq |\psi_0\rangle$ — that holds for our isolated quantum system². However, such recurrence times scale as a double exponential in N ³, i.e., $\sim e^{e^{\text{const} \times N}}$, which is an extraordinarily long time which can quickly (in N) surpass the age of the universe.

1.1.1. The eigenstate thermalization hypothesis

So far we have described what thermalization means, but we did not discuss any mechanism that could possibly resolve our previous objections. First hints were provided in

²In fact, Poincare recurrence theorem, the classical analogue, already appeared as an objection to the early works by Boltzmann about the time-reversibility of the fundamental equations.

³In fact, it scales with the effective dimension of the initial state $|\psi_0\rangle$. However, we are preparing a “physical” initial state which has overlap with exponentially many energy eigenstates. See details in Ref. [79].

1985 by the numerical work of Jensen and Shankar [82] which already highlighted the important roles of the initial state, the observable and the Hamiltonian, and in 1991 by J.M. Deutsch [29], which used random matrix theory to introduce a tractable model to prove the emergence of microcanonical averages. Later on in 1994 M. Srednicki [30], assuming Berry's conjecture [83] — saying that energy eigenfunctions behave as if they were Gaussian random variables— proved for a gas of hardcore particles, that one would recover thermal (Maxwell, Dirac-Fermi and Bose-Einstein) distributions from single energy eigenstates and hence for certain families of initial states with sufficiently small energy fluctuations. Finally, in 1998 he also conjectured [84] an ansatz for the matrix elements of an observable $O_{nm} = \langle n|\hat{O}|m\rangle$ evaluated on the energy eigenstates of a generic quantum many-body Hamiltonian. This ansatz received the name of *eigenstate thermalization hypothesis* (ETH) and takes the form

$$O_{nm} = \underbrace{O(\bar{E})\delta_{n,m}}_{\text{Diagonal ETH}} + \underbrace{e^{-S(\bar{E})/2}f_O(\bar{E},\omega)R_{nm}}_{\text{Off-diagonal ETH}}, \quad (1.8)$$

where $\bar{E} = (E_n + E_m)/2$, $\omega = E_n - E_m$, $\{R_{nm}\}$ are random variables with zero mean and unit variance, and $S(E) > 0$ is the thermodynamic entropy at energy E , which is an extensive quantity ($S(E) \sim V$). Notice that $e^{S(E)}$ is proportional to the density of states: $e^{S(E)} \propto \sum_n \delta(E - E_n)$ at energy E . Importantly, $O(E)$ and $f_O(E, \omega)$ are smooth functions of their arguments, and often $O(E)$ is directly assumed to coincide with the expectation value on the microcanonical ensemble on an energy window centered at E (unlike in the original Ref. [84] where such an assumption was not taken). Additional properties of the function $f_O(E, \omega)$ can be found in Section 4.3 of Ref. [21]. Finally, we notice that the ETH ansatz is preserved under sum and multiplication, e.g., if it holds for \hat{O} it also holds for $(\hat{O})^n$ [84]. Let us now see how this ansatz can resolve some of the difficulties we encountered in the previous section.

- **Diagonal-ETH.** The diagonal contribution implies that quantum thermalization takes place already at the level of energy eigenstates with $O(E_n)$ agreeing with its thermal value. This already suggests the different nature of quantum and classical thermalization, the latter being understood to rely on dynamical chaos [85]. This contribution helps to explain the agreement between time-average and thermal values discussed in difficulty (iii) of the previous section. Our aim is to show the equivalence between the diagonal $\hat{\rho}_{\text{DE}}$ and a thermal $\hat{\rho}_{\text{th}}$ ensemble (in particular we could consider the microcanonical one). The latter, is defined as the equal probability over all energy eigenvalues within a small energy window Δ : $\hat{\rho}_{\text{MC}} = \sum_{E_n \in [E - \frac{\Delta}{2}, E + \frac{\Delta}{2}]} |E_n\rangle\langle E_n|$. The former is fixed by the probabilities $|c_n|^2$ specifying the initial state. From here, it is clear that the only way such equivalence can hold is by restricting the possible family of initial states and in particular the distribution $|c_n|^2$. Let us assume that $|\psi_0\rangle$ has a small energy uncertainty $(\Delta E)^2 \equiv \sum_n |c_n|^2 (E_n - E)^2$ around the average energy $E = \sum_n |c_n|^2 E_n$. In particular, we need $(\Delta E)^2 |O''(E)|/O(E) \ll 1$, where $O''(E)$ is the second derivate of $O(E)$ with respect its argument. From here one finds

$$\bar{O} = \sum_n |c_n|^2 O(E_n) = O(E) + \frac{1}{2}\Delta^2 O''(E). \quad (1.9)$$

Using again the ETH in the expression for $\langle \hat{O} \rangle_{\text{th}}$ in some thermal ensemble leads to the agreement between the time-average value \bar{O} and the thermal value $\langle \hat{O} \rangle_{\text{th}}$

$$\bar{O} = \langle \hat{O} \rangle_{\text{th}} + O(\Delta^2) + O\left(\frac{1}{N}\right). \quad (1.10)$$

The ability to satisfy $(\Delta E)^2 |O''(E)/O(E)| \ll 1$ can be understood as a definition of what we mean by a *physical* state $|\psi_0\rangle$. Given an extensive quantity $\hat{H} = \sum_j \hat{h}_j$, with each \hat{h}_j having support on a finite number of lattice sites around site j , Ref. [31] showed (see Supplementary Material) that it is sufficient to prove that $\Delta E/N \rightarrow 0$ as $N \rightarrow \infty$ to show the equivalence between diagonal and microcanonical ensembles (similarly to classical statistical mechanics). This is the case in the absence of long-range correlations in $|\psi_0\rangle$ ⁴, such that

$$\Delta E_{|\psi_0\rangle} = \sqrt{\sum_{j_1, j_2} \left[\langle \psi_0 | \hat{h}_{j_1} \hat{h}_{j_2} | \psi_0 \rangle - \langle \psi_0 | \hat{h}_{j_1} | \psi_0 \rangle \langle \psi_0 | \hat{h}_{j_2} | \psi_0 \rangle \right]} \sim N^\nu \quad (1.11)$$

with $\nu < 1$. This implies that $|\psi_0\rangle$ has only subextensive fluctuations of the energy E . It is common to choose $|\psi_0\rangle$ to be a simple product state, or more generally the ground state of a *gapped* Hamiltonian \hat{H}_0 different from the one governing the dynamics, which has exponentially decaying correlations [86]. On the other hand, Eq. (1.11) will not be satisfied for (macroscopic) cat states, which combined two configurations corresponding to different energy densities and hence the fluctuations won't be small. See Ref. [87] for a discussion of this topic.

Finally, using that $O(E)$ is a smooth function of E , together with the fact that the typical energy difference between consecutive energy levels inversely scales with the density of states at energy E ($\sim e^{-\text{const} \times N}$), one can show that the eigenstate-to-eigenstate fluctuations of O_{nn} evaluated on two close-in-energy eigenstates, are exponentially suppressed in N : $O_{mm} - O_{nn} = O'(E_m) \cdot e^{-\text{const} \times N}$. In fact, looking at the distribution of O_{nn} as a function of E_n , provides a standard way to diagnose whether a system satisfies the ETH. If so, one expects that O_{nn} becomes a smooth function of E_n with fluctuations exponentially decreasing with increasing system size. Nevertheless, it is important to highlight that this is the case when looking at the distribution of O_{nn} on energy eigenstates sharing all other quantum numbers (at least same density in the thermodynamic limit) which are associated to extensive global conserved quantities $\{\hat{Q}_k\}$. Otherwise, O_{nn} is not only a function of the energy but also of the Lagrange multipliers λ_k (or equivalently the quantum numbers) associated to them, and hence, one could find two eigenstates which being close in energy, correspond to distant values of λ_k leading to discontinuities in $O(E, \lambda_k)$. It is always assumed that these conserved quantities have to be extensive and local. Recall that in general, any system has exponentially many conserved quantities $|E_n\rangle\langle E_n|$. However fixing all of them will make the statement of the ETH completely trivial. In Chapters 2 and 3 we will explicitly address the question of which conserved quantities should be resolved when checking the ETH in a quantum system. Finally, we notice that quite generally and without invoking the ETH, one can still show that fluctuations of intensive observables will decay polynomially with system size (see Supplementary Material of Ref. [88]).

- **Off-diagonal-ETH.** We can also explain objections (i) and (ii) noticing that the off-diagonal contributions O_{nm} in Eq. (1.8), are proportional to $e^{-S(E)/2} \sim e^{-\text{const} \times N}$. First, one can argue that $O_{\text{osc}}(t) \sim e^{-S(E)/2}$ [31] which could explain the finite equilibration times usually observed in experiments, instead of the long time scales we naively predicted. However, for the small system sizes that can be numerically simulated $O_{\text{osc}}(t)$ will still show strong fluctuations. Hence it is important to perform

⁴This roughly means that $\langle \psi_0 | \hat{h}_{j_1} \hat{h}_{j_2} | \psi_0 \rangle$ has only non-vanishing contributions when $j_1 \approx j_2$, i.e., $\langle \psi_0 | \hat{h}_{j_1} \hat{h}_{j_2} | \psi_0 \rangle \propto \delta_{j_1, j_2}$.

a proper finite-size scaling of the results. On the other hand, Ref. [89] has proven equilibration for generic initial states and Hamiltonians without requiring this contribution. There, the authors showed that it is sufficient to consider an initial state that has overlap over sufficiently many energy eigenstates, and not necessarily satisfying $\Delta E_{|\psi_0\rangle}/N \rightarrow 0$.

Finally, one can show that the time-fluctuations around the time average value are also exponentially suppressed with the number of degrees of freedom

$$\lim_{T \rightarrow \infty} \frac{1}{T} \int_0^T dt (O(t) - \bar{O})^2 = \sum_{n,m \neq n} |c_n|^2 |c_m|^2 |O_{nm}|^2 \sim O(e^{-\text{const} \times N}), \quad (1.12)$$

which ensures that once the system has equilibrated, it will acquire that value for almost all times. Nevertheless, quantum fluctuations of the observable \hat{O} can be shown to decay only polynomially in N

$$\lim_{T \rightarrow \infty} \frac{1}{T} \int_0^T dt \langle \psi(t) | (\hat{O} - \bar{O})^2 | \psi(t) \rangle = \overline{(O^2)} - \bar{O}^2 \sim O\left(\frac{1}{N}\right). \quad (1.13)$$

Therefore, the eigenstate thermalization hypothesis, provides a sufficient condition for thermalization, which is supported by a large body of numerical evidence (see review [21]). Particularly relevant was Ref. [31], which performed a very detailed numerical study of quantum thermalization, bringing up the ETH as a correct ansatz. Currently, there is no rigorous understanding of which observables and systems satisfy ETH or which do not⁵, although some rigorous results exist [29, 30]. As we previously discussed, the expectation is that it applies to those which only involve a small number of degrees of freedom. A more detail discussion about this question can be found in Ref. [91]. In particular, the authors argue that the ETH can also hold for observables with support on up to a half of the system size.

Important remarks. The ETH is expected to be satisfied by eigenstates in the bulk of the spectrum, i.e., excluding its edges [33]. With this restriction in mind, a generic system is believed to satisfy the strong version of the ETH (*strong-ETH*), which includes all eigenstates in the bulk. Alternatively, if certain outlying *non-thermal* — meaning not fulfilling ETH — eigenstates exist and as long as their ratio (with respect the full Hilbert space dimension) is vanishingly small at any given energy, the system satisfies the weak formulation of the ETH (known as *weak-ETH*) [42, 88, 92]. Equivalently, one says that the system *weakly* breaks ETH if almost all eigenstates of the system are thermal. In this situation, we can always find initial conditions which have narrow energy distributions but nevertheless fail to thermalize. Examples of this case will be discussed later in this thesis. It is often the case that a system satisfying the ETH is called *ergodic*, hence referring to systems being either *strongly-* or *weakly-ergodic* respectively. In this thesis, we will find examples of both. In addition, while ETH provides a sufficient condition for thermalization, it is often used as a synonym of the system being thermal. In fact, a recent work has argued that in fact ETH is not only sufficient but also a necessary condition [93]. As it might become apparent, many questions still remain unanswered.

1.1.2. Random matrix theory

Most of the motivation behind the ETH comes from random matrix theory (RMT) [94], which allows to make general statements about the eigenvalues and eigenvectors of Hermitian random matrices (see an introduction to the topic in the review [21], or a more in

⁵In fact, there is a recent work showing that whether a given system thermalizes or not is undecidable [90].

detail discussion in Ref. [94]). When addressing the daunting task of understanding the spectra of complex atomic nuclei, Eugene Wigner came up with the insight of rather focusing on its statistical properties. He realized that if one looks into a small energy window where the density of states is constant, then the Hamiltonian in a generic non fine-tuned basis (in particular different to its eigenbasis), will pretty much look like as a random matrix, subjected to the symmetries of interest. From here one can deduce the distribution of energy separations, i.e., $P(s \equiv E_{n+1} - E_n)$ with $E_{n+1} \geq E_n$, known as Wigner-Dyson distribution or Wigner Surmise⁶. These take the general form $P_\beta(s) = A_\beta s^\beta e^{-B_\beta s^2}$ with $\beta = 1$ for systems with time-reversal symmetry (and after resolving other unitary symmetries like e.g., particle number or translations). In this case matrices are drawn from the Gaussian Orthogonal Ensemble (GOE). These distributions exhibit a generic level repulsion, namely vanishing probability when $s \rightarrow 0$. Extending these ideas to other quantum systems, the authors of Ref. [95] conjectured that the level statistics of quantum systems with a classical chaotic analog are described by RMT, hence providing yet another potential insight into the thermalization of quantum many-body systems. See Ref. [96] for an interesting discussion about chaos and semiclassical limits.

It turns out that the ETH reduces to the RMT prediction when restricted to a very narrow energy window [21]. For a random Hamiltonian (e.g., drawn from the Gaussian orthogonal ensemble) with eigenstates $\{|E_n\rangle\}$ spanning a Hilbert space of dimension \mathcal{D} , the matrix elements of any operator \hat{O} are given by

$$O_{nm} \approx \bar{O} \delta_{nm} + \frac{1}{\sqrt{\mathcal{D}}} R_{nm}, \quad (1.14)$$

up to $1/D$ corrections, where R_{nm} is a random variable with zero mean and finite variance, and $\bar{O} = \text{tr}(\hat{O})/\mathcal{D}$ is the infinite-temperature equilibrium value of \hat{O} . From this point of view, the ETH can be understood as saying that eigenstates of thermal Hamiltonians basically behave as random states. Moreover, this connection suggests that the level statistics of systems satisfying the ETH should follow the Wigner-Dyson distributions $P_\beta(s)$ when considering sufficiently small energy windows. In fact, this is the case for generic systems and it has become a standard numerical approach to study the level spacing distribution, and referred to the system as *chaotic*, if it is of the Wigner-Dyson type. If so, one then expects the ETH to be satisfied, at least in the weak sense. Hence, it is also common to find chaotic as a synonym of ergodic, and also as a synonym of *non-integrable* as we will discuss in a later section.

1.1.3. Emerging classical hydrodynamics

The problem we are concerned is a complex one because of two reasons: (1) We are dealing with systems that involved many interacting degrees of freedom, which leads to an exponential growth of the Hilbert space with system size; and (2) we want to understand the emergence (or absence) of thermalization, which potentially requires tracking those exponentially many parameters for long times. These two difficulties strongly limit the numerical methods we can use [97] and makes difficult to apply analytical techniques. Nevertheless, there exist certain situations for which a universal answer can be predicted. That is the case of systems with continuous symmetries [98–102]. As they will play a crucial role in this thesis, let me recall before continuing that for every continuous symmetry — that is, a transformation $\hat{U} = \exp(i\theta\hat{Q})$ of the system that acts at all times, — there exists an associated conserved quantity \hat{Q} usually written as a sum of local densities, that is independent of time and that in fact, generates the symmetry

⁶The former refers to the exact result, which lacking a closed analytic form can be to a good degree approximated by the latter.

transformation⁷. The symmetry (and hence the conserved quantity) is called global, if it acts on the whole system. For physical systems, these generally include energy and particle number. However, in this thesis we will extend such conservation laws to less conventional ones.

Let us now consider a thermalizing system which only conserves the total particle number, and prepare a finite-energy density initial state with a local excess of this quantity somewhere in the system. At short times — at reach using several numerical and analytical techniques— interactions among the particles quickly entangle the degrees of freedom on local sub-regions, maximizing the local entropy and the subsystem reduced density matrix becoming thermal. At this time, the system has reached local equilibrium with the chemical potential, or equivalently the particle density, slowly varying in space. In fact, in the absence of conserved quantities, one expects this to decay exponentially in time: Such a finite-energy initial configuration has a large number of available physical processes, usually called channels, into which decay [98]. However, particle number is conserved, and this excess cannot simply disappear locally, but has to spread over the system. This is governed by the continuity equation $\partial_t n(\mathbf{x}, t) = -\nabla_{\mathbf{x}} \mathbf{j}(\mathbf{x}, t)$, where $n(\mathbf{x}, t)$, $\mathbf{j}(\mathbf{x}, t)$ are coarse-grained expectation values of the particle density and current operators. Since at equilibrium the density distribution is homogeneous, a gradient of density creates a current flow $\mathbf{j} = -\mathbf{f}(\nabla n, \nabla n^2, \dots)$ which can be expanded in powers of density gradients allowed by the symmetries of the system. Assuming that $n(x, t)$ only varies at long length scales, we find Fick’s law $\mathbf{j} \propto -\nabla n$ and hence charge is diffusively transported throughout the system. Thus, a classical hydrodynamic description can capture the relaxation of an isolated quantum many body system to the global equilibrium state with quantum properties merely entering the effective diffusion constant. Alternatively, one can probe such slow modes by studying the evolution of density-density correlators $\langle \hat{n}(\mathbf{x}, t) \hat{n}(\mathbf{0}, t) \rangle_{\text{eq}}$ evaluated on a thermal equilibrium state (see e.g., Ref. [98]). These relax according to same diffusion equation as do induced non-equilibrium fluctuations. In the presence of additional conserved quantities, one will generically find a set of coupled differential equations. E.g., a gradient of density can cause an energy flow or viceversa. In any case, the resulting hydrodynamic equation defines a “scaling fixed point” [99] solution relative to which one should investigate the relevance of other contributions that are allowed by symmetry. If all those are indeed irrelevant, the resulting equation contains the leading order contributions describing how the system relaxes. Moreover, while we have discussed diffusive transport, other universal hydrodynamic classes exist ranging from sub- to super-diffusive transport. In fact, understanding and validating this physical picture is an active area of research with theoretical [99, 103–110] and experimental [111–113] contributions. Specially relevant for us are the experimental results in Ref. [113] when discussing the late-time dynamics of systems with dipole conservation in Chapter 5. An introduction to classical hydrodynamics can be found in Refs. [100, 101, 114].

1.2. Dynamical probes of interest

Apart from tracking the evolution of local observables and their expectation value on energy eigenstates as probes of thermalization, we will also consider the evolution of unequal-time correlation functions and the growth and saturation of the half-chain entanglement entropy. Moreover, out-of-time-ordered correlators, so-called OTOCs, have also been used as signatures of chaos in quantum systems [115].

⁷This was the content of Noether’s theorem linking symmetries and conservation laws [49].

1.2.1. Thermal correlations and Mazur's bound

In the following chapters we will study how local-perturbations propagate throughout the system via unequal-time correlation functions $\langle \delta \hat{O}_j(t) \delta \hat{O}_i(0) \rangle_{\text{th}}$ where we have defined $\delta \hat{O}_j \equiv \hat{O}_j - \langle \hat{O}_j \rangle_{\text{th}}$ for some local observable \hat{O}_j evaluated for a thermal density matrix. Here i, j are two different sites of the lattice and $\hat{O}_j(t) = e^{it\hat{H}} \hat{O}_j e^{-it\hat{H}}$ is Heisenberg's time evolution. Such correlations probe the off-diagonal contribution of the ETH, where fluctuation-dissipation relations at the level of a single eigenstate can be derived (see Section 6.8 of Ref. [21]). In particular, we will focus on infinite-temperature correlations $\langle \cdot \rangle = \frac{1}{D} \text{tr}[\cdot]$ where D is the dimension of the Hilbert space on which the trace is evaluated.

In general, we can use Mazur's bound [116] (see also Refs. [117]) to lower bound its long-time average. While for ergodic systems this bound vanishes in the thermodynamic limit, there exist certain circumstances, as the ones we will find in Chapter 2 of this thesis, where this bound (and its scale with system size) becomes finite. Given a set of conserved quantities $\{\hat{Q}_\alpha\}$, Mazur's bound $M_{\hat{O}_j}$ is given by

$$\lim_{T \rightarrow \infty} \frac{1}{T} \int_0^T dt \langle \delta \hat{O}_j(t) \delta \hat{O}_j(0) \rangle \geq \sum_{\alpha, \beta} \langle \delta \hat{O}_j, \hat{Q}_\alpha \rangle (K^{-1})_{\alpha, \beta} \langle \hat{Q}_\beta, \delta \hat{O}_j \rangle \equiv M_{\hat{O}_j}, \quad (1.15)$$

where K is the the matrix with elements $K_{\alpha, \beta} = \langle \hat{Q}_\alpha, \hat{Q}_\beta \rangle$. In particular, this formula simplifies whenever $\{\hat{Q}_\alpha\}$ form an orthogonal set with respect to the inner product $\langle \cdot \rangle$ such that $K_{\alpha, \beta} = \langle \hat{Q}_\alpha, \hat{Q}_\beta \rangle \delta_{\alpha, \beta}$. This bound can be proven quite generically for both classical and quantum systems as long as the infinite-time average value of $\langle \hat{O}_j(t) \hat{O}_j(0) \rangle$ is non-negative [116]. Indeed, this is the case for the unitary evolution of closed quantum systems we investigate in Chapters 2 and 3, as well as for the classical dynamics we consider in Chapters 5 and 6. The proof of the latter is given in Appendix D.

1.2.2. Bipartite entanglement entropy

Complementary information to that provided by two-point correlation functions can be obtained from tracking the evolution of the bipartite entanglement entropy when starting from a low-entangled initial state $|\psi_0\rangle$. Let us consider a 1D system with L sites and let's split it into a region A and its complement A^c . Then, the bipartite entanglement entropy is given by the von Neumann entropy of any of its reduced density matrices $S(\hat{\rho}_A) \equiv -\text{tr}(\hat{\rho}_A \log(\hat{\rho}_A)) = S(\hat{\rho}_{A^c})$, which is a measured of quantum entanglement between the two subsystems. As we already explained, a closed quantum system will thermalize, if it is efficient in maximally entangling its degrees of freedom. In particular, most of the time we will be interested in the half-chain entanglement entropy which we write $S_{L/2}(t)$. Let's moreover assume the initial state has energy E (with subextensive fluctuations) and that the system eventually thermalizes with inverse temperature β . Then, $\hat{\rho}_A(t) \rightarrow \text{tr}_{A^c}[\hat{\rho}_{\text{th}}]$, and hence we find that $S(\hat{\rho}_A)(t) \rightarrow s_{\text{eq}}(\beta) V_A$ converges to the (extensive) thermal entropy at inverse temperature β . The scaling of the entanglement entropy with the volume of the region is known as *volume law* scaling, in comparison to the *area law* of ground states of gapped Hamiltonians [86]. If in particular we choose an initial state in the middle of the spectrum (i.e., $\beta = 0$), canonical typicality (introduced in Section 1.4.1) will tell us that the late-time-evolved state behaves as a random state. Don Page [118] showed that the average entanglement entropy of a random state is given by

$$S^{\text{Page}} \simeq \log(\text{dim}(\mathcal{H}_A)) - \frac{\text{dim}(\mathcal{H}_A)}{2\text{dim}(\mathcal{H}_{A^c})}, \quad (1.16)$$

with $1 \ll \dim(\mathcal{H}_A) \leq \dim(\mathcal{H}_{A^c})$. In particular, for a half partition, i.e., $\dim(\mathcal{H}_A) = d^{L/2}$ for a system with local Hilbert space dimension d , this becomes

$$S_{L/2}^{\text{Page}} \simeq \frac{L}{2} \log(d) - \frac{1}{2}. \quad (1.17)$$

Notice the finite deviation from the largest possible bipartite entanglement entropy. Recently, this result has been extended to other families of random states. Ref. [119] showed that a larger deviation than the one computed by Page can appear as a consequence of a constrained Hilbert space, of special interest for us. This could be interpreted as saying that a subsystem has more information regarding the global state than in an unconstrained system. On the other hand, Ref. [120] considered sparse random states, which while not assuming a specific constrained, have non-zero elements on a fractal size of the full Hilbert space, i.e., $(\dim(\mathcal{H}))^\alpha$ for $0 < \alpha \leq 1$. When $\alpha = 1$ these correspond to the random states considered by Page, but when $\alpha < 1$ these are “non-ergodic” states which have support only on a vanishing fraction of the Hilbert space. The authors showed that even when $\alpha < 1$, their bipartite entanglement entropy can still be given by Eq. (1.17). Consequently, the entanglement entropy takes a thermal value even though the wave function is not spread over the whole Hilbert space. Hence, using this quantity to probe thermalization could be misleading and complementary analysis is required.

The approach to this extensive scaling of $S(\hat{\rho}_A)(t)$ from a low-entangled initial state is generally believed to be linear in time $S(\hat{\rho}_A)(t) \sim t$ for non-integrable systems [121], even while energy is diffusively transported. While this expectation is mostly based on numerical evidence, a more rigorous proof of this fact has been shown for integrable systems [122–125]. Here, the physical interpretation is that entangled quasi-particles pairs forming the highly excited initial state, ballistically propagate throughout the system entangling further and further spatial regions.

Finally, since diagonal-ETH implies that energy eigenstates are thermal, their bipartite entanglement entropy coincides with the equilibrium entropy, i.e., they have volume law entanglement. Specifically, $S_{L/2}(|E_n\rangle) = s_{\text{th}}(T, \dots) \frac{L}{2}$, where $s_{\text{th}}(\beta, \dots)$ is the thermodynamic entropy density at inverse temperature β fixed by the eigenvalue E_n . In particular, for an infinite temperature state, $S_{L/2}(|E_n\rangle)$ is given by the average entropy of a random pure state [118]. This provides an additional diagnostic of the ETH that we use in this thesis.

1.3. Many body localization and weak-ergodicity breaking

While the ETH and quantum thermalization appear to hold for a large class of quantum systems, not all systems thermalize. One class of systems that avoid thermalization are integrable systems (see Ref. [126] for a discussion of the notion of quantum integrability), which possess infinitely many extensive conserved quantities. Nonetheless, they have been argued to thermalize to a Generalized Gibbs ensemble that includes extensively many (but not all) (quasi-)local conserved quantities [127]. However, these are fine-tuned (exactly solvable) models [128] which thermalize, as defined above, in the presence of small perturbations which break integrability.

The other class of systems that avoid thermalization and do not fulfill the ETH (in any useful formulation) are systems that localize in the presence of sufficiently strong spatial disorder. The phenomenon of localization in quantum systems was realized by P.W. Anderson [129] when dealing with the behavior of a non-interacting system in the presence of a disorder potential. It turns out that in one-dimension —our main focus on most of the subsequent chapters — energy-eigenstates are exponentially localized at a particular site of the lattice, and the system does not transport neither energy nor charge.

However, it was not clear how robust localization is to the presence of interactions. Many years later Refs.[34, 130] showed that the localized phase survives to the presence of weak interactions and the existence of a new type of quantum phase transition. This takes place when varying the disorder strength or the energy density, separating a thermal phase, in which all eigenstates obey ETH and the system thermalizes; and the many-body localized (MBL) phase, where all eigenstates do not obey ETH and the system does not thermalize. Hence this quantum phase transition takes place even at the level of many-body eigenstates, with equilibrium quantum thermodynamics breaking down on one of the sides. Importantly, while there is also no transport of energy and charge, the bipartite entanglement entropy now grows in the MBL phase, although logarithmically in time for short-range models [131]. This saturates to a volume law value which does not correspond to a thermal entropy density at the corresponding temperature. This behavior is usually taken as a defining property, and will be important in the discussion of the results in Chapter 4.

In this thesis, we are particularly interested in the characterization of the MBL phase in terms of local integrals of motion (lioms [51] or l-bits [50]), that will be confronted to the statistical localized integrals of motion that we will uncover in Chapter 3. In the strong disorder regime and for weak tunneling rates, the MBL system can be diagonalized by the action of a quasi-local — unlike for ergodic systems— unitary which brings the Hamiltonian to the form

$$\hat{H}_{\text{MBL}} = \sum_i h_i \hat{\tau}_i^z + \sum_{i<j} J_{ij} \hat{\tau}_i^z \hat{\tau}_j^z + \sum_{i<j<k} J_{ijk} \hat{\tau}_i^z \hat{\tau}_j^z \hat{\tau}_k^z + \dots, \quad (1.18)$$

where the coefficients decay exponentially with the distance ($J_{ij} \propto J_0 e^{-|i-j|/\kappa}, \dots$), and the operators $\{\hat{\tau}_i^z\}$ are the lioms, whose eigenstates completely specified a single eigenstate of \hat{H}_{MBL} . Moreover, from this construction one can deduce that a MBL system preserves an infinitely-long lived memory of the initial state which explicitly shows that indeed the system avoids thermalization. Refs. [132–134] are reviews that provide a more extended discussion of the MBL phase as well as the MBL-to-ergodic phase transition. Moreover, we notice that there is currently an ongoing debate about the MBL phase being a truly robust phase of matter in the thermodynamic limit [135, 136].

Encouraged by this exception to quantum thermalization, there has been an increasing interest to understand whether localization can appear in the absence of disorder, as well as to find scenarios which not being completely localized, do also fail to thermalize for certain initial states. While different scenarios have been discussed in the literature, here we focus on quantum many-body scars as these will be related to the systems we study in Chapter 3. There already exist two available review articles on the topic [137, 138], the first of which we followed in this brief presentation.

The experimental results for a 1D array of interacting Rydberg atoms presented in Ref. [43], showed significant differences in the dynamics depending on the choice of the initial state. While certain initial states relaxed to thermal ensembles, others exhibited periodic revivals. Such revivals were unexpected given that the system did not have any conserved quantities other than total energy and it was free of disorder. To understand the underlying reason explaining such experimental observations it is necessary to first explain the experimental setup. Each individual Rydberg atom can be in the ground state $|\circ\rangle$ or in the so-called Rydberg state $|\bullet\rangle$. When subject to a microwave field, each atom undergoes Rabi oscillations, $|\circ\rangle \leftrightarrow |\bullet\rangle$, freely flipping between the two states. However, when assembled in an array, nearby atoms in the Rydberg state interact via repulsive van der Waals interactions whose strength strongly depends on the distance between atoms. By tuning the inter-atom distance, one can achieve the regime of the so-called Rydberg blockade [139] where Rydberg excitations of neighboring atoms are energetically prohibited. Such kinetic

constraints can be captured by the idealized “PXP” model, which approximately describes the experimental findings in the regime of strong Rydberg blockade. This is given by

$$\hat{H}_{\text{PXP}} = \sum_i P_{i-1} X_i P_{i+1}, \quad (1.19)$$

where $P_i = |\circ\rangle\langle\circ|_i$ and $X_i = |\bullet\rangle\langle\circ| + |\circ\rangle\langle\bullet|$. The analysis of its spectrum provided the key insight to understand the cause of the revivals. This was rooted to the presence of a vanishing fraction of non-thermal eigenstates in the highly excited energy spectrum, hence providing an example of weak ergodicity breaking. In fact, it is worth mentioning that this Hamiltonian is an instance of the general construction introduced in Ref. [42] for examples of weak-ergodicity breaking. Such eigenstates were dubbed quantum many-body scars in analogy to the quantum scars found in the quantization of classical periodic orbits [140]. In Chapter 3 we will find that precisely the same dynamics emerges in a rather different context. This will explicitly connect the phenomenon of quantum many-body scars to Hilbert space fragmentation.

Finally, as we address in the concluding Chapter 7, the physics we uncover in Chapter 2 appear to be related to the disorder free localization phenomenon appearing in lattice gauge theories [38, 39, 141].

1.4. Simulating quantum many-body dynamics

1.4.1. Numerical methods and canonical typicality

Classical numerical simulations of quantum interacting many-body systems are limited to rather small system sizes when aiming to simulate the system exactly, or to short time scales when certain approximations, as it is the case for the use of tensor networks, are performed [97, 142]. The main approach that we use in this thesis is exact diagonalization (ED). This simply means that we construct the full Hamiltonian matrix representation in the appropriate Hilbert space. When our goal is to access the whole energy spectrum, as to e.g., validate the ETH, this requires us to store the whole matrix elements in memory, which limits the system sizes we can simulate. This depends on the local Hilbert space dimension. For example, for models with spin- $\frac{1}{2}$ degrees of freedom one can simulate system sizes as large as $L \approx 16$ sites. Alternatively, if we are only interested in probing the system dynamics, and since the Hamiltonians we are interested are local, i.e., have sparse matrix representations, we can use efficient Krylov space based numerical methods [143] to compute $e^{-i\hat{H}t}|\psi_0\rangle$ via vector multiplication, reaching $L = 28$ sites [144]. Both of these approaches substantially benefit from the use of conserved quantities, that will play a special role in this thesis. It is relevant to notice that most of the evidence we have about thermalization of quantum many-body systems and the validity of ETH is based on numerical results using ED.

As we said, in this thesis we will make use of the rich structure that the conserved quantities we investigate yield. Then, instead of constructing the full Hilbert space as a tensor product of local ones, we will directly obtain the matrix representation of \hat{H} restricted to a given symmetry subspace. Moreover, we will simulate the evolution of the two-point correlation functions $\langle\delta\hat{O}_j(t)\delta\hat{O}_i(0)\rangle_{\text{eq}}$ at infinite temperature. At first glance this requires to evolve the observable \hat{O}_j in the Heisenberg picture and then compute exponentially many overlaps $\langle\delta\hat{O}_j(t)\delta\hat{O}_i(0)\rangle$ in some given basis. Instead, we will use the fact that the reduced density matrix of the overwhelming majority of pure states, drawn according to the uniform measure on the appropriate Hilbert space (which is induced by the Haar measure [145]), agrees with the canonical thermal matrix. In Chapter 3 we will call such pure states *Haar random states* (see Appendix B.2). This result is known as

canonical typicality [146, 147], and can also be used to compute other properties of the system [148, 149]. The main ingredient is that the subsystem of interest is much smaller than its orthogonal complement. If so, fluctuations among different random states are exponentially small in the system size. In particular, sampling a random state in the full Hilbert space approximates the infinite temperature ensemble that we will study in Chapter 2. For additional details about the numerical implementation see Ref. [149], and Appendix B.2 for relevant analytic formulae.

We note that typicality arguments date back to Schrödinger and von Neumann when trying to justify the methods of statistical mechanics (see review [22] for an extended discussion). From this point of view, quantum equilibration appears as the overwhelming likelihood that an initial atypical — although physical — state moves towards typical configurations and almost never comes back.

1.4.2. Experiments with ultracold atoms

An alternative and perhaps more promising approach is to directly simulate these systems in the lab. The experimental revolution of the recent years has given rise to new platforms that allow for a great level of tunability of the system parameters, which to a high degree can be regarded isolated from its environment. This provides a new arena to study the physics of many body interacting systems, going beyond observing existing materials and pure academic curiosity. In particular, we focus on ultracold atoms in optical lattices, where some of the theoretical results we report in Chapters 2 and 3 can be investigated. In the following we provide a brief description of the main physical principles and techniques underlying this experimental platform, which is mostly based on review Refs. [8, 150, 151].

Ultracold atoms in optical lattices offer a way to design artificial materials. The crystal structure and the electronic cloud of the conventional material are now replaced by a crystal structure made of light and a confined gas of neutral alkali atoms, respectively. The latter are atoms with a single valence electron and hence with total spin angular momenta $S = 1/2$ in its ground state. The former is synthesized via two counter-propagating laser beams which couple to the induced dipole moment of the atoms shifting their energy $\Delta E \propto |\mathcal{E}(x)|^2 = V_0 \sin^2(kx)$ (the so-called AC Stark shift), where $|\mathcal{E}(\mathbf{x})|^2$ is the intensity of the laser beam and the lattice depth V_0 is usually given in units of the so-called recoil energy E_r . This denotes the change in kinetic energy associated with the emission or absorption of a photon with momentum k : $E_r = \frac{\hbar^2 k^2}{2m}$. Hence, the depth V_0 of the potential and the lattice spacing can be freely tuned, the latter by interfering laser beams at different relative angles. This gives rise to lattice spacings that are of the order of 10^4 times larger than in real materials (of the order of the angstrom), and a number of different techniques can be used to characterize them [152, 153]. This also translates into a much smaller density of particles n : 10^{14}cm^{-3} versus 10^{23}cm^{-3} in conventional materials. Being so, one might worry that we are far from being able to probe purely quantum phenomena, like Bose-Einstein condensation, which requires the average interparticle distance $n^{-1/3}$ to be of the size of the thermal de-Broglie wavelength $n\lambda_{\text{dB}}^3 \gtrsim 1$. However, exceptional cooling techniques in combination from an almost perfect isolation via a vacuum chamber, permit to reach really low temperatures on the order of the nano Kelvin, allowing us to investigate this quantum regime. The experimental results discussed in Chapter 4 are for a degenerate Fermi gas of ^{40}K atoms, where the relevant energy scale is instead $T/T_F \approx 0.15$ [3, 154], where T_F is the Fermi temperature. Finally, interactions between atoms remarkably simplify at such low temperatures and particle densities, and are extremely sensitive of the spin state of the valence electrons. This can be used to widely tune the interaction strength via a Feshbach resonance by tuning an external magnetic field. In conclusion, we have now a highly tunable and rather isolated system, hosting of the order of 10^4 interacting atoms which are confined in a periodic lattice potential. As

such, we can also apply the same tools as in standard solid systems and obtain a tight-binding Hamiltonian in terms of localized Wannier functions. Here the strength of the hopping amplitude is controlled by the lattice depth V_0 . This yields lattice models that are amenable to numerical and analytical studies. The measurement protocols for the experimental results presented in Chapter 4 are described in detail in Refs. [3, 4].

Part I.

Hilbert space fragmentation

2. Ergodicity breaking arising from Hilbert space fragmentation in dipole-conserving Hamiltonians

Experience teaches that we will be led to new discoveries almost exclusively by means of special mechanical systems.

Ludwig Boltzmann from *Lectures on gas theory* [155].

In this chapter, we study the consequences of dipole conservation associated with a global $U(1)$ charge (i.e., the conservation of total spin S^z) in one-dimensional (1D) spin systems, for which a numerical study is feasible. Apart from fracton systems, such charge and dipole conserving Hamiltonians also occur naturally in other contexts, for example in the quantum Hall effect [70, 71, 73, 74, 156] and in systems of charged particles exposed to a strong electric field [76, 157]. Interestingly, Ref. [158] argued that random local unitary dynamics with such symmetries fails to thermalize. We find the same non-ergodic behavior in a minimal Hamiltonian that contains only three-site interactions. We discover that the source of this non-ergodicity is an extensive fragmentation of the Hilbert space into exponentially many disconnected sectors in the local z -basis. In particular, based on the Hilbert space structure, we obtain a lower bound for the long-time auto-correlation, which remains finite in the thermodynamic limit. This is a novel type of non-ergodic behavior, arising in a translation invariant system, but nevertheless sharing certain features of MBL, which we denote by *strong fragmentation* of the Hilbert space.

However, we find that this strongly non-ergodic behavior disappears once we add longer-range interactions, such as a four-site term. In this case, the dipole constraint is no longer sufficient to violate ergodicity, and the infinite temperature autocorrelator decays to zero. Nevertheless, the model still violates the strong version of ETH and exhibits exponentially many non-thermal eigenstates, disconnected from the bulk of the spectrum, and co-existing with thermal eigenstates at the same energies. We term this behavior, which is reminiscent to quantum many-body scars, *weak fragmentation* and give an analytical lower bound on the number of product eigenstates for arbitrary finite range of dipole-conserving interactions. We compare our results to random unitary circuit dynamics, and find the same behavior: while circuits constructed from three-site gates fail to thermalize, adding four-site gates is sufficient to delocalize the system and lead to thermalization for typical initial states. We numerically verify that the invariant subspaces for Hamiltonian and random circuit dynamics coincide exactly.

This chapter is organized as follows. In Section 2.1 we introduce the Hamiltonians we study, and describe their relevant symmetries. In Section 2.2 we investigate the minimal model containing only three-site interactions and show that it fails to thermalize. We prove that the Hilbert space fragments into exponentially many invariant subspaces, some of which we construct analytically, and connect these to the finite saturation value of the auto-correlation function. In Section 2.3 we extend the model by adding four-site interactions and show that while these are sufficient to make the majority of eigenstates thermal—leading to ergodic behavior for typical initial states—the system still violates strong ETH. In Section 2.4 we compare our results to random unitary circuit dynamics

and find similar behavior. We conclude in Section 2.5 with a summary and discussion of the results which takes into account recent developments of the field.

2.1. Model and symmetries

We consider two spin-1 Hamiltonians on a chain of length N of the form

$$H_3 = - \sum_n \left[S_n^+ (S_{n+1}^-)^2 S_{n+2}^+ + \text{H.c.} \right], \quad (2.1)$$

and

$$H_4 = - \sum_n \left[S_n^+ S_{n+1}^- S_{n+2}^- S_{n+3}^+ + \text{H.c.} \right], \quad (2.2)$$

acting on three and four consecutive sites, respectively. Here S^\pm are raising and lowering spin operators. Apart from being translation and inversion symmetric, both Hamiltonians share two additional global symmetries: they conserve a U(1) charge Q and its associated dipole moment P_{n_0} :

$$Q \equiv \sum_n S_n^z \quad \text{and} \quad P_{n_0} \equiv \sum_n (n - n_0) S_n^z, \quad (2.3)$$

with respective eigenvalues q and p defining the symmetry sector $\mathcal{H}_{q,p}$ [159]. The definition of the dipole symmetry P_{n_0} depends on the reference position n_0 , except when $Q = 0$. Since $[Q, P_{n_0}] = 0$, the local S^z -basis, denoted by $|+\rangle, |0\rangle, |-\rangle$, is a common eigenbasis of Q and P_{n_0} . Unless specified otherwise, we choose open boundary conditions and take $N = 2m + 1$ odd, labeling sites $n = -m, \dots, 0, \dots, m$. For periodic boundary conditions, the discussion would be similar to that of the position operator on a ring [160], and one would have to define the dipole moment through the unitary operator $\exp(i\frac{2\pi}{N}P)$. However, the choice of boundary conditions does not affect the dynamics at finite times in the thermodynamic limit. We choose the reference site n_0 to be the center site, $n_0 = 0$, and denote $P \equiv P_{n_0=0}$. The operator P does not commute with spatial translations and changes sign under inversion; thus, it is not an internal symmetry [66]. Dipole conservation is the relevant global symmetry appearing in the description of fracton phases of matter with U(1) symmetry group [60–66]. Motivated by this, we use the following notations: we call the states $|\pm\rangle$ on a given site a *fracton* with charge $q = \pm 1$, and a two-site configuration $|+-\rangle$ ($|-+\rangle$) a *dipole* with zero charge and dipole moment $p = -1$ ($+1$). Notice that the dipole moment of a (\pm) -fracton on a site n is $p = \pm n$. Thus, in order to conserve the total dipole moment, a fracton can only move by emitting dipoles [60, 158].

Moreover, there are symmetries which are specific for Hamiltonians H_3 and H_4 separately. In particular, the former is invariant under the sublattice parity symmetry $\Pi_{\text{odd}}^z = \exp(i\pi \sum_{n \text{ odd}} S_n^z)$, which is fixed by the dipole moment $\Pi_{\text{odd}}^z = \exp(i\pi P)$ ¹. From this it is clear that the total parity $\Pi^z = \exp(i\pi \sum_n S_n^z)$ is obtained as $\Pi^z = \Pi_{\text{odd}}^z \Pi_{\text{even}}^z$ and is related to the total charge as $\Pi^z = \exp(i\pi Q)$. In general, the terms in H_3 are also invariant under the parity transformations given by $\Pi^x = \exp(i\pi \sum_n S_n^x)$ and $\Pi^y = \exp(i\pi \sum_n S_n^y)$, which map

$$S_{n_1}^+ S_{n_2}^- S_{n_3}^- S_{n_4}^+ \xrightarrow{\Pi^x, \Pi^y} S_{n_1}^- S_{n_2}^+ S_{n_3}^+ S_{n_4}^- \quad (2.4)$$

for all n_1, n_2, n_3, n_4 . However, both Π^x and Π^y anticommute with Q or P . Finally, the unitary $\mathcal{C} = \exp[i\pi \sum_n (S_{4n}^z + S_{4n+1}^z)]$ anti-commutes with H_3 , but commutes with

¹we have used the fact that for spin-1 a 2π -rotation is equal to the identity.

both Q and P . Consequently, the spectrum of H_3 is symmetric around zero in every (q, p) -sector. The same holds true when H_4 is considered separately (in this case the unitary is given by $\mathcal{C}_4 = \exp i\pi \sum_n S_{4n}^z$), but not for the combined Hamiltonian $H_3 + H_4$. These anti-commuting symmetries can also be broken by adding terms diagonal in the S^z basis, which would not change any of the physics, in terms of non-ergodicity, we will describe in the following. There is also at least one additional anti-commuting operator $\tilde{\mathcal{C}} = \prod_n e^{i\pi(S_{4n+2}^z + S_{4n+3}^z)}$ but since $\mathcal{C}\tilde{\mathcal{C}} = \Pi^z$, they are not independent.

We note in passing that similar charge and dipole-conserving Hamiltonians can be written for any spin representation, in any spatial dimension, as well as for fermionic and bosonic systems. For the latter, the dipole symmetry becomes the center of mass of the particle number operator and the corresponding Hamiltonian consists of a symmetric redistribution of charges with respect to the center sites. A similar fermionic Hamiltonian appears in the study of fractional quantum Hall on a torus in the Tao-Thouless limit [70, 71, 73, 74, 156]. In addition, such dipole-conserving chains naturally arise in the presence of strong electric fields, as we will be discussed in Chapter 4.

2.2. Hamiltonian H_3

We start by investigating the three-site Hamiltonian H_3 in Eq. (2.1), as a minimal model that conserves both the total charge Q and the dipole moment P . We detail its unusual non-ergodic dynamics and identify it as a consequence of extensive fragmentation of the Hilbert space into invariant subspaces. In Section 2.3 we will add longer-range terms to this minimal model and describe their effect on the dynamics.

2.2.1. Lack of thermalization

We first investigate the behavior of the auto-correlation function $C_0^z(t) \equiv \langle S_0^z(t) S_0^z(0) \rangle$ at infinite temperature, namely $\langle \cdot \rangle = \frac{1}{\dim(\mathcal{H})} \text{tr}[\cdot]$. Relying on quantum typicality [148, 161, 162], we compute $C_0^z(t)$ for a random state on the full Hilbert space. For thermalizing and translational invariant spin-1 systems, $C_0^z(t)$ is expected to decay to $2/(3N)$ for a chain of length N , up to potential boundary contributions [163]. In Figure 2.1(a) we show $C_0^z(t)$, obtained via an iterative Krylov space based algorithm [143], for system sizes $N = 13, 15$. Instead of relaxing to the thermal expectation value, the auto-correlation saturates to a finite value $C_0^z(t) - 2/(3N) \sim 0.2$ at long times. In Appendix A we also analyze the behavior of the auto-correlation function within the largest charge and dipole sector (given by $(q, p) = (0, 0)$) showing the same qualitative behavior. Moreover, the long-time values appear to be largely independent of N , indicating truly localized behavior that persists even in the thermodynamic limit. Figure 2.1(b) shows the spatially resolved correlation function $\langle S_n^z(t) S_0^z(0) \rangle$, which exhibits a peak in the center site at all times.

We complement our analysis on auto-correlations with a different measure of thermalization: the evolution and scaling of the saturation value of the bipartite entanglement entropy $S_{L/2}$. We generate initial states Haar randomly generated on each site, i.e., a random product state but not necessarily in the local z -basis, and average over several realizations. For an ergodic system, the long-time state will resemble a global random state in the entire Hilbert space and thus, the bipartite entanglement entropy is expected to agree with the Page value, which in our case (maximal bi-partition of a spin-1 chain with odd lengths) reads [118] $S_{\text{Page}} = \frac{N-1}{2} \log 3 - \frac{1}{6}$. We evaluate the time evolution starting from the aforementioned random product states exactly for the minimal Hamiltonian H_3 . As shown in Fig. 2.2(a), we find that while the entanglement quickly saturates to a volume law $S_{L/2} = s \frac{L}{2}$, the associated entropy *density* is smaller than the expected Page value ($s < \log(3)/2$). This is consistent with our results on auto-correlation functions in

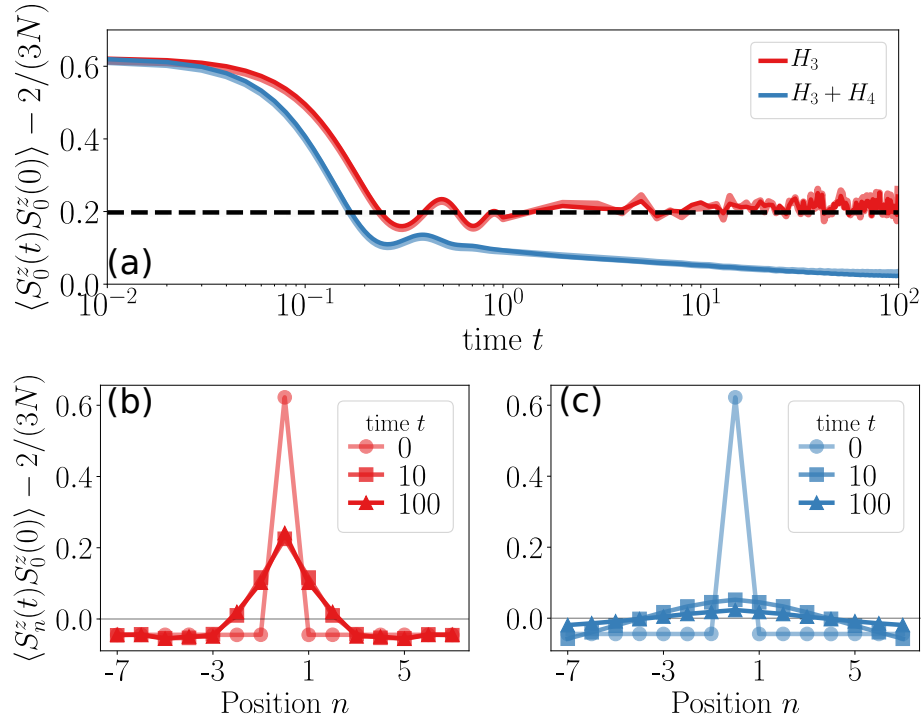


Figure 2.1.: **Thermalization and its absence in the auto-correlation function.**

Panel (a) shows the auto-correlation function $C_0^z(t) \equiv \langle S_0^z(t)S_0^z(0) \rangle$ in the full Hilbert space at infinite temperature for $N = 13$ (transparent curves) and $N = 15$ (opaque curves) spins. For Hamiltonian H_3 in Eq. (2.1), $C_0^z(t)$ saturates to a finite value at long times, closely matching the lower bound in Eq. (2.5) (dashed line). The auto-correlation function of the combined Hamiltonian $H_3 + H_4$ decays to zero at long times. Panels (b) and (c) show the spatially resolved correlator $\langle S_n^z(t)S_0^z(0) \rangle$ for H_3 and $H_3 + H_4$ respectively.

Fig. 2.1, signaling non-ergodic behavior. In the following we explain the origin of this behavior.

2.2.2. Hilbert space fragmentation

In this section, we demonstrate that the constrained dynamics of H_3 leads to a *fragmentation* of the many-body Hilbert space: Most (q, p) symmetry sectors split into many smaller invariant subspaces in the local S^z -basis, such that the total number of such subspaces grows exponentially with system size. These disconnected sectors come in a variety of different sizes; they include ‘frozen’ states (product eigenstates of H_3) and finite dimensional subspaces, where the chain splits into spatially disconnected regions. In chapter 3, the cause of this fragmentation will be explained and a complete labeling of all these invariant subspaces will be provided. But before that let us get some intuition about their existence.

Frozen states

We begin by constructing a family of exponentially many (in the size of the system) exact eigenstates of the Hamiltonian, which are all product states in the local z -basis. We will refer to these as *frozen states*. What is shocking is not the fact that these many-body eigenstates exist, but rather that their number scales exponentially with system size. In fact, any Hamiltonian with an extensive U(1) symmetry, for example generated by particle number or total magnetization, will at least have two of them corresponding

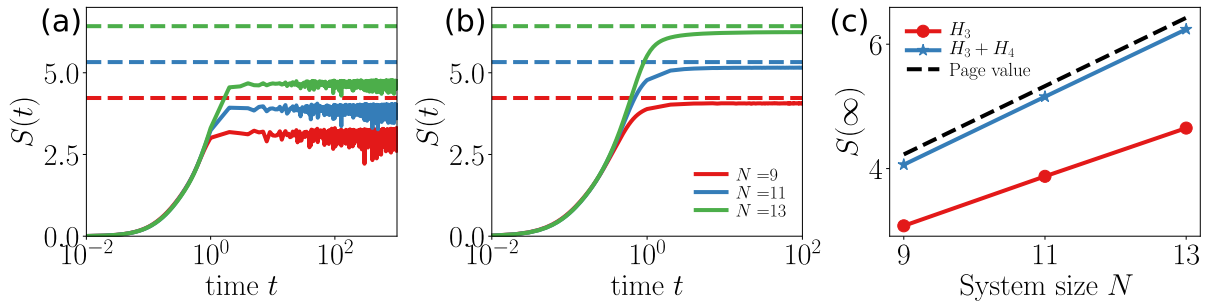


Figure 2.2.: **Evolution of the bipartite entanglement entropy.** Half-chain entanglement entropy (EE) for an initial random product state for different system sizes. The dashed line signals the Page value [118] numerically computed using random pure states. Panel (a) shows the behavior of the EE for the minimal model H_3 . The entanglement reaches a volume-law saturation value below the Page value. When the combined Hamiltonian $H_3 + H_4$ is considered in panel (b), the EE almost reaches the Page value. (c) Scaling of the time-averaged saturation value for EE reached at long times.

to the largest and smallest eigenvalues of the associated conserved quantities. For H_3 , the simplest example is the *vacuum* state $|0\rangle \equiv |\cdots 0000 \cdots\rangle$, which is annihilated by all terms in H_3 , due to $(S^\pm)^2|0\rangle = 0$. We can easily construct other frozen states by adding blocks of at least two contiguous charges of equal sign on top of the vacuum, e.g., $|0 \cdots 0 + + 0 \cdots 0 - - - 0 \cdots\rangle$. These are annihilated by all terms, since $S_n^+ S_{n+1}^- |\pm \pm\rangle = 0$. We conclude that any configuration where charges always occur in blocks of at least two consecutive sites are zero energy (mid-spectrum) eigenstates of H_3 . It is clear from the construction that their number is exponentially large in system size.

We can follow Pauling [164, 165] to estimate the total number of frozen states. To do this, we map the spin chain of length N to a triangular ladder with spins placed on the vertices as shown in the inset of Fig. 2.3(a). Treating the constraints on each triangle as independent, and using that there are $N - 2$ triangles and 19 frozen states per triangle, we estimate their total number to be $3^N \times (19/27)^{N-2} \approx 2.02 \times 2.11^N$. In Fig. 2.3(a), we numerically verify that the estimate is quite close to the actual number of frozen states, as obtained by exact diagonalization. The numerical results together with an explicit computation for small system sizes, suggest that this estimate gives a lower bound of the actual number of frozen states. However, we do not have a proof of this general statement. Nevertheless, in Section 2.3.2 we provide an analytical lower bound for arbitrary finite-range dipole-conserving Hamiltonians.

Larger dimensional sectors

Above we saw that blocks of two or more consecutive charges of equal sign are annihilated by the local terms in H_3 that act on them. Let us now consider the empty region ($|00 \cdots 0\rangle$) between two such frozen blocks and fill it with a random configuration of charges. These charges can now move around and potentially destroy the blocks on the two sides. However, we now argue that there are initial configurations where this *cannot* happen: when the sign of the rightmost charge within the region matches the charge of the frozen block to its right, then this block remains inert at all times. The same holds for the frozen block on the left when its charge is of the same sign as the leftmost charge within the region. When the charges match on both sides, then both blocks are stable and the charges in the middle bounce back-and-forth between them, disconnected from the rest of the chain. This appears as a direct consequence of the general rule: *For a region surrounded by*

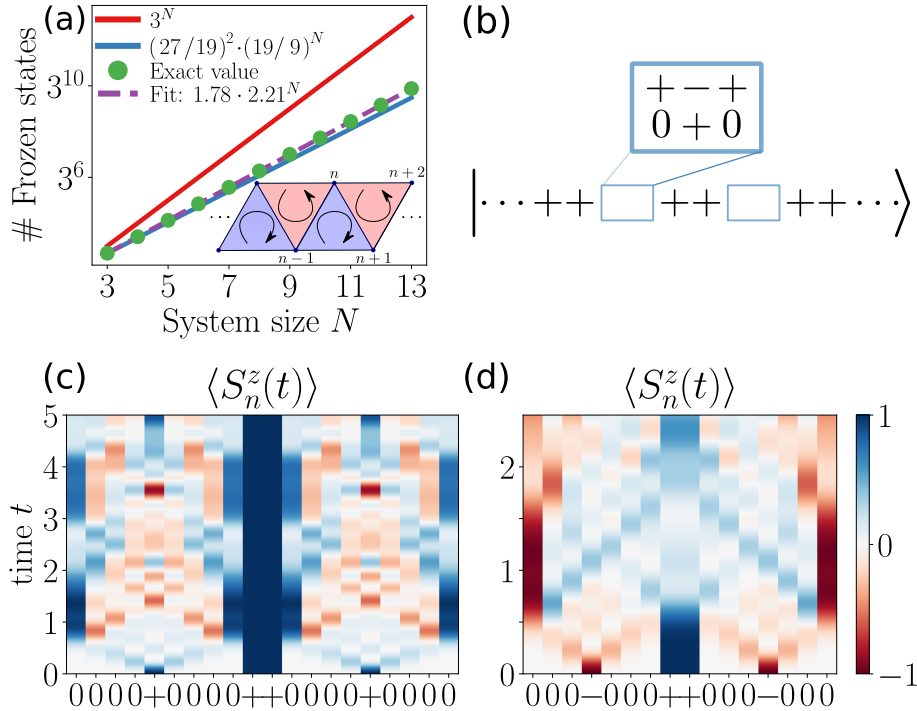


Figure 2.3.: **Fragmentation of the Hilbert space into smaller subspaces.** (a) Exponential scaling of frozen states, which correspond to invariant subspaces of dimension $D = 1$, and comparison to the Pauling estimate, (b) example of higher dimensional sectors, in the form of spatially separated 2-level ‘bubbles’. (c-d) Time evolved charge density $\langle S_n^z(t) \rangle$ for the two initial states indicated under each figure. (c) The $++$ block in the middle cuts the system in half when $(+)$ -fractons are placed on each side. (d) When they are replaced by $(-)$ -fractons, the block melts and the two halves become connected.

empty sites, the signs of the left- and rightmost charges are invariant under the dynamics generated by H_3 . Notice that this rule is broken by H_4 .

The simplest example where we can observe this behavior is as a 2-level system shown in Fig. 2.3(b), defined by the states $|++0+0++\rangle$ and $|+++ - + + +\rangle$. We can check that these two states can only evolve to each other under H_3 , defining a 2-dimensional invariant subspace. More generally we can consider states of the form $|++0 \dots 0+0 \dots 0++\rangle$: An isolated fracton surrounded by two ‘walls’ of positive charge. Acting on this state with H_3 , maps the configuration $00+00$ in the middle to $0+ - +0$, showing that the $(+)$ -fracton can move by emitting a dipole $+-$ (or $-+$) in the opposite direction [60, 158]. The fracton can then move forward by emitting further dipoles, until it reaches one of the walls. However, when it eventually hits the wall, we end up with the configuration $+++$, which is annihilated by H_3 ; the wall therefore remains intact and the fracton bounces back harmlessly. Consequently, if the fractons on both sides of a $++$ block have positive charge, the chain is cut into two disconnected halves, as shown in Fig. 2.3(c). To destroy the wall, we would need to flip the charge of the isolated fracton to get a $(-)$ -fracton: the resulting $-++$ configuration can then peel off a freely-moving $-+$ dipole, eventually melting the walls that surround it as shown in Fig. 2.3(d).

A similar situation occurs for the initial configuration $|--0 \dots 0-+0 \dots 0++\rangle$. In this case the walls on the two sides have opposite charges and a single dipole is placed between them. For a single dipole surrounded by empty sites, the Hamiltonian H_3 acts as a free hopping term $H_3 \rightarrow -\sum_n |n\rangle\langle n+1| + |n\rangle\langle n-1|$, moving the dipole from sites n to $n \pm 1$. Eventually it reaches one of the surrounding walls, but since the charges in the dipole

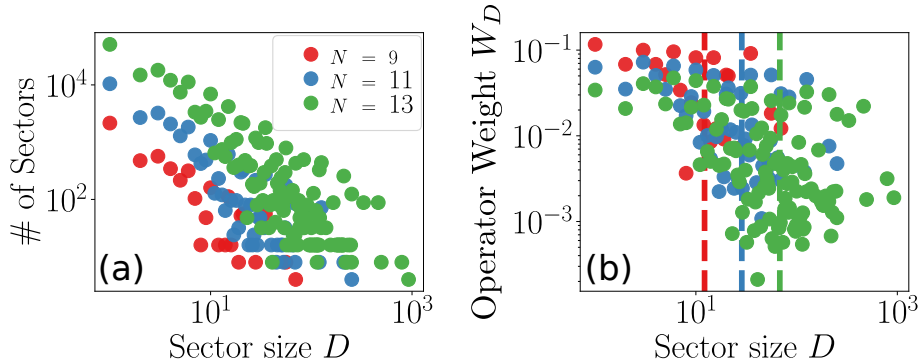


Figure 2.4: **Sector size and weight distributions.** (a) Distribution of invariant subspaces of size D and (b) operator weight W_D (see text for its definition) of the operator S_0^z in each invariant subspace \mathcal{H}_i of dimension D in the full Hilbert space. The vertical dashed lines indicate the averaged sector size of the distribution, which is exponentially smaller than the largest sector.

are aligned with those of the walls, it always bounces back, effectively defining a single particle hopping problem on a finite region. If, on the other hand, the initial dipole in the middle was of the form $+-$ it could again peel off charges from the two walls, eventually melting them.

The previously stated general rule, together with the fact that blocks with a given charge are frozen, allow us to construct more general spatially disconnected regions in the chain: take an arbitrary configuration in some finite interval and surround it with walls that have the same charge as the one closest to them on the inside. One can then cover the entire chain with such regions, each of which has its own conserved charge and dipole moment, giving rise to many invariant subspaces within each global (q, p) symmetry sector. In the following we will indistinctly refer to them as fragments, Krylov subspaces or sectors, or simply as invariant subspaces when the context is clear. After the dipole quantum number is fixed, translation/inversion symmetry is generically broken (as the dipole moment does not commute with neither of those symmetry transformations), which allows us to derive conservation laws within different spatially disconnected regions. In fact, this intuitive idea would be the key to completely identify and label the fragments in the following chapter. The resulting eigenstates clearly break translation invariance and have small amounts of entanglement, limited by the size of the largest connected spatial region.

These constructions highlight the intertwined relation between dipole conservation, spatial translations, and locality. Our construction also shows that in order to determine which invariant subspace a given initial configuration belongs to, one has to consider it on the entire chain: even if a certain region looks initially frozen, it can eventually be melted by additional charges coming from the outside. This indicates that it might not be possible to systematically label all invariant subspaces in terms of quantum numbers of *local* conserved quantities, as it would be the case for a lattice gauge theory (see chapter 3).

Distribution of dimensions of invariant subspaces

Above we explicitly constructed invariant subspaces of H_3 of various dimensions within given (q, p) symmetry sectors. The distribution of these invariant subspaces can be studied by numerically identifying the connected components of the Hamiltonian written in the S^z basis. In particular, given a Hamiltonian \hat{H} , we want to get the block-diagonal structure of its matrix representation H in some particular basis $\{|e\rangle_i\}_{i=1}^{\dim(\mathcal{H})}$ of the many-body Hilbert (Fock) space \mathcal{H} . To do so, we can view H as the adjacency matrix of a graph and use a standard algorithm to find its connected components. The resulting distribution is plotted

in Fig. 2.4(a), showing exponentially many sectors with a broad distribution. In fact, the number of sectors has been recently proved to scale as $\frac{1}{\sqrt{2}}(\sqrt{2}+1)^{L+1}$ [166]. We point out that since the sectors are obtained in the local z -basis, they remain invariant under any perturbation that is diagonal in this basis. However, such diagonal perturbations would have the effect of changing the energy of the different frozen states, moving them away from zero energy, and distributing them throughout the entire spectrum.

Based on the constructions in the previous section, we infer that the existence of these invariant subspaces is a consequence of the interplay between the conservation of dipole moment (which fails to commute with translation and inversion) and the locality of interactions. In particular, in Section 2.3.2 we prove that exponentially many invariant subspaces exist for any extension of the model that only involves dipole-conserving interactions with finite range.

We close this section by noting that, apart from the overall fragmented structure of the Hilbert space, which is our main concern in this chapter, there is also the possibility of interesting dynamics *within* certain connected components. For example, as we will show in the next chapter, there are particular subspaces where the Hamiltonian H_3 maps exactly to the so-called PXP Hamiltonian [167], studied in the context of quantum many-body scars [44, 168]. A similar mapping has been uncovered in a spin-1/2 version of this model in a related work [169].

2.2.3. Saturation value of $C_0^z(t)$

Equipped with the knowledge of the fragmented Hilbert space structure, we are now able to explain the long-time value of the auto-correlation function observed in Fig. 2.1(a). To this end, let us define \mathcal{P}_i as the projection onto the Krylov subspace \mathcal{H}_i . These projectors form an orthogonal set of conserved quantities ($\mathcal{P}_i\mathcal{P}_j = \delta_{ij}\mathcal{P}_i$), such that one can use Mazur's inequality [116, 126, 170] to lower bound the infinite time average of the charge auto-correlator as

$$\lim_{T \rightarrow \infty} \frac{1}{T} \int_0^T dt \langle S_0^z(t) S_0^z(0) \rangle \geq \sum_i \frac{[\text{tr}(Z_i)]^2}{3^N D_i} \equiv C_0^z(\infty), \quad (2.5)$$

where $Z_i \equiv \mathcal{P}_i S_0^z \mathcal{P}_i = \mathcal{P}_i S_0^z$ is the projection of S_0^z onto \mathcal{H}_i , and $D_i = \text{tr}(\mathcal{P}_i)$ is the dimension of the Krylov subspace.

The bound $C_0^z(\infty)$ is shown in Figure 2.1(a) for $N = 15$ by the dashed horizontal line; we observe that it is close to being tight, indicating that the main cause of the lack of ergodicity is indeed the fragmentation of the Hilbert space. We computed the estimated value for $C_0^z(\infty) - 2/(3N)$ for a variety of different system sizes, and found that the result appears to remain finite in the thermodynamic limit, even increasing slightly with N for the system sizes available in our numerics (blue dots in Fig. 2.5).

Since the \mathcal{H}_i 's are invariant and disjoint subspaces, the weight of the operator S_0^z within a given Krylov subspace, $\text{tr}(Z_i^2)$, remains constant under time evolution. Therefore, we introduce the operator weight $W_D \equiv \sum_{D_i=D} \text{tr}(Z_i^2) / \text{tr}[(S_0^z)^2]$ as a function of the sector size D for all invariant subspaces \mathcal{H}_i . This defines a probability distribution, shown in Fig. 2.4(b). We find a wide distribution with significant weight on small sectors, in sharp contrast to for example, systems with whose global symmetry sectors are fully connected. While the number of frozen states scales as $\sim 2.2^N$, the size of the largest sector in the entire Hilbert space scales as $\sim 1.9^N$, both much smaller than the total dimension 3^N . This suggests that sectors of all sizes have significant contributions to the evolution of $S_0^z(t)$, even in the thermodynamic limit. We also confirm the same behavior when considering only the largest symmetry sector $(q, p) = (0, 0)$ (see Appendices A.1 and A.2); this emphasizes the relevance of the fragmentation within each (q, p) -sector.

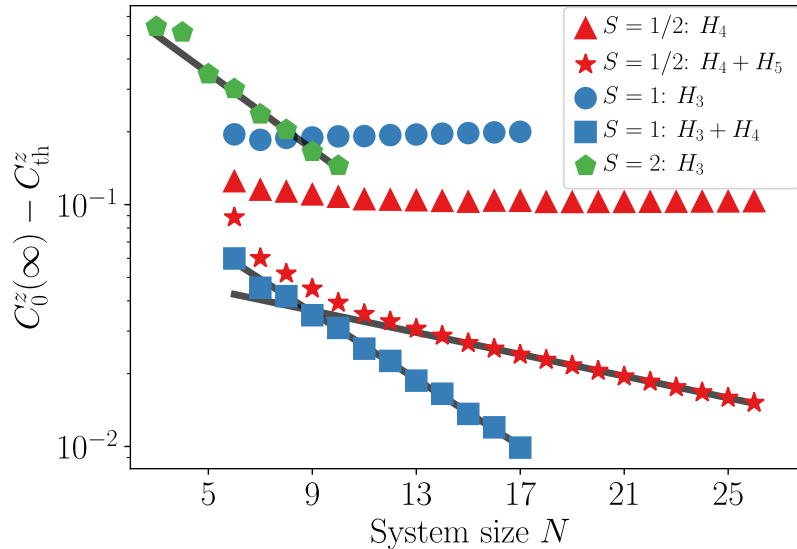


Figure 2.5.: **Saturation value of the autocorrelator.** Finite-size study of the lower bound in Eq. (2.5) for the time-averaged correlation function $C_0^z(t)$ as a function of system size. We have subtracted the thermal value $C_{\text{th}}^z \equiv \frac{1}{N} \text{tr}[(S_0^z)^2]/((2S+1)^N)$ for a general spin S and a chain of length N . For the minimal spin-1 model H_3 (blue dots) the lower bound is slightly increasing with system size. On the other hand, it decays to zero exponentially for the combined Hamiltonian $H_3 + H_4$ (blue squares). For comparison, we also show results for other local spin S : the larger the on-site Hilbert space dimension, the easier it is for the system to thermalize [171].

2.3. Combined Hamiltonian $H_3 + H_4$

So far we have only considered the ‘minimal model’, defined by the Hamiltonian H_3 in Eq. (2.1). We will now investigate to which extent the features found above are robust against local perturbations that preserve the symmetries Q and P .

2.3.1. Thermalization for $H_3 + H_4$

In the following, we add the four-site terms defined in Eq. (2.2) and consider the combined Hamiltonian $H_3 + H_4$. We find that, while this Hamiltonian shares certain features with H_3 —in particular, it has exponentially many invariant subspaces—it nevertheless thermalizes at infinite temperature. Indeed, the auto-correlation function $C_0^z(t)$ for the Hamiltonian $H_3 + H_4$ decays to zero at long times, in contrast to the dynamics governed by H_3 alone; see Fig. 2.1 for a comparison. This is accompanied by the spatially resolved correlation function, $\langle S_n^z(t) S_0^z(0) \rangle$, becoming approximately homogeneous at long times, as shown in Fig. 2.1(c). The remaining small peak is due to finite size effects, as we show in Appendix A.2. Moreover, as shown in Fig. 2.2.(b), an initial random product state evolving under $H_3 + H_4$ leads to the thermal (Page) value of the half-chain entanglement entropy at long times, providing an additional indication that the system thermalizes. There is still a constant offset, which we associate to the influence of the remaining non-thermal eigenstates whose fraction vanishes in the thermodynamic limit, but this does not affect the entropy density in the thermodynamic limit. This qualitative difference suggests that the Hilbert space structure uncovered in Section 2.2.2 is affected by adding H_4 to the Hamiltonian. Figure 2.6(a) compares the distribution of sector sizes D for $H_3 + H_4$ (blue stars) with the minimal Hamiltonian H_3 (red dots). While exponentially many invariant

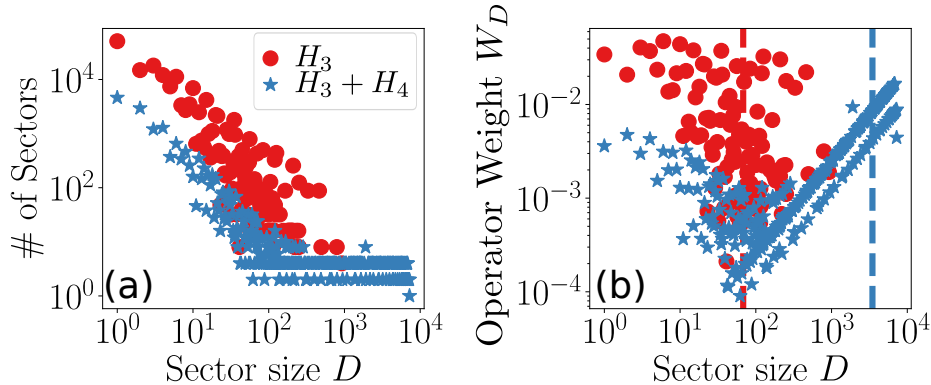


Figure 2.6.: **Comparison of the Hilbert space connectivity.** (a) Sector size distribution for H_3 (red dots) and $H_3 + H_4$ (blue stars). (b) The operator weight W_D distribution for S_0^z is qualitatively different, dominated by large sectors in the latter case.

subspaces still exist, their total number is drastically reduced, as many previously disconnected sectors are coupled to each other by the perturbation H_4 . Thus the number of sectors of small dimension D decreases and there are new larger blocks appearing; in fact, the largest global symmetry sector, $q = p = 0$, becomes almost (but not exactly) fully connected, as we discuss in Section 2.3.3. This effect is even more apparent in the distribution of the operator weight W_D (defined in Section 2.2.3) for the operator S_0^z , which we show in Fig. 2.6(b). Most of the weight is now concentrated around the largest sector, similarly to the case of a single global U(1) symmetry. Thus, even though invariant subspaces within symmetry sectors still exist, they do not appear to be sufficiently relevant to make the system non-ergodic. This is also reflected in the long-time value of the auto-correlation function as predicted in Eq. (2.5): plugging in the invariant subspaces of $H_3 + H_4$ we find that $C_0^z(\infty)$ approaches the thermal value, $2/(3N)$, exponentially fast in the size of the system, as shown in Fig. 2.5.

From these results we infer that including longer-range interactions makes the system sufficiently ergodic to thermalize. One possible reason for this qualitative difference is that the 4-site terms break the rule stated at the beginning of Section 2.2.2: *For a region surrounded by empty sites, the signs of the left- and rightmost charges are invariant under the dynamics.* A clear counter-example to this rule is the fact that the state $|0000\rangle$ can be mapped via H_4 to both the $|+ - - +\rangle$ and $|- + + -\rangle$ configurations. This then allows for the destruction of blocks of charges that would be inert under the dynamics of H_3 . A different path to break the non-ergodicity of H_3 would be to increase the local Hilbert space dimension, making the dynamics less constrained. Consequently, we expect that for larger spin, even a three-site Hamiltonian of the form (2.1) would lead to thermalization. Indeed, computing the lower bound $C_0^z(\infty)$ for the charge autocorrelator using Eq. (2.5) for H_3 acting on a spin-2 chain, we find that it decays to zero in the thermodynamic limit, as shown in Fig. 2.5. Similarly, if we consider spin-1/2 chains, the shortest range non-trivial model is H_4 , which appears to be non-ergodic, while adding 5-site interactions restores ergodicity. In fact, the Hilbert space structure of this system for spin-1/2 has been analyzed in detail in Ref. [172].

2.3.2. Constructing frozen states

While the combined Hamiltonian $H_3 + H_4$ appears thermalizing at infinite temperature, it nonetheless violates the strong version of the Eigenstate Thermalization Hypothesis [29–31, 33]. In particular, certain frozen states continue to exist not only for $H_3 + H_4$, but

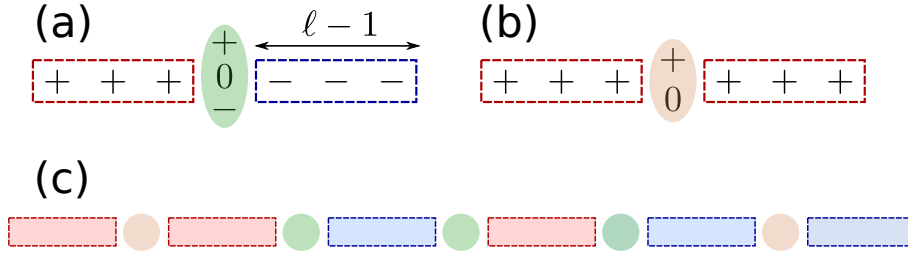


Figure 2.7.: **Constructing frozen states for arbitrary finite-range interactions.**

For interactions of maximal range ℓ , one can create frozen patches of $2\ell - 1$ sites with a flippable spin surrounded by domains of (a) opposite or (b) the same charges (shown here for $\ell = 4$, relevant for $H_3 + H_4$). These can then be combined to cover the entire chain, resulting in exponentially many frozen states, such as the one in panel (c).

even in the presence of longer finite-range interactions. In fact, as we now prove, for a spin-1 chain that conserves charge and dipole, and involves only local terms with range at most ℓ , there exist at least $2 \cdot 5^{N/\ell}$ frozen states. While for $\ell = 3$ this lower bound is not as tight as the Pauling estimate discussed in Section 2.2.2, it provides useful insight into generic longer-range Hamiltonians and can be generalized to any spin representation.

We begin our construction by considering the configuration shown in Fig. 2.7(a) for $S = 1$, with a center site surrounded by a block of $\ell - 1$ (+)-fractons on one side and $\ell - 1$ (-)-fractons on the other. We now prove that this configuration is an eigenstate of any dipole-conserving term with range at most ℓ , where without loss of generality we can measure the dipole moment relative to the center site. It is sufficient to consider off-diagonal terms (in the z basis), consisting of spin raising and lowering operators. Due to the way we constructed the state, the only such terms that do not annihilate it are those that have only S^- on one side and S^+ on the other. However, any such term would lead to a change in the dipole moment and is thus prohibited. Terms only acting on the center site do not change P but they are also excluded due to charge-conservation. We conclude that this configuration is frozen, independently of the state of the center spin, as promised.

Next, we consider a similar configuration, but one where the center spin is surrounded by blocks of the same, rather than opposite, charges, as shown in Fig. 2.7(b). Let these blocks be made out of (+)-fractons. Then the only off-diagonal operators that can act on them are powers of S^- , decreasing the total charge Q . One has to compensate for these charges by adding additional charges on the center site. Therefore the only allowed terms that could change this configuration are of the form $(S_{-n}^-)^q (S_0^+)^{2q} (S_n^-)^q$ for some $q \in \mathbb{N}$. For $S = 1$, only terms with $q = 1$ ² can update the state and only when the central spin is occupied by a (-)-fracton. When it is either 0 or +, the state is frozen.

One can combine these two types of ‘frozen patches’ we constructed above to cover the entire 1D chain, resulting in a globally frozen state. These states are made up by blocks of + or - charges, with a single site between any two consecutive blocks, as shown in Fig. 2.7(c). As we showed above, these sites host “flippable” spins: the ones separating blocks of equal charge can take two values (e.g + or 0 between blocks of + charge), while those that separate blocks of opposite charge can be in any of the 3 possible spin states. This construction then results in exponentially many frozen states, coming from both the possible arrangements of \pm blocks and from flipping the spins between blocks within a given arrangement.

We can count the total number of frozen states resulting from this construction iter-

²Notice that terms with $q > 1$ only reduce the number of “flippable” configurations of the central spin.

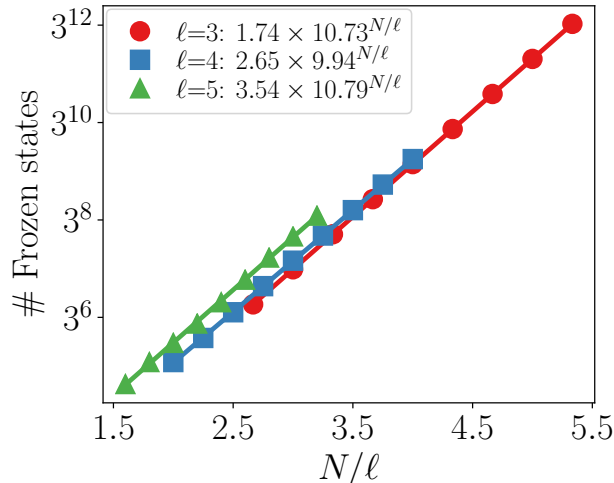


Figure 2.8.: **Scaling of the number of frozen states for Hamiltonians with at most range ℓ terms.** We consider Hamiltonians with all possible combinations of charge and dipole conserving terms, quartic in spin operators of range at most ℓ , for $\ell = 3, 4, 5$. The number of frozen states grows exponentially with system size N , with an exponent that decreases with ℓ , but is larger than the analytical lower bound $2 \cdot 5^{N/\ell}$.

atively, starting from the left edge of the system (assuming open boundaries). We cut the systems into blocks of ℓ sites, consisting of a wall of $\ell - 1$ positive/negative charges, followed by a flippable spin. Let F_k^\pm denote the number of different such configurations to the left of the k -th wall (but before the flippable spin), ending in a (\pm) -block. Then the considerations outlined above lead to the following recursion formula:

$$\begin{pmatrix} F_{k+1}^+ \\ F_{k+1}^- \end{pmatrix} = \begin{pmatrix} 2 & 3 \\ 3 & 2 \end{pmatrix} \begin{pmatrix} F_k^+ \\ F_k^- \end{pmatrix} = \begin{pmatrix} 2 & 3 \\ 3 & 2 \end{pmatrix}^k \begin{pmatrix} 1 \\ 1 \end{pmatrix} = 5^k \begin{pmatrix} 1 \\ 1 \end{pmatrix}, \quad (2.6)$$

where we have used that $F_1^+ = F_1^- = 1$, i.e., there is only one possible configuration of each type to start with. Since each step $k \rightarrow k + 1$ corresponds to a shift by ℓ sites, we conclude that the number of frozen states we constructed scales as $2 \cdot 5^{N/\ell}$. This is only a lower bound on the total number of frozen states, which can include other configurations not captured by this construction. In particular one could systematically improve the bound by allowing blocks to be separated by more than one site.

We compare the lower bound $\sim 5^{N/\ell}$ to the numerical results on the number of frozen states for Hamiltonians with interactions of range at most $\ell = 3, 4, 5$ in Fig. 2.8, where we extract the asymptotic scaling. The comparison to numerical data in Fig. 2.8 shows that the scaling is relatively close to $\sim 10^{N/\ell}$ [173]: $10.73^{N/3}$ ($\ell = 3$), $9.94^{N/4}$ ($\ell = 4$) and $10.79^{N/5}$ ($\ell = 5$). Thus, the lower bound is not tight but it proves the exponential scaling of frozen states.

We conclude this section with some comments about the construction we presented. First, while above we did not distinguish between different overall (q, p) -sectors, one could similarly construct frozen states with a given q and p . For example one can apply the construction on only the left half of the chain and for each state repeat the same configuration on the right half to obtain a state with $p = 0$. Second, the bound can be easily extended to chains with local spin $S > 1$. For example one can consider blocks that have maximal positive/negative charge; repeating the same arguments then gives a scaling ³

³Note that the ratio of the estimated number of frozen states, $(2S + 3)^{N/\ell}$, and the total Hilbert space dimension $(2S + 1)^N$, decreases with S for $\ell > 1$.

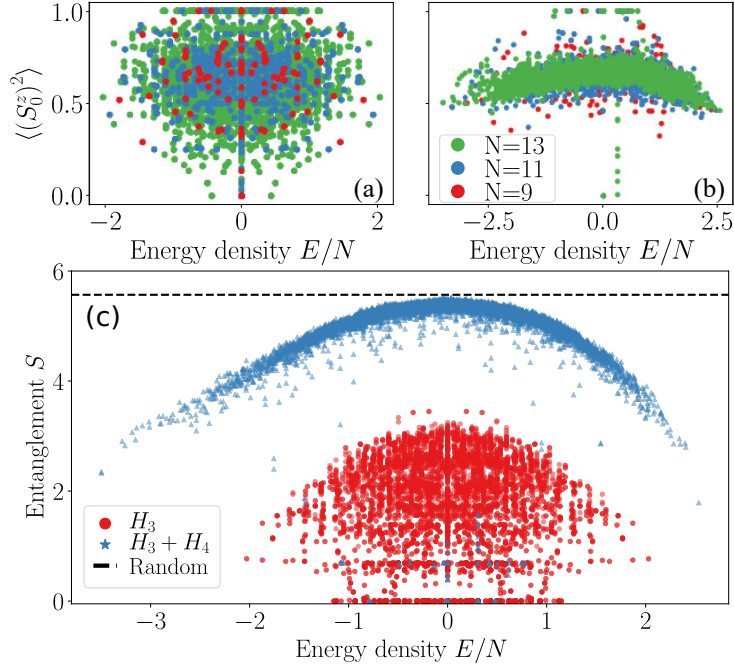


Figure 2.9.: **Ergodicity breaking due to strong and weak fragmentation.** Expectation value of the local operator $(S_0^z)^2$ for eigenstates within the $(q, p) = (0, 0)$ sector as a function of energy for different system sizes. (a) *Strong fragmentation*: for the minimal Hamiltonian H_3 , the width of the distribution does not decrease with N , violating the Eigenstate Thermalization Hypothesis. (b) *Weak fragmentation*: for $H_3 + H_4$ most eigenstates appear thermal, and the bulk of the distribution narrows with N , but outliers remain, showing that the system obeys weak, but not strong ETH. (c) Half-chain entanglement entropy of the eigenstates for H_3 (red dots) and $H_3 + H_4$ (blue stars), for $N = 13$, leads to the same conclusion. The black dashed line shows the entanglement entropy of a random state in the $(q, p) = (0, 0)$ sector.

$(2S + 3)^{N/\ell}$. We note that in the limit $\ell \rightarrow \infty$ the lower bound tends to one, consistent with the fact that for all possible charge and dipole conserving infinite-range interactions every (q, p) sector becomes completely connected.

A natural extension of this construction is to consider dipole-conserving systems with semi-infinite or infinite local Hilbert spaces, as for example bosonic local degrees of freedom ($\hat{b}_i(\hat{b}_{i+1}^\dagger)^2\hat{b}_{i+2} + \text{H.c.}$) and rotor models ($e^{i\theta_i}e^{-2i\theta_{i+1}}e^{i\theta_{i+2}} + \text{H.c.}$) respectively. In the former case one would expect that the fragmented structure, and thus the number of frozen states, depends on the average filling of particles becoming more fragmented at low fillings. On the other hand, the latter is expected to realize no fragmentation and thus having no frozen states.

2.3.3. Strong versus weak fragmentation

As the previous section shows, the combination of dipole conservation and strictly local interactions is sufficient to lead to an emergence of exponentially many dynamically disconnected sectors in the many-body Hilbert space, even after fixing Q and P . While we only showed this rigorously for the case of one-dimensional sectors, we find numerically that others with larger dimension also exist (see Fig 2.6). While both H_3 and $H_3 + H_4$ share this feature, their behavior with respect to thermalization appears to be quite different, as we already observed in Fig 2.1. This motivates us to distinguish two cases, dubbed

weak and *strong fragmentation*, which violate strong and weak ETH, respectively.

Let us first make precise what we mean by violation of ETH. In particular we only analyze the diagonal contribution of ETH, evaluating the expectation value of few-body observables for all eigenstates of the Hamiltonian within a fixed global (q, p) symmetry sector. As explained in Chapter 1, by strong ETH we mean the statement that the expectation values are the same for *all* eigenstates at the same energy density in the thermodynamic limit. Weak ETH, on the other hand, means that this statement only holds up to a small number of outlying states, where ‘small’ means here measure zero in the thermodynamic limit. Here we follow the approach of only fixing (extensive) local symmetries, namely those corresponding to the extensive sum of local contributions, as non-local ones usually do not lead to distinct distributions for the diagonal matrix elements [174–176]. In our case, this means fixing Q and P , but not the additional symmetries that correspond to the invariant subspaces, since we expect these to be non-local. In the next chapters, and after having a deeper understanding of strongly fragmented systems, we will contrast and justify why we follow this approach, instead of for example considering a particular Krylov sector.

Our construction in the previous section then proves that any dipole-conserving strictly local Hamiltonian, has weak fragmentation in the above sense, leading to the existence of non-thermal eigenstates in the middle of the spectrum. Apart from frozen states, these also include other low-entangled eigenstates, stemming from small invariant subspaces, analogous to the ones discussed in Section 2.2.2. Generically, however, their ratio compared to thermal ones is vanishingly small within any energy shell in the thermodynamic limit; this is the case of $H_3 + H_4$ as we argue below. Thus the weak version of ETH [42, 88, 92] is still obeyed, and the system thermalizes for typical initial states, provided they have narrow energy distributions. On the other hand, we argue that the Hamiltonian H_3 , discussed in Section 2.2, has strong fragmentation in the sense that at least a finite fraction of the eigenstates is non-thermal, leading to the manifestly non-thermalizing behavior we observed.

The difference is illustrated in Figs. 2.9(a,b), which shows the expectation value of a simple observable $\langle (S_0^z)^2 \rangle$, where 0 is the central spin) for all energy eigenstates within the (largest) $q = p = 0$ symmetry sector, for H_3 and $H_3 + H_4$. For the combined Hamiltonian, $H_3 + H_4$, the majority of eigenstates, which all belong to the same invariant subspace, behave as predicted by ETH: $\langle (S_0^z)^2 \rangle$ takes similar values for states within a narrow energy shell, with the width of its distribution decreasing with system size. Nevertheless, we also observe outlying eigenstates, stemming from small invariant subspaces, that *do not* approach this line, violating strong ETH. The minimal Hamiltonian, H_3 , on the other hand, violates even the weak version of ETH: the distribution of $\langle (S_0^z)^2 \rangle$ does not become narrower with increasing N , as shown in Fig. 2.9(a). This is in contradiction with ETH, which predicts a vanishing width in the thermodynamic limit. Similar behavior occurs in the half-chain entanglement entropy of the eigenstates, shown in Fig. 2.9(c): the non-thermalizing nature of H_3 is reflected by the fact that the entropies of its eigenstates do not fall on a line (in the thermodynamic limit) when plotted as a function of the energy, instead being distributed over values much smaller than what is predicted at infinite temperature (maximum density of states attained in the middle of the spectrum), as realized by a random state in the $(0, 0)$ sector.

The above discussion suggests that the difference between strong and weak fragmentation can be diagnosed by considering the sizes of the connected subspaces, in comparison with the size of the global (q, p) symmetry sector they belong to. In the strongly fragmented case of H_3 studied above, for a typical (q, p) symmetry sector — those with $q \approx 0, p \approx 0$ — the dimension of the largest connected subspace is exponentially smaller than the dimension of the full symmetry sector, i.e., $\max[D_{(q,p)}^i]/D_{(q,p)} \propto \exp(-\alpha N)$ for

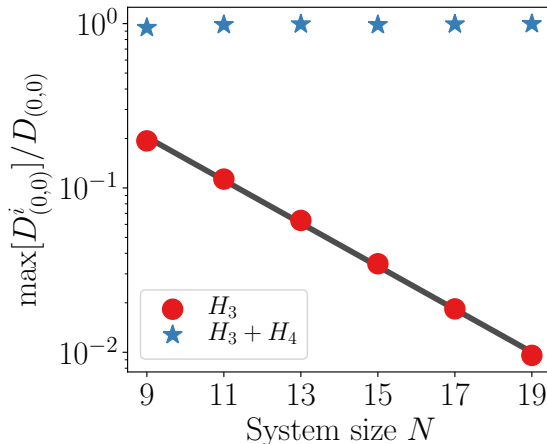


Figure 2.10.: **Diagnosing strong and weak fragmentation.** Ratio between the dimension of the largest invariant subspace \mathcal{H}^i within the $(0,0)$ symmetry sector, and the total dimension of the $(0,0)$ sector $D_{(0,0)}$. For H_3 (red dots), this ratio vanishes exponentially fast with system size while it approaches one for $H_3 + H_4$ (blue stars).

some $\alpha > 0$. Notice that this does not rule out that $\max[D_{(q,p)}^i]$ scales exponentially with the volume of the system, but just implies that its associated fractal dimension (see e.g., Ref. [120]), defined via $\log\{\max[D_{(q,p)}^i]\}/\log[D_{(q,p)}]$, is strictly smaller than one in the thermodynamic limit. In Fig. 2.10 we verify that this is indeed the case for the largest symmetry sector $(0,0)$ of H_3 . We propose that this decay indicates strong fragmentation, naturally leading to the absence of thermalization for physical observables such as the auto-correlation function considered above.

In the weakly fragmented case, the symmetry sectors can still split into many subspaces. However, the largest of these spans almost the entire (q,p) -sector hosting it up to polynomial corrections in the volume of the system: $\max[D_{(q,p)}^i] \approx D_{(q,p)}$. Equivalently, the associated fractal dimension $\log\{\max[D_{(q,p)}^i]\}/\log[D_{(q,p)}]$ tends to one in the thermodynamic limit. Figure 2.10 shows that this is the case for $H_3 + H_4$ for the largest symmetry sector $(0,0)$. Consequently, the vast majority of eigenstates within any energy shell in that sector belong to the same *large* invariant subspace, and look thermal as a consequence. Thus, while weakly fragmented systems violate strong ETH—due to outlying non-thermal eigenstates—they nevertheless thermalize for *typical* (but not all) initial states. This weak fragmentation is reminiscent to what has been observed in other models in the context of *many-body quantum scars*: although the majority of the eigenstates obey ETH, non-thermal eigenstates exist even in the bulk of the spectrum [42, 44, 48, 168, 177]. However, while the number of these ‘scarred’ states is usually $\mathcal{O}(N)$, in our case we find exponentially many such states. Note that the non-thermal eigenstates belonging to low-dimensional invariant sectors in our system have finite overlap with simple product states which can potentially be prepared in experimental settings. This implies that a lack of thermalization up to *infinite times* could be observed, even in the weakly fragmented case, for appropriately chosen initial states.

The main features characterizing strong and weak fragmentation for a symmetry sector (or the relevant Hilbert space) of dimension D^N are summarized in the following table.

Fragmentation	Strong	Weak
# of sectors	$\sim \exp(N)$	$\sim \exp(N)$
Size of largest sector	$\sim d^N$ with $d < D$	$\sim D^N$
Violates*	weak ETH	strong ETH

where \sim indicates the scaling up to logarithmic corrections in the size of the system N , and * refers to the formulations of weak and strong ETH as defined in the text.

In the above we observed that the ratio $\max[D_{(q,p)}^i]/D_{(q,p)}$ either decays (exponentially) to zero or approaches unity. It is an interesting question, whether systems with intermediate behavior—with either slower than exponential decay or convergence to a finite fraction—can exist, and whether they exhibit strong or weak fragmentation. Moreover, a typical symmetry sector being weakly fragmented does not rule out the possibility for some symmetry sectors to be strongly fragmented. In fact, Ref. [178] showed a phase transition between weak and strong fragmentation for $H_3 + H_4$ as a function of the charge density q/N for fixed dipole moment $p = 0$.

2.4. Comparison to random unitary circuits

We now show that our findings are not specific to the Hamiltonians we considered so far, and generalize to arbitrary systems with the same global symmetries and a fixed range of interactions. In particular, we compare with random unitary circuits of the form originally introduced in Ref. [158]. These define a discrete time evolution, the building blocks of which are unitary gates U acting on ℓ sites, each of which is required to be block diagonal in Q and P , but is otherwise chosen randomly. In particular, these gates are represented by $(2S + 1)^\ell \times (2S + 1)^\ell$ dimensional matrices

$$U = \bigoplus_{q,p} U_{q,p}, \quad (2.7)$$

where every block $U_{q,p}$ corresponding to a given charge q and dipole moment p on ℓ -sites is independently Haar random. In particular, for $\ell = 3$ and $S = 1$, the local gates U split up into four 2-dimensional blocks and nineteen one-dimensional ones (i.e., local frozen configurations).

In Ref. [158] it was argued that such circuits always lead to localized behavior. Here we argue that this is in fact only the case for gates with $\ell = 3$ (and $S = 1$), where the circuit exhibits exactly the same Hilbert space structure as the Hamiltonian H_3 above, and is therefore indeed localized. When introducing larger gates of size $\ell = 4$, we find that the system thermalizes, also in complete agreement with our results on the Hamiltonian $H_3 + H_4$.

The two circuit geometries, with gates of size $\ell = 3$ and 4, are shown in Fig. 2.11. In both cases we compute the connectivity of the Hilbert space. Instead of the Hamiltonian, we consider the unitary operator defined by the first ℓ layers of the circuit. This is a matrix with random entries, but its connected components are independent of the particular realizations. We find numerically that the connected components for $\ell = 3$ ($\ell = 4$) coincide *exactly* with those of the Hamiltonians H_3 ($H_3 + H_4$), shown previously in Fig. 2.6. This follows from the fact that the allowed local transitions are the same in the Hamiltonian and the random unitary circuit. The fact that the invariant subspaces coincide supports the idea that the additional invariant subspaces are a consequence of dipole conservation and locality alone, and do not depend on any additional structure that might be present

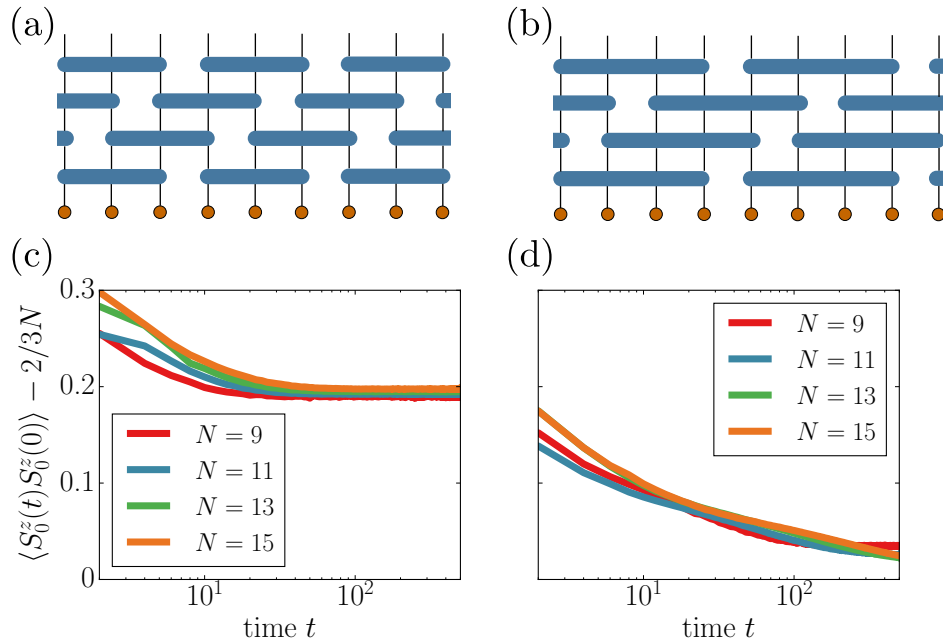


Figure 2.11.: **Thermalization in charge and dipole conserving random circuit models.** The two versions of the circuit, with (a) three-site (b) four-site gates resemble the Hamiltonians H_3 and $H_3 + H_4$ respectively. Consequently, (c) the auto-correlator obtained for the three-site circuit has a finite long-time value, while (d) in the four-site circuit it slowly decays to zero. The curves correspond to the infinite temperature correlator, averaged over 50 random states and circuit realizations for $N \leq 13$ and 20 realizations of $N = 15$.

in the Hamiltonian case. Based on our previous analysis, we therefore expect that the three-site circuit does not thermalize, but the four-site circuit does. This is confirmed by calculating the autocorrelator $C_0^z(t)$, which (after subtracting its thermal value) goes to a constant in the former case, while it decays to zero in the latter, as shown in Fig. 2.11. In Appendix A.3 we also consider the spatial spreading of an initial S_n^z operator and similarly find that for $\ell = 4$ the operator is delocalized at long times. We therefore conclude that the localized behavior observed in Ref. [158] is particular to the case of the circuit with three-site gates, contrary to what was suggested there.

The fact that the Hilbert space fragmentation coincides exactly between the random circuit and Hamiltonian cases also means that the conclusions we drew regarding non-thermal eigenstates in Section 2.3.3 also generalize to time-periodic (Floquet) models built out of similar local gates. In particular this implies the presence of exponentially many frozen eigenstates for such models, especially for the $\ell = 3$ case where we predict that the majority of eigenstates should be nonthermal.

2.5. Summary and discussion

We have studied the out-of-equilibrium dynamics of spin chains conserving a charge and its associated dipole moment. For the minimal spin-1 Hamiltonian which is restricted to only three-site interactions, we found a non-vanishing value of the charge-charge auto-correlation function. We explained this finding in terms of a *strong fragmentation* of the Hilbert space into exponentially many disconnected sectors which all contribute significantly to the dynamics even at infinite temperature. We found that a weaker form of fragmentation survives for more general, longer-range Hamiltonians, and while it is no longer

sufficient to make the infinite-temperature dynamics non-ergodic, it nevertheless results in exponentially many non-thermal eigenstates. Furthermore, we showed numerically that the fragmentation of the Hilbert space exactly matches that of random circuit dynamics with the same range of interactions, giving rise to similar dynamical behavior. In fact, the fragmented structure we studied applies not just to a given k -local Hamiltonian (with a particular choice of microscopic parameters) but rather to the family of Hamiltonians with the same local terms $\hat{H} = \sum_n J_n \hat{h}_n$. To be specific: While we focused on Hamiltonian H_3 (Eq. (2.1)), the family of Hamiltonians (up to arbitrary diagonal contributions in S^z)

$$H_3(\{J_n\}) = - \sum_n J_n \left[S_n^+ (S_{n+1}^-)^2 S_{n+2}^+ + \text{H.c.} \right] \quad (2.8)$$

for a generic choice of couplings J_n , realize the same fragmented structure as H_3 . This implies that the Hilbert space fragmentation we discussed in this chapter, is completely determined by local terms of the Hamiltonian [166] and thus, whatever underlying (non-local) conserved quantities do not depend on the particular choice of $\{J_n\}$, unlike for integrable systems [179]. Nevertheless, the specific choice of couplings $\{J_n\}$ can lead to additional structure and will certainly become relevant when studying the system dynamics. E.g., while a uniform distribution leads to the saturation of Mazur bound (see Fig. 2.1), a random distribution could lead to even more localized dynamics while their fragmented structure match.

The observed fragmentation lies in-between the known cases of systems with a few global symmetries and that of systems with extensively many, like integrable and many-body localized systems. The former have at most polynomially many symmetry sectors in the volume of the system—most of which are exponentially large—while the latter have $\sim N$ independent conserved quantities which are sufficient to identify a many-body energy eigenstate. In our case, however, sectors of all sizes co-exist and in the case of strong fragmentation they all are relevant for the dynamics, even at infinite temperature. Thus, the underlying structure appears more reminiscent to that of super-selection sectors in lattice gauge theories (with finite local Hilbert space dimension for the gauge degrees of freedom). However, unlike for lattice gauge theories, fragments are labeled by the eigenvalues of non-local conserved quantities as we will find in the following chapter.

3. Statistical localization: From strong fragmentation to strong edge modes

... the unfortunate victim collapses spontaneously, with the spontaneous emission of an antitachyon. Happening to be passing, I catch the antitachyon into the barrel of my gun, and so prevent possible injury to other passers-by.

John Stewart Bell from *The nouvelle cuisine* [180].

We have identified the (extensive) fragmentation of the Hilbert space — naturally appearing in dipole-conserving systems with finite-range interactions and finite local Hilbert space dimensions— as a mechanism which leads to non-ergodic behavior even at infinite temperatures. Especially interesting is the case of *strong fragmentation*, where the size of the largest connected sector is exponentially smaller than the total number of states. In the particular example discussed in the previous chapter (Ref. [1]), it was found that this can lead to not only a complete breakdown of ETH, but also to effectively localized behavior in the form of infinitely long-lived autocorrelations, similar to true localization. However, establishing a clear connection between such localization and the structure of the Hilbert space has not yet been addressed.

While Refs. [1, 181] provided a general mechanism for Hilbert space fragmentation and uncovered many of the intriguing features resulting from it, understanding the nature of the corresponding integrals of motion was left as an open question. In the present chapter we uncover these conserved quantities in two illustrative cases, focusing on strongly fragmented Hilbert spaces. We also formulate the general principle behind such conserved quantities and discuss both their similarities and their differences compared to the *localized integrals of motion* (LIOMs) characterizing MBL systems [50, 51, 182, 183] that we briefly introduced in Section 1.3. We first consider a simple example that exhibits strong fragmentation (without conserving dipole moment), where we can illustrate the nature of the integrals of motion in an intuitive and straightforward manner. Later we return to the dipole-conserving minimal model of the previous chapter and identify *all* the conserved quantities that label the components of its strongly fragmented Hilbert space. This is achieved via a non-local mapping to a different model with explicit local constraints. We analytically show that these conservation laws lead to spatial localization and finite autocorrelations in the thermodynamic limit.

A unifying feature of the conserved quantities we uncover is what we name *statistical localization*. These are non-local operators, whose expectation values in typical states pick up contributions primarily from specific spatial regions that are sub-extensive in their size. Unlike the case of LIOMs, this region depends on properties of the quantum state in question; in particular, the models we consider possess a conserved U(1) charge and the localization properties of the new integrals of motion turn out to depend on the overall filling fraction. Moreover, while some of these integrals of motion are effectively localized to finite regions in the dipole-conserving case (much like LIOMs), others are only ‘partially localized’, i.e. they correspond to regions that grow sub-linearly with system size.

Having identified the new conserved quantities, we show that they give rise to another exciting possibility: *statistically localized strong zero modes* localized at the boundaries of

a finite system. These are analogous to the strong boundary zero modes (SZM) discussed in the literature [184–189], but unlike previous instances, they occur in non-integrable systems, co-existing with a completely thermalizing bulk. We explicitly construct such zero modes (which commute exactly with the Hamiltonian even for finite systems), by perturbing the strongly fragmented Hamiltonians in specific ways, destroying the integrals of motion in the bulk, while leaving them intact at the boundaries. The resulting models exhibit similar phenomenology as previously studied cases of SZM, with infinite edge coherence times, as well as *exact* degeneracies throughout the spectrum. Our construction provides an example of *exact* strong zero modes in a non-integrable system, stabilized by the dynamical constraints. We also propose an experimental setup for realizing such models with Rydberg atoms in an optical lattice.

Finally, we discuss how in cases with strong Hilbert space fragmentation, the edge modes can lead to the appearance of highly excited states with non-trivial topological string order. This further reinforces the analogy between strong fragmentation and many-body localization, as the latter can also lead to excited states exhibiting forms of order that are not otherwise allowed at finite temperature [190, 191].

To summarize, our main results are the following.

- We introduce the concept of SLIOMs and illustrate their usefulness for two separate models.
- Using this concept, we construct experimentally relevant non-integrable models with exact strong zero modes at their edges.
- We construct all the SLIOMs for a 3-site dipole-conserving model, and show explicitly that they lead to localized dynamics.
- We show that the same conservation laws protect topological string order in a subset of excited states at finite energy densities.

The remainder of this chapter is organized as follows. In Section 3.1 we provide a detailed discussion of a simple model that exhibits strong fragmentation. We introduce the model in Section 3.1.1 and then construct the full set of conserved quantities that characterize the connected subspaces, using them to illustrate the concept of SLIOMs, which we define in Section 3.1.2. We describe the effect of SLIOMs on thermalization in the bulk and at the boundary in Section 3.1.3, constructing a perturbed model with strong zero modes and a thermalizing bulk. In Section 2.2 we extend our discussion to the strongly fragmented, dipole-conserving Hamiltonian introduced in the previous chapter. We use a non-local mapping to analytically construct the complete set of conserved quantities that describe its fragmentation, and discuss both the similarities and differences compared to the model of Section 3.1. We discuss how the SLIOMs in this case lead to localized dynamics, and discuss the implications for entanglement growth in Section 3.2.3. We comment on the appearance of string order in excited states in Section 3.2.4, and the relation to quantum many-body scars in Section 3.3, before concluding in Section 3.5.

3.1. Illustrative example of SLIOMs: $t - J_z$ model

Here we introduce the main concept of this chapter, that of *statistically localized integrals of motion* (SLIOM), which are non-conventional integrals of motion responsible for the lack of thermalization in the systems we consider. It will be useful to contrast these with the well known case of LIOMs [50, 51, 182], which play a similar role in MBL systems.

Such a LIOM τ_n^z is localized around some given site n in an operator sense: when written as a sum of “physical” operators, $\tau_n^z = \sum_i \mathcal{O}_i^n$, the spectral norm of \mathcal{O}_i^n —

that is the norm induced by the L^2 -norm $\|\cdot\|_2$ on linear operators and is given by $\|\mathcal{O}_i^n\| \equiv \sup_{\psi \neq 0} \|\mathcal{O}_i^n \psi\|_2 / \|\psi\|_2$ — that have support on sites far from n is exponentially suppressed¹. The operators we consider are not localized in this sense: they are equal weight superpositions of operators with supports of all sizes, and then $\|\mathcal{O}_i^n\| \sim \text{const.}$ However, when the expectation values are taken in ‘typical states’ (to be specified below), these values $\langle \mathcal{O}_i^n \mathcal{O}_i^n \rangle$ only pick up contributions from a region that consists of a vanishingly small fraction of the whole system (and whose precise location and width depends on the state in question): hence the term *statistically localized*.

3.1.1. Definition of the model

This general concept is best illustrated through a simple example. We consider a one-dimensional Fermi-Hubbard model under the assumption that the Hubbard on-site repulsion is sufficiently strong as to prohibit double occupancy of sites. In this limit, and after replacing Heisenberg by Ising interactions, one obtains the so-called $t - J_z$ model [192, 193]. In this work we consider the following simplified version of it²:

$$H_{t-J_z} = -t \sum_{\substack{i=1 \\ \sigma=\uparrow,\downarrow}}^{N-1} (\tilde{c}_{i,\sigma} \tilde{c}_{i+1,\sigma}^\dagger + \text{H.c.}) + J_z \sum_{i=1}^{N-1} S_i^z S_{i+1}^z, \quad (3.1)$$

where the dressed fermionic operators $\tilde{c}_{i,\sigma} \equiv c_{i,\sigma}(1 - c_{i,-\sigma}^\dagger c_{i,-\sigma})$ incorporate the hard-core constraint. $\sigma = \uparrow, \downarrow$ is a spin index, and the on-site constrained Hilbert space consists of only three states: $0, \uparrow, \downarrow$, with 0 denoting an empty site. The first term in Eq. (3.1) describes the constrained hopping of fermions and the second term is a nearest neighbor Ising-type interaction with spin operators defined as

$$S_i^\alpha = (\tilde{c}_{i,\uparrow}^\dagger, \tilde{c}_{i,\downarrow}^\dagger) \sigma^\alpha (\tilde{c}_{i,\uparrow}, \tilde{c}_{i,\downarrow})^T \quad \text{with } \alpha = x, y, z; \quad (3.2)$$

where we omit a factor of $1/2$ for later convenience. In our numerics we fix $t = 1$ and take $J_z = 1/4$, avoiding the integrable point $J_z = 0$ [194]. This Hamiltonian conserves both the fermion number, $N_F \equiv \sum_j (\tilde{n}_{j,\uparrow} + \tilde{n}_{j,\downarrow})$, and the total spin, $S_{\text{tot}}^z \equiv \sum_j (\tilde{n}_{j,\uparrow} - \tilde{n}_{j,\downarrow})$, with the number operator defined as $\tilde{n}_{j,\sigma} \equiv \tilde{c}_{i,\sigma}^\dagger \tilde{c}_{i,\sigma}$.

The constrained hopping implies that the dynamics of the model consists entirely of a ‘re-shuffling’ of the hole positions, with the direction of each individual spin always remaining unchanged [195, 196]. Thus, for fixed particle number N_F , any product state in the $0, \uparrow, \downarrow$ basis is characterized by a pattern of N_F spins, each pointing either up or down. This pattern is a conserved quantity: only states with the same spin pattern are connected by the dynamics³. Therefore, the 3^N dimensional many-body Hilbert space fragments into exponentially many (in the size of the system) disconnected sectors completely labeled by the different spin patterns. This provides an (trivial) example of strong fragmentation. Moreover, as pointed out in the previous chapter, these conservation laws are shared among the family of Hamiltonians

$$H(\{t_i\}) = - \sum_{\substack{i=1 \\ \sigma=\uparrow,\downarrow}}^{N-1} t_i (\tilde{c}_{i,\sigma} \tilde{c}_{i+1,\sigma}^\dagger + \text{H.c.}) + J_z \sum_{i=1}^{N-1} S_i^z S_{i+1}^z, \quad (3.3)$$

¹One usually chooses a complete set of basis operators, for example direct products (‘strings’) \mathcal{S} of local Pauli operators in the case of a spin-1/2 chain as we did in Chapter 2. One can then write $\tau_n^z = \sum_{\mathcal{S}} c_{\mathcal{S}}^n \mathcal{S}$; the Pauli strings all have unit spectral norm, so the exponential (in the spatial support of \mathcal{S}) decay is carried entirely by the coefficients $c_{\mathcal{S}}^n$.

²The definition of the $t - J_z$ model usually includes an additional density-density interaction [192]. We drop that term for simplicity, but keeping it would not change the following discussion.

³A classical, discrete time model with the same symmetries was considered in Refs. [197, 198].

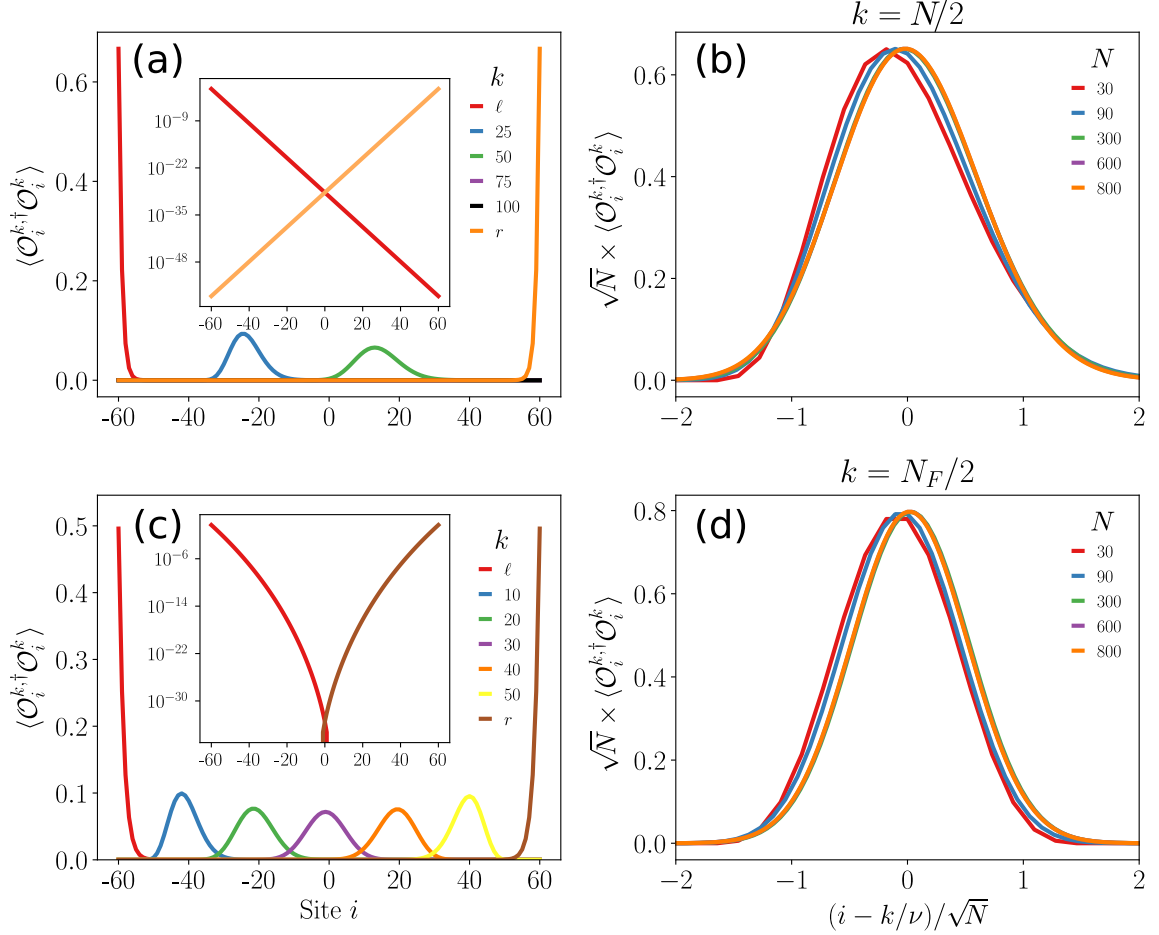


Figure 3.1.: **Statistical locality of SLIOMs.** Expectation value $\langle \psi | \mathcal{O}_i^{k,\dagger} \mathcal{O}_i^k | \psi \rangle$ for the string operators appearing in the definition of SLIOMs $\hat{q}_k = \sum_i \mathcal{O}_i^k$, see Eq. (3.6). The averages are performed over: a Haar random state $|\psi\rangle$ in the full Hilbert space with average filling fraction $\nu = 2/3$ in panels (a,b), and a random state with a fixed filling fraction $\nu = N_F/N = 1/2$ in panels (c,d), evaluated analytically via Eqs. (3.7) and (3.9) respectively. (a,c): In both cases, the k -th particle, is statistically localized around the average position $\bar{i} = k/\nu$. **Inset:** the statistical localization of the boundary SLIOMs \hat{q}_ℓ, \hat{q}_r (defined in Eqs. (3.12) and (3.13)), with at least exponential decay towards the bulk. (b,d): When considering SLIOMs in the bulk, $k \propto N$ ($k = N/2$ for (c) and $k = N_F/2 = N/4$ for (d)), the width of the distribution scales as \sqrt{N} , and the height as $1/\sqrt{N}$.

rather than being a property of a particular microscopic model.

In the following we focus on a chain with open boundaries, where the fermions can be labeled by a number k , starting from either the left or the right edge of the system (we discuss periodic boundary conditions in Appendix B.5). In this case, the dimension of a given sector, regardless of the spin pattern, is $\binom{N}{N-N_F} = \binom{N}{N_F}$, which counts the number of ways to re-shuffle the $N - N_F$ holes. Note that the largest connected sectors are attained for $N_F = N/2$ and there exist 2^{N_F} of those corresponding to different choices of spin pattern. Their dimension scales asymptotically as 2^N (up to logarithmic corrections), and thus it is a vanishing fraction of the full Hilbert space dimension. This also applies when comparing with the dimension of the (typical) global symmetry sectors ($N_F = N/2, S_{\text{tot}}^z$) they are contained in. Their dimension is then given by $\binom{N}{N_F} \binom{N_F}{(S_{\text{tot}}^z + N_F)/2}$ which scales as d^N with $2 < d \leq 2^{3/2}$ for values of S_{tot}^z far from the fully-polarized regimes, i.e., $S_{\text{tot}}^z \approx \pm N_F$. The size of the latter scales as 2^N , thus (almost) coinciding with the largest connected sector. One could easily generalize this model, by allowing for fermions with a larger spin S [199] or any other local degree of freedom not mixed by the hopping term. This would not change the size of the sectors, but increase their number to $(2S + 1)^{N_F}$, thus increasing the fragmentation (decreasing the ratio of the largest component to the whole Hilbert space).

While here we focus on a version of the model where no double occupancy is allowed, in fact, the spin pattern is also conserved in the presence of doublons, as long as their total number, together with the total spin, is conserved and spin exchange interactions are replaced by Ising interactions. Such terms appear in the limit of strong onsite interactions $n_{i,\uparrow}n_{i,\downarrow}$ [196], taking the form

$$H_{N_{\text{doub}}} = -t \sum_{\substack{i=1 \\ \sigma=\uparrow,\downarrow}}^{N-1} P_{i,i+1} c_{i,\sigma} c_{i+1,\sigma}^\dagger + \text{H.c.}, \quad (3.4)$$

with the projector $P_{i,i+1} = 1 - (n_{i,-\sigma} - n_{i+1,-\sigma})^2$.

3.1.2. Statistically localized integrals of motion

Fixing the complete spin pattern is analogous to fixing the eigenvalues of *all* LIOMs in a many-body localized system, which determines a single eigenstate of the many-body localized Hamiltonian [50, 51]. The difference is that the spin pattern only fixes a particular Krylov sector, rather than a single many-body state, due to the fact that the holes are free to move. Therefore the analogue of a *single* LIOM is the operator which measures *the spin of the k -th fermion*. This is our first example of a statistically localized integral of motion.

Definition (SLIOM). A statistically localized integral of motion (SLIOM) is an operator $\hat{q} \equiv \sum_{i=1}^N \mathcal{O}_i$ satisfying the following two properties:

1. \hat{q} is a conserved quantity, $[\hat{H}, \hat{q}] = 0$;
2. For almost all states $|\psi\rangle$, the expectation value $\langle \psi | \mathcal{O}_i^\dagger \mathcal{O}_i | \psi \rangle = \|\mathcal{O}_i |\psi\rangle\|^2$, when treated as a probability distribution over sites i , is localized to a sub-extensive region in space

$$\frac{\Delta x}{N} \equiv \frac{\sqrt{\sum_i \langle \psi | \mathcal{O}_i^\dagger \mathcal{O}_i | \psi \rangle i^2 - \left(\sum_i \langle \psi | \mathcal{O}_i^\dagger \mathcal{O}_i | \psi \rangle i \right)^2}}{N} \xrightarrow{N \rightarrow \infty} 0. \quad (3.5)$$

For example, the average global magnetization in a spin-1/2 chain, $\frac{1}{N} \sum_i \sigma_i^z$, is not a SLIOM since it has $\Delta x/N = 1/\sqrt{12}$. In Appendix B.1 we give a slightly different and more refined version of the definition, which captures more of the structure of the conserved quantities we discuss in the following (see also Section 3.2.2).

Some comments are in order. **i)** In the definition *almost all* is meant in the sense that states $|\psi\rangle$ violating this condition are of measure zero with respect to some uniform measure over the relevant Hilbert space in the thermodynamic limit. **ii)** In the definition we did not specify the form of the operators \mathcal{O}_i , except that there is one for each site in the chain and that their sum gives a conserved quantity. In the examples below they will turn out to be *string-like* objects, extending from one end of an *open* chain up to site i . Moreover, in these cases $\mathcal{O}_i^\dagger \mathcal{O}_i$ is a projector, such that treating $\langle \psi | \mathcal{O}_i^\dagger \mathcal{O}_i | \psi \rangle$ as a probability distribution is quite natural. In general, one might need to normalize the distribution to sum up to 1. We also ignore the trivial cases when all $\langle \mathcal{O}_i^\dagger \mathcal{O}_i \rangle = 0$. **iii)** In the definition, we have characterized localization in a rather weak sense: instead of requiring that the distribution is localized to a finite region, we only required that its width is sub-extensive. In the following we will distinguish two cases: the *fully localized* one, where $\Delta x \sim O(1)$ (which is most similar to MBL) and the *partially localized* one, where $\Delta x \sim N^\kappa$ for some $0 < \kappa < 1$. In fact, we will see that for the $t - J_z$ model, the SLIOMs that are relevant for the bulk are all partially localized with $\kappa = 1/2$. This localization is therefore much weaker than the case of MBL, but still has non-trivial consequences for the dynamics, as we will show in Section 3.1.3. On the other hand, a subset of the conserved quantities, are in fact localized near the boundaries, and behave very similarly to so-called strong boundary zero modes. The dipole-conserving Hamiltonian considered in Section 2.2, however, has fully localized SLIOMs also in the bulk (along with partially localized ones) as we show in Section 3.2.

Example: Spin configurations in the $t - J_z$ model

We now illustrate how the above definition applies to the $t - J_z$ Hamiltonian introduced in Section 3.1.1. Taking open boundary conditions (OBC), we can define an operator that measures the spin of the k -th fermion from the left edge of the chain:

$$\hat{q}_k \equiv \sum_{i=1}^N \mathcal{O}_i^k = \sum_{i=1}^N \hat{\mathcal{P}}_i^k S_i^z, \quad (3.6)$$

where $\hat{\mathcal{P}}_i^k$ is a projection operator, diagonal in the computational basis, that projects onto those configurations where the k -th charge is exactly on site i . The operators \hat{q}_k form a set of extensively many conserved quantities for H_{t-J_z} with OBC⁴, whose combined eigenvalues label all the different possible spin patterns, such that $\sum_k \hat{q}_k = S_{\text{tot}}^z$. Each \hat{q}_k has three eigenvalues, $\gamma_k = +1, -1, 0$, the latter corresponding to configurations with $k > N_F$ (consequently, \hat{q}_k^2 is a projection onto configurations with $k \leq N_F$). However, not all possible combinations are allowed: if $\gamma_k = 0$ for some k then $\gamma_{k' > k} = 0$ as well. The total number of possible configurations is therefore $\sum_{N_F=0}^N 2^{N_F} = 2^{N+1} - 1$, each corresponding to one of the connected sectors in the theory. Note that the definition of \hat{q}_k explicitly breaks spatial parity. One could alternatively define a set of operators starting from the right edge; these encode the same information regarding the block structure of the Hamiltonian.

As we now argue, the operator \hat{q}_k falls under the above notion of a statistically localized integral of motion, with the role of \mathcal{O}_i in the definition played by the operator $\hat{\mathcal{P}}_i^k S_i^z$. The reason for the statistical localization in this case can be seen intuitively: For a random

⁴See discussion in Appendix B.5 for the case of periodic boundary conditions.

state with some fixed average filling $\nu = \langle N_F \rangle / N$, the k -th charge is most likely to be found in the vicinity of position $i = k/\nu$. The width of the distribution should also depend on ν , going to zero in the limit $\nu \rightarrow 1$. On the other hand, one can always find atypical states with the same filling where the k -th charge is localized at some different position, or not localized at all. To better understand the nature of the conserved quantities \hat{q}_k , we now consider their expectation values for two different ensembles of randomly chosen pure states.

Global Haar random states. Let us first consider the case when $|\psi\rangle$ is chosen Haar randomly from the entire Hilbert space [148, 161]. This is a state with a fermion density $\nu = 2/3$ on average: As $|\psi\rangle$ is a random state, its single-site reduced density matrix is proportional to the identity matrix and thus every local spin is equally likely. Thus, $\nu = \text{prob}(\uparrow) + \text{prob}(\downarrow) = 2/3$ (see also Appendix B.2 for a rigorous computation). We are interested in the average and variance of the expectation value of the operator $\mathcal{O}_i^{k\dagger} \mathcal{O}_i^k = \hat{P}_i^k$, which is a projector onto configurations where site i is occupied and the leftmost $i - 1$ sites host a total of $k - 1$ fermions. When averaged over the Haar ensemble, the expectation value is the same as in an infinite temperature ensemble, simply given by the relative number of such configurations

$$p_{\text{Haar}}(i; k) \equiv \mathbb{E}_{\text{Haar}}[\langle \psi | \mathcal{O}_i^{k\dagger} \mathcal{O}_i^k | \psi \rangle] = \nu^k (1 - \nu)^{i-k} \binom{i-1}{k-1}, \quad (3.7)$$

vanishing for $i < k$ and with $\nu = 2/3$. $\sum_i p_{\text{Haar}}(i; k)$ is the probability of having at least k charges in the system, i.e., $p_{\text{Haar}}(N_F \geq k)$. As the probability of having at least k particles decays with k for $k > \nu N$, we focus on $k/N < \nu$, in which case we have numerically verified that this probability is exponentially close to 1.

The distribution p_{Haar} is peaked around the position $\bar{i} = k/\nu$. For the leftmost charge ($k = 1$), it simply decays exponentially into the bulk as $\sim 3^{-i}$. In general, for a fixed finite value of k , $p_{\text{Haar}}(i; k)$ is independent of the system size N and has some finite width. However, to probe the bulk of the system, one should choose $k = \alpha N$ for some constant $0 < \alpha < \nu$. In this case, the distribution has a standard deviation that scales with system size as $\sim \sqrt{N}$. Nevertheless, it is still ‘partially localized’ in the sense defined previously, such that the width relative to the system size vanishes as $1/\sqrt{N}$ in the thermodynamic limit. This is shown in Figs. 3.1(a-b). Outside of the $O(\sqrt{N})$ region, the distribution has a tail that falls off asymptotically faster than exponentially. To leading order in the thermodynamic limit, $N \rightarrow \infty$ and for $x \equiv i/N \geq \alpha$, the distribution becomes $p_{\text{Haar}}(x; \alpha) \propto \exp[-N(x \log 3 - \alpha \log 2 - x h_2(\alpha/x))]$, where $h_2(\lambda) \equiv -\lambda \log \lambda - (1 - \lambda) \log(1 - \lambda)$ is the binary entropy function. Note that the exponent vanishes when $x = \alpha/\nu = 3\alpha/2$, i.e., it attains a maximum, and is negative otherwise.

Similarly, one can calculate the variance over a set of Haar random states (see Appendix B.2 for details). This gives

$$\mathbb{E}_{\text{Haar}}[|\langle \psi | \mathcal{O}_i^{k\dagger} \mathcal{O}_i^k | \psi \rangle|^2] - |\mathbb{E}_{\text{Haar}}[\langle \psi | \mathcal{O}_i^{k\dagger} \mathcal{O}_i^k | \psi \rangle]|^2 = \frac{1}{3^N + 1} [p_{\text{Haar}}(i; k) - p_{\text{Haar}}(i; k)^2], \quad (3.8)$$

which is exponentially suppressed compared to the average⁵, indicating that indeed the vast majority of states in the Hilbert space gives rise to very similar distributions for $\langle \mathcal{O}_i^{k\dagger} \mathcal{O}_i^k \rangle$.

⁵Notice that $p_{\text{Haar}}(i; k) \leq 1$.

Random states with fixed particle number. While the above calculation shows that most states lead to a sharply peaked distribution, it is also natural to consider states that are randomly chosen within a sector with fixed total fermion number N_F . As we now show, the distributions in this case are still (partially) localized in space, but their location and width now depends explicitly on the filling fraction $\nu = N_F/N$. One can perform the averaging over the restricted Haar ensemble (see Appendix B.2) to obtain

$$p_{N_F}(i; k) \equiv \mathbb{E}_{N_F}[\langle \psi | \mathcal{O}_i^{k\dagger} \mathcal{O}_i^k | \psi \rangle] = \frac{\binom{i-1}{k-1} \binom{N-i}{N_F-k}}{\binom{N}{N_F}}, \quad (3.9)$$

with $i \geq k$. The interpretation of this result is straightforward: The probability for the k -th particle being located at site i , is given by the number of ways to place $k-1$ particles on the previous $i-1$ sites, namely $\binom{i-1}{k-1}$; times the number of possible locations of the remainder $N_F - k$, $\binom{N-i}{N_F-k}$; divided by the total number of ways to locate N_F particles on a chain of length N . This distribution differs from the previous one in several aspects. First, p_{N_F} is invariant under the change of variables $i \rightarrow N - i + 1$ together with $k \rightarrow N_F - k + 1$, which implies that the distribution for \hat{q}_k can be obtained from \hat{q}_{N_F-k+1} via a spatial reflection around the center of the chain, as shown in Figs. 3.1(c). Moreover, unlike Eq. (3.7), this distribution depends explicitly on N ; however, for a fixed finite k it still approaches a well-defined finite distribution in the limit $N \rightarrow \infty$. For $k \propto N$, it once again has a width $\sim \sqrt{N}$, as shown in Figs. 3.1(c-d). Both the position of the peak and the width of the distribution are now functions of the filling fraction $\nu = N_F/N$. The position is $\bar{i} = k/\nu$, while the width goes to zero as $\nu \rightarrow 1$. In the thermodynamic limit, to leading order in N , one finds $p_{\nu N}(xN; \alpha N) \propto \exp\left[-N\left(h_2(\nu) - xh_2\left(\frac{\alpha}{x}\right) - (1-x)h_2\left(\frac{\nu-\alpha}{1-x}\right)\right)\right]$, where the exponent is zero if $x = \alpha/\nu$ and negative otherwise. One can also calculate the variance (see Appendix B.2), which has the same form as Eq. (3.8), with p_{Haar} replaced by p_{N_F} and 3^N replaced by $\binom{N}{N_F}$, the dimension of the symmetry sector.

In principle, we could fix not only the particle number, but also the total magnetization S_{tot}^z . However, since the string operators $\hat{\mathcal{P}}_i^k$ do not depend on the local magnetization, the probability distribution $p_{N_F}(i; k)$ remains the same for any S_{tot}^z . For the same reason, one also finds the same distribution for a random state within a sector with a fixed spin pattern, i.e., labeled by the eigenvalues of $\{\hat{q}_k\}_{k=1}^{N_F}$.

Although jumping a bit ahead of our current discussion, one might already wonder what these distributions look like for specific eigenstates of the Hamiltonian H_{t-J_z} . As we saw in Chapter 1, one expects that in a sector where ETH is fulfilled, highly-excited energy eigenstates $|\psi\rangle$ in the middle of the spectrum look like random states, and thus the spatial distribution of $\langle \psi | \mathcal{O}_i^{k\dagger} \mathcal{O}_i^k | \psi \rangle$ is expected to agree with $p_{N_F}(i; k)$ in Eq. 3.9. In particular, we fix a global symmetry sector with half filling ($N_F = N/2$) and vanishing total magnetization $S_{\text{tot}}^z = 0$. We consider two eigenstates within this sector: i) the ground state |G.S.), that has the lowest energy within this symmetry sector; and ii) a randomly chosen, highly excited eigenstate $|E\rangle$ within the fixed spin pattern sector corresponding to $\gamma_k = 1$ (spins pointing up) for $k \leq N_F/2$ and $\gamma_k = -1$ (spins pointing down) for $k > N_F/2$. As shown in Fig. 3.2(b), we find that the distribution of $\langle E | \mathcal{O}_i^{k\dagger} \mathcal{O}_i^k | E \rangle$ is well approximated by Eq. (3.9), up to finite size corrections. The ground state, on the other hand, is a highly atypical state. For this reason, the distribution is noticeably different from the Haar average. Nevertheless, we find that it is in fact *more* tightly localized, as one can observe from Fig. 3.2(a). In the following, we will continue this discussion and investigate the consequences of a fragmented Hilbert space on the many-body spectrum.

We end this section showing the conceptual comparison between LIOMs and SLIOMs in Table 3.1. We emphasize that, although the two concepts play a similar role (providing labels for eigenstates and connected subspaces, respectively), there is also an important

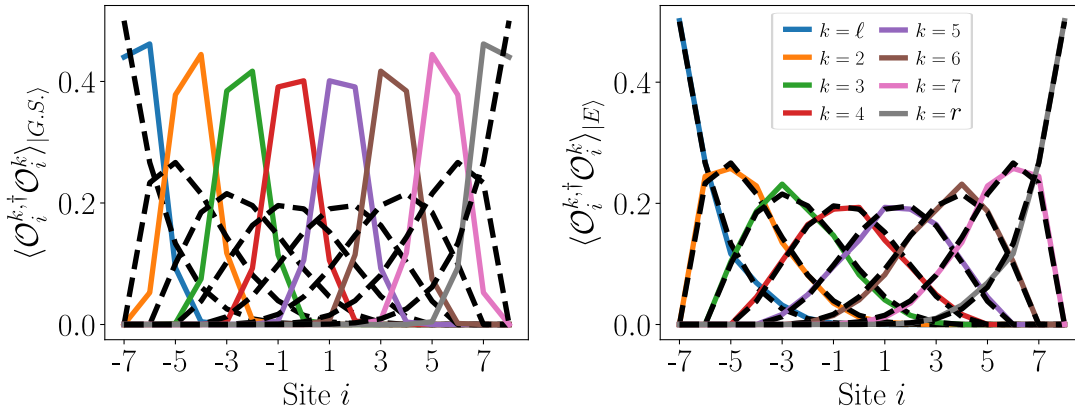


Figure 3.2.: **Spatial distribution of SLIOMs for energy eigenstates.** Spatial distribution of the expectation value $\langle \psi | \mathcal{O}_i^{k\dagger} \mathcal{O}_i^k | \psi \rangle$, for the ground state (left) and an excited state (right) within the sector $N_F = N/2$, $S_{\text{tot}}^z = 0$ for a system size $N = 16$. The excited state is randomly picked from within a sector with a fixed spin pattern (see main text). Both states correspond to (partially) localized distributions. For the excited state, this is close to the Haar average (dashed lines), while for the ground state the distribution is more tightly localized.

difference: LIOMs exist throughout the entire MBL phase and are only slightly modified by perturbations. SLIOMs, on the other hand, are destroyed by generic perturbations (i.e., those not diagonal in the S^z basis).

A similar comparison could be made between SLIOMs and conserved quantities of integrable models. We highlight that the two are rather different: SLIOMs can not be written as sums of (quasi)-local densities, unlike the conserved quantities in (Bethe ansatz) integrable models (see e.g., Ref. [200]). Another difference is that SLIOMs can be used to block-diagonalize the Hamiltonian, while in interacting integrable systems, most conserved quantities have non-degenerate spectra, so diagonalizing them would be equivalent to fully diagonalizing the Hamiltonian [127].

Moreover, a structure similar to the SLIOMs defined above also arises for the strongly-fragmented system we studied in the previous chapter (Hamiltonian H_3 in Section 2.2 for $S = 1$), where the conserved quantities are harder to identify, as we shall see below in Section 3.2.

3.1.3. Bulk vs boundary SLIOMs and their relationship to thermalization

Having defined the conserved quantities that characterize the $t - J_z$ model and its fragmented Hilbert space, we now turn to the question of how these affect the dynamics. As we shall see, the effect of SLIOMs is strongest near the boundary, where they lead to infinitely long coherence times, in complete analogy with the case of strong zero modes [184–189]. In the bulk, we find that coherence times are finite in the thermodynamic limit, despite the presence of infinitely many conservation laws. Nevertheless, even in the bulk, the SLIOMs lead to a weaker form of non-equilibration, wherein correlations remain trapped in a sub-extensive region, as well as to a violation of the eigenstate thermalization hypothesis within global symmetry sectors.

Bulk behavior

A natural question to ask regarding thermalization is whether the presence of an extensive number of SLIOMs manifests itself in infinite autocorrelation times, as is the case in MBL.

LIOMs	SLIOMs
j^{th} site	k^{th} charge
$\tau_j^z = \sigma_j^z + \sum_{\mathcal{S}} c_{\mathcal{S}}^{(j)} \mathcal{S}$	$\hat{q}_k = \sum_i \mathcal{O}_i^k$
with $c_{\mathcal{S}}^{(j)} \sim e^{-d(\mathcal{S};j)/\xi}$	$\langle \mathcal{O}_i^{k\dagger} \mathcal{O}_i^k \rangle$ sub-extensive in typical states
$[\tau_j^z, H] = 0$	$[\hat{q}_k, H] = 0$
$\{\tau_j^z = \pm 1\}_{j=1}^N \longleftrightarrow$ eigenstates of H	$\{\hat{q}_k = \pm 1, 0\} \longleftrightarrow$ connected subspaces

Table 3.1.: **Comparison between LIOMs and SLIOMs in the $t - J_z$ model.** While LIOMs label many-body eigenstates, SLIOMs label larger dimensional connected subspaces. LIOMs are localized around a given position in a state-independent way (operator strings \mathcal{S} with support far from i are exponentially suppressed). SLIOMs, on the other hand, are restricted to regions that depend on the state considered (e.g. its filling fraction for the $t - J_z$ model). Unlike LIOMs, which are always exponentially localized, the SLIOMs in the $t - J_z$ model are only partially localized with a width that is sub-extensive but infinite in the thermodynamic limit.

A way to gain insight into this question is by considering Mazur's inequality [116, 126, 170], which as we found in Chapter 1, provides a lower bound on the time-averaged autocorrelation of an observable based on its overlap with the conserved quantities. Focusing on a single-site S_j^z operator, and considering only the SLIOMs \hat{q}_k , the inequality in our case reads

$$\begin{aligned}
 \lim_{T \rightarrow \infty} \frac{1}{T} \int dt \langle S_j^z(t) S_j^z(0) \rangle_{\beta=0} &\geq \sum_k \frac{|\langle S_j^z \hat{q}_k \rangle_{\beta=0}|^2}{\langle \hat{q}_k^2 \rangle_{\beta=0}} \\
 &= \sum_k \frac{\left[3^{-j} 2^k \binom{j-1}{k-1} \right]^2}{1 - 3^{-L} \sum_{N_F=0}^{k-1} 2^{N_F} \binom{N}{N_F}} \equiv C_j^z(\infty),
 \end{aligned} \tag{3.10}$$

where $\langle A \rangle_{\beta=0} \equiv \text{tr}(A)/3^N$ is the infinite temperature average, and the denominator in the last expression is the probability of having at least k particles in the system. Here we have used that $\langle \hat{q}_k^2 \rangle_{\beta=0} = \sum_i \text{tr}(\mathcal{O}_i^{k\dagger} \mathcal{O}_i^k)/3^N = \sum_i p_{\text{Haar}}(i; k)$ since $\text{tr}(S_i^z S_j^z) = \delta_{i,j} \text{tr}[(S_j^z)^2]$.

If the expression on the right hand side of this inequality was finite in the limit $N \rightarrow \infty$, it would imply infinitely long-coherence times. However, evaluating it for a bulk observable, $j \propto N$, one finds that it decays with system size as $N^{-1/2}$, as shown by Fig. 3.3(a). This implies that the conservation laws $\{\hat{q}_k\}$ are not sufficient to prevent the autocorrelation from decaying to zero at long times.

Even though the bound vanishes in the thermodynamic limit, it nevertheless leads to anomalous behavior. For a conserved density like S_j^z , i.e., $\sum_{j=1}^N \langle S_j^z(t) S_j^z(0) \rangle$ is constant, one expects the spatially resolved autocorrelation $\langle S_j^z(t) S_i^z(0) \rangle$ to eventually spread out uniformly over the whole system and thus become $O(1/N)$ on every site j (for fixed i). However, in our case the lower bound $\sim N^{-1/2} \gg N^{-1}$ implies that this cannot be the case, and instead suggests that the charge remains trapped within a much smaller region of size $O(N^{1/2})$. This can be understood from the distribution of $\mathcal{O}_i^{k\dagger} \mathcal{O}_i^k$ in Fig. 3.1, which we discussed in the previous section. In particular, note that the infinite temperature overlap $\langle S_j^z \hat{q}_k \rangle_{\beta=0} = \text{tr}(\mathcal{O}_j^{k\dagger} \mathcal{O}_j^k)/3^N$ equals the value of the probability distribution $p_{\text{Haar}}(j; k)$ in

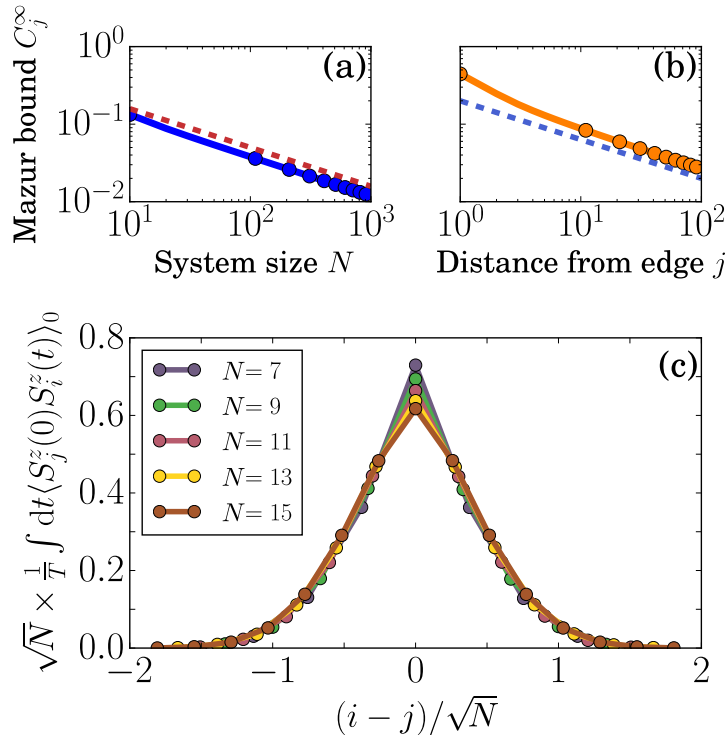


Figure 3.3.: **Autocorrelations for the $t - J_z$ model in the bulk** (a) Mazur bound (3.10) on autocorrelations in the bulk, at $j = N/2$, decays as $\propto N^{-1/2}$ as a function of the system size N . (b) The same bound, shown for a fixed $N = 600$, decays as $\propto j^{-1/2}$ as a function of the distance j from the boundary. (c) The long-time average of spatially resolved correlations, computed numerically for small chains (and averaged between times $t = 50$ and 100), shows a persistent peak, instead of the complete spreading expected from thermalization.

Eq. (3.7) and thus

$$C_j^z(\infty) = \sum_k \frac{p_{\text{Haar}}(j; k)^2}{p_{\text{Haar}}(N_F \geq k)}. \quad (3.11)$$

As we saw above, the SLIOMs in the bulk, namely $p_{\text{Haar}}(j; k)$, are localized around position $\bar{j} = k/\nu$ with a width $\propto N^{1/2}$. Therefore, a given S_j^z overlaps significantly with only $O(N^{1/2})$ different conserved quantities \hat{q}_k , and these define the region in which the charge can spread out. This conclusion is supported by numerical results on the spatially resolved correlator $\langle S_j^z(t) S_i^z(0) \rangle_{\beta=0}$ at long times for small chains, as shown by Fig. 3.3(c). These results suggest a scaling $\langle S_j^z(t) S_i^z(0) \rangle_{\beta=0} \approx \frac{1}{\sqrt{N}} f\left(\frac{i-j}{\sqrt{N}}\right)$ in the limit of large N . While autocorrelations in the bulk thus decay to zero at long times in the thermodynamic limit, they do it in an anomalous manner. Indeed, an initial product state in the fermion occupation basis would clearly not relax to a thermal state solely specified by the global conserved quantities H_{t-J_z} , N_F and S_{tot}^z . In particular, since each sector with a fixed pattern of spins is effectively a chain of spinless fermions with 2 possible states per site, time evolving from such an initial state will result in half-chain entanglement entropies at most $\frac{N}{2} \ln 2$, much smaller than the entropy of a chain with 3-dimensional local Hilbert space at (or close to) infinite temperature ($\frac{N}{2} \ln 3$). It is also true that each of these initial states thermalizes with respect to the associated effective spinless fermion Hamiltonian,

i.e. the $t - J_z$ Hamiltonian projected to a given connected sector with a fixed value of the SLIOMs. Note, however, that this effective Hamiltonian is non-local: to know the sign of the interaction between a given pair of (spinless) fermions, one in principle has to know the entire spin pattern in the original variables.

This sensitivity to initial conditions, due to the presence of bulk SLIOMs, is also reflected in the properties of the eigenstates of H_{t-J_z} . As the above explanation shows, they have at most $\frac{N}{2} \ln 2$ entanglement (for a half chain), much smaller than a generic Hamiltonian with 3 states per site would have in the middle of the spectrum. Moreover, due to the strong fragmentation of the Hilbert space, different eigenstates at the same energy density, and with the same global quantum numbers N_F and S_{tot}^z , can have very different expectation values for simple local observables. This is trivially true for the symmetry sectors with $N_F = NL$, where all states are completely frozen, but it in fact holds more generally. To confirm this, we consider the global symmetry sector with $N_F = N/2$ and $S_{\text{tot}}^z = 0$, and numerically evaluate the eigenstate expectation values of the observable $S_{N/2}^z S_{N/2+1}^z$. We find (see Fig. 3.4) that the expectation values of this operator have a wide distribution over different eigenstates. Approximating the eigenstates by an equal weight superposition of all possible hole positions with a given spin pattern, on the other hand, suggests that in fact there is a very slow narrowing of this distribution, with the width scaling as $N^{-1/4}$ in the thermodynamic limit as obtained from Monte Carlo simulation (see Appendix 3). This slow algebraic narrowing should be contrasted with the ETH ansatz, which as we found in Chapter 1 predicts an exponentially narrowing distribution. In fact, the $N^{-1/4}$ scaling is even slower than the case of integrable systems, which typically have a width $\sim N^{-1/2}$ [201–203]. In general, even in the absence of the ETH, the eigenstate-to-eigenstate fluctuations of a local observable in any generic translation invariant system should decay at least as fast as $\sim N^{-1/2}$ [88, 92]. This difference is consistent with our picture of SLIOMs wherein the local observable only ‘sees’ an $O(\sqrt{N})$ part of the system.

From these results, we conclude that if one considers only the global (N_F, S_{tot}^z) symmetry sector, without resolving the additional non-local symmetries, then the diagonal matrix elements of local observables violate ETH. This can be understood as follows: each connected sector has a different ‘embedded’ Hamiltonian, depending on the spin pattern, and the properties of the associated eigenstates can therefore differ from sector to sector. Note that this situation is different from the case of more commonly occurring non-local symmetries, such as spin-flips or lattice translations, which *do not* lead to distinct distributions of diagonal matrix elements [175, 176, 204, 205]. Of course one can instead consider only eigenstates within a given sector, in which case ETH is fulfilled for typical spin patterns (with the exception of a few integrable sectors, which we discuss below). Note, however, that this requires fixing an extensively large number of non-local symmetries (the SLIOMs)⁶, making difficult to meaningfully take the thermodynamic limit. In this sense, our case is similar to that of integrable models, where one usually considers matrix elements without resolving all the extensively many conserved quantities, and finds a similarly slow, algebraic decay of their fluctuations with system size [201–203].

So far we discussed the non-ergodicity originating from the fragmented Hilbert space, whose components are labelled by the SLIOMs. Our conclusions about the lack of thermalization when not resolving the SLIOMs symmetry sectors therefore apply independently of the structure of the Hamiltonian *inside* the connected blocks. For the $t - J_z$ Hamiltonian (3.1) it turns out that there is some additional structure for sectors with a completely ferromagnetic or completely antiferromagnetic spin pattern. These can be mapped [192] onto a spin-1/2 XXZ Heisenberg chain (with anisotropy $\Delta > 0$ and $\Delta < 0$, respectively),

⁶We note here that not all different spin patterns give rise to distinct distributions of diagonal matrix elements. We leave it as an open question to identify exactly which combinations of the SLIOMs would need to be fixed to obtain a set of eigenstates that obey ETH.

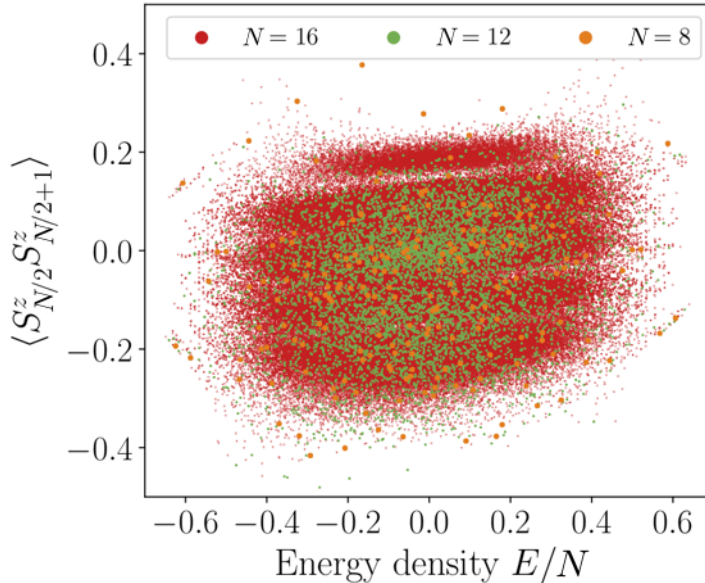


Figure 3.4.: **Diagonal matrix elements in the $t - J_z$ model.** Expectation value of the average nearest neighbor antiferromagnetic correlations in eigenstates of H_{t-J_z} with global quantum numbers $N_F = N/2$ and $\sum_j S_j^z = 0$, and open boundary conditions. For the system sizes shown ($N = 8, 12, 16$), the distribution becomes *wider* with increasing system size, while asymptotically it is expected to narrow as $\sim N^{-1/4}$. This is a consequence of the strong fragmentation labeled by the SLIOMs, and is in contrast with ETH, which predicts an exponentially narrow distribution.

which is quantum integrable. However, most of the other sectors are not. The integrability of the FM and AFM sectors could also be broken by additional perturbations that are diagonal in the S^z basis (e.g. a staggered field). These commute with all the SLIOMs, and therefore do not change our conclusions about the overall non-ergodicity of the model.

Statistically localized strong zero modes

It is worthwhile to consider separately those constants of motion \hat{q}_k that are localized at the boundary of an open chain. In this case k does not scale with the system size and therefore its distribution $p_{\text{Haar}}(i; k)$ remains finite in the thermodynamic limit. Consequently, one expects that an observable near the boundary has finite overlap with these SLIOMs and, under time evolution, a non-vanishing fraction of it would remain localized in a finite region near the boundary. Indeed, computing the lower bound from Eq. (3.10) for a position j that does *not* scale with N , one finds that it remains finite in the limit $N \rightarrow \infty$. The bound is largest at the boundary, $j = 1$, where it takes the value $4/9$, and decays away from the boundary as $j^{-1/2}$. This is shown in Fig. 3.3(b). Obviously, the same holds near the right edge, when j is replaced by $N + 1 - j$. Therefore, at the boundaries the SLIOMs lead to infinite coherence times. In fact, in order to derive infinite coherence times at the edge, one does not need infinitely many SLIOMs, it is sufficient to consider just *one*. In particular let us take the spin of the leftmost fermion,

$$\hat{q}_\ell \equiv \sum_i \left(\prod_{j < i} (1 - \tilde{n}_j) \right) S_i^z, \quad (3.12)$$

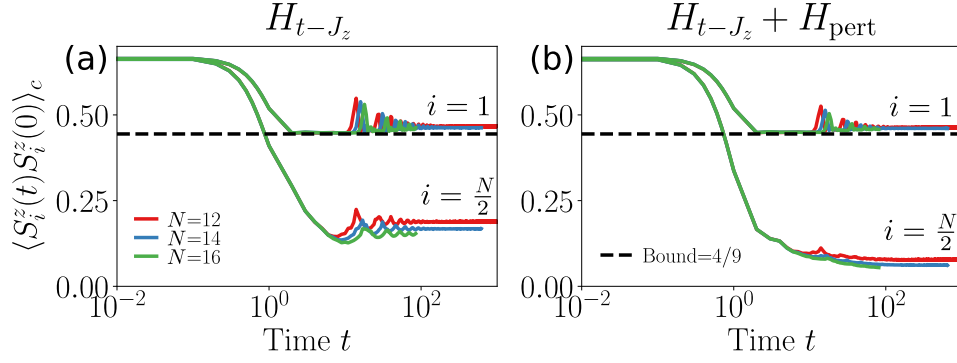


Figure 3.5.: **Bulk vs edge autocorrelations.** Connected infinite temperature autocorrelation function for the center site $i = N/2$ and at the left boundary $i = 1$ for system sizes $N = 11, 13, 15$. (a) In the $t - J_z$ model (Eq. (3.1)), which conserves both bulk and boundary SLIOMs \hat{q}_k , the edge autocorrelator shows infinite coherence times while in the bulk it decays to a value $\propto N^{-1/2}$, which is anomalously large but vanishing in the thermodynamic limit. (b) Once the perturbation Eq. (3.15) is added, SLIOMs in the bulk are broken and the bulk autocorrelations decay to the value $\propto 1/N$ expected for thermalizing systems. The boundary SLIOMs \hat{q}_ℓ, \hat{q}_r , on the other hand, are still conserved, leading to a finite long-time value for autocorrelations at the edge, well approximated by the analytical lower bound (dashed horizontal line).

which is equivalent to $\hat{q}_{k=1}$ in the above definition, with the projection taking a particularly simple form $\hat{P}_i^1 = \prod_{j < i} (1 - \tilde{n}_j) \tilde{n}_i$, using the local constrained fermion density $\tilde{n}_j = \tilde{n}_{j,\uparrow} + \tilde{n}_{j,\downarrow}$. There is another similar operator localized near the right edge

$$\hat{q}_r \equiv \sum_i S_i^z \left(\prod_{j > i} (1 - \tilde{n}_j) \right). \quad (3.13)$$

We will make use of Mazur's inequality once again. The conservation law $[\hat{q}_\ell, H] = 0$ implies that

$$\lim_{T \rightarrow \infty} \frac{1}{T} \int dt \langle S_j^z(t) S_j^z \rangle_{\beta=0} \geq \frac{|\langle S_j^z \hat{q}_\ell \rangle_{\beta=0}|^2}{\langle \hat{q}_\ell^2 \rangle_{\beta=0}} = \frac{4/9^j}{1 - 3^{-N}} \rightarrow \frac{4}{9^j} \quad (3.14)$$

in the thermodynamic limit. In evaluating the right hand side we used the fact that $\langle S_j^z \hat{q}_\ell \rangle_{\beta=0} = p_{\text{Haar}}(j; 1) = 2/3^j$ as given by Eq. (3.7), and that $\hat{q}_\ell^2 = 1 - \hat{P}_{\text{empty}}$, where \hat{P}_{empty} is a rank 1 projector onto the completely empty state. One can do the same calculation near the right boundary, for S_{N+1-j}^z , using the conservation of \hat{q}_r , which leads to the lower bound $4/9^{N+1-j}$.

While this result is weaker than the one taking all the \hat{q}_k into account — it decays exponentially, rather than algebraically $j^{-1/2}$ towards the bulk —, it follows from much weaker conditions. This implies that it is possible to add perturbations to the Hamiltonian that destroy the strong fragmentation in the bulk, but nevertheless lead to non-thermalizing dynamics at the edge. A simple example of such a perturbation is

$$H_{\text{pert}} = \sum_{i=2}^{N-2} \tilde{n}_{i-1} (S_i^x S_{i+1}^x + S_i^y S_{i+1}^y) \tilde{n}_{i+2}, \quad (3.15)$$

which allows a spin exchange, but only if both neighboring sites are occupied by a fermion. Therefore, this perturbation no longer conserves the spin pattern, but it still commutes with the two boundary SLIOMS, $\hat{q}_{\ell,r}$.

3.1. Illustrative example of SLIOMs: $t - J_z$ model

SZMs	Boundary SLIOMs
$\hat{\Psi} = \sum_n e^{-n/\xi} \mathcal{S}^{(n)}$	$\hat{q}_\ell = \sum_i \mathcal{O}_i$ $\langle \mathcal{O}_i^\dagger \mathcal{O}_i \rangle \leq e^{-i/\xi}$ for typical states
$[\hat{\Psi}, H] = \varepsilon$ with $ \varepsilon < e^{-\alpha N}$	$[\hat{q}_\ell, H] = 0$
$\hat{\Psi}^2 = 1$	$\hat{q}_\ell^2 = 1 - P_{\text{empty}}$
$\{R_x, \hat{\Psi}\} = 0 \rightarrow$ degeneracies	$\{R_x, \hat{q}_\ell\} = 0 \rightarrow$ degeneracies

Table 3.2.: **Comparison between boundary SLIOMs and strong zero modes (SZM).** The SZM is a sum of string operators \mathcal{S} (e.g. Jordan-Wigner strings), ending at distance n from the edge, with coefficient decaying exponentially with n . For the boundary SLIOMs, on the other hand, localization appears upon taking the expectation value in typical states with finite particles density. While SZM are usually only conserved in the thermodynamic limit, the SLIOMs are exact integrals of motion at any finite size N . The existence of an additional symmetry, in this case $R_x = \prod_j \exp\left(i\pi \frac{S_j^x}{2}\right)$, anti-commuting with the SLIOMs or edge modes, implies degeneracies throughout the many-body spectrum. SZM square to 1, while in our case $\hat{q}_{\ell,r}^2$ is 1 everywhere except in a particular one-dimensional subspace (i.e., a state with no particles).

As a consequence, the bound (3.14), evaluated at the boundaries, applies to the perturbed Hamiltonian $H_{t-J_z} + \lambda H_{\text{pert}}$, despite that it is now completely thermalizing in the bulk. As shown in Fig. 3.5, the lower bound derived from Mazur's inequality appears to be tight for the boundary autocorrelation, while the bulk autocorrelation in the perturbed system now decays to an $O(1/N)$ value, as expected for a thermalizing system.

The appearance of infinitely long coherence times at the boundaries is strongly reminiscent to the case of strong edge modes previously discussed in the literature [184–189]. The operators $\hat{q}_{\ell,r}$ play the same role as the strong zero modes (SZM), whose presence prevents boundary operators with a finite overlap with those from spreading into the bulk. The differences are twofold: i) Our boundary modes are only statistically localized, in the sense defined above, unlike the usual SZM which are localized in the operator norm. ii) On the other hand, in our case $\hat{q}_{\ell,r}$ commute *exactly* with the Hamiltonian for arbitrary system sizes, unlike the strong zero modes which only commute up to $O(e^{-N})$ corrections. One can find a comparison between SZMs and boundary SLIOMs in Table. 3.2.

The fact that $H = H_{t-J_z} + \lambda H_{\text{pert}}$ commutes with the two edge mode operators means that it admits a block diagonal form according to the spin of the left- and rightmost fermions, written formally as $H = H_{\uparrow\uparrow} \oplus H_{\downarrow\downarrow} \oplus H_{\uparrow\downarrow} \oplus H_{\downarrow\uparrow}$ (excluding the empty state on which it acts trivially). Eigenstates can therefore be labeled by the left- and rightmost spins. In the presence of additional symmetries, not commuting with \hat{q}_ℓ and \hat{q}_r , this implies degeneracies in the energy spectrum at all energies, just as in the case of usual strong edge modes. In particular, H_{t-J_z} and H_{pert} are both invariant under flipping all spins simultaneously i.e., $R_x = \prod_j \exp\left(i\pi \frac{S_j^x}{2}\right)$ (recall the unusual factor of 1/2 that we omitted in the definition of spin operators in Eq. (3.2)). This operator flips the eigenvalues of both \hat{q}_ℓ and \hat{q}_r (since $\{R_x, \hat{q}_{\ell,r}\} = 0$), and therefore interchanges the blocks $H_{\uparrow\uparrow} \leftrightarrow H_{\downarrow\downarrow}$ and $H_{\uparrow\downarrow} \leftrightarrow H_{\downarrow\uparrow}$. This implies that the spectrum is at least 2-fold degenerate everywhere; since the Hamiltonian commutes with $\hat{q}_\ell, \hat{q}_r, R_x$ at any finite size, this degeneracy is *exact*: Given an eigenstate $|E\rangle$ with energy E , then $R_x|E\rangle$ is an eigenstate with the same energy

but it is different than $|E\rangle$. Indeed, assuming $\hat{q}_{\ell,r}|E\rangle = \gamma_{\ell,r}|E\rangle$ with $\gamma_{\ell,r} \neq 0$ which holds for all eigenstates excluding the empty state, then $\hat{q}_{\ell,r}R_x|E\rangle = -\gamma_{\ell,r}R_x|E\rangle$, which implies $\langle E|R_x|E\rangle = 0$.

Given the presence of such edge modes throughout the entire spectrum, it is natural to ask whether the ground state of H_{t-J_z} is in a topological phase. This is in fact not as obvious as it might seem, for two reasons: firstly, the type of edge mode operators we have discussed will also emerge in symmetry-breaking phases — one can think of the edge mode as measuring a spontaneous boundary magnetization. If the bulk is magnetized, the edge magnetization is simply picking this up. This happens in the large J_z limit. Secondly, we have already noted that we can essentially trivialize the bulk whilst preserving the edge mode (with perturbations of the type in Eq. (3.15)), in which case the ground state can be trivial in the bulk⁷.

Nevertheless, it turns out that the ground state of the $t - J_z$ model can be in a topologically non-trivial phase. This is all the more intriguing when one observes that this model, as defined in Eq. (3.1), is *gapless* for $0 < J_z < t$ [206] (notice that we have considered $J_z = t/4$), whereas (symmetry-protected) topological phases are usually gapped. Recently, frameworks for gapless topological phases have been introduced [207, 208]. In fact, the ground state of the $t - J_z$ model appeared as a particular example of a (topologically non-trivial) symmetry-enriched critical point in Section VII.A of Ref. [208]; there it was discussed in the formulation as a spin-1 chain, with the Hamiltonian arising as the simplified version of the gapless Haldane phase first introduced in Ref. [206] protected by the $\mathbb{Z}_2 \times \mathbb{Z}_2$ group of π rotations R^x , R^y and R^z . Interestingly, the topologically non-trivial nature of the gapless $t - J_z$ model was noted over two decades ago in Ref. [192] in terms of a hidden antiferromagnetic order, although the twofold ground state degeneracy was not observed. As we have noted above, this twofold degeneracy is *exact* in this case. The $\mathbb{Z}_2 \times \mathbb{Z}_2$ symmetry group of the spin-1 chain studied in Ref. [208], maps to the fermionic parity $R^z \rightarrow (-1)^{N_F}$ and to $R^x \rightarrow U = \prod_i U_i$ with $U_i \equiv |0\rangle\langle 0| - |\uparrow\rangle\langle \downarrow| - |\downarrow\rangle\langle \uparrow|$ in the fermionic formulation [206]. Our above definition of R_x in terms of the fermionic variables, replaces the second \mathbb{Z}_2 by a \mathbb{Z}_4 symmetry group instead⁸.

If we add an *arbitrary*⁹ perturbation (breaking the bulk *and* edge SLIOMs) that preserves either of the above symmetry groups, then this twofold degeneracy would only persist at low energies and would acquire an exponentially small finite-size splitting, per the arguments in Refs. [207, 208].

3.1.4. Experimental realization

Ultracold atoms in a shallow optical lattice that are optically dressed with a Rydberg state, realize a variant of the $t - J_z$ model of Eq. (3.1) [210, 211]. The Hamiltonian of the Rydberg system is given by

$$H_{\text{Rydberg}} = -t \sum_{i,\sigma} (\tilde{c}_{i,\sigma} \tilde{c}_{i+1,\sigma}^\dagger + \text{H.c.}) + \sum_{i \neq j} \frac{U_0/8}{1 + (r_{ij}/R_c)^6} |\uparrow_i \uparrow_j\rangle \langle \uparrow_i \uparrow_j|.$$

Here, the first term describes the hopping of the atoms, which possess two internal states, $|\downarrow\rangle$ and $|\uparrow\rangle$, in a one-dimensional optical lattice. The atoms can have either fermionic or bosonic statistics, as for the latter a hard-core constraint is typically enforced due to the strong Rydberg interactions. The interaction potential is of strength $U_0 = \Omega^4/8|\Delta|^3$

⁷This would mean that the edge mode is not stabilized by symmetry alone but requires the boundary SLIOM.

⁸This unusual symmetry protection was later investigated in Ref. [209]. The authors found that the ground state is in fact topologically non-trivial with respect to this \mathbb{Z}_4 symmetry and constitutes an example of an intrinsically gapless topological state.

⁹We note that the edge mode is stable against opening up a bulk gap, as discussed in Ref. [208]

and has a cutoff at $R_c = 2\Delta$, where Ω is the Rabi frequency and Δ the detuning from the Rydberg state [212]. This potential can be adjusted such that it effectively acts only on nearest-neighbor sites with some strength J_z [211]. Since the two Hamiltonians only differ by diagonal terms, our results for SLIOMs in the $t - J_z$ model Eq. (3.1) carry directly over to the Rydberg system.

Moreover, we can partially break the structure of the SLIOMs in the bulk by engineering for the Rydberg system a perturbation in the spirit of the one in Eq. (3.15). In particular, when coupling the two internal states, $|\downarrow\rangle$ and $|\uparrow\rangle$, with a global microwave of strength $\Omega_{\text{mw}} \ll J_z$ that is blue detuned by $2J_z$ from the atomic transition, an effective coupling of the form $\sum_i (|\uparrow\rangle\langle\uparrow|)_{i-1} S_i^x (|\uparrow\rangle\langle\uparrow|)_{i+1}$ is generated in the rotating frame of the Rydberg interaction [213, 214]. One can realize this perturbation in addition to the Rydberg interaction, for example by pulsing the microwave drive. This perturbation does not preserve the total charge but nevertheless has an effect similar to Eq. (3.15), destroying the SLIOMs in the bulk while maintaining them at the boundary.

Note that the systems considered in this section are different from those in Eqs. (3.1) and (3.15), in that they are not invariant under the symmetry transformation $R_x = \prod_i \exp\left(i\pi \frac{S_i^x}{2}\right)$. Therefore, these models do not show the exact twofold degeneracy of the spectrum previously discussed. Nevertheless, they exhibit the same physical phenomena with respect to thermalization as the ones discussed above.

3.2. Dipole-conserving Hamiltonian H_3

In the previous chapter we showed that infinite temperature correlations evolving under Hamiltonian H_3 Eq. (2.1), fail to thermalize due to the strong fragmentation of the Hilbert space (in the local S^z basis) into exponentially many invariant subspaces. In fact, this also had a strong effect on the distribution of expectation values of local observables on energy eigenstates which led to the breaking of the weak formulation of ETH. We developed some intuition about the underlying reason for this fragmentation which allowed us to construct exponentially many frozen states as well as other higher-dimensional sectors. However, a complete understanding of the underlying structure was not fully addressed. Here we remedy this, constructing a full set of *non-local* conserved quantities which completely characterize the block structure of H_3 .

While the previous example of the $t - J_z$ model may have seemed somewhat trivial, the same general concept of statistically localized integrals of motion applies to the more complicated dipole-conserving Hamiltonian H_3 for spin-1 local degrees of freedom. However, the latter has a much richer structure. This additional structure accounts for the fact that H_3 has a much broader distribution of the sizes of connected sectors and a localized behavior *in the bulk* in the form of infinite autocorrelation times, a feature not present in H_{t-J_z} . This appears as a consequence of SLIOMs that are statistically localized on finite regions. In particular, while in the $t - J_z$ model the starting point of the identification of sectors was related to the number of fermions, a usual $U(1)$ symmetry, and the explicit local kinetic constraint of no spin-exchange; in the case discussed below the analogous quantity — the number of objects whose pattern is conserved — is already non-local in terms of the physical degrees of freedom.

Before embarking on this construction, let us briefly recall the form of Hamiltonian H_3

$$H_3 = - \sum_{i=1}^{N-2} S_i^+ (S_{i+1}^-)^2 S_{i+2}^+ + \text{H.c.}, \quad (3.16)$$

which we take on a chain $j \in \{1, \dots, N\}$ with open boundary conditions, and as before denote the three on-site eigenstates of S_i^z by $|+\rangle, |-\rangle, |0\rangle$ corresponding to eigenvalues

+1, -1, 0 respectively, and refer to them as + and - charges and empty site respectively. As we already pointed out before, SLIOMs are completely determined by local terms of the Hamiltonian and in particular, are shared among the family of Hamiltonians $H_3(\{J_i\})$ introduced in Eq. (2.8) as well as the associated circuit dynamics of dipole-conserving size 3 gates.

3.2.1. Mapping to bond spins and defects

In order to identify the structure of connected sectors, it is useful to rewrite the dynamics in terms of a new set of variables. These new variables consist of two different types of degrees of freedom:

1. spin-1/2 variables associated to the *bonds* of the original chain, with corresponding Pauli operators denoted by $\sigma_{i,i+1}^{x,y,z}$ on the bond $(i, i + 1)$;
2. and hard-core particles living on the sites, which we will refer to as *defects* •.

To get a one-to-one mapping between basis states in the original S_i^z basis and the new variables, we require the spins on the two bonds surrounding a defect to be aligned. Introducing the defect occupation number operator n_i^d on site i , we can write this requirement formally as $\sigma_{i-1,i}^z n_i^d |\psi\rangle = \sigma_{i,i+1}^z n_i^d |\psi\rangle$ for any physical state $|\psi\rangle$. With this constraint, the two Hilbert spaces match up and we get a mapping between basis states in the original S_i^z basis and the new variables, as we now explain.

In order to understand how the mapping works, let us start considering those configurations of the original variables, which obey the following rule: *subsequent charges—ignoring empty sites in-between—have alternating signs*. In other words, these are the set of states that have perfect antiferromagnetic ordering after eliminating the intermediate empty sites.

We can map a configuration of charges satisfying this rule to a configuration of bond spins with the following convention: we represent eigenstates of the local $\sigma_{i-1,i}^z$ as pointing left (\leftarrow) or right (\rightarrow), with corresponding eigenvalues -1 ($+1$) respectively; and map each (+)-charge to a domain wall of type $\leftarrow\rightarrow$, and each (-)-charge to a domain wall of type $\rightarrow\leftarrow$, as shown in the example of Fig. 3.6(a). To account for all configurations, we need to include two additional auxiliary bonds ($N + 1$ bonds in total), at the left and right ends of the chain, whose spin configuration is fixed by the sign of the left- and rightmost charges respectively. A way of visualizing the mapping is to think of the bond spins as an electric field, emanating from positive charges and ending at negative charges, satisfying Gauss's law

$$\frac{1}{2} (\sigma_{i,i+1}^z - \sigma_{i-1,i}^z) = S_i^z, \quad (3.17)$$

where the operator S_i^z measures the on-site charge in the original (spin-1) variables. The rule of alternating signs ensures that this prescription is consistent within the spin-1/2 representation on the bonds. In fact, one can understand this mapping as a restriction on the values of standard height field constructions appearing in the context of quantum dimers (see e.g., Ref. [215] and Ref. [216] for a generalization applied to systems with multipole moment conservation in one and two dimensions.)

The mapping to bond spins runs into a problem when there are *two subsequent charges with the same sign*. To generalize the mapping to these cases, we introduce extra *defect* degrees of freedom on the sites, which keep track of those charges that do not conform to the rule of alternating signs. To do this, we sweep through the chain from left to right, putting spins on the bonds in accordance with the previous rule. When, at some position i , we encounter a charge that has the same sign as the one preceding it, we fix the spin of the bond $(i, i + 1)$ to coincide with preceding one, $\sigma_{i,i+1}^z = \sigma_{i-1,i}^z$. At the same time,

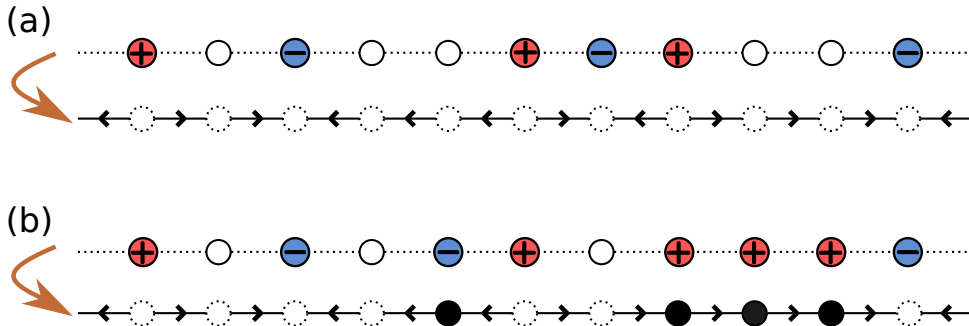


Figure 3.6.: **Mapping from spin-1 chain to bond spins and defects.** (a) A charge configuration with alternating signs can be mapped to spin-1/2 variables on the bonds. (b) For a generic configuration, one also has to introduce defects, living on sites, whenever a charge would violate the rule of alternating signs. Note that defects with neighboring bond spins pointing to the right (left) correspond to positive (negative) charges in the original.

in order to keep track of the charge, we place a *defect* on the site i . This way we end up with a model with two types of degrees of freedom: spins on the bonds and defects on the sites. The resulting Hilbert space is 3^N dimensional¹⁰, since a site combined with the bond on its right only have together three possible configurations: either (1) ($\circ \rightarrow$), (2) ($\circ \leftarrow$) or (3) ($\bullet \sigma$) where σ is specified by the spin on the previous bond. An example of this mapping with four defects is shown in Fig. 3.6(b).

It is important to note that while defects themselves do not carry a sign, we can still distinguish whether they correspond to positive or negative charges in the original variables by looking at the spins surrounding them: a defect with neighboring spins pointing right is mapped to a positive charge, while a defect with neighboring spins pointing left is mapped to a negative charge. We refer to these as (+)- and (-)-defects, and they correspond to eigenvalues ± 1 of the operator $n_i^d \sigma_{i,i+1}^z = \sigma_{i-1,i}^z n_i^d$. The old and new degrees of freedom are related to each other by the generalized Gauss's law

$$\frac{1}{2}(\sigma_{i,i+1}^z - \sigma_{i-1,i}^z) = S_i^z - \sigma_{i-1,i}^z n_i^d, \quad (3.18)$$

such that the right hand side vanishes in the presence of a defect. This allows us to write the global charge and dipole moment in terms of the new variables as

$$Q = \frac{1}{2}(\sigma_{N,N+1}^z - \sigma_{0,1}^z) + \sum_{i=1}^N \sigma_{i-1,i}^z n_i^d, \quad (3.19)$$

$$P = -\frac{1}{2} \sum_{i=0}^{N-1} (\sigma_{i,i+1}^z - \sigma_{N,N+1}^z) + \sum_{i=1}^N i \sigma_{i-1,i}^z n_i^d. \quad (3.20)$$

Notice that in the absence of defects, Q is set entirely by the configuration of the bond spins on the boundaries, while P maps onto the total magnetization (up to a constant), i.e., a usual global U(1) internal symmetry.

The mapping we defined is a non-local one. For example, to identify a defect ($n_i^d = 1$) on a given site i , one needs to measure the sign of the closest charge to the left (or right) of i , which requires non-local string operators analogous to the ones we introduced for the $t - J_z$ model. A natural question to ask is: when does there exist a Hamiltonian in

¹⁰There is some ambiguity regarding the completely empty state which can be mapped to two different states: by convention we choose it to correspond to a state with all bond spins pointing right and no defects.

the new bond variables and when is this a local one? Let us assume for a moment that there are no defects, such that the mapping simplifies to Eq. (3.17). In this situation one finds $\sigma_{i,i+1}^z = \sigma_{0,1}^z + \frac{1}{2} \sum_{j \leq i} S_j^z$. One is then tempted to conclude that any local range- ℓ charge-conserving process only involves the intermediate $(\ell - 1)$ bond variables, such that this process is mapped to a local one in terms of bond variables. However, the constraint $\sigma^z = \pm 1$, rules out those which do not preserve the sign of the left- and rightmost charges, as otherwise this leads to $|\sigma^z| > 1$ on some bonds or equivalently, require to update all bonds to the right (left) of the given site. Thus, the relevant property of H that ensures this is the same as the one encountered above as a necessary condition for statistically localized strong boundary modes. Namely, we require the following condition: terms of the Hamiltonian acting on a given region of space can not change the sign of the left- and rightmost charges within this region. In fact, we already noticed in the previous chapter that H_3 satisfies this property. Consequently, H_3 also conserves $\hat{q}_{\ell,r}$ and therefore exhibits strong boundary modes. We return to this point in the following section.

Before proceeding we notice that the mapping we just presented also holds in the presence of diagonal interactions expressed as sums of products of local S^z operators. For example, the term $m \sum_i (S_i^z)^2$ counting the number of non-zero spins becomes $\frac{m}{2} \sum_i (1 - \sigma_{i-1,i}^z \sigma_{i,i+1}^z)$ leading to the XXZ model within the sector with $N^d = 0$. Moreover, this same mapping also applies to the $t - J_z$ Hamiltonian in Eq. (3.1), which for $J_z = 0$ becomes $H_{t-J_z}|_{N^d=0} \propto \sum_{j=1}^{N-1} (\sigma_{i,i+1}^x - \sigma_{i-1,i}^z \sigma_{i,i+1}^x \sigma_{j+1,j+2}^z)$.

3.2.2. Labeling of connected sectors: Non-local conserved quantities

Armed with this mapping, we can now identify the integrals of motion that label the fragmented Hilbert space, and show how they fit into the general notion of statistically localized operators discussed above.

Pattern of defects

We start by noting that H_3 Eq. (3.16) does not contain any terms that could create or destroy defects: *the number of defects, $N^d \equiv \sum_i n_i^d$, is conserved* ①. This can be confirmed explicitly by considering the effect of local terms in H_3 acting on charge configurations. The possible non-trivial transitions of a 3-site charge configuration are given by

Spin-1	Bond variables
$0 + 0 \leftrightarrow + - +$	No defect: $\leftarrow 0 \leftarrow + \rightarrow 0 \rightarrow \leftrightarrow \leftarrow + \rightarrow - \leftarrow + \rightarrow$ Defect: $\rightarrow 0 \rightarrow \bullet \rightarrow 0 \rightarrow \leftrightarrow \rightarrow \bullet \rightarrow - \leftarrow + \rightarrow$
$0 + - \leftrightarrow + - 0$	No defect: $\leftarrow 0 \leftarrow + \rightarrow - \leftarrow \leftrightarrow \leftarrow + \rightarrow - \leftarrow 0 \leftarrow$ Defect: $\rightarrow 0 \rightarrow \bullet \rightarrow - \rightarrow \leftrightarrow \rightarrow \bullet \rightarrow - \leftarrow 0 \leftarrow$

as well as those obtained by exchanging $+ \leftrightarrow -$, and \leftarrow with \rightarrow . In particular, if the left-most charge were a defect (highlighted in red), it remains being a defect and by the action of H_3 , only an alternating pattern of charges is created after it conserving the sign of the left- and rightmost charges on those 3 sites and thus the number of defects.

Thus the number of defects acts as an emergent U(1) symmetry (different from the original U(1) symmetry of charge conservation), emergent in the sense that it is non-local in the original variables and only becomes local after the mapping outlined above. One can use the operators \hat{q}_k , defined for the physical variables in Eq. (3.6), to express the number of defects as

$$N^d = \frac{1}{2} \sum_{k=1}^N (\hat{q}_{k+1})^2 (1 + \hat{q}_k \hat{q}_{k+1}), \quad (3.21)$$

which further emphasizes the non-local nature of the defects.

In fact, the Hamiltonian H_3 conserves not only the total number of defects, but also ② the pattern of their signs (similarly to how H_{t-J_z} conserved not just the number of fermions, but also the spin orientation of each fermion). For example, the state shown in Fig. 3.6(b), with (from left to right) a $(-)$ -defect followed by three $(+)$ -defects, can only go to configurations with the same pattern. Thus we see that the mechanism behind the fragmented Hilbert space is analogous in the two cases, except that for H_3 it originates from a ‘hidden’, rather than explicit, $U(1)$ symmetry.

The pattern of defects can be characterized by eigenvalues of statistically localized operators, similar to the ones discussed above in the case of the $t - J_z$ model. In fact, after mapping to bond spins and defects, one can directly use the same set of operators to label the defect patterns, as defined in Eq. (3.6), by replacing S_i^z for the $t - J_z$ model with the local defect charge operator $\sigma_{i-1,i}^z n_i^d$ and $\hat{\mathcal{P}}_i^k$ with a projector onto configurations with $k - 1$ defects to the left of site i , i.e., $\sum_{j < i} n_j^d = k - 1$, and $n_i^d = 1$. In the original variables, these are rather complicated non-local operators. Nevertheless, a Haar random state in the thermodynamic limit will have a finite density of defects, $\nu_d \equiv \langle N^d \rangle / N = \frac{1}{3}$ (see Appendix B.2). Indeed, since for large N the variance is once again exponentially suppressed ($\mathbb{E}_{\text{Haar}}[\langle n_i^d \rangle^2] - \mathbb{E}_{\text{Haar}}[\langle n_i^d \rangle]^2 \propto 3^{-N}$), almost all states have a similar defect density. For such states, one could repeat the argument in Section 3.1.2 to argue that the probability distribution of finding the k -th defect on site i is peaked around a position $\bar{i} = k/\nu_d$, with a width that scales as \sqrt{k} ¹¹. Similarly, a random state with a fixed total charge Q will also have a finite ν_d and therefore leads to a partially localized probability distribution. Thus the operators that label the defect patterns and the corresponding Hilbert space sectors of H_3 are at least statistically localized in the sense we previously defined.

We conclude this paragraph by noting that apart from the charges of each defect, H_3 also conserves the sign of the leftmost and rightmost *physical* charges, as measured by the operator \hat{q}_ℓ and \hat{q}_r defined in Eqs. (3.12) and (3.13) respectively (as mentioned above, this condition is in fact necessary to ensure that the Hamiltonian remains local after mapping to the new variables). This implies that our conclusions about the lack of thermalization at the boundary, and about exact degeneracies in the spectrum, discussed in Section 3.1.3 for the $t - J_z$ model, apply also to H_3 . However, H_3 is different from H_{t-J_z} , in that it shows fully localized behavior also *in the bulk*. To understand the reason for this, we now turn to a further set of conserved quantities possessed by H_3 .

Dipole moment of dynamical disconnected regions

While the conservation of the pattern of defect charges is sufficient to fragment the Hilbert space into exponentially many disconnected sectors, it does not account for all the sectors of H_3 . The conservation of the signs of defects (which are in fact a subset of the conserved quantities exhibited by H_{t-J_z}) is also insufficient to explain the localized behavior (i.e., infinitely long-lived autocorrelations) occurring in the *bulk* that we uncovered in the previous chapter. As we now argue, this rich non-ergodic dynamics originates from an interplay between the SLIOMs discussed in the previous section (that is, the pattern of defects), and the conservation of the total dipole moment. Thus, while on their own neither of those ingredients leads to fully localized behavior, their combination is sufficient to make H_3 localized.

The zero defect sector $N^d = 0$ with a given boundary condition (corresponding to a fixed total charge $Q = 0, \pm 1$) further splits up into sectors, as seen from Eqs. (3.19) and (3.20), according to the total magnetization of the bond spins, $\sum_i \sigma_{i,i+1}^z$, which in this case is

¹¹Notice that $k \sim O(1)$ at the boundary, but $k \sim O(N)$ at the bulk for a finite density of particles.

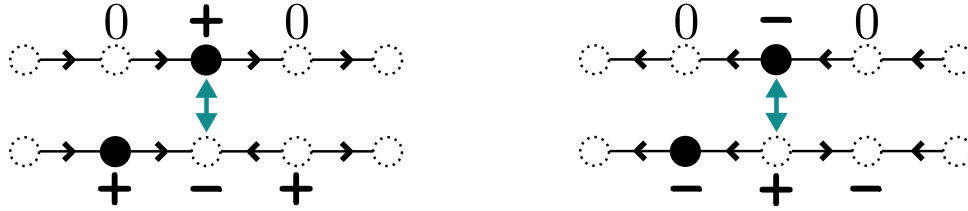


Figure 3.7.: **Hopping of defects.** To maintain the constraints, when a defect hops it has to flip a bond spin to its right, making its dynamics asymmetrical. In the original variables, this process is equivalent to emitting/absorbing a dipole from the right.

equal to the dipole moment P up to a constant shift.

When defects are present, they also carry a dipole moment, as shown by Eq. (3.20). The asymmetric definition of the defect—same charge as the nearest *on its left*—makes that its hopping only modifies the configuration on bonds that are to its right (see for example Fig. 3.7). This is the same as saying that defects can only emit (absorb) dipoles to (from) their right and never from their left. Thus, for every defect *the total dipole moment of charges to its right (including the defect itself) is conserved*. This implies that the dipole to the left of the defect (*not counting the defect*) is also separately conserved.

We thus find that each defect gives rise to an additional conserved quantity. Equivalently, we could take a configuration with N^d defects, which separate the chain into $N^d + 1$ regions, and associate a conserved dipole moment to each of these regions. In assigning the dipole moment $\hat{P}_{[k,k+1]}$ to the region between defects k and $k+1$, one should include the k -th defect (at the left boundary) but not the $(k+1)$ -th on its right (e.g. $|\dots[\bullet \rightarrow \dots \leftarrow][\bullet \leftarrow \dots]\rangle$). The total dipole moment then becomes¹² $P = \sum_{k=0}^{N^d} \hat{P}_{[k,k+1]}$, where k labels the region between the k th and $(k+1)$ th defect, each with its own conserved dipole moment $\hat{P}_{[k,k+1]}$. Moreover, we notice that while the total charge \hat{Q}_k in each of these regions is also conserved, this does not give rise to new independent constants of motion, since the value of these charges are already fixed by the pattern of defects. More explicitly, the total charge between two equally signed defects, e.g., $\overset{+}{\bullet} \dots \overset{+}{\bullet}$ is given by the charge of any of the defects (in this case $\hat{Q}_k = +1$); and equals to zero otherwise. This is shown in Fig. 3.8 in terms of the original spin-1 degrees of freedom.

Note that, while the position of the k -th defect in the bulk has fluctuations that grow with system size as $\propto \sqrt{N}$ (much like the case of the k -th charge in the $t - J_z$ model before), the average *distance* between neighboring defects remains finite in the thermodynamic limit for states with a finite defect density ν_d . This implies that the dipole moment $\hat{P}_{[k,k+1]}$ within a region of two consecutive defects, is a conserved quantity that is more localized than the previously introduced SLIOMs. We can make this point more explicit, by defining the operator that measures $\hat{P}_{[k,k+1]}$ as

$$\hat{P}_{[k,k+1]} = \sum_{ij} \hat{Q}_{ij}^k P_{ij}, \quad (3.22)$$

where \hat{Q}_{ij}^k is a projector onto configurations where the k -th defect sits on site i and the $(k+1)$ -th defect is on site j , while P_{ij} measures the dipole moment in the region $[i, j-1]$ (including the former but not the latter defect). Given Eq. (3.22), we can go to center of mass and relative coordinates: while the expectation value $\langle \hat{Q}_{ij}^k \rangle$, as a probability

¹²By definition, $\hat{P}_{[0,1]}$ corresponds to the dipole moment between the left boundary of the chain and the first defect; while $\hat{P}_{[N^d, N^d+1]}$ corresponds to the dipole moment between the last defect (including it) and the right boundary.

$$\begin{array}{cccccccc}
 \hat{P}_{[0,1)} & \hat{P}_{[1,2)} & & \hat{P}_{[2,3)} & & \hat{P}_{[3,4)} & \hat{P}_{[4,5)} & & \hat{P}_{[5,6)} & & \hat{P}_{[6,7)} & \hat{P}_{[7,8)} \\
 + & \left[\oplus - \ominus \right] & & + & & \left[\oplus \right] & \left[\oplus - \ominus \right] & & + - + - & & \left[\ominus + \oplus \right] & \left[\oplus \right]
 \end{array}$$

Figure 3.8.: **Labeling of connected sectors in the original variables.** Charges that have the same sign as the ones to their left (circled) correspond to *defects*, whose total number (N^d) and pattern is conserved by the Hamiltonian H_3 . Moreover, the dipole moment \hat{P}_k within each region between two subsequent defects (including the defect on the left but not the one on the right, as indicated by the brackets) is also independently conserved, such that the total dipole becomes $P = \sum_{k=0}^{N^d} \hat{P}_{[k,k+1)}$.

distribution, is only partially localized in $\frac{i+j}{2}$; it is *exponentially* localized in the relative coordinate, decaying as $(1 - \nu_d)^{(j-i)}$. In this sense, $\hat{P}_{[k,k+1)}$ is statistically localized to a *finite region* of length $\sim 1/|\log(1 - \nu_d)|$ (see Appendix B.1 for more details on the definition of SLIOMs appropriate to this case). As we show in the next section, the existence of these additional conserved quantities lead to additional dynamical constraints on the mobility of defect configurations. These constraints, together with the statistical localization of $\hat{P}_{[k,k+1)}$, account for the fact that H_3 has infinite coherence times for charge autocorrelations in the bulk, (as well as a broad distribution of entanglement in energy eigenstates, which we discuss in Section 3.2.3).

To summarize, let us compare the conservation laws of H_3 with those of the $t - J_z$ model discussed above. In the latter case, we had a conserved number of fermions, each of which carries a spin-1/2 whose S^z components are all separately conserved — defining what we have named the *pattern of spins*. H_3 is different for two reasons. First, the objects, whose pattern is conserved are the defects, which are non-local in the original variables. Furthermore, H_3 has an additional set of conserved quantities $\{\hat{P}_{[k,k+1)}\}_{k=0}^{N^d}$, arising due to the interplay between dipole conservation and the defect pattern: all the spatial regions separated by defects have separately conserved dipole moments. Altogether, we have identified the following set of conserved quantities for H_3 : the total charge Q and dipole P , the left- and rightmost charges $\hat{q}_{\ell,r}$, the number of defects N^d , the charge of each defect $\{Q_k = \pm 1\}_{k=1}^{N^d}$ (or charge pattern) and the dipole moment of regions between defects, $\{\hat{P}_{[k,k+1)}\}_{k=0}^{N^d}$. We have numerically confirmed that these integrals of motion together *uniquely* label *all* the connected sectors of H_3 in the local S^z basis, i.e., two different sectors correspond to two different sets of values of the conserved quantities. Moreover, since a dipole-conserving random circuit of 3-site gates has the same fragmentation of the Hilbert space as H_3 , it consequently also conserves all of the quantities identified above.

3.2.3. Implications for dynamics

We have seen how the conserved quantities of H_3 fit into the scheme of SLIOMs (see also Appendix B.1). However, their precise nature is different from the simpler case of the $t - J_z$ model discussed in Section 3.1. As mentioned above, this difference is responsible for the fact that, despite both being strongly fragmented, the two models exhibit rather different dynamics in their bulk: H_3 has infinite correlation times when evaluated on infinite temperature states, unlike H_{t-J_z} . Here we explain how the SLIOMs constructed in the previous section bring about localized dynamics, highlighting the role played by the dipole moments $\hat{P}_{[k,k+1)}$.

Charge localization

To see how the conservation laws lead to localized behavior, consider a configuration where there are two subsequent defects with a + charge, at sites i and $j > i$: $\bullet_i^+[\dots]\bullet_j^+$. By the definition of defects, the region $[i + 1, j - 1]$ between them has 0 total charge and a dipole moment $p \geq 0$, namely, every + charge is paired with a - one to its left within the region. As long as the position i is fixed, p is conserved, as the sum $i + p$ is a conserved quantity. This dipole p cannot be compressed to a region of less than $p + 1$ sites by dipole-conserving processes, forcing the position of the second defect to obey $j > i + p + 1$. But the right hand side of this inequality is in fact one of the conserved quantities \hat{P}_k , and therefore time-independent¹³. Therefore, the position j of the second defect can *never* cross this particular location and remains restricted to half of the chain. Similarly, since $p \geq 0$ at all times, and $i + p$ is conserved, we have that the left defect can move at most p sites to the right. Clearly, the same argument applies to a pair of (-)-defects. On the other hand, for two defects with *opposite* signs, one gets a weaker constraint $j - i > |P_k|$, i.e., a lower bound on their *distance*.

Let us now consider a defect somewhere in the bulk of the chain for a typical configuration in the z -basis. How far can it travel to the left? If the nearest defect to its left is of the same sign, it constrains its motion by the above argument. More generally, consider the closest pair of subsequent equal sign defects on the left; due to the hard-core constraint, these restrict the motion of all defects to their right, including the original one. Therefore, the only way for a given defect to travel a distance ℓ to the left is if all the defects originally within this region have an exactly alternating sign pattern. However, the relative number of such configurations scales as $e^{-\gamma\ell}$ for some constant $0 < \gamma < 1$, and therefore a defect will typically travel a finite distance in the thermodynamic limit. The same argument applies to travelling to the right, which shows that almost all defects are localized to finite regions¹⁴.

Consider now the infinite temperature charge autocorrelator. We can expand it in terms of product states $|\mathbf{s}\rangle = \bigotimes_i |s_i\rangle$ in the original variables (i.e., $s_i = +, -, 0$) as

$$\langle S_i^z(t) S_i^z \rangle_{\beta=0} = \frac{1}{3^N} \left[\sum_{\substack{\mathbf{s} \\ s_i=+}} \langle \mathbf{s}(t) | S_i^z | \mathbf{s}(t) \rangle - \sum_{\substack{\mathbf{s} \\ s_i=-}} \langle \mathbf{s}(t) | S_i^z | \mathbf{s}(t) \rangle \right]. \quad (3.23)$$

In half of the cases, the initial + charge on site i is a defect. In that case, as the above argument shows, it is almost surely restricted to live in a final spatial region with an overall charge of +1, thus yielding a positive contribution to the autocorrelator. If the size of the region is ℓ , the infinite-time contribution is expected to be $O(1/\ell)$, and in the thermodynamic limit, their sum gives $\sum_{\ell=1}^{\infty} e^{-\gamma\ell}/\ell = -\ln(1 - e^{-\gamma}) > 0$. There is another equal contribution stemming from the (-)-defects. This shows that the SLIOMs lead to charge localization even at infinite temperature.

Entanglement growth

Another signature of localized behavior in H_3 is the fact that the entanglement entropy of the long-time steady state is sub-thermal (see Fig. 2.2), even for an initial random product state that is not in the z -basis and therefore has weight in all the connected sectors. In Ref. [181] it was argued that this saturation value is determined by the size of the largest

¹³Note that the condition of having zero total charge in the middle region is important, as it allows us to always shift the reference frame and measure p from the position i .

¹⁴One could also define defects starting from the right, rather than the left, edge of the chain. These could be used to further constrain the possible transitions.

well defined quantum numbers for all SLIOMs. Consequently, the reduced density matrix of a bi-partition ρ_A can be block diagonalized by e.g., the number of defects on one side. As noted in Section 3.2.2, for a randomly chosen z -product state, which has a finite density of defects, the movement of almost all defects will be restricted to $O(1)$ regions due to the conservation laws. Therefore, a particular entanglement cut can only be crossed by a small subset of defects, and consequently many of the blocks of ρ_A , will be identically zero. Furthermore, each block with k defects to the left of the cut can be further decomposed into smaller blocks using the conserved dipole moment $\hat{P}_{[k,k+1]}$ (see Fig. 3.9). Since the k -th defect can only travel a finite distance to the left, it can only emit a finite number of dipoles, such that the reduced density matrix for most initial configurations is restricted to a few blocks of size $O(1)$. Consequently, it only has a finite number of non-vanishing eigenvalues, limiting its entanglement to an area law, i.e., constant for one-dimensional systems. The same argument explains the broad distribution of entanglement entropies observed for the eigenstates of H_3 in Fig. 2.9.

The above discussion shows that the structure of SLIOMs we uncovered gives clear restrictions for the entanglement growth of initial states in the z bases. While we expect that the same underlying mechanism is responsible for the sub-thermal saturation value for completely random product initial states, a complete explanation of this fact has not yet been accomplished. Recently, two different groups have generalized Page's seminal work on the mean entanglement entropy of pure random states [118] to sparse random pure states [120] and systems with local constraints [119]. The former work showed that the (half chain) entanglement entropy of certain states can saturate its Page value even though their fractal dimensions, defined via the inverse participation ratio and measuring their spreading on Hilbert space, are strictly smaller than one. However, this work dealt with a random partition of the chain and thus spatial locality arguments were not considered. On the other hand the latter work took into account local constraints and, e.g., explicitly computed the modification of Page's correction value ($-1/2$) for the Rydberg chain. I believe that the combination of these two approaches is a promising route to better understand the dynamics of the half-chain entanglement entropy in systems with dipole conservation.

3.2.4. Largest sectors and SPT order

A particular corollary of the discussion in Section 3.2.2 is that increasing the number of defects decreases the connectivity of the Hilbert space, since each new defect leads to a further conservation law (the associated dipole moment), which one needs to fix in order to specify a sector. Indeed, one can check numerically that the largest connected sectors all have zero defects. Moreover, we confirm numerically that the overall ground state of H_3 (which is 4-fold degenerate, as we discuss below) also belongs to these four largest sectors. Motivated by this, we now turn our attention to the subspace with no defects.

In fact, H_3 takes a particularly simple form within this subspace. Since there are no defects, the only degrees of freedom are the bond spin-1/2's, which can take any configuration. Let us consider a local term of the Hamiltonian $h_3 = S_i^+(S_{i+1}^-)^2S_{i+2}^+ + \text{H.c.}$ acting on the set of consecutive sites $\{i, i+1, i+2\}$. From Eq. (3.18) we get that the state of a given bond is given by the total charge on sites preceding that bond, i.e., $\sigma_{n,n+1}^z = \sigma_{0,1}^z + \frac{1}{2} \sum_{j \leq n} S_n^z$. Thus, the configuration of bonds with $n \leq i-1$ remains intact under the action of h_3 . Similarly happens for $n \geq i+2$, since h_3 locally conserves the total charge. Thus, the Hamiltonian in terms of bond variables only has a non-trivial action on the bonds $(i+1, i+2)$ and $(i+2, i+3)$, and we recover that in fact the Hamiltonian is given by the sum of local terms. In particular, the possible local processes are shown in

Table 3.3 and lead to the local Hamiltonian

$$H_3|_{N^d=0} = -2 \sum_{j=2}^{N-1} \left(\sigma_{i-1,i}^x \sigma_{i,i+1}^x + \sigma_{i-1,i}^y \sigma_{i,i+1}^y \right), \quad (3.24)$$

i.e. a spin-1/2 XY model on a chain of length $N - 1$ (note that the two auxiliary spins, $\sigma_{0,1}^z$ and $\sigma_{N,N+1}^z$ do not appear in the Hamiltonian), exactly solvable via a Jordan-Wigner transformation to free fermions. Considering the spin-1/2 variables as the original physical degrees of freedom, one can interpret H_3 restricted to the zero-defects sector, as governing the dynamics of kink ($|\leftarrow\rightarrow\rangle$) / anti-kink ($|\rightarrow\leftarrow\rangle$) configurations of the XY model, with $|0\rangle$ representing an empty site. This Hamiltonian conserves $Z_{\text{tot}} \equiv \sum_i \sigma_{i,i+1}^z$, equal to the dipole moment in the original model, with the largest symmetry sector being the one with half-filling ($Z_{\text{tot}} = 0$)¹⁵. The ground state of this model is gapless due to the presence of Fermi points and has an effective low energy Luttinger liquid description. We confirm that this is also the ground state of H_3 overall, by finding the ground state in DMRG and comparing its energy with that of the ground state of the XY chain at half filling, finding perfect agreement.

Spin-1: $\{i, i+1, i+2\}$	Bond variables: $(i, i+1) (i+1, i+2)$
$ 0+0\rangle \leftrightarrow +-+\rangle$	$ \leftarrow\rightarrow\rangle \leftrightarrow \rightarrow\leftarrow\rangle$
$ 0+-\rangle \leftrightarrow +00\rangle$	
$ 0+0\rangle \leftrightarrow -+-\rangle$	$ \rightarrow\leftarrow\rangle \leftrightarrow \leftarrow\rightarrow\rangle$
$ +-0\rangle \leftrightarrow 0+-\rangle$	

Table 3.3.: Action of local terms in Hamiltonian H_3 in the spin-1/2 variables.

However, this is not the full story. As mentioned above, the ground state has a 4-fold degeneracy. In fact, this is true for all eigenstates within the zero defect sector: as seen above, this sector consists of 4 equivalent XY chains with 4 different boundary conditions. These correspond to the four possible choices of the leftmost and rightmost charge in the system, which are conserved under H_3 . Moreover, we find numerically that even eigenstates *with* defects are 4-fold degenerate throughout the entire spectrum. This degeneracy is due to zero modes at the boundaries of an open chain, and is not present with periodic boundary conditions¹⁶. Nevertheless, the exact 4-fold degeneracy is specific to H_3 and can be lifted to a 2-fold degeneracy by adding perturbations, diagonal in the S^z -basis, which preserve the block structure of H_3 . The 2-fold degeneracy, on the other hand, is robust as long as we preserve the spin rotation symmetry $R_x = e^{i\pi \sum_i S_i^x}$ and the signs of the left- and rightmost charges, analogously to the case of the $t - J_z$ model discussed before.

The (strong) zero modes at the boundary appear concurrently with symmetry protected topological (SPT) order in the bulk. Consider the string order parameter $\langle S_i^z e^{i\pi \sum_{l=i+1}^{j-1} S_l^z} S_j^z \rangle$. This measures the ‘hidden antiferromagnetic order’ of the Haldane phase [217–219], which becomes apparent after dropping all the empty sites. States with no defects have such a hidden AFM order by construction. More formally, acting on states without defects, the string factorizes due to the Gauss’s law (3.18) as $e^{i\pi \sum_{l=i+1}^{j-1} S_l^z} \rightarrow \sigma_{i,i+1}^z \sigma_{j-1,j}^z$, an explicit example of symmetry fractionalization. Consequently, the string order parameter

¹⁵The dimension of the largest connected sector is therefore (assuming an odd number of sites) $\binom{N-1}{(N-1)/2}$, scaling asymptotically as $\propto 2^N$ up to logarithmic corrections. This confirms earlier numerical results [1, 181].

¹⁶ H_3 still has a significant amount of degeneracies with PBC, but it also has non-degenerate eigenvalues.

simplifies to

$$\langle S_i^z e^{i\pi \sum_{l=i+1}^{j-1} S_l^z} S_j^z \rangle = \frac{1}{4} \langle (1 - \sigma_{i-1,i}^z \sigma_{i,i+1}^z) (\sigma_{j-1,j}^z \sigma_{j,j+1}^z - 1) \rangle. \quad (3.25)$$

In the limit $|j - i| \rightarrow \infty$ this factorizes into the product of local expectation values¹⁷. Now, the expectation value $\langle 1 - \sigma_{i-1,i}^z \sigma_{i,i+1}^z \rangle$ is non-zero for any translation invariant state, except for a completely spin polarized one (i.e. the empty state in the original variables). In principle the non-vanishing string order parameter is also compatible with the symmetry R_x being spontaneously broken. However, R_x becomes the parity transformation $\prod_i \sigma_{i,i+1}^x$ within the zero defect sector, which is unbroken in the ground state of the XY chain (3.24). We hence associate the presence of string order with a symmetry protected topological state. In fact, as $\langle S_i^z e^{i\pi \sum_{l=i+1}^{j-1} S_l^z} S_j^z \rangle$ is non-zero for every eigenstate of the zero defect sector, this is suggestive of there being a non-trivial SPT order for the whole spectrum, which is reminiscent to the appearance of topological order in excited states of MBL systems [190, 191].

3.3. Embedded PXP dynamics: Relation to quantum many-body scars

The realization of Hilbert space fragmentation in dipole-conserving systems and the study of fractonic dynamics, were almost concurrent to the experimental observation and later theoretical characterization of quantum many-body scars with Rydberg atoms [43, 44]. Both phenomena appear as a consequence of kinetically constraints in the action of the Hamiltonian, although appearing only implicitly in the former case. Thus, it is natural to compare these two systems and wonder whether there exist some more explicit relation among the two.

In Chapter 1, we already explained that in the strong interacting regime the system can be approximately described by the so-called PXP model which corresponds to the spin-1/2 Hamiltonian [44]

$$H_{\text{PXP}} = \sum_{n=1}^N P_{n-1} \sigma_n^x P_{n+1}, \quad (3.26)$$

where the projectors $P_n \equiv (1 - \sigma_n^z)/2$, ensure that not two adjacent Rydberg atoms (with \downarrow and \uparrow representing the ground and excited states of isolated atoms respectively) become simultaneously excited, a phenomenon known as Rydberg blockade. Thus, different number of adjacent excited states correspond to distinct disconnected components, as any two local adjacent excited states $\dots \uparrow \uparrow \dots$ are completely frozen, i.e., the system is fragmented. Restricted to the lowest energy subspace with no adjacent excited states, the dimension of the constrained Hilbert space can be shown to be [168] $d_N = F_{N+2}$ for open (OBC) — in the presence of additional boundary terms [220] — and $d_N = F_{N-1} + F_{N+1}$ for periodic boundary conditions (PBC), where F_n is the n th Fibonacci number. Note that in particular, this subspace contains the Néel states $|\mathbb{Z}_2\rangle = |\downarrow \uparrow \downarrow \uparrow \dots\rangle$ and $|\mathbb{Z}'_2\rangle = |\uparrow \downarrow \uparrow \downarrow \dots\rangle$, whose atypical real-time dynamics has been experimentally realized [43] and has been identified as a probe of the existence of quantum many-body scars [168].

In the following we show that the dynamics of certain fragments of the H_3 Hamiltonian for $S = 1$, are governed by the PXP dynamics (3.26) and identify the analogs to the Néel states in the fractonic language [167]. In fact, such relation was already obtained in Ref. [169] for Hamiltonian H_4 with $S = 1/2$. Let us consider states of the form

$$|\mathbb{F}_2\rangle = |\dots \boxed{-+-} - \boxed{-+-} \overset{2(k-1)}{2k} \overset{2(k+1)}{-+-} - \boxed{-+-} \dots\rangle, \quad (3.27)$$

¹⁷This is the case quite generally as long as the state on which we evaluate it is not a cat state.

3.3. Embedded PXP dynamics: Relation to quantum many-body scars

with a $|+\rangle$ state on every fourth site separated by three $|-\rangle$'s. In the following we fix the length of the chain to be a multiple of four, such that we contain an integer number of unit cells. For OBC the dipole moment of this configuration is given by $p(n_+) = N/2(1 - N/2 + n_+)$, where n_+ is the location of the first $|+\rangle$ state starting from the left boundary. Thus, the location n_+ labels different symmetry sectors containing the same spin pattern. However, due to the periodicity of the configuration, there only exist four different dipole moments $p(n_+)$ containing such types of configurations. When considering PBC, the dipole is defined modulo N .

Recalling that every local term h_n in the Hamiltonian $H_3 = \sum_n h_n$ takes the form

$$h_n \equiv S_{n-1}^+ (S_n^-)^2 S_{n+1}^+ + \text{H.c.}, \quad (3.28)$$

it is clear that the *only non-trivial* local actions of H_3 on the state $|\mathbb{F}_2\rangle$, are those contained within the blocks shown in Eq. (3.27) which are centered around even sites. After applying two local terms h_n centered around the location of $|+\rangle$ states at sites $n = 2(k \pm 1)$, $|\mathbb{F}_2\rangle$ becomes

$$|\mathbb{F}_2\rangle \longrightarrow h_{2(k-1)} h_{2(k+1)} |\mathbb{F}_2\rangle = |\dots \boxed{-+-} - 0 \overset{2(k-1)}{-} \overset{2k}{\boxed{0-0}} \overset{2(k+1)}{-} 0 - \boxed{-+-} \dots\rangle. \quad (3.29)$$

Now the action on the intermediate site $2k$ becomes non-trivial

$$\begin{aligned} & h_{2(k-1)} h_{2(k+1)} |\mathbb{F}_2\rangle \\ & \longrightarrow h_{2k} h_{2(k-1)} h_{2(k+1)} |\mathbb{F}_2\rangle = |\dots \boxed{-+-} - 0 \overset{2(k-1)}{-} \overset{2k}{\boxed{-+-}} \overset{2(k+1)}{-} 0 - \boxed{-+-} \dots\rangle. \end{aligned} \quad (3.30)$$

One can then realize that only terms h_{2k} centered around even sites generate non-trivial dynamics conditioned to the states on odd near sites, such that the only allowed local transition is $| - + - \rangle \leftrightarrow | 0 - 0 \rangle$. Then, the restriction of the Hamiltonian H_3 to subspaces containing configurations of the form given by Eq. (3.27) becomes

$$H_3|_{\text{PXP}} = \sum_{k=1}^{N/2} h_{2k} = 4 \sum_{k=1}^{N/2} | - +_{2k} - \rangle \langle 0 -_{2k} 0 | + \text{H.c.} \quad (3.31)$$

Note also that there are never two $|+\rangle$ states in adjacent even sites, i.e., the local configuration $|+\rangle_{2k} |+\rangle_{2(k+1)}$ is not generated under the evolution of H_3 . This effectively implements the Rydberg blockade as imposed by the projectors in Eq. (3.26). With these observations in mind, we can construct a reversible map relating local spin-1 configurations centered around even sites $\{2k-1, 2k, 2k+1\}$, to spin-1/2 configurations on even sites $\{2(k-1), 2k, 2(k+1)\}$ in the PXP model via

$$\begin{aligned} |0-0\rangle &\leftrightarrow |\downarrow\downarrow\downarrow\rangle, & | - + - \rangle &\leftrightarrow |\downarrow\uparrow\downarrow\rangle, & |0--\rangle &\leftrightarrow |\downarrow\downarrow\uparrow\rangle, \\ | - - 0 \rangle &\leftrightarrow |\uparrow\downarrow\downarrow\rangle, & | - - - \rangle &\leftrightarrow |\uparrow\downarrow\uparrow\rangle, \end{aligned} \quad (3.32)$$

such that Eq. (3.31) becomes

$$\begin{aligned} H_3|_{\text{PXP}} &= 4 \sum_{k=1}^{N/2} |\downarrow\uparrow\downarrow\rangle \langle \downarrow\downarrow\downarrow| + \text{H.c.} \\ &= 4 \sum_{k=1}^{N/2} |\downarrow\rangle \langle \downarrow|_{2(k-1)} \otimes |\uparrow\rangle \langle \downarrow|_{2k} \otimes |\downarrow\rangle \langle \downarrow|_{2(k+1)} + \text{H.c.} = 4H_{\text{PXP}}, \end{aligned} \quad (3.33)$$

i.e., the restriction of H_3 into this family of connected subspaces becomes equivalent to a PXP model on a chain of length $N/2$ up to a factor of 4. Thus, there exist eight different symmetry sectors (the other four subspaces are obtained applying the Π^x parity symmetry to the configuration $|\mathbb{F}_2\rangle$), whose evolution is governed by the PXP Hamiltonian. This explicitly shows that quantum many-body scars phenomenology appears in the dipole conserving Hamiltonian H_3 , similarly to Ref. [169].

3.4. Summary of results

We have explicitly constructed integrals of motion for two models that exhibit the phenomenon of strong Hilbert space fragmentation, including a complete characterization of the fragmented structure of the family of Hamiltonians $H_3(\{J_i\})$ and the associated 3-local circuit dynamics we studied in the previous chapter. These extensively many non-local integrals of motion label the different disconnected sectors of the many-body Hilbert space, playing a role analogous to local integrals of motion in many-body localized systems. They are dominated by contributions from a sub-extensive region in space, but in such a way that the location and width of this region can be tuned by, for example, changing the average filling fraction in the system. This lead us to term these observables *statistically localized*.

In the $t - J_z$ model (which we argued can be realized in Rydberg atom experiments), all SLIOMs in the bulk are localized to regions of size $O(\sqrt{N})$. As a result, autocorrelations evaluated on an infinite temperature states (after fixing the number of up- and down-pointing spins) saturate to values $O(1/\sqrt{N})$, which are anomalously large compared to generic thermalizing systems, but nevertheless vanish as $N \rightarrow \infty$. For the dipole-conserving Hamiltonian H_3 , on the other hand, we have shown that some of the bulk conserved quantities are effectively localized to $O(1)$ regions and lead to finite autocorrelations even in the thermodynamic limit.

SLIOMs near the boundary, on the other hand, are localized to finite regions and lead to infinitely long coherence times for *both* models. We showed that these boundary SLIOMs can survive certain perturbations that destroy the strong fragmentation in the bulk, defining a statistically localized analogue of strong zero modes, where a thermalizing bulk co-exists with an explicitly non-ergodic boundary. We also analyzed the relationship between these zero modes and the ground states of the two models, which exhibit symmetry protected topological order, despite being gapless.

3.5. Discussion and outlook

3.5.1. Hilbert space fragmentation and commutant algebras

In this chapter we understood that a sufficient condition for fragmentation is the existence of extensively many SLIOMs. However, it is not clear how generic this construction is and whether it could be applied to other systems exhibiting fragmentation, like for example weakly fragmented or even two-dimensional systems. Building on this result, Ref. [166] introduced a formalism that allows to resolve some of these questions, by studying fragmentation in terms of the *commutant algebra* \mathcal{C} , defined as the algebra of conserved quantities associated to a family of Hamiltonians $\hat{H} = \sum_j J_j \hat{h}_j$. More formally, \mathcal{C} is the associative algebra formed by operators \hat{O} which commute with every local term of \hat{H} , i.e., $[\hat{O}, \hat{h}_j] = 0 \forall j$. For example, for a system with no symmetries, \mathcal{C} is just the identity operator and is thus one-dimensional, similarly to the case of systems with discrete global symmetries for which $\dim(\mathcal{C}) \sim O(1)$. Generically, systems with Abelian continuous global symmetries instead have a commutant whose dimension grows polynomially with system

size, as an extensive quantity have polynomially different eigenvalues, each of them corresponding to degenerate symmetry sectors. We will suggest possible counter examples at the end of Chapter 5. Using this approach, one then defines a system as fragmented if the dimension of the commutant algebra grows exponentially in system size, which corresponds to the number of different sectors labeled by eigenvalues of the SLIOMs. In fact, SLIOMs turned out to be a generating set (together with the identity operator) of the commutant algebra for the two cases studied in this chapter. This means that any of the exponentially many elements of \mathcal{C} , can be constructed as a linear combinations of product of SLIOMs.

An additional insight coming from this construction is the possibility to explore systems which are fragmented in an entangled basis — unlike the previous examples of fragmentation in the local z -basis— denoted as quantum fragmentation in Ref. [166]. This corresponds to a non-Abelian commutant algebra which leads to degenerate Krylov subspaces and richer structure in the Mazur bound. Moreover, while this formulation makes a first step into formalizing the concept of Hilbert space fragmentation, certain unresolved issues still remain. By this definition, systems with local conservation laws, like lattice gauge theories and related systems (e.g., height field or dimer models), are also examples of fragmentation, although the spatial locality properties of the underlying generating set (or elements of the commutant) are quite different. Thus, it would be desirable to include locality on this analysis to be able to distinguish these in principle two distinct systems. A conjecture is whether it is true that certain fragmented systems can be understood as “linear combinations” of lattice gauge theory models (with truncated gauge degrees of freedom) where gauge invariance is broken, and instead, only certain non-local combinations of local Gauss laws are preserved. We discuss this problem in more detail in Chapter 7.

3.5.2. Reducibility in classical kinetically constrained systems

The concept of fragmentation is reminiscent to that of *reducibility* in the context of stochastic processes and kinetically constrained systems [221, 222] for example appearing in the study of glasses. Consider a classical stochastic system evolving under a discrete or continuous Markov evolution. Then the probability for the system being in a given configuration at time t , namely $P(C, t)$, follows the master equation $\partial_t |P(t)\rangle = \mathcal{W}|P(t)\rangle$. Here $|P(t)\rangle$ is the probability vector $|P(t)\rangle = \sum_C P(C, t)|C\rangle$, and \mathcal{W} is the stochastic generator whose matrix elements in the basis $\{|C\rangle\}$ give the transition rates from one to another configuration [222]. A necessary condition, apart from detailed balance, for such equation to have a unique stationary state is that the dynamics is irreducible, i.e., “that the system can pass from any to any other configuration by some number of allowed transitions” [221]. This translates into the requirement for the matrix $\mathcal{W}_{C,C'}$ not being able to become block-diagonal by reordering the configurations in the basis. Therefore, both fragmentation and reducibility refer to the same splitting of Hilbert or configuration space into different disconnected partitions.

Apart from the different realms on which the consequences of fragmentation are studied, taking into account the additional insights gained in the context of quantum many-body systems as e.g., with respect to the ETH, the novelty of the systems we studied is the *lack of explicit* constraints in local terms of the Hamiltonian. In the study of glassy behavior [221], e.g., via the use of spin-facilitated models, one imposes specific kinetic constraints that have to be fulfilled in order to apply a certain update. These constrain the transition rates or the analogous local terms in the Hamiltonian [222]. This is also the case for the Shiraishi-Mori construction of models leading to weak ergodicity-breaking [42]. However, when aiming to generalize it to longer ranges or larger onsite occupations, there is not a unique unambiguous way to do so in general. Instead, the construction of dipole- (and higher-moment) conserving systems is based on a symmetry principle, permitting all

possible terms that are compatible with the global symmetry. Using this, we managed to prove that any dipole-conserving system with any finite spin representation and finite-range interactions is always fragmented.

3.5.3. Non-local conserved quantities and ETH

In the study of kinetically constrained systems [221, 222], particular emphasis is made on the distinction between reducibility and ergodicity. The latter is defined to mean that “any two configurations — with the exception of possibly a vanishingly small fraction of configuration space — remain mutually accessible on timescales that remain finite in the thermodynamic limit” [221]. From there the following conclusion follows: “Of course, reducibility implies non-ergodicity, but the reverse is not true.” [221]. However, by this definition of irreducibility a system with a global conserved quantity is always reducible, unless a given symmetry sector is fixed, and then is also non-ergodic.

In the study of quantum many-body systems, on the other hand, a system is said to be ergodic if either satisfies ETH or thermalizes, after fixing all, usually *global*, conserved quantities (recall the discussion in Chapter 1 about the meaning of these terms). Otherwise, random matrix theory would not hold in a narrow energy window and the expectation value of local observables evaluated on energy eigenstates, could not only depend on the energy but also on other quantum numbers. This suggests — after having identified the non-local SLIOMs as the cause for the strong fragmentation of the Hilbert space— that one should study thermalization properties within each of the disconnected subspaces independently after fixing the associated quantum numbers. In fact, this appears a natural thing to do, since the formulation in terms of commutant algebras treats “on equal footing conventional and non-local conserved quantities” [166], only distinguished by the size of the commutant. When doing so, one finds subspaces on which the system either thermalizes or not, a phenomenon that has been coined *Krylov restricted-thermalization* [172]. For example, we have found subspaces within which the dynamics can be governed by non-interacting, integrable, non-integrable, as well as the PXP Hamiltonian, as if different types of behaviors were embedded in the same system. Instead in this chapter, we only resolved the conventional global conserved quantities, e.g., charge and dipole, and concluded that systems with Hilbert space fragmentation provide examples of ergodicity-breaking violating the *diagonal* contribution of ETH. Following Ref. [42] and the discussion in Refs. [204, 205], this approach appears to be meaningful: Generically, one does not expect symmetry sectors associated to different eigenvalues of non-local charges to lead to distinct distributions for the expectation values of local observables [204, 205]. Moreover, one could advocate for this approach arguing that if non-local symmetries have to be fixed, projectors on energy eigenstates should also be included, which would make the statement of ETH trivial. A possible way out would be to realize that projectors on energy eigenstates depend, unlike SLIOMS, on the microscopic parameters of the system and thus cannot be defined for a family of systems.

Nevertheless, the root and resolution of this conflict lies on specifying what entitles a conserved quantity to be fixed when studying thermalization and agree on a precise, perhaps experimentally oriented, definition of what is meant by ergodicity breaking.

3.5.4. Future directions

Several questions remain to be explored. First of all it is unclear whether the construction presented in this chapter could be used to find the relevant conserved quantities in the case of longer-range generalizations of H_3 (which exhibit weak fragmentation). Even within the subset of strongly fragmented models (i.e., with the largest symmetry sector being a vanishing fraction of the full Hilbert space), qualitatively very different behaviors

can arise, as the two examples in this chapter demonstrate. Hence, it would be interesting to understand whether other “degrees” of fragmentation can exist, providing a full classification. The structure of conservation laws we uncovered could also be useful for understanding the dynamics of entanglement and out-of-time-ordered correlators in these systems [223].

Another direction is to explore the stability of the boundary SLIOMs to additional perturbations, i.e., whether they can still lead to unusually long coherence times even when they are not explicitly conserved. It would also be interesting to use the formalism of commutant algebras to look for other models featuring quantum fragmentation, both in the strong and weak sense, and extend them to higher dimensions. Finally, understanding the robustness of fragmentation to open quantum dynamics is a question worth exploring.

Part II.

**Experimental realization in tilted
interacting systems**

4. The tilted Fermi-Hubbard model: An experimental platform for constrained systems

The ability to reduce everything to simple fundamental laws does not imply the ability to start from those laws and reconstruct the universe.

Philip Warren Anderson from *More is different* [224].

Is there a system where the dipole moment of some global U(1) charge is conserved or is this just a theory model? It turns out this symmetry is approximately conserved and becomes important to understand certain experimentally accessible physics scenarios. In particular, this is the case for a system of interacting particles (or rather atoms) hopping on a one-dimensional chain with tunneling amplitude J in the presence of a tilted field setting an energy difference Δ between consecutive sites (see Fig. 4.1). For the moment, we just think about this tilt as coupled to the center of mass of the particles $\sum_x x \hat{n}_x$, but we will provide the actual experimental realization in Section 4.5.

When $\Delta \gg J$, a single particle hopping up or down the tilt is energetically suppressed due to the large energy difference between the initial and final configurations. In fact, a single particle in the presence of a tilt is known to be Wannier-Stark localized and the dynamics to be trapped in a finite region of size $\sim J/\Delta$ leading to Bloch oscillations (Section 4.1). However, in the presence of interactions, a simultaneous pairwise hop of two (or more) particles in opposite directions can balance this cost leading to a much smaller energy difference and eventually avoiding localization. Hence the dynamics can be approximated by an effective Hamiltonian which conserves the center of mass location, or equivalently, the dipole moment associated to the total particle number. In such scenario, the real-time dynamics will strongly depend on the particular initial state one prepares, as a consequence of the approximate Hilbert space fragmentation which emerges at short to intermediate time scales. However, in the presence of additional weak disorder [157] or a harmonic confinement potential [225], theoretical studies have found characteristic MBL phenomenology, since then dubbed Stark MBL.

In this chapter we study the (non-ergodic) behavior in the tilted one-dimensional (1D) Fermi-Hubbard model (Fig. 4.1a) which hence lies at the interface of Stark MBL and Hilbert space fragmentation. Starting from an initial charge-density wave (CDW) of singlons (singly-occupied site), we study (including numerical and experimental simulations) relaxation dynamics for a large range of interaction strengths and moderate values of the tilt ($\Delta < 4J$) (Section 4.5), where none of the two mechanisms described above would in principle apply and where naively one may expect the system to thermalize. At short times we experimentally observe coherent dynamics due to Bloch oscillations, whose amplitude strongly depends on the Hubbard interactions (Section 4.5.2). Surprisingly we find that after intermediate times and even close to resonance between the tilt and interaction strengths, the evolution converges to a non-thermal steady-state, that persists for long evolution times up to 700 tunneling times, signaling a robust memory of the initial CDW throughout (Section 4.5.3). Using numerical calculations we show that the observed non-

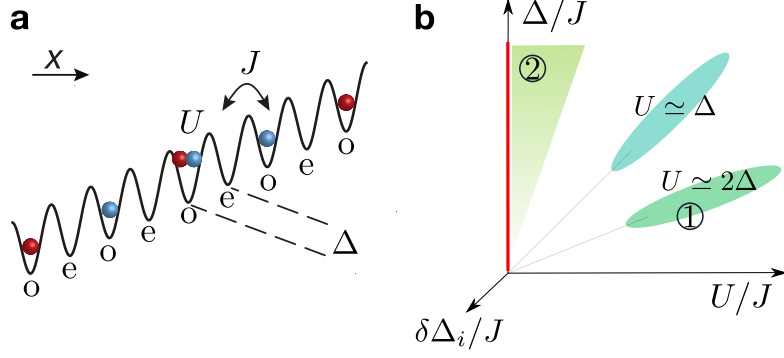


Figure 4.1.: **Tilted one-dimensional lattice.** **a)** Schematic of a tilted 1D model (with odd o and even e sites) with tunneling J , on-site interaction U and tilt Δ . **b)** Regimes of interest where an effective constrained Hamiltonian can be derived. The green area corresponds to a dipole-conserving regime. $\delta\Delta_i$ represents a slightly non-uniform or random field. Figure in panel a has been taken from Ref. [3].

ergodicity cannot be explained by the phenomenon of Stark-MBL, i.e., the robust memory is not due to experimental imperfections, such as residual harmonic confinement or disorder, and the bipartite entanglement entropy does not exhibit the characteristic behavior of MBL systems [76] (see Fig. 4.8). Hence, nonergodicity appears to have a different origin, despite similar experimental signatures. This raises the question about the origin of the observed non-ergodicity. We construct effective Hamiltonians in two distinct regimes (① and ②), Fig. 4.1b) by taking the large tilt limit and find fragmented Hamiltonians in both cases (Section 4.3). While these models are only expected to describe the dynamics at large tilt values and for intermediate times (on the order of a few tens of tunneling times), they allow us to identify the microscopic processes that initiate dynamics at short times. In both regimes these are correlated tunneling processes, which result in the formation of doublons (doubly-occupied sites), either resonantly (regime ①) or detuned by the Hubbard interaction energy U (regime ②). Higher-order terms are expected to eventually drive the system towards thermalization. However, we are able to show that energy penalties for the second- or higher-order tunneling processes, which occur naturally in the model, render these dynamics inefficient. This results in extremely slow relaxation (Section 4.4.1), which appears stable for long times (> 104 tunneling times) in exact diagonalization studies of small systems, in agreement with the experimental observations (Fig. 4.14).

We conclude the chapter suggesting future research directions to study the phenomenology of Hilbert space fragmentation in the lab as well as possible ways to understand the role of the harmonic confinement (Section 4.6).

4.1. Single particle dynamics in a tilted field

Let us place a single particle on a *discrete* lattice in the presence of a tilt

$$H = -J \sum_{i \in \mathbb{Z}} |i\rangle\langle i+1| + \text{H.c.} + \Delta \sum_{i \in \mathbb{Z}} i |i\rangle\langle i|, \quad (4.1)$$

where $|i\rangle$ corresponds to the Wannier orbital localized at site i , and Δ sets the energy difference between consecutive sites. Its eigenstates, usually called Wannier-Stark orbitals, can be expressed in terms of the Wannier orbitals via the orthogonal transformation

$$|\beta_m\rangle = \sum_{i \in \mathbb{Z}} \mathcal{J}_{i-m} \left(\frac{2J}{\Delta} \right) |i\rangle, \quad (4.2)$$

where \mathcal{J}_n is the n th order Bessel function of the first kind [226]. These are spatially localized on a region of size $\frac{4J}{\Delta}$ in units of the lattice spacing, centered around site m for any non-zero value of the tilt, and decay (at least) exponentially fast outside that region $\mathcal{J}_{i-m}(\frac{2J}{\Delta}) \sim \gamma^{|i-m|}$ for any finite tilt Δ (see review Ref. [75]). In this basis, Hamiltonian Eq. (4.1) takes the diagonal form

$$H_{\text{WS}} = \Delta \sum_{m \in \mathbb{Z}} m |\beta_m\rangle \langle \beta_m|, \quad (4.3)$$

whose spectrum, with a constant energy gap Δ between consecutive eigenvalues, is usually denoted as Wannier-Stark ladder. Such commensurate spectrum translates into long-coherent oscillations in observable quantities, known as Bloch oscillations, which in fact have been experimentally observed [227]. Bearing in mind the limitations of the experimental setup used to investigate this system, we use the local imbalance to probe its dynamics, which is defined as the difference of probabilities to occupy even and odd sites

$$\mathcal{I}(t) = \sum_{i \in \mathbb{Z}} (-1)^i n_i(t). \quad (4.4)$$

In particular, this quantity becomes useful to study localization (delocalization) phenomena when considering specific initial configurations which break the symmetry between even and odd sites. For example, consider an initial state $|i_0\rangle$ with a particle sitting on an even site i_0 . Then, the probability to occupy any other site i evolves in time as

$$n_i(t) = \mathcal{J}_{i-i_0}^2 \left[\frac{4J}{\Delta} \sin \left(\frac{\Delta t}{2} \right) \right], \quad (4.5)$$

which using Graf's identity theorem [228] leads to an imbalance

$$\mathcal{I}(t) = \mathcal{J}_0 \left[\frac{8J}{\Delta} \sin \left(\frac{\Delta t}{2} \right) \right]. \quad (4.6)$$

This leads to a non-vanishing signal which coherently oscillates with period $T_B = 2\pi/\Delta$ ¹ around a potentially non-zero mean value given by

$$\bar{\mathcal{I}} = \lim_{T \rightarrow \infty} \frac{1}{T} \int_0^T dt \mathcal{I}(t) = \mathcal{J}_0^2 \left(\frac{4J}{\Delta} \right). \quad (4.7)$$

This is for example the case in the limit $\Delta/J \gg 1$, where the Wannier-Stark eigenstates are (super-)exponentially localized and approximate the completely localized Wannier states $|\beta_m\rangle \rightarrow |m\rangle$. However, the imbalance can still vanish even if the system has a finite localization length when $\mathcal{J}_0(4J/\Delta) = 0$. This happens for infinitely many values of $\Delta/J < 2$ as shown in Fig. 4.2. Therefore, the imbalance is only a good measure to check for localization, since it can vanish for both localized and non-localized systems.

This vanishing value of the imbalance—even when the system is fully localized—can be understood as follows. In the absence of extensive degeneracy in the spectrum the time average imbalance is given by the diagonal ensemble prediction

$$\lim_{T \rightarrow \infty} \frac{1}{T} \int_0^T dt \mathcal{I}(t) = \sum_{m \in \mathbb{Z}} |\langle \beta_m | i_0 \rangle|^2 \sum_{i \in \mathbb{Z}} (-1)^i |\langle \beta_m | i \rangle|^2 = \sum_{m \in \mathbb{Z}} |\langle \beta_m | n_0 \rangle|^2 \mathcal{I}_m, \quad (4.8)$$

where \mathcal{I}_m is the value of the imbalance evaluated on an eigenstate $|\beta_m\rangle$. However, all eigenstates, while localized at different sites, have the same spatial structure and then acquires the same value of the imbalance

$$\mathcal{I}_m = \sum_{n \in \mathbb{Z}} (-1)^n \mathcal{J}_{n-m}^2 \left(\frac{2J}{\Delta} \right) = (-1)^m \mathcal{J}_0 \left(\frac{4J}{\Delta} \right),$$

¹Use the relation $\mathcal{J}_n(-x) = \mathcal{J}_{-n}(x) = (-1)^n \mathcal{J}_n(x)$.

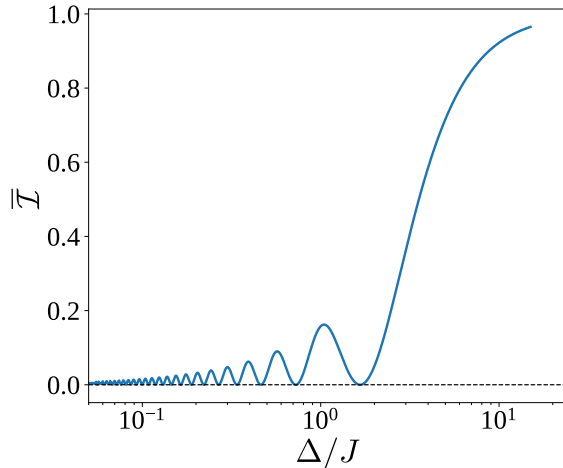


Figure 4.2.: **Time-average value of the imbalance as a function of Δ/J .** The curve shows the non-monotonic dependence of the time-average value of the imbalance on the ratio Δ/J as obtained in Eq. (4.7). It also exemplifies that the imbalance can vanish even though the system is localized.

up to an overall phase. All together this leads to $\bar{\mathcal{I}} = (-1)^{i_0} \mathcal{I}_m^2$, which vanishes if and only if $\mathcal{I}_m = 0$, i.e., if every eigenstate has the same probability weight on even and odd sites.

In general, a realistic experiment will be exposed to all sorts of noise and experimental imperfections that differ from the ideal theory model. As a result, the coherent dynamics will be dephased leading to a damping of Bloch oscillations towards a constant steady-state imbalance. It can then be that, e.g., in the absence of atom losses in the relevant time scales or similar technical limitations, this value can be related with the mean imbalance $\bar{\mathcal{I}}$. However, fully characterizing such sources of error and their effects the dynamics is a hard question that is not addressed in this thesis. Nevertheless, an analysis of the effect of certain experimental imperfections can be found in Section 3 of the Supplementary Material of Ref. [4]. Moreover, we also notice that while we solved the (non-interacting) problem in an infinitely long chain, finite size effects are negligible for the system sizes considered in the experiment $L_{\text{Exp}} \sim 200$ and even for numerical results with smaller system sizes.

4.2. Tilted Fermi-Hubbard model

We just found that the tilted non-interacting system leads to localized eigenfunctions for any non-zero value of the tilt with a constant gap between consecutive energy levels. This turns into coherent Bloch oscillations which are confined on a spatial region determined by the tilt strength. However, the presence of interactions can delocalize the system. For example, while a non-interacting 1D system is Anderson localized in the presence of a (even infinitesimal) random potential [129], this localization disappears for sufficiently strong interactions among the particles, which in turn leads to the ergodic-to-MBL phase transition [34] that we discussed in Chapter 1. Influenced by this long-standing problem, it is then a natural question to wonder what the fate of Wannier-Stark localization is in the presence of interactions. In fact, two independent works [76, 157] studied this scenario although in the presence of an additional (small) disorder [157] and harmonic [76] potentials.

The reason for this apparently arbitrary potential will become clear once we understand the underlying mechanisms by which such interacting tilted system may avoid localization.

As a matter of fact, both of these potentials naturally appear in experimental realizations, and thus it is a relevant question to understand their effect on the observed phenomena.

In an effort to explain the experimental observations, we consider the 1D tilted Fermi-Hubbard model

$$\hat{H} = -J \sum_{i=1}^L \sum_{\sigma=\uparrow,\downarrow} \left(\hat{c}_{i,\sigma}^\dagger \hat{c}_{i+1,\sigma} + \text{h.c.} \right) + U \sum_{i=1}^L \hat{n}_{i,\uparrow} \hat{n}_{i,\downarrow} + \sum_{i=1}^L \sum_{\sigma=\uparrow,\downarrow} \Delta_\sigma i \hat{n}_{i,\sigma}, \quad (4.9)$$

on a finite chain of length L with open boundary conditions. This describes a 1D chain of fermionic atoms with an internal spin degree of freedom $\sigma = \uparrow, \downarrow$ hopping on a lattice with tunneling amplitude J and a contact on-site interaction of strength U . Moreover, these couple to *a priori* spin-dependent tilt Δ_σ , that unless otherwise stated we assume to be uniform $\Delta \equiv \Delta_\uparrow = \Delta_\downarrow$. As we will find in Section 4.5, this system can be naturally realized with ultracold atoms.

Hamiltonian Eq. (4.9) conserves the total particle number for each spin degree of freedom independently, namely $\hat{N}_\uparrow = \sum_{i=1}^L \hat{n}_{i,\uparrow}$, $\hat{N}_\downarrow = \sum_{i=1}^L \hat{n}_{i,\downarrow}$. Equivalently, these correspond to the conservation of total particle number $\hat{N} = \hat{N}_\uparrow + \hat{N}_\downarrow$ and the global magnetization along z direction $S_{\text{total}}^z = \frac{1}{2}(\hat{N}_\uparrow - \hat{N}_\downarrow)$. In fact, when $\Delta_\uparrow = \Delta_\downarrow$, this second continuous U(1) symmetry becomes a complete SU(2) internal symmetry given by spin rotations generated by $\hat{S}_{\text{total}}^\alpha = \frac{1}{2} \sum_{i=1}^L \hat{c}_{i,a}^\dagger \sigma_{a,b}^\alpha \hat{c}_{i,b}$ with $\alpha = x, y, z$ for σ^α the Pauli matrices.

Moreover, both the hopping and interaction terms are invariant under lattice translations, but the tilted energy contribution is not. This in particular implies that at finite temperature, the thermal expectation value of a local quantity is necessarily not spatially homogeneous. More striking is the fact that this term scales faster than extensively with the total particle number, as expected for an energy contribution (in particular $\langle \sum_{i=1}^L i \hat{n}_i \rangle$ scales as $O(L^2)$). This leads to difficulties, as the inability to meaningfully — or at least unambiguously — take the thermodynamic limit; or the need to re-scale the tilted energy when considering the canonical thermal density matrix, to, e.g., meaningfully associate an effective temperature to a given initial state². However, this problem can be circumvented for certain initial configurations when taking into account the symmetries of the system. In particular, let us project onto a sector with fixed particle number and rewrite the Hamiltonian as follows

$$\hat{H} = -J \sum_{i=1}^L \sum_{\sigma=\uparrow,\downarrow} \left(\hat{c}_{i,\sigma}^\dagger \hat{c}_{i+1,\sigma} + \text{h.c.} \right) + U \sum_{i=1}^L (\hat{n}_{i,\uparrow} - \bar{n})(\hat{n}_{i,\downarrow} - \bar{n}) + \sum_{i=1}^L \Delta \sum_{\sigma=\uparrow,\downarrow} \left(i - \frac{L}{2} \right) \hat{n}_{i,\sigma}, \quad (4.10)$$

with $\bar{n} = 1/2$. This agrees with Hamiltonian Eq. (4.9) up to an overall constant and thus it does not change the physics of the problem. However, with this choice we now find that $\text{tr}(\hat{H}) = 0$, since $\text{tr}(\hat{n}_{i,\sigma} - \bar{n}) = 0$ and $\sum_{i=1}^L \text{tr}((i - \frac{L}{2})(\hat{n}_{i,\uparrow} + \hat{n}_{i,\downarrow})) = 0$. Consider now an initial product state $|\psi_0\rangle$ with a charge density wave pattern where even sites are occupied ($n_{i,\uparrow} + n_{i,\downarrow} = 1$) and odd sites are empty. This state generically overlaps with exponentially many different eigenstates of the Hamiltonian and satisfies $\langle \psi_0 | \hat{H} | \psi_0 \rangle = 0$, and because $\text{tr}(\hat{H}) = 0$, it has an associated infinite effective temperature. Thus, its (reduced) thermal density matrices are translational invariant, and we then expect an homogeneous distribution of spin and charge at sufficiently long times. Notice this would also hold for $\Delta_\uparrow \neq \Delta_\downarrow$ for particular spin configurations. However, a proper “stat-mech-like” formulation of the problem which addresses the super-extensive scaling of the tilted energy contribution is

²In fact, a similar problem arises in the realm of systems with long-range interactions which requires a normalization of the interaction term to turn it extensive [229].

yet to be addressed³. In the following we provide an alternative presentation of the Hamiltonian which makes use of the gauge covariance of the Schrödinger equation — namely, the equivalency of different pictures with Heisenberg and the interaction one being two particular instances—, transforming Eq. (4.9) into a time-dependent translation invariant Hamiltonian with no super-extensive energetic contributions. In fact, this was already realized for this particular system in Refs. [157, 230, 231].

4.2.1. Choice of gauge: From a tilted to a driven lattice

To do so we apply a unitary time-dependent transformation $\hat{T}(t) \equiv e^{it\hat{H}_0}$ with $\hat{H}_0 = \sum_{\sigma} \Delta_{\sigma} \sum_i i\hat{n}_{i,\sigma}$ which maps the Hamiltonian in Eq. (4.9) to the time-dependent Hamiltonian [157, 231, 232]

$$\hat{H}_I(t) = \hat{T}(t)\hat{H}\hat{T}^{\dagger}(t) - i\hat{T}(t)\partial_t\hat{T}^{\dagger}(t), \quad (4.11)$$

with

$$\hat{H}_I(t) = -J \sum_{i,\sigma} (e^{-i\Delta_{\sigma}t} \hat{c}_{i,\sigma}^{\dagger} \hat{c}_{i+1,\sigma} + \text{h.c.}) + U \sum_i \hat{n}_{i,\uparrow} \hat{n}_{i,\downarrow}, \quad (4.12)$$

which now allows to impose periodic boundary conditions in space. Notice that for incommensurate $\Delta_{\uparrow} \neq \Delta_{\downarrow}$ gives rise to a quasi-periodic Hamiltonian [233]. This is the lattice analog of (1D) Maxwell electromagnetism where a constant electric field $E(x, t)$ can be realized either by a time dependent “vector” $A(x, t)$ potential (and $V = 0$) or a linearly increasing $V(x, t) \propto x$ scalar potential (and $A = 0$). Hence we find that the Hamiltonian Eq. (4.12) in this picture, in the following called “rotated frame” explicitly commutes with lattice translations, is well-defined in the thermodynamic limit [157, 231, 232] and avoids the superextensive-scaling contribution of the potential energy to the total energy of the system. Together with the Hamiltonian, we also need to rotate the states as well as the observables we use to probe the dynamics of the system. In particular, for initial product states in the local particle number basis (which are our main focus in this chapter) this transformation results into an overall time dependent phase. Moreover, local density operators are gauge invariant $\hat{n}_{i,I}(t) = \hat{T}(t)\hat{n}_i\hat{T}^{\dagger}(t) = \hat{n}_i$, and then we can study the evolution and long-time value of the imbalance directly in this picture without requiring an additional change of frames.

4.2.2. Dynamical symmetry: Attractive versus repulsive interactions

According to the theorem proven in Ref. [234] (Supplementary material section SD), the Fermi-Hubbard model exhibits, apart from the previously discussed internal symmetries, a dynamical symmetry between repulsive and attractive interactions for any observable that is invariant under both time-reversal and the π -boost $\hat{B}_Q = e^{i\pi \sum_{i,\sigma} i\hat{n}_{i,\sigma}}$, when considering initial states, that are time reversal invariant and only acquire a global phase under the π -boost transformation. While these conditions do not hold in the presence of a tilt, we can extend this result by including additional restrictions. Under a spatial inversion $\hat{\mathcal{P}}$, which sends $i \rightarrow -i$ with respect to the center of the chain, the confining linear potential changes sign

$$\hat{H}(U, \Delta_{\uparrow}, \Delta_{\downarrow}) \xrightarrow{\hat{\mathcal{P}}} \hat{H}(U, -\Delta_{\uparrow}, -\Delta_{\downarrow}). \quad (4.13)$$

Using the π -boost \hat{B}_Q together with the inversion $\hat{\mathcal{P}}$

$$\hat{\mathcal{P}}\hat{B}_Q\hat{H}(U, \Delta_{\uparrow}, \Delta_{\downarrow})\hat{B}_Q^{\dagger}\hat{\mathcal{P}}^{\dagger} = -\hat{H}(-U, \Delta_{\uparrow}, \Delta_{\downarrow}) \quad (4.14)$$

³I thank Anushya Chandran for a really useful discussion we had about this topic when attending the American March Meeting 2022.

an equation similar to Eq. (S11) in [234] can be obtained. As an observable, we consider the spin-resolved imbalance $\hat{\mathcal{I}}^\sigma = \sum_{i=-\frac{L}{2}}^{\frac{L}{2}} (-1)^i \hat{n}_{i,\sigma}$ (which should be normalized by particle number N_σ fixed by the initial state), which is invariant under inversion $\hat{\mathcal{I}}^\sigma \xrightarrow{\hat{\mathcal{P}}} \hat{\mathcal{I}}^\sigma$ and the π -boost $\hat{\mathcal{I}}^\sigma \xrightarrow{\hat{B}_Q} \hat{\mathcal{I}}^\sigma$, but breaks time-reversal symmetry $\hat{\mathcal{T}}$. This symmetry is violated, because the spin degrees of freedom of the density operator $\hat{n}_{i,\sigma}$ are exchanged: $\hat{n}_{i,\uparrow} \leftrightarrow \hat{n}_{i,\downarrow}$.

Assuming that $\Delta_\uparrow = \Delta_\downarrow$, the Hamiltonian Eq. (4.9) is invariant under $\hat{\mathcal{T}}$ and has the additional SU(2) spin symmetry we already encountered before, which includes the invariance under spin-rotations around $\hat{S}^x = \sum_{\beta,\gamma=\uparrow,\downarrow} 1/2 \hat{c}_\beta^\dagger \sigma_{\beta\gamma}^x \hat{c}_\gamma$. The local observable $\hat{n}_{i,\sigma}$ is invariant under the product of time reversal $\hat{\mathcal{T}}$ and π -rotations around x , and thus we obtain for the time-evolved imbalance operator $\hat{\mathcal{I}}_{(U,\Delta_\uparrow,\Delta_\downarrow)}^\sigma$

$$\hat{\mathcal{P}} \hat{B}_Q e^{-i\pi \hat{S}^x} \hat{\mathcal{T}} \hat{\mathcal{I}}_{(U,\Delta_\uparrow,\Delta_\downarrow)}^\sigma(t) \hat{\mathcal{T}}^{-1} e^{i\pi \hat{S}^x} \hat{B}_Q^\dagger \hat{\mathcal{P}}^\dagger = \hat{\mathcal{I}}_{(-U,\Delta_\uparrow,\Delta_\downarrow)}^\sigma(t). \quad (4.15)$$

Therefore, as long as $|\Delta_\downarrow - \Delta_\uparrow|$ is sufficiently small, an approximate dynamical symmetry between repulsive and attractive interactions is present for our observable.

We next focus on the required symmetries of the initial state. For all experiments, we consider initial states that are an incoherent sum within the zero magnetization sector (thus $N_\uparrow = N_\downarrow$) with density matrix $\hat{\rho} = \frac{1}{\mathcal{N}} \sum_{\{\sigma\} | \sum_i \sigma_i = 0} |\psi_0(\{\sigma\})\rangle \langle \psi_0(\{\sigma\})|$, where each product state $|\psi_0(\{\sigma\})\rangle$, is given by a CDW of singlons where $|\uparrow\rangle$ and $|\downarrow\rangle$ states are randomly distributed on even lattice sites. The sum runs over all possible permutations $\{\sigma\}$ of the spins within the zero magnetization sector. Under the combined action of time reversal and π -rotation around x , this state is left invariant up to a global phase. This is also the case for the π -boost \hat{B}_Q . Moreover under spatial inversion $\hat{\mathcal{P}}$ a configuration $\{\sigma_i\}$ is mapped onto another one $\{\sigma'_i\}$ appearing in the mixed state $\hat{\rho}$ with equal weight. Thus, the mixed state is also invariant under $\hat{\mathcal{P}}$. In conclusion, we find for our initial states

$$\mathcal{I}_{(U,\Delta_\uparrow,\Delta_\downarrow)}^\sigma(t) = \mathcal{I}_{(-U,\Delta_\uparrow,\Delta_\downarrow)}^\sigma(t). \quad (4.16)$$

Note that this dynamical symmetry will be broken when $\Delta_\uparrow \neq \Delta_\downarrow$ as well as by other experimental imperfections such as the harmonic confinement (see Section 4.5.1) and the non-zero variation of the onsite-interaction strength (see supplementary information in Ref. [3])

4.3. Perturbative construction of effective constrained Hamiltonians

Our goal in this chapter is two-fold: (i) Understanding whether localization persists in the presence of interactions, and (ii) experimentally realized systems that (approximately) feature the phenomenon of Hilbert space fragmentation. In this section we analytically derive several effective Hamiltonians, starting from the clean tilted Fermi-Hubbard model (without harmonic confinement) and without spin-dependent tilt, described by the Hamiltonian

$$\hat{H}_{\text{tFH}} = -J \sum_{i,\sigma} \left(\hat{c}_{i,\sigma}^\dagger \hat{c}_{i+1,\sigma} + \text{h.c.} \right) + U \sum_i \hat{n}_{i,\uparrow} \hat{n}_{i,\downarrow} + \Delta \sum_{i,\sigma} i \hat{n}_{i,\sigma}. \quad (4.17)$$

Given a general static Hamiltonian $\hat{H} = g\hat{H}_0 + \hat{V}$ and \hat{H}_0 having integer spectrum, there are different approaches to perturbatively obtain an effective Hamiltonian in the limit $g \rightarrow \infty$. The general idea is to find a unitary transformation, that brings \hat{H} close to a block-diagonal form in the basis of \hat{H}_0 , order-by-order in $1/g$. However, due to the

4.3. Perturbative construction of effective constrained Hamiltonians

many-body nature of the system this series won't ever converge: While the spectral gap of $g\hat{H}_0$ is large, the norm of \hat{V} at finite energy-density grows with the volume of the system, and hence it will eventually hybridize the different subspaces of \hat{H}_0 . Nevertheless, the rate at which this will happen can still slow for sufficiently large g . Ref. [235] proved that in this regime there exists a quasi-local unitary transformation Y , i.e., one that maps a local operator to a local operator under its conjugate action, such that the original Hamiltonian is mapped to

$$Y(g\hat{H}_0 + \hat{V})Y^\dagger = g\hat{H}_0 + \hat{H}_{\text{eff}} + \hat{R}, \quad (4.18)$$

where (i) $[\hat{H}_{\text{eff}}, \hat{H}_0] = 0$, and (ii) $\|\hat{R}\|$ is exponentially small in g . From here they deduced that in the limit $g \rightarrow \infty$, the dynamics will be governed by the effective Hamiltonian $g\hat{H}_0 + \hat{H}_{\text{eff}}$ for exponentially long times in g , when truncating the expansion at an optimal order that scales linearly in g . This then implies that the original Hamiltonian, approximately conserves $Y^\dagger \hat{H}_0 Y$ and $Y^\dagger \hat{H}_{\text{eff}} Y$ for exponentially long times in g . After that time, different subspaces of \hat{H}_0 will be resonantly connected by the perturbation \hat{V} .

Hamiltonian (4.9), including the spin-dependent tilt, offers several energetic regimes where effective constrained Hamiltonians can be realized. When $\Delta_\uparrow = \Delta_\downarrow$, such constraints involve only the charge, i.e., whether a site is occupied or not, rather than the spin degrees of freedom. In particular, we will derive effective Hamiltonians corresponding to: (1) the resonant $|U| \simeq 2\Delta$, and (2) large tilt regime $\Delta \gg J, |U|$; although another natural resonance appears at $|U| \simeq \Delta$. Effective descriptions at other resonant points $|U| \simeq n\Delta$ for $n \in \mathbb{N}$ follow an analogous derivation. When $\Delta_\uparrow \neq \Delta_\downarrow$ and the tilts strengths Δ_σ can be independently tuned, one can then realized analogous constrained systems explicitly involving the spin degrees of freedom. For example, the average occupation is $\langle \hat{n}_{i,\uparrow} \rangle + \langle \hat{n}_{i,\downarrow} \rangle = 1$, one can realize a spin-1/2 dipole conserving, where the dipole moment corresponds to $\sum_i i \hat{S}_i^z$.

4.3.1. Resonant regime $|U| \simeq 2\Delta$

The reason we focus on this particular resonance comes from the spatial structure of the initial states considered in the experiment. Such singlon CDW configuration makes the resonance $|U| \simeq 2\Delta$ more prominent in the dynamics than the one at $|U| = \Delta$, where any hopping process from the initial state would require an energy Δ . Nevertheless, if other family of initial states are considered, as e.g., with double-occupied sites, one can find rich dynamics featuring quantum many-body [236]. In fact, these resonant regimes $U \simeq n\Delta$ have already been considered in the literature, when studying the response of a bosonic Mott-phase to a resonant tilt field [237], which later on open the possibility of simulating an antiferromagnetic spin chain with ultracold atoms, as well as to investigate a quantum phase transition between a paramagnetic and the antiferromagnetic phase [238–240].

Consider the family of states for which $\hat{H}_0 = \Delta \sum_{i,\sigma} i \hat{n}_{i,\sigma} + 2\Delta \sum_i \hat{n}_{i,\uparrow} \hat{n}_{i,\downarrow}$ takes the same value. This defines a subspace, within which an effective Hamiltonian \hat{H}_{eff} with $[\hat{H}_0, \hat{H}_{\text{eff}}] = 0$ can be obtained as an expansion in $\lambda = J/\Delta$. Such Hamiltonian can either independently conserve the dipole moment and the number of doublons or the sum of the two. Using a Schrieffer-Wolff (SW) unitary transformation $e^{\lambda \hat{S}}$ [235, 241, 242] with non-Hermitian generator $\hat{S} = \sum_{n=0} \lambda^n \hat{S}_n$ up to an optimal order n^* , we can generate order-by-order an effective local Hamiltonian that is “close” to a block diagonal form with respect to \hat{H}_0

$$e^{\lambda \hat{S}_{n \leq n^*}} \hat{H} e^{-\lambda \hat{S}_{n \leq n^*}} = \hat{H}_{\text{eff}}^{(n^*)} + \hat{V}_{n \geq n^*}, \quad (4.19)$$

where $[\hat{H}_0, \hat{V}_{n \geq n^*}] \neq 0$ with $\hat{V}_{n \geq n^*}$ exponentially small in $1/\lambda$ [235, 243, 244]. In particular,

we can obtain the explicit form of the effective Hamiltonian to second order in λ ⁴:

$$\hat{H}_{\text{eff}}^{\text{res}} = \hat{H}_0 + \frac{8J^2}{3\Delta} \sum_i \hat{n}_{i,\uparrow} \hat{n}_{i,\downarrow} - \frac{4J^2}{3\Delta} \hat{T}_{XY} + \frac{4J^2}{3\Delta} \hat{H}_D + \frac{J^2}{\Delta} \hat{T}_1 - \frac{2J^2}{\Delta} \hat{T}_2 + \frac{2J^2}{3\Delta} \hat{T}_3^D, \quad (4.20)$$

with

$$\begin{aligned} \hat{T}_1 &= \sum_{i,\sigma} (1 - \hat{n}_{i+2,\bar{\sigma}})(1 - 2\hat{n}_{i+1,\bar{\sigma}}) \hat{n}_{i,\bar{\sigma}} \hat{c}_{i,\sigma}^\dagger \hat{c}_{i+2,\sigma} + \text{h.c.}, \\ \hat{T}_2 &= \sum_{i,\sigma} (1 - \hat{n}_{i+2,\bar{\sigma}}) \hat{n}_{i,\sigma} \hat{c}_{i,\bar{\sigma}}^\dagger \hat{c}_{i+1,\bar{\sigma}} \hat{c}_{i+1,\sigma}^\dagger \hat{c}_{i+2,\sigma} + \text{H.c.}, \\ \hat{T}_3^D &= \sum_{i,\sigma} (\hat{n}_{i,\sigma} - \hat{n}_{i+2,\bar{\sigma}})^2 (1 - 2(\hat{n}_{i+2,\bar{\sigma}} - \hat{n}_{i,\sigma})) \hat{c}_{i,\bar{\sigma}} \hat{c}_{i+1,\bar{\sigma}}^\dagger \hat{c}_{i+1,\sigma}^\dagger \hat{c}_{i+2,\sigma} + \text{H.c.}, \\ \hat{H}_D &= -2 \sum_i \hat{n}_{i,\uparrow} \hat{n}_{i,\downarrow} (\hat{n}_{i+1} - \hat{n}_{i-1}) - \sum_{i,\sigma} \hat{n}_{i,\sigma} \hat{n}_{i+1,\bar{\sigma}}, \end{aligned} \quad (4.21)$$

where $\bar{\sigma}$ refers to the opposite spin: $\bar{\uparrow} = \downarrow$ and $\bar{\downarrow} = \uparrow$. The first term in the expansion of the SW generator $\hat{S} = \sum \lambda^n \hat{S}_n$ takes the form

$$\hat{S}_0 = \sum_{i,\sigma} (1 - 2\hat{n}_{i,\bar{\sigma}} - \frac{2}{3}\hat{n}_{i+1,\bar{\sigma}} + \frac{8}{3}\hat{n}_{i,\bar{\sigma}}\hat{n}_{i+1,\bar{\sigma}}) \hat{c}_{i+1,\sigma}^\dagger \hat{c}_{i,\sigma} - \text{H.c.} \quad (4.22)$$

Hamiltonian $\hat{H}_{\text{eff}}^{\text{res}}$ includes the term \hat{T}_3^D term which conserves both the dipole moment and the number of doublons independently, giving rise to doublon-assisted dipole conserving processes. This is the diagonal part of dipole-conserving term

$$\hat{T}_3 = \sum_{i,\sigma} \hat{c}_{i,\bar{\sigma}} \hat{c}_{i+1,\bar{\sigma}}^\dagger \hat{c}_{i+1,\sigma}^\dagger \hat{c}_{i+2,\sigma} + \text{H.c.}, \quad (4.23)$$

commuting with $\hat{N}_{\text{doub}} = \sum_i \hat{n}_{i,\uparrow} \hat{n}_{i,\downarrow}$.

However, a perfect agreement between interaction and tilt strengths is not necessary but just that $\delta \equiv |2\Delta - |U|| \ll J$ as long as $\Delta, |U| \gg J$. In this case, an additional diagonal term appears $(U - 2\Delta) \sum_i \hat{n}_{i,\uparrow} \hat{n}_{i,\downarrow}$ and modifies the amplitude of every second order process appearing in Eq.(4.20). In the following, we show that just keeping the diagonal contribution is sufficient at second order of perturbation theory. Once again we can use degenerate perturbation theory, with well-defined degenerate subspaces of the Hamiltonian $H_0 = U \sum_x \hat{n}_{x,\uparrow} \hat{n}_{x,\downarrow} + \Delta \sum_x x \hat{n}_x$. We will follow [245] in the following derivation and assume without loss of generality that $U > 0$. In particular let us focus on the off-diagonal second order contributions in comparison to the detuning term which scales as $O(\delta)$, although the discussion applies to all terms. These are

$$\begin{aligned} & -J^2 \left(\frac{1}{U + \Delta} + \frac{1}{U - \Delta} \right) \hat{T}_{XY} + \frac{J^2}{2} \left(\frac{1}{\Delta} + \frac{1}{U - \Delta} \right) \hat{T}_1 - \frac{2J^2}{U - \Delta} \hat{T}_2 \\ & + J^2 \left(\frac{1}{U - \Delta} + \frac{1}{\Delta} \right) \hat{T}_3^L - J^2 \left(\frac{1}{\Delta} - \frac{1}{U + \Delta} \right) \hat{T}_3^R + (U - 2\Delta) \sum_i \hat{n}_{i,\uparrow} \hat{n}_{i,\downarrow} + \hat{H}_0, \end{aligned} \quad (4.24)$$

where we used the notation

$$\begin{aligned} \hat{T}_3^L &= \sum_{i,\sigma} \hat{n}_{i,\sigma} (1 - \hat{n}_{i+2,\bar{\sigma}}) \hat{c}_{i,\bar{\sigma}} \hat{c}_{i+1,\bar{\sigma}}^\dagger \hat{c}_{i+1,\sigma}^\dagger \hat{c}_{i+2,\sigma} + \text{h.c.}, \\ \hat{T}_3^R &= \sum_{i,\sigma} (1 - \hat{n}_{i,\sigma}) \hat{n}_{i+2,\bar{\sigma}} \hat{c}_{i,\bar{\sigma}} \hat{c}_{i+1,\bar{\sigma}}^\dagger \hat{c}_{i+1,\sigma}^\dagger \hat{c}_{i+2,\sigma} + \text{h.c.} \end{aligned}$$

⁴This computation took me several pages of algebra which are not included in this thesis.

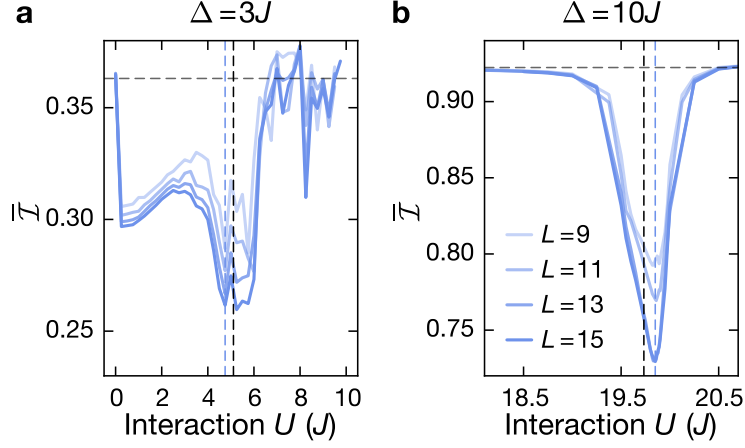


Figure 4.3.: **Identification of the resonance** $|U| \simeq 2\Delta$. ED calculation of the time-averaged imbalance $\bar{\mathcal{I}} = 1/T \int_0^T \mathcal{I} dt$ for system sizes $L = 9, 11, 13, 15$ with increasing opacity and $T = 1000\tau$. We use $\Delta_{\uparrow} = \Delta_{\downarrow}$. The horizontal dashed line shows the analytical value $\mathcal{J}_0(4J/\Delta)^2$ in the non-interacting case ($U = 0$) in the limit $T \rightarrow \infty$. The vertical black dashed line indicates the resonant point, including the second order correction $U_{\text{res}} = 2\Delta - 8J^2/(3\Delta)$. **a** Time-averaged imbalance for $\Delta = 3J$. We use a uniform grid of $\delta U = 0.25J$ and identify the lowest point in the resonance window at $U = 4.75J$ (blue dashed line). **b** Time-averaged imbalance for $\Delta = 10J$. Close to the minimum we use a grid with steps $\delta U = 0.01J$, allowing us to locate the minimum at $U = 19.85J$ (blue dashed line).

It is important to notice that all coefficients match with those in Eq. (4.20) in the limit $U \rightarrow 2\Delta$. In fact, let us write $U = 2\Delta + \delta$ with $|\delta| \ll J$. Then any coefficient J_{eff} in Eq. (4.24) can be expressed as

$$J_{\text{eff}} = J^2 \frac{1}{c\Delta \pm \delta} = \frac{J^2}{c\Delta} \frac{1}{1 \pm \delta/(c\Delta)} = \frac{J^2}{c\Delta} \left(1 \mp \frac{\delta}{c\Delta} + O\left(\frac{\delta^2}{\Delta^2}\right) \right) \approx \frac{J^2}{c\Delta},$$

for some order one number c . Therefore, we conclude that to second order, these corrections can be neglected whenever $|U - 2\Delta| < J$, though we should still keep the correction term $\delta \sum_i \hat{n}_{i,\uparrow} \hat{n}_{i,\downarrow}$.

Renormalized Fermi-Hubbard interaction

The diagonal terms of the effective Hamiltonian in Eq. (4.20) add long-range interactions and renormalize the Fermi-Hubbard interaction such that the resonant point is shifted for finite λ according to $U + \frac{8J^2}{3\Delta} + \mathcal{O}\left(\frac{J^2}{\Delta}\right) = 2\Delta$ and the overall resonance is broadened. We numerically identify the resonance for large tilt $\Delta = 10J$ (Fig. 4.3a) and intermediate tilt $\Delta = 3J$ (Fig. 4.3b) using different system sizes $L = 9, 11, 13, 15$ probing the time-averaged imbalance $\bar{\mathcal{I}}(T) \equiv \frac{1}{T} \int_0^T dt \mathcal{I}(t)$. Fig. 4.3 depicts a sharp resonance at strong tilt, while a rather broad feature is present at intermediate tilt. Away from $|U| \simeq 2\Delta$ in the large U regime, we find that the system is Wannier-Stark localized. For both regimes, the numerical results are consistent with the analytic prediction for the shifted resonance to second order even after 1000τ .

Fragmentation of the effective Hamiltonian

The off-diagonal terms of the effective Hamiltonian in Eq. (4.20) consist of three different kinds of correlated hoppings $\hat{T}_1, \hat{T}_2, \hat{T}_3^D$ (see Fig. 4.4a) with all hopping rates scaling as

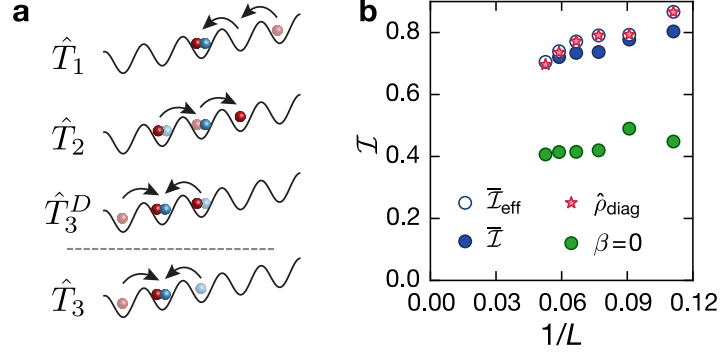


Figure 4.4.: **Effective description at resonance and long-time value of the imbalance.** **a** Schematic of the correlated hopping processes obtained in Eq. (4.21). **b** Finite size scaling of the long-time value of the imbalance calculated with the effective Hamiltonian in Eq.(4.20) using a time-averaged imbalance with $T = 3000\tau$ ($\bar{\mathcal{I}}_{\text{eff}}$), a diagonal ensemble ansatz ($\hat{\rho}^{\text{diag}}$) and an infinite temperature prediction ($\beta = 0$). Additionally, the original Hamiltonian in Eq. (4.17) is used to compare to the time-averaged imbalance calculated with $T = 1000\tau$ ($\bar{\mathcal{I}}$). All ED calculations were done with a Néel-ordered CDW initial state.

J^2/Δ . Since $[\hat{H}_{\text{eff}}^{\text{res}}, \hat{H}_0] = 0$, \hat{H}_0 becomes a new global quantum number fixed by the initial configuration, i.e. the linear combination of the dipole moment and the number of doublons is perturbatively conserved. After fixing this new global quantum number, the corresponding symmetry sector \mathcal{S} is generically fully connected by the action of the effective Hamiltonian and the Krylov subspace \mathcal{K} , hosting the initial state, agrees with \mathcal{S} (see Fig. 4.6). In contrast, the effective Hamiltonian in Eq. (4.20) is fragmented. Fig. 4.5a shows that \mathcal{S} splits up into exponentially many (in system size) disconnected sectors and the initial state remains trapped within a fragment whose relative size $D_{\mathcal{K}}$ with respect that of \mathcal{S} , appears to become irrelevant with increasing system sizes (see Fig. 4.5a right y -axis). In particular, Fig. 4.5b shows the connectivity of the fragment \mathcal{K} containing the Néel-ordered CDW state. Vertices in the graph correspond to product states spanning \mathcal{K} .

For the subsequent numerical analysis, we use this Néel-ordered CDW initial state ($|\psi_0\rangle = |0, \uparrow 0, \downarrow 0, \uparrow, 0, \downarrow, \dots\rangle$), expected to show the strongest interaction effects and fastest dynamics. The correlated hoppings $\hat{T}_1, \hat{T}_2, \hat{T}_3^D$ of the effective Hamiltonian connect the initial state with a set of states defining the fragment \mathcal{K}^{res} . Experimentally, we do not realize Néel-ordered CDW states, but the connectivity of our initial state with random CDW spin-sector (with zero magnetization) is the same as for the Néel-ordered CDW state. In Fig. 4.4b we analyze the system size scaling of both the infinite temperature (within the fragment containing the initial state) and diagonal ensemble predictions for the imbalance, obtaining a positive result in both cases for system sizes $L = 9, 11, 13, 15, 17, 19$ with no clear convergence towards zero imbalance in the thermodynamic limit. The scaling of the infinite temperature prediction suggests a finite value even in this limit. This apparent finite imbalance for $\hat{H}_{\text{eff}}^{\text{res}}$ could be interpreted as follows: Given an initial state that breaks even-odd sublattice symmetry, most dynamical processes in Eq.(4.20), except those generated by \hat{T}_3^D , do only transport particles in one of the sublattices. Thus, most states within the fragment have positive imbalance in agreement with the positive infinite temperature value. This explanation is reminiscent of the observed ergodicity-breaking in dipole-conserving systems. Nevertheless, a more careful and detailed analysis should be performed, which could in particular address the temperature associated to the specific initial state and study thermalization within the fragment is contained in.

We also include simulations with the exact Hamiltonian \hat{H}_{tFH} [Eq. (4.17)] for $\Delta = 10J$,

4.3. Perturbative construction of effective constrained Hamiltonians

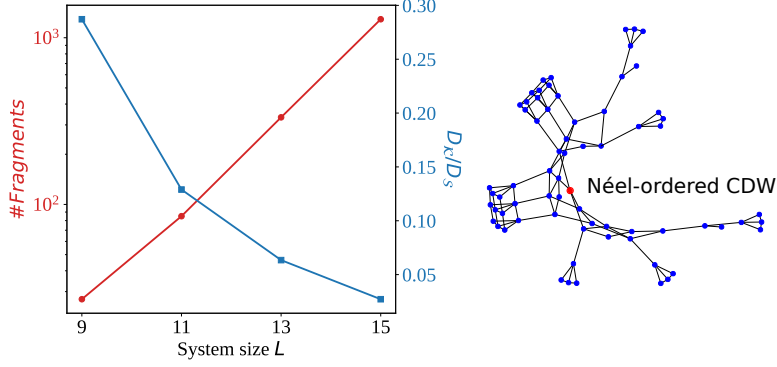


Figure 4.5.: **Hilbert space fragmentation at resonance.** **a)** Exponential system-size scaling of the number of fragments within the symmetry sector with fixed $(N_\uparrow, N_\downarrow, \sum_i in_i + 2N_{\text{doub}})$. **b)** Connectivity of the subspace containing the Néel-ordered CDW state for system size $L = 11$. This state corresponds to the red vertex. Calculations were done using ED.

$U = 19.85J$. These agree well with the results of the effective Hamiltonian even up to remarkably long times $T \sim 10^3\tau$ and without including the SW transformation. As we found, the exact and effective Hamiltonians are related by the conjugate action of a unitary transformation $e^{\hat{S}}$ that should then act on the observable and the initial state. However, such rotation tends to the identity in the limit $\lambda \rightarrow 0$. Consistent with a perturbative expansion in λ , which neglects higher order terms in the effective Hamiltonian, it yields a systematically larger imbalance compared to the original Hamiltonian. Since the conservation law, i.e. the linear combination of the dipole moment and the number of doublons, only holds perturbatively, one would expect that it is valid only up to a certain finite timescale as we discuss in Section 4.3.3.

4.3.2. Strong tilt regime: dipole conservation

Here, we focus on the parameter regime $\Delta \gg |U|, J$ and derive an effective Hamiltonian using the high-frequency expansion (HFE) in the rotated frame. The Hamiltonian in the rotated frame Eq. (4.12) is time-periodic $\hat{H}_I(t + \frac{2\pi}{\Delta}) = \hat{H}_I(t)$. According to Floquet theory [246, 247] the unitary evolution generated by $\hat{H}_I(t)$ can then be written as

$$\hat{U}_I(t, t_0) = e^{-i\hat{K}_{\text{eff}}(t)} e^{-i(t-t_0)\hat{H}_{\text{eff}}} e^{i\hat{K}_{\text{eff}}(t_0)}, \quad (4.25)$$

with a time-independent Floquet-gauge invariant Hamiltonian \hat{H}_{eff} and a gauge-dependent and time-periodic kick operator $\hat{K}_{\text{eff}}(t)$. It has been noticed that the first orders in the perturbative SW transformation approach for static Hamiltonians (see e.g., [241]), coincide with those in the HFE in the rotated frame (which provides the gauge-invariant effective Hamiltonian) [247, 248], with the SW generator given by the kick operators. Following this approach, we obtain the effective Hamiltonian as a Floquet expansion in powers of $1/\Delta$ with $\hat{H}_{\text{eff}} = \sum_n \hat{H}_{\text{eff}}^{(n)}$ and $\hat{K}_{\text{eff}}(t) = \sum_n \hat{K}_{\text{eff}}^{(n)}(t)$. Up to third order the effective Hamiltonian is [246, 247, 249, 250]:

$$\hat{H}_{\text{eff}}^{\text{dip}} = J^{(3)}\hat{T}_3 + 2J^{(3)}\hat{T}_{XY} + U\left(1 - \frac{4J^2}{\Delta^2}\right) \sum_i \hat{n}_{i,\uparrow}\hat{n}_{i,\downarrow} + 2J^{(3)} \sum_{i,\sigma} \hat{n}_{i,\sigma}\hat{n}_{i+1,\bar{\sigma}}, \quad (4.26)$$

or equivalently,

$$\hat{H}_{\text{eff}}^{\text{dip}} = J^{(3)} \hat{T}_3 + 4J^{(3)} \sum_i \hat{\mathbf{S}}_i \cdot \hat{\mathbf{S}}_{i+1} + U \left(1 - \frac{4J^2}{\Delta^2}\right) \sum_i \hat{n}_{i,\uparrow} \hat{n}_{i,\downarrow} + J^{(3)} \sum_{i,\sigma} \hat{n}_i \hat{n}_{i+1}, \quad (4.27)$$

up to constant terms, where $\bar{\sigma} = \{\downarrow, \uparrow\}$ indicates the respective opposite spin of $\sigma = \{\uparrow, \downarrow\}$, $J^{(3)} = \frac{J^2 U}{\Delta^2}$ and

$$\hat{T}_3 = \sum_{i,\sigma} \hat{c}_{i,\sigma} \hat{c}_{i+1,\sigma}^\dagger \hat{c}_{i+1,\bar{\sigma}}^\dagger \hat{c}_{i+2,\bar{\sigma}} + \text{h.c.}, \quad (4.28)$$

$$\hat{T}_{XY} = \sum_{i,\sigma} \hat{c}_{i,\bar{\sigma}}^\dagger \hat{c}_{i+1,\bar{\sigma}} \hat{c}_{i+1,\sigma}^\dagger \hat{c}_{i,\sigma}. \quad (4.29)$$

The kick-operator to third order is expressed as

$$\begin{aligned} \hat{K}_{\text{eff}}(t) &= i \frac{J}{\Delta} \sum_{i,\sigma} (\hat{c}_{i,\sigma}^\dagger e^{-it\Delta} \hat{c}_{i+1,\sigma} - \text{h.c.}) \\ &\quad - i \frac{JU}{\Delta^2} \sum_{i,\sigma} (\hat{n}_{i+1,\bar{\sigma}} - \hat{n}_{i,\bar{\sigma}}) (\hat{c}_{i,\sigma}^\dagger e^{-it\Delta} \hat{c}_{i+1,\sigma} - \text{h.c.}) \end{aligned} \quad (4.30)$$

and the time-evolution operator is approximated as

$$\hat{U}_I(t, t_0) \approx e^{-i\hat{K}_{\text{eff}}(t)} e^{-i(t-t_0)\hat{H}_{\text{eff}}} e^{i\hat{K}_{\text{eff}}(t_0)}. \quad (4.31)$$

Rotating back to the Schrödinger picture, we find

$$\hat{U}(t, t_0) = e^{-it\hat{H}_0} \hat{U}_I(t, t_0) e^{-it_0\hat{H}_0} \approx e^{-\hat{S}} e^{-i(t-t_0)(\hat{H}_{\text{eff}} + \hat{H}_0)} e^{\hat{S}}, \quad (4.32)$$

where we have used the fact that $[\hat{H}_{\text{eff}}, \hat{H}_0] = 0$ and that $e^{-it\hat{H}_0} \hat{K}_{\text{eff}}(t) e^{it\hat{H}_0} = \hat{K}_{\text{eff}}(0)$ [248], namely the product on the left hand side does not depend on time. Therefore, the Hamiltonian in the large-tilt limit can be approximated (up to higher-order terms) via

$$\hat{H} \approx e^{-\hat{S}} (\hat{H}_{\text{eff}} + \hat{H}_0) e^{\hat{S}}, \quad (4.33)$$

taking the form of a perturbative SW transformation at third order in J/Δ , with the SW generator given by $\hat{S} = i\hat{K}_{\text{eff}}(0)$. We have thus obtained an effective Hamiltonian which conserves the dipole moment (or center of mass $\sum_{i,\sigma} i\hat{n}_{i,\sigma}$), with \hat{T}_3 in Eq. (4.28) resembling the strongly-fragmented dipole-conserving Hamiltonian we studied in previous chapters, up to additional spin degrees of freedom (see Fig. 4.4a). In particular, we can identify a double occupied site $|\uparrow\downarrow\rangle$ with a (+)-fracton $|+\rangle$ and an empty site with a (-)-fracton $|-\rangle$. Then, it is clear that the \hat{T}_{XY} term (or the spin exchange term in Eq. (4.27)) only act on single occupied (i.e., spin degrees of freedom), while the term \hat{T}_3 lead to local processes like e.g., $|\uparrow - \downarrow\rangle, |\downarrow - \uparrow\rangle \leftrightarrow |-\ +\rangle$ as well as $|\uparrow + -\rangle \leftrightarrow |-\ +\uparrow\rangle$.

The fact that the hopping rate $J^{(3)}$ is proportional to the interaction strength highlights that interactions are necessary to generate dipole-conserving processes [251] (pure off-diagonal non-interacting contributions destructively interfere at any order). Moreover, $J^{(3)}$ agrees with the two particle picture provided in Ref. [251] yielding $J_{\text{eff}} \propto \frac{UJ^2}{\Delta^2 - U^2}$ with $|U| \ll \Delta$. For CDW initial states of singlons, the connected dynamical sector \mathcal{K} only represents a vanishing fraction of the whole (effective) symmetry sector \mathcal{S} , thus severely restricting the dynamics of the system. The dipole-conserving processes in general involve the generation of doublons. This is, however, penalized by the Fermi-Hubbard on-site interaction in

4.3. Perturbative construction of effective constrained Hamiltonians

Eq. (4.26) and therefore, we expect a slowing down of the dipole-conserving dynamics (see Section 4.4.1). The additional spin-exchange \hat{T}_{XY} increases the connectivity, but cannot fully connect the whole dipole symmetry sector and the system remains fragmented.

Before closing this section it is interesting to point out that as the original tilted Fermi-Hubbard Hamiltonian in Eq.(4.17), the resulting effective one is also SU(2) invariant. From the presentation in Eq.(4.27) this implies that the term \hat{T}_3 is U(1)×SU(2) invariant on its own. This additional non-Abelian symmetry could provide an example of a quantum fragmented model in the nomenclature of Ref. [166] as we discuss at the end of this chapter.

Effective Hamiltonian with tilt difference

The effective Hamiltonian in Eq. (4.26) was obtained under the assumption of a spin-independent tilt $\Delta \equiv \Delta_\downarrow = \Delta_\uparrow$, together with $\Delta \gg J, |U|$. Nevertheless, the experimental setup we will investigate has a small but finite detuning between the two and in fact, this could be intentionally tuned as in Ref. [4]. As long as $\delta \equiv \Delta_\downarrow - \Delta_\uparrow > 0$ is small compared to the hopping rate J ($\delta \ll J$) our perturbative expansion also works up to some additional contribution. To see how this happens let us write Eq. (4.9) as follows

$$\hat{H} = -J \sum_{i,\sigma} \hat{c}_{i,\sigma}^\dagger \hat{c}_{i+1,\sigma} + \text{h.c.} + U \sum_i \hat{n}_{i,\uparrow} \hat{n}_{i,\downarrow} + \Delta_\uparrow \sum_i i \hat{n}_i + \delta \sum_i i \hat{n}_{i,\downarrow}. \quad (4.34)$$

Since $\Delta_\uparrow \gg J \gg \delta$, we just keep the small contribution in δ and follow the same expansion in J/Δ_\uparrow as for a spin-independent tilt. Since $[\sum_i i \hat{n}_{i,\downarrow}, \sum_i i \hat{n}_i] = 0$, this contribution appears already at first order. Thus, the resulting effective Hamiltonian becomes

$$\hat{H}_{\text{eff}}^{\text{dip}} = J^{(3)}(\hat{T}_3 + 2\hat{T}_{XY}) + 2J^{(3)}\hat{V} + \tilde{U} \sum_i \hat{n}_{i,\uparrow} \hat{n}_{i,\downarrow} + \Delta_\uparrow \sum_i i \hat{n}_i + \delta \sum_i i \hat{n}_{i,\downarrow}. \quad (4.35)$$

To understand the effect of the additional term in δ , we consider the following family of states $\{|n\rangle\} = \{|\dots \uparrow\uparrow\uparrow \overset{n}{\downarrow} 0 \uparrow\uparrow\uparrow \dots\rangle\}$ with a doublon \downarrow at lattice site n on the chain surrounded by a polarized background. This background acquires a uniform polarization. This family defines a Krylov subspace left invariant under the action of $\hat{H}_{\text{eff}}^{\text{dip}}$. In particular, the term \hat{T}_{XY} has a trivial action and every diagonal contribution, except the term in δ , is proportional to the identity in this subspace. Thus, we project Eq. (4.35) into this subspace leading to the single-particle Hamiltonian

$$\hat{H}_{\text{eff}}^{\text{dip}} \Big|_{\{|n\rangle\}} = -J^{(3)} \sum_n |n\rangle \langle n+1| + \text{h.c.} + \delta \sum_n n |n\rangle \langle n|,$$

that describes a doublon-hole pair surrounded by a uniform polarized background and that propagates as a single-particle with hopping amplitude $J^{(3)}$ in the presence of a tilt δ , similarly to Eq. (4.1). Therefore, when quenching the system from an initial state $|n\rangle$ this leads to Bloch oscillations with the doublon localized in a region of size $\propto J/\delta$.

However, when $J \geq \delta$ and for generic tilts such that $\Delta_\uparrow/\Delta_\downarrow \notin \mathbb{Q}$ the previous perturbative expansion is not valid. This requires a different approach and it is in fact a direct application of the theory developed in [252] (see in particular Section VIII.B and Appendix A) for quasiperiodically driven systems. Let us write Eq. (4.9) in the rotated frame where it becomes a quasiperiodic Hamiltonian

$$\hat{H}(t) = -J \sum_{i,\sigma} \hat{c}_{i,\sigma}^\dagger \hat{c}_{i+1,\sigma} e^{-i\Delta_\sigma t} + \text{h.c.} + U \sum_i \hat{n}_{i,\uparrow} \hat{n}_{i,\downarrow}, \quad (4.36)$$

with periods $T_\sigma = 2\pi/\Delta_\sigma$ for $\sigma = \uparrow, \downarrow$. Then we can decompose

$$\hat{H}(t) = \sum_{n_1, n_2} e^{i(\Delta_\uparrow n_1 + \Delta_\downarrow n_2)t} \hat{H}_{(n_1, n_2)}$$

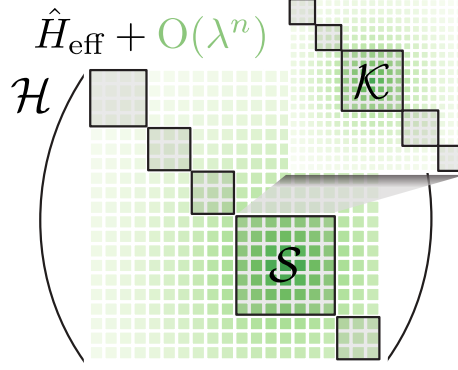


Figure 4.6.: **Illustration of the structure of the Hilbert space.** Fragmentation of the approximate symmetry sectors \mathcal{S} of the Hilbert space \mathcal{H} of an effective Hamiltonian \hat{H}_{eff} , derived perturbatively in the small parameter λ (black), into dynamically disconnected fragments \mathcal{K} . Higher-order terms $\mathcal{O}(\lambda^n)$ (green) soften the block-diagonal structure. Figure adapted from Ref. [3].

in terms of a Fourier series with the only non-vanishing terms $\hat{H}_{(0,0)}$, $\hat{H}_{(\pm 1,0)}$, $\hat{H}_{(0,\pm 1)}$.

Following Appendix A in [252], we can obtain an effective static Hamiltonian as a perturbative expansion in J/Δ_σ . The 0th order contribution is given by the diagonal term $\hat{H}_{(0,0)} = U \sum_i \hat{n}_{i,\uparrow} \hat{n}_{i,\downarrow}$ and the first order contribution vanishes up to boundary terms, in both cases agreeing with the result for a spin-independent tilt. Using [252], we explicitly obtain the second order contribution

$$\sum_{\mathbf{n} \neq 0} \left(\frac{1}{2(\mathbf{n} \cdot \boldsymbol{\omega})^2} [\hat{H}_{\mathbf{n}}, [\hat{H}_0, \hat{H}_{-\mathbf{n}}]] + \sum_{\mathbf{m} \neq 0, \mathbf{n}} \frac{1}{3(\mathbf{n} \cdot \boldsymbol{\omega})(\mathbf{m} \cdot \boldsymbol{\omega})} [\hat{H}_{-\mathbf{n}}, [\hat{H}_{\mathbf{n}-\mathbf{m}}, \hat{H}_{\mathbf{m}}]] \right),$$

where we have used the notation $\mathbf{n} = (n_1, n_2)$ and $\boldsymbol{\omega} = (\Delta_\uparrow, \Delta_\downarrow)$. Since $[\hat{H}_{(\pm 1,0)}, \hat{H}_{(0,\pm 1)}] = 0$ as well as $[\hat{H}_{(+1,0)}, \hat{H}_{(-1,0)}] = 0$ (up to boundary terms), the only non-trivial contribution is given by $\sum_i (\hat{n}_{i+1,\uparrow} - \hat{n}_{i,\uparrow})(\hat{n}_{i+1,\downarrow} - \hat{n}_{i,\downarrow})$, namely a diagonal contribution but no correlated hopping process. This is in line with the fact that dipole-conserving processes require the presence of interactions among the involved degrees of freedom [253]. For a spin-independent tilt, the Hubbard interaction mediates these hoppings involving the two spin species and leading to the conservation of the dipole moment $\sum_i i \hat{n}_i$. On the other hand, when the tilts are different and incommensurate, the dipole moment for each spin is independently conserved. However, these processes require interactions involving the same spin species (e.g., $\sum_{i,\sigma} \hat{n}_{i,\sigma} \hat{n}_{i+1,\sigma}$). Thus, unless such interactions can be generated at higher orders (or appear in the particular experimental implementation), the effective Hamiltonian for $J, U \ll \Delta_\sigma$ with $J \geq \delta$ and $\Delta_\uparrow/\Delta_\downarrow \notin \mathbb{Q}$ obtained from Eq. (4.9), will lead to frozen dynamics for initial product states in the local number occupation basis.

4.3.3. Role of the Schrieffer-Wolff transformation

In the two previous regimes the resulting effective Hamiltonians were fragmented. Therefore, in addition to the emergent symmetry $[\hat{H}_0, \hat{H}_{\text{eff}}] = 0$, the effective Hamiltonian \hat{H}_{eff} at that finite order n , which includes terms whose coefficients scale as λ^n (denoted as $\hat{H}_{\text{eff}}^{(n)}$), is fragmented in the local number basis $|\mathbf{n}\rangle = |\{n_{i,\sigma}\}\rangle$ for the regimes of interest (see Fig. 4.6). Each of these fragments defines a subspace $\mathcal{K} = \{|\mathbf{n}\rangle\}$ to which we can associate a projector $P_{\mathcal{K}}$ such that $[P_{\mathcal{K}}, \hat{H}_{\text{eff}}^{(n)}] = 0$. Thus, in the limit $\lambda \rightarrow 0$, we find that $[\hat{H}, \tilde{P}_{\mathcal{K}}] \sim \mathcal{O}(\lambda^{n+1})$ with $\tilde{P}_{\mathcal{K}} = e^{-\hat{S}} P_{\mathcal{K}} e^{\hat{S}}$. This means that fragmentation physics of the

n^{th} -order effective Hamiltonian $\hat{H}_{\text{eff}}^{(n)}$ is expected to survive to times scaling only polynomially $t\lambda^{n+1} \sim 1$, unlike the quasi-exponential scaling that applies to $e^{-\hat{S}}\hat{H}_0e^{-\hat{S}}$ [254]. This implies that fragmentation physics is a transient phenomenon when realized perturbatively - with the fragment spanned by the states $\tilde{\mathcal{K}} = \{e^{-i\hat{S}}|\mathbf{n}\rangle\}$. This is not a fragment in the number basis but some locally dressed version of it since \hat{S} is quasi-local and $\lambda \ll 1$. However, since $e^{i\hat{S}} \xrightarrow{\lambda \rightarrow 0} 1$, this means $\tilde{\mathcal{K}} \rightarrow \mathcal{K}$. Notice that in this limit the coefficients in front of the correlated hopping terms for the previous effective Hamiltonians also vanish in this limit.

4.4. Numerical results and perturbative picture

In the previous section we focused on regimes where effective microscopic Hamiltonians could be derived. However, such descriptions are only valid for strong tilts ($\Delta \gg J$) and at short to intermediate time scales. Thus, we cannot derive any conclusions about the dynamics of the full interacting system (Eq.(4.9)) from the non-ergodic behavior that appears as a result of the approximate fragmentation of the Hilbert space. However, these constructions can still be useful to understand the relevant microscopic processes that activate the dynamics (for a given family of initial states) and what can prevent the system to thermalize.

4.4.1. Higher order contributions and relevant on-site interactions in the dipole-conserving regime

Dynamics caused by fragmentation is captured by effective Hamiltonians and is therefore a transient phenomenon. The perturbative derivation of the effective Hamiltonian neglects higher-order terms which will eventually couple different fragments, such that the dynamics no longer solely occur within a certain fragment. While we know that the dipole moment will be conserved for exponentially long times in the tilt strength, estimating the time scales, which capture the dynamics caused due to fragmentation, requires a detailed analysis of both the diagonal and off-diagonal terms of the effective Hamiltonian. Note that the off-diagonal term \hat{T}_3 , occurring at a rate $J^{(3)} = \frac{J^2U}{\Delta^2}$ in the dipole conserving limit ($\Delta/J \rightarrow \infty$, Eq. (4.26)), requires the production of doublons when starting from an initial CDW of singlons. Creating a doublon is, however, penalized by the diagonal Fermi-Hubbard interaction with strength $\sim U$ that is much larger than $J^{(3)}$, since $U/J^{(3)} = (\Delta/J)^2$. Therefore, such an initial state remains frozen for exponentially long times $t \geq e^{c(\Delta/J)^2}$, analogously to the stability of doublons in the repulsive Fermi-Hubbard model in the $U \gg J$ regime [255, 256]. This effectively gives rise to a fragmentation not only due to the conservation law of the respective effective Hamiltonian, but additionally due to the conservation of the doublon number [4]. A similar argument can be made for the time scale on which higher-order off-diagonal terms, coupling different fragments, become effective and eventually destroy fragmentation. We will give a brief outline here for the dipole conserving limit, where higher order terms are easier to capture. These terms add longer-range processes to the effective Hamiltonian and in general order- n terms generate longer range- n processes whose effective hopping rate scales as $J^{(n)} \sim J^{2k}U^{n-2k}/\Delta^{n-1}$ for some k . Any even order vanishes due to destructive interference: For every process started by a particle hopping to the left, there exists another process with a particle hopping to the right, thus contributing with opposite signs. The hopping rate of the next non-vanishing fifth-order scales as $J^{(5)} \sim J^4U/\Delta^4$.

Using a qualitative Kato-Bloch perturbative approach [257, 258], which is easier to handle than a Schrieffer-Wolff transformation or a Floquet expansion [259] for higher-order terms, two terms emerge at fifth order in the dipole conserving limit: a 5-local

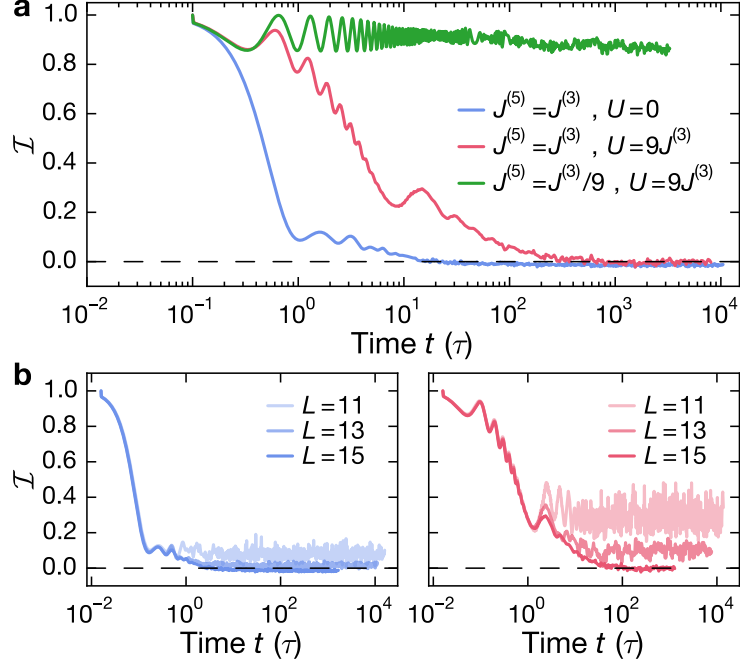


Figure 4.7.: **Role of higher-order diagonal and off-diagonal terms.** ED calculation of the imbalance for the Hamiltonian $\hat{H} = J^{(3)}(\hat{T}_3 + \hat{T}_{XY}) + J^{(5)}(\hat{T}_4 + \hat{T}_5) + U\hat{N}_{\text{doub}}$. **a** Imbalance for $J^{(5)} = J^{(3)}$, $U = 0$ (blue), $J^{(5)} = J^{(3)}$, $U = 9J^{(3)}$ (red), and $J^{(5)} = J^{(3)}/9$, $U = 9J^{(3)}$ (green) for system size $L = 15$. **b** Finite size scaling of the imbalance for $J^{(5)} = J^{(3)}$, $U = 0$ (left) and for $J^{(5)} = J^{(3)}$, $U = 9J^{(3)}$ (right). In both cases, we use $L = 11, 13, 15$ and increasing opacity corresponds to increasing system size. All calculations were done using ED.

Hamiltonian

$$\hat{T}_5 = \sum_{i,\sigma} \left(\hat{c}_{i,\sigma} \hat{c}_{i+2,\sigma}^\dagger \hat{c}_{i+2,\bar{\sigma}}^\dagger \hat{c}_{i+4,\bar{\sigma}} + \text{h.c.} \right), \quad (4.37)$$

with two opposite spins hopping to an intermediate site, requiring the creation of a doublon in the central site; and a 4-local term \hat{T}_4 similar to the \hat{H}_4 Hamiltonian we studied in Chapter 2

$$\hat{T}_4 = \sum_{i,\sigma} \left(\hat{c}_{i,\sigma} \hat{c}_{i+1,\sigma}^\dagger \hat{c}_{i+2,\bar{\sigma}}^\dagger \hat{c}_{i+3,\bar{\sigma}} + \text{h.c.} \right), \quad (4.38)$$

which populates nearby sites with opposite spin, thus interacting via the nearest-neighbor interaction appearing at third order. We now consider the time-evolution of a Néel-ordered CDW initial state for system size $L = 15$ with the toy model Hamiltonian

$$\hat{H} = J^{(3)}(\hat{T}_3 + \hat{T}_{XY}) + J^{(5)}(\hat{T}_4 + \hat{T}_5) + U\hat{N}_{\text{doub}}, \quad (4.39)$$

using $J^{(3)} = 1$ as unit of energy. Here, \hat{N}_{doub} measures the number of doublons in the system. In Fig. 4.7a we clearly observe an exponential decay of the imbalance for $J^{(3)}, J^{(5)} \sim O(1)$ and $U = 0$ in agreement with our results in Chapter 2. The decay time scale steeply increases when adding on-site interactions such that $J^{(3)} = J^{(5)} = 1$, $U = 9$ corresponding to a ratio $U/J^{(3)} = 9$ in the perturbative expansion, which is consistent with $\Delta = 3J$ although the higher-order term is still unrealistically large ($J^{(5)} = J^{(3)}$).

A more realistic regime is captured with $J^{(5)} = J^{(3)}/9$ and $U = 9$ from the appropriate perturbative scalings. Here, the imbalance clearly stays finite on the observed time scales. Thus, the energy penalty given by the on-site interaction has a drastic effect on the decay

of the imbalance caused by higher order terms, slowing down the dynamics tremendously. Fig. 4.7b and Fig. 4.7c show a finite-size scaling in the regimes $J^{(5)} = J^{(3)}$ with $U = 0$ and $J^{(3)} = J^{(5)}$ with $U = 9$, clearly indicating that large system sizes are necessary to capture the correct steady-state imbalance. In general, we expect such energy mismatches among diagonal and off-diagonal contributions to occur at higher-orders in perturbation theory.

Does this mean that the system will remain localized to infinite long times? What is then the role of the harmonic or disorder potentials considered in Refs. [76, 157] assumed to be required to stabilize Stark MBL? First of all notice that such arguments do only apply to certain families of initial states. For example, considering an initial finite density of doublons will allow certain resonant processes (as e.g., \hat{T}_3^D in Eq. (4.21)) to activate the dynamics. Secondly, as discussed in Ref. [253], the standard signatures of MBL, as for example a logarithmic — instead of a fast linear— growth of entanglement, only appear in the presence of a finite harmonic potential. However, the actual fate of the clean system at long times is still a matter of debate as we review in Section 4.6. My current understanding is that due to the existence of these many-body dipole-conserving processes, which in many circumstances lead to resonances, there is no reason to think that the system will remain localized to infinite times, although the scaling of such time scale with the system size is still an open question whose answer appears complicated. On the one hand, numerical methods can only simulate small system sizes ($L \sim \mathcal{O}(10)$), while experimental results might not be able to coherently reach sufficiently long-times.

Finally, let us address the role of the harmonic or disorder potentials ($\sum_i \delta\Delta_i \hat{n}_i$). As we just said, in the regime where $\Delta \gg J$, dipole-conserving processes will appear whose coupling decay exponentially with its range $\sim (J/\Delta)^R$. When a disorder potential is added, this has to compete with these processes which can give rise to conventional disorder-induced MBL [260] (at least in the perturbative picture). Similarly, the addition of a harmonic trap will make processes with a range larger than a critical one ineffective to delocalize the system. In that circumstance, localization might survive (see discussion in Section 4.6).

4.4.2. Real-time evolution of the imbalance and the entanglement entropy at resonance

In this section, we study the long-time dynamics of the clean system without spin-dependent tilt and harmonic confinement for a large range of tilts and different system sizes: We choose a weak $\Delta = 1J$, an intermediate $\Delta = 3J$ and a large tilt $\Delta = 10J$. We focus on the dynamics close to the resonant point $|U| \approx 2\Delta$, and consider an initial Néel-ordered CDW state. This state has a symmetric charge distribution with respect to the center site and thus its dipole moment coincides with that of a homogeneous charge distribution. In Fig. 4.8a we show numerical simulations of the imbalance \mathcal{I} up to late times for different system sizes. In the large tilt regime, we find a stable imbalance for all system sizes, whereas the intermediate and weak tilt regime show an imbalance decay. This decay is very weak in the intermediate tilt regime and a conclusive answer on whether and at what timescale the imbalance decays to zero cannot be given. In contrast, the imbalance calculated with the effective Hamiltonian $\hat{H}_{\text{eff}}^{\text{res}}$ [Eq.(4.20)], *without including the SW rotation*, is stable (grey shaded trace in Fig. 4.8a), as expected due to the absence of higher-order terms in the perturbative construction. Additionally, we find that the imbalance weakly scales down with system size. For small tilts, we clearly observe a decay of the imbalance to zero for large enough system sizes.

Note that, while we used $L = 13, 15, 17$ for the intermediate and large tilt regime to minimize edge effects with an unoccupied odd site at the left and the right end of the system, we choose $L = 12, 14, 16$ for the weak tilt regime. In this regime, the initial CDW relaxes to a potentially thermal density distribution and such a distribution only

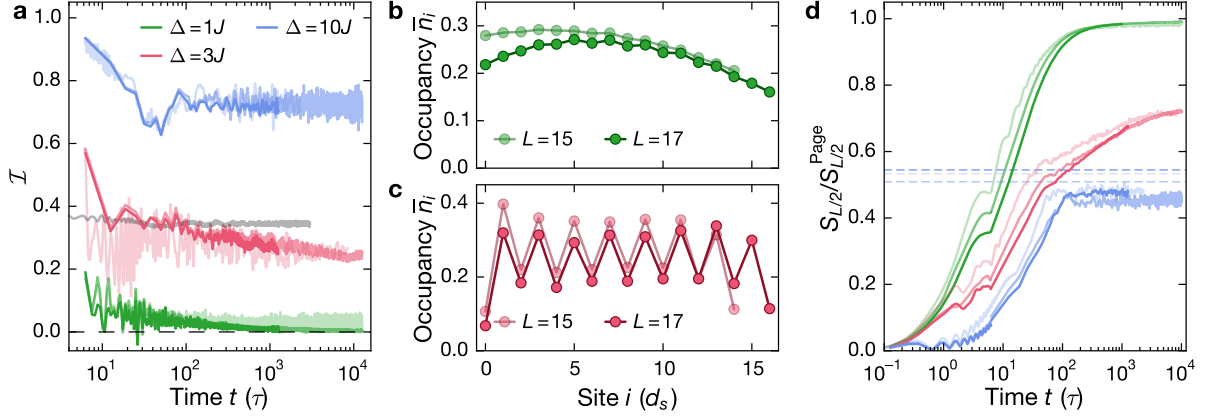


Figure 4.8.: **Finite-size scaling analysis of imbalance, entanglement entropy and occupancy.** **a** Long-time behavior of imbalance \mathcal{I} for system sizes $L = 13, 15, 17$ and $(\Delta = 10J, U = 19.85J)$ (blue), $(\Delta = 3J, U = 4.75J)$ (red) and system sizes $L = 12, 14, 16$ for $(\Delta = 1J, U = 4.75J)$ (green). The grey line corresponds to a simulation of the imbalance according to the effective Hamiltonian $\hat{H}_{\text{eff}}^{\text{res}}$ [Eq.(4.20), Eq. (4.32)] for $L = 15$ and $\Delta = 3J$ up to 3000τ . Fluctuations in the data are reduced by using a running average with a time-window of 10τ . **b, c** Time-averaged on-site occupancy $\bar{n}_i = 10/T \int_{0.9T}^T n_i dt$ for system sizes $L = 15, 17$ and **b** $(\Delta = 1J, U = 4.75J)$ and **c** $(\Delta = 3J, U = 4.75J)$. The time average was performed with $T = 12600\tau$ for $L = 15$ and $T = 1260\tau$ for $L = 17$. **d** Long-time behavior of the half-chain entanglement entropy $S_{L/2}$ normalized to the Page value $S_{L/2}^{\text{Page}}$, i.e., the half-chain entanglement entropy of a random state (see Section 1.2), within the symmetry sector $(N_{\uparrow}, N_{\downarrow})$ for the same parameters as in (a) and system sizes $L = 13, 15, 17$. The dashed horizontal lines shows the entanglement entropy of a random state within the fragment \mathcal{K}^{res} containing the Néel-ordered CDW initial state. Increasing opacity corresponds to increasing system size. All calculations were done using ED.

has zero imbalance for an equal number of even and odd sites. Additionally, the breathing amplitude of the dynamics for $\Delta = 1J$ is four sites and boundary effects cannot be easily prevented by including an empty site at the edges. We confirm in Fig. 4.8b that the on-site occupancy shows no more memory of the initial CDW order in the regime of weak tilt, consistent with a zero imbalance. For the intermediate tilt in Fig. 4.8c, we find a remaining CDW order.

In Fig. 4.8d we show numerical simulations of the half-chain entanglement entropy $S_{L/2}$, normalized to the Page value $S_{L/2}^{\text{Page}}$ [118, 120, 261] (see also the definition provided in Section 1.2.). This corresponds to the half-chain entanglement entropy of a pure random state within the symmetry sector fixed by particle numbers $N_{\uparrow}, N_{\downarrow}$. In the weak tilt regime, the half-chain entanglement entropy converges towards the thermal Page value for large enough system sizes, which is consistent with a lack of memory of the initial state as observed with the imbalance and the on-site occupancy. For an intermediate tilt, we observe a sub-thermal entanglement entropy, growing only very slowly at late times, which is consistent with the finite imbalance up to the latest times accessible in the simulations. For large tilt, the entanglement entropy reaches a plateau, which slightly depends on the system size. This saturation value of the entanglement entropy is slightly smaller than the entanglement entropy of a random state within the fragment \mathcal{K}^{res} (blue dashed lines for the different system sizes) in which the initial state is contained.

Unlike the dipole-conserving regime, at perfect resonance $U_{\text{res}} = 2\Delta \gg J$, neither the lowest-order dynamical processes generated by $\hat{H}_{\text{eff}}^{\text{res}}$ in Eq. (4.20) nor in general higher-order terms, are energetically suppressed. Thus, at a time scale given by the fourth-order term $t \propto \Delta^3/J^4$, fragmentation phenomena are expected to breakdown with the result that imbalance decays. Note that the third-order and in general any odd-order term vanishes due to the CDW initial state, requiring an even number of hoppings for a resonant exchange between tilt and interaction energy. However, locating such a resonant point (at finite Δ) requires fine-tuning: every order in perturbation theory gives a diagonal contribution renormalizing the Fermi-Hubbard interaction. As numerically shown in Fig. 4.3a, this is even more subtle at lower values of the tilt. In general, we expect a finite detuning from the resonance, which can be comparable to higher-order contributions, thus 'shielding' the fragmentation of the lowest order Hamiltonian and slowing down the dynamics. Nevertheless, and as we already emphasized, we cannot use this perturbative result to draw any conclusion about the system long time dynamics.

4.5. Experimental results

A systematic presentation and discussion of the experimental setup, measurement techniques and data acquisition of the experimental results we discuss in the following section, have been the topic of two different experimental dissertations [262, 263] which extend the content published in Refs. [3, 4]. Moreover, Ref. [263] discusses the effect of experimental imperfections which depart from the ideal tilted Fermi-Hubbard model Eq. (4.9). Hence, we will focus on the main experimental observations that provide evidence about the behavior of the system at long-times as well as the effect of interactions referring the reader to Refs.[262, 263] for additional details.

The experimental setup consists of a degenerate Fermi gas of $50(5) \times 10^3$ ^{40}K atoms that is prepared in an equal mixture of two spin components $|\uparrow\rangle = |m_F = -7/2\rangle$ and $|\downarrow\rangle = |m_F = -9/2\rangle$ in the $F = 9/2$ ground-state hyperfine manifold. The atoms are loaded into a 3D optical lattice with lattice constant $d_s = 266$ nm along the x direction and deep transverse lattices, with constant $d_{\perp} = 369$ nm, to isolate the 1D chains along x . The residual coupling along the transverse directions is less than $3 \times 10^{-4}J$. The dynamics along x is described by the tilted 1D Fermi-Hubbard model in Eq. (4.9). The on-site interaction strength U is controlled by a Feshbach resonance [8] centered at 202.1 G and a magnetic field gradient is used to create the tilt Δ_{σ} , with $\Delta_{\uparrow} \simeq 0.9\Delta_{\downarrow}$. The weak spin-dependence arises due to the different m_F quantum numbers. Moreover, one can tune this spin-dependence using the technique of radio-frequency dressing [4, 264], realizing dressed states that see a weighted average of Δ_{\uparrow} and Δ_{\downarrow} . A general description of the experimental sequence as well as additional details on the experimental setup can be found in the Supplementary Material of Ref.[4].

The initial state for all subsequent measurements is an incoherent mixture of site-localized singlons with random local spin configuration and zero total magnetization ($N_{\uparrow} = N_{\downarrow}$). The fraction of residual holes on even lattice sites, due to imperfections in the loading sequence and due to removed doublons is expected to be about 10% [265].

In the experiment, the subsequent evolution of the spin-resolved imbalance is tracked

$$\mathcal{I}^{\sigma} = (N_e^{\sigma} - N_o^{\sigma})/N^{\sigma}, \quad (4.40)$$

where $N_{e(o)}^{\sigma}$ denotes the total number of spin- σ atoms on even (odd) sites and $N^{\sigma} = N_e^{\sigma} + N_o^{\sigma}$. In the non-interacting limit we already obtained its time-dependence analytically (Eq.(4.6)) leading to Bloch oscillations with a characteristic period $T_{\sigma} = h/\Delta_{\sigma}$, set by the spin-dependent tilt. This enables a precise calibration of the model parameters Δ_{σ} and

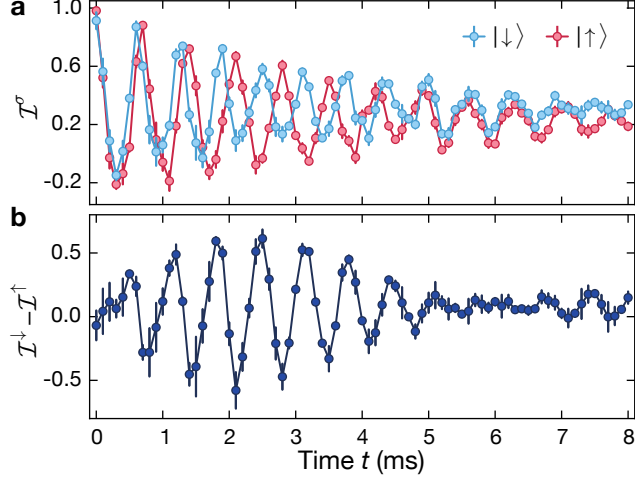


Figure 4.9.: **Spin-resolved Bloch oscillations.** **a** Typical calibration measurement of the tilt Δ_σ for both spin-components using the spin-resolved imbalance \mathcal{I}^σ . Here, $J = 540$ Hz, $\Delta_\downarrow = 2.96(3)J$ and we extract a frequency difference of $(\Delta_\downarrow - \Delta_\uparrow)/h = 170(2)$ Hz, which is in reasonable agreement with the calculated difference. Each data point is averaged four times and error bars denote the standard deviation of the mean (SEM). **b** Imbalance difference between $|\downarrow\rangle$ and $|\uparrow\rangle$. The resulting pattern exhibits a beat note similar to the trigonometric identity $\cos(\omega_1 t) - \cos(\omega_2 t) = -2 \sin((\omega_1 + \omega_2)t/2) \sin((\omega_1 - \omega_2)t/2)$. Solid lines in all panels are numerical simulations using TEBD algorithm performed by Bharath Hebhe Madhusudhana [3].

J at short times. A typical calibration measurement is illustrated in Fig. 4.9 for a spin-mixture at $\Delta_\downarrow = 2.96(3)J$. We clearly see the different tilts in the oscillation frequency of the respective spin component. We observe that the signal includes a decaying envelope function thus departing from the analytical result in Eq.(4.6). Notice that observing perfect revivals with period T_σ in the imbalance, requires no spatial inhomogeneities within the system, as coming from disorder or spatial dependent tunneling J and tilt Δ_σ . In fact, this experimental setup includes a residual harmonic confinement that results in a weak local variation δT_σ of the Bloch oscillation period T_σ between adjacent sites.

4.5.1. Harmonic confinement

Any correction to the linear on-site potential leads to a spectrum of Bloch oscillation frequencies in the system that are averaged over in the imbalance measurement. A relevant such correction is caused by the residual harmonic confinement, modelled as a quadratic contribution to the linear potential, $\Delta_\downarrow i + \alpha(i - i_0)^2$, where i_0 is the center of the lattice. Equivalently, we can think of a locally varying tilt strength given by $\Delta + 2\alpha(i - i_0)$. The observed Bloch oscillation is then a sum of Bloch oscillations with frequencies ranging between $\Delta_\downarrow - 2\alpha L/2$ and $\Delta_\downarrow + 2\alpha L/2$ with a step of 2α for a system size of L sites. In order to understand the result of such a sum, consider, for instance, a sum of sinusoidal oscillations

$$f(t) = \sum_{i=-L/2}^{L/2} \cos(2\pi(\Delta_\downarrow + \alpha i)t) = \cos(2\pi\Delta_\downarrow t) \frac{\sin(2\pi(L+1)\alpha t)}{\sin(2\pi\alpha t)}. \quad (4.41)$$

This is an oscillation at frequency Δ_\downarrow together with a “beat note” envelope at a frequency $(L+1)\alpha \approx L\alpha$ and nodes located at $1/(2L\alpha)$. The Bessel-type Bloch oscillations would

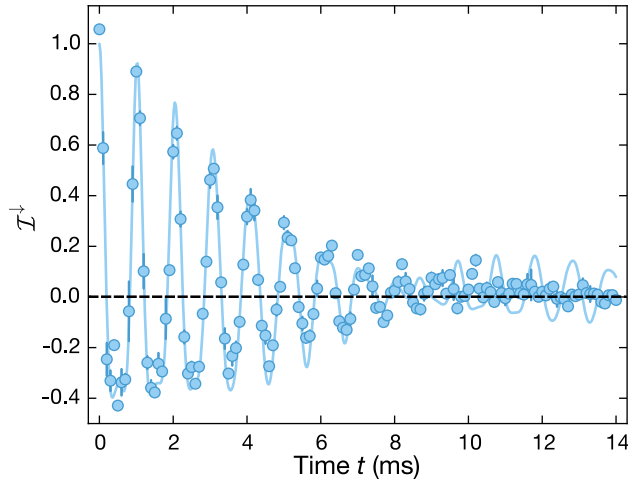


Figure 4.10.: **Calibration of the harmonic confinement.** Imbalance \mathcal{I}^\downarrow for a spin-polarized gas at $\Delta_\downarrow = 1.8J$ and $J = h \cdot 540$ Hz. Each data point is averaged twice and error bars denote the SEM. The solid line is a fit to the data using an ED calculation, which includes the harmonic confinement. The resulting collapse time is $T_c = 8$ ms. The dashed line corresponds to the time-average value of the imbalance $\bar{\mathcal{I}}$ as obtained in Eq.(4.7). Solid lines in all panels are numerical simulations using TEBD algorithm performed by Bharath Hebbe Madhusudhana [3].

behave in a qualitatively, and also quantitatively for $\Delta_\downarrow \gg J$, similar manner. Therefore, we expect a collapse at time $T_c \approx 1/(2L\alpha)$, before the imbalance revives. Even for a weak harmonic potential, its effect on the imbalance can be observed at short times for sufficiently large system sizes. We use numerical calculations of the imbalance time trace for a non-interacting system in a lattice of size $L = 290(20)d_s$ to determine the value of α , as a fit parameter. Corresponding to an experimentally measured imbalance time trace $\mathcal{I}^\downarrow(t_j) : j = 1, 2, \dots, n$, where n is the number of data points in time, we compute, numerically, the trace $\mathcal{I}_{\text{num}}^\downarrow(t_j; J, \Delta_\downarrow, \alpha)$ and then minimize $\sum_j |\mathcal{I}^\downarrow(t_j) - \mathcal{I}_{\text{num}}^\downarrow(t_j; J, \Delta_\downarrow, \alpha)|^2$ over α to determine the fit value. The harmonic confinement is extracted in Fig. 4.10. We find a collapse time of $T_c = 8$ ms (for $J = h \cdot 540$ Hz), corresponding to $\alpha = h \cdot 0.216$ Hz. Due to the local nature of the dynamics in the Stark Hamiltonian, α is the important energy scale for the dynamics, characterizing the amount of curvature, experienced by every single atom. In this system, the tilt is on the order of $\Delta_\downarrow \approx h \cdot 1000$ Hz and the curvature is very weak ($\alpha/\Delta_\downarrow \approx 10^{-4}$). Theoretically, the imbalance oscillations should revive partially (as it happens in numerical simulations only including the harmonic trap), but due to anharmonic confinement, residual onsite disorder and other dephasing mechanisms such revivals are not seen and instead the imbalance saturates to a stationary value. All these artifacts can affect the envelope of the Bloch oscillations in addition to the dephasing of the harmonic confinement and are also included in the extracted collapse time. Hence, extracting the harmonic confinement from the collapse time yields an overestimation of the true harmonic confinement.

4.5.2. Many-body dynamics at short time scales

In a first set of measurements the effect of interactions on the coherent short-time dynamics are studied. In the presence of interactions, Bloch oscillations persist, showing a rich variety of dynamics, such as interaction-induced dephasing and amplitude modulation [232, 266, 267]. Generically, interactions lead to a hybridization of the non-interacting

multi-particle Wannier-Stark orbitals, lifting the degeneracy of the equispaced spectrum, resulting in GOE level statistics for sufficiently small tilts [232]. For weak tilt values, $\Delta_\downarrow = 1.2J$, we find that the dynamics of the interacting spin-mixture ($U = 3J$) exhibits the same dominant frequency components as the non-interacting Bloch oscillations, while the dephasing — referring to the damping of the oscillations — is strongly enhanced (see Fig. 4.11a). This can be seen more directly by calculating the power spectral density (PSD) $|\tilde{\mathcal{I}}^\sigma(\nu)|^2$, which corresponds to the Fourier transform of the time-dependent imbalance (inset of Fig. 4.11a). Time traces up to the collapse time at 8 ms have been used, which correspond to a frequency resolution of 125 Hz in $|\tilde{\mathcal{I}}^\sigma(\nu)|^2$.

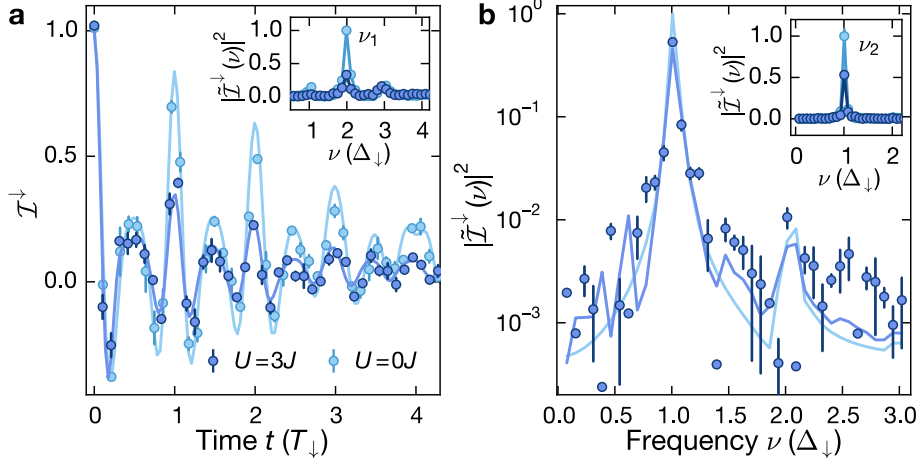


Figure 4.11.: **Short-time interacting Bloch oscillations.** **a** Imbalance \mathcal{I}^\downarrow for $U = 0J$ (spin-polarized gas, light blue) and $U = 3J$ (spin-resolved measurement, dark blue) with $J/h = 0.88(2)$ kHz and $\Delta_\downarrow = 1.22(1)J$. Inset: Power spectral density (PSD) $|\tilde{\mathcal{I}}(\nu)|^2$ of the time traces shown in the main panel, normalized to the maximum of the non-interacting spectrum; $\nu_1 = 2\Delta_\downarrow/h$ indicates the dominant frequency component. **b** PSD $|\tilde{\mathcal{I}}(\nu)|^2$ for $U = 3J$ (spin-resolved measurement, dark blue), normalized to the maximum of the non-interacting spectrum; $J/h = 0.54(1)$ kHz and $\Delta_\downarrow = 2.96(3)J$. The data was obtained from time-traces as in (a). Inset: PSD as in the main panel and for $U = 0J$ (spin-polarized gas, light blue). $\nu_2 = \Delta_\downarrow/h$ indicates the dominant frequency. Each data point in (a),(b) consists of four independent measurements and the error bars denote the standard error of the mean (SEM). Solid lines in all panels are numerical simulations using TEBD algorithm performed by Bharath Hebhe Madhusudhana [3].

We find three distinct peaks in the spectrum, the Bloch frequency Δ_\downarrow and an admixture of two higher harmonics with the largest spectral weight in the second harmonic at $\nu_1 = 2\Delta_\downarrow/h$. For $U = 3J$ its weight is decreased by 70% compared to the non-interacting case. The higher-order harmonics originate from the real-space evolution within one Bloch cycle and are determined by the Bloch oscillation amplitude $A_\sigma/d_s = 4J/\Delta_\sigma$. Recall that the non-interacting Wannier-Stark orbitals are localized around sites of the chain extending over a region of size $4J/\Delta_\sigma$ (in units of the lattice constant d_s) with energy given by the site coordinate (on the Wannier-Stark ladder) times the tilt [75]. We thus can anticipate frequency components at integer multiples of Δ_σ , with an upper bound determined by A_σ/d_s , in agreement with our data.

Interaction effects are expected to be less relevant once the Bloch oscillation amplitude is smaller than one site, resulting in negligible overlap between neighboring particles for our CDW initial state. In Fig. 4.11b we show the PSD of the coherent short-time dynamics

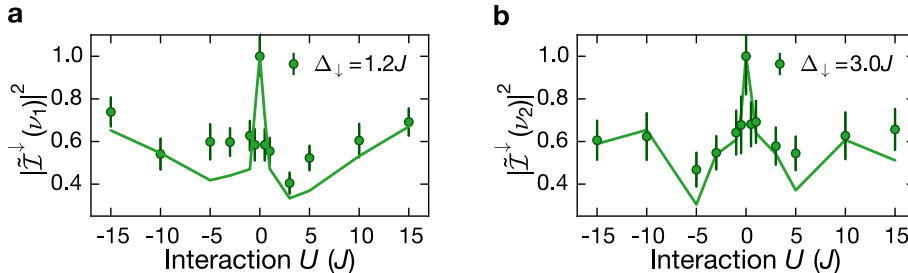


Figure 4.12.: **Short-time interacting Bloch oscillations.** Interaction scan of the peak power spectral density $|\tilde{\mathcal{I}}(\nu_j)|^2$ evaluated by summing the PSD in a window of ± 3 data points around the dominant frequency ν_j , $j = \{1, 2\}$ at (a) $\Delta_{\downarrow} = 1.22(1)J$ and (b) $\Delta_{\downarrow} = 2.96(3)J$ obtained from traces as in Fig. 4.11a. Solid lines in all panels are numerical simulations using TEBD performed by Bharath Hebbe Madhusudhana. The experimental and numerical data in this plot were published in Ref. [3].

for $\Delta_{\downarrow} = 3J$. While the largest spectral weight of the PSD is now contained in the Bloch frequency $\nu_2 = \Delta_{\downarrow}/h$, the reduction is still about 50% compared to the non-interacting case. Indeed, the spectral weight is a sensitive measure of the interaction-induced dephasing. Moreover, the on-site interactions lift the degeneracy of the energy levels in the Wannier-Stark spectrum, which results in additional frequency components in the PSD. In particular, for the parameters used in the data of Fig. 4.11b, these lead to particularly clear signals at $\approx \nu_2 \pm 0.5\Delta_{\downarrow}/h$ in the time-evolving block decimation (TEBD) simulations [268–271], which is consistent with the experimental data. A recent work [272] has found that these additional frequency contributions can be explained using the two-particle picture in the presence of a tilt [253] leading to a shift $\nu_2 \pm J_{\text{eff}}$ with $J_{\text{eff}} \propto J^2 U / (\Delta^2 - U^2)$.

The sensitivity of the coherent short-time dynamics on the interaction strength is further highlighted by the strong interaction-dependence of the peak power spectral density (PPSD) $|\tilde{\mathcal{I}}(\nu_j)|^2$ of the respective dominant frequency components ν_j , $j = \{1, 2\}$ in each regime with $\Delta_{\downarrow} = 1.2J$ and $\Delta_{\downarrow} = 3.0J$ respectively (Fig. 4.12). We find a sharp decrease of the PPSD by about 40% already for small interaction strength $U = \pm 0.5J$ for $\Delta_{\sigma} = 1.2J$. After reaching a global minimum at intermediate interaction strength, it slowly recovers to the non-interacting value in the limit of large interactions as long as $|\Delta_{\uparrow} - \Delta_{\downarrow}| \ll J$.

From this analysis we conclude that interactions do have an effect on the system dynamics for the range of parameters considered in the experiment. However, what happens at long times?

4.5.3. Non-ergodic behavior at late times

In this section we measure time in units of tunneling times $\tau = \hbar/J$, which is given by the inverse of the hopping amplitude J . For large enough evolution times, the coherent Bloch oscillations are dephased and a finite steady-state imbalance develops in the non-interacting limit (see light-blue time trace in Fig. 4.13a). The observed finite steady-state imbalance is caused by Wannier-Stark localization and agrees with the analytical prediction for the time-average value of the imbalance obtained in Eq. (4.7) (black dashed line). The excellent agreement between experimental data and the analytical result provides strong evidence that the effect of the harmonic confinement is negligible for the late-time steady-state imbalance value (while relevant for the damping of Bloch oscillations). This is further supported by the data in Fig. 4.14a, where the steady-state value is probed for a larger range of tilt values, even reproducing the non-monotonous behavior that we found in Fig. 4.2, including values at which the imbalance vanishes.

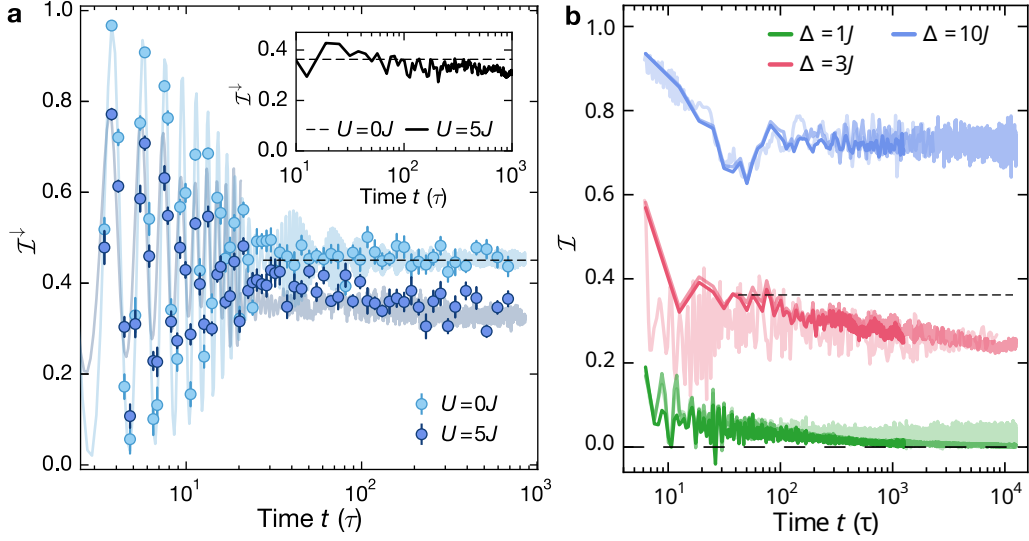


Figure 4.13.: **Long-time dynamics.** **a** Imbalance time traces at $\Delta_{\downarrow} = 3.30(3)J$ and $J/h = 0.54(1)$ kHz for $U = 0J$ (spin-polarized, light blue) and $U = 5J$ (spin-resolved measurement, dark blue). The shaded trace is an ED calculation for $L = 16$. Inset: ED calculation for $L = 16$ in a clean system with $\Delta_{\downarrow} = \Delta_{\uparrow} = 3J$, $\omega_h = 0$ and $U = 5J$ using a Néel-ordered initial CDW. The dashed lines show the analytic prediction for the non-interacting steady-state imbalance [Eq. (4.7)]. Error bars denote the SEM. Numerical simulations in this plot were performed by Bharath Hebbe Madhusudhana. **b** Long-time behavior of imbalance \mathcal{I} for system sizes $L = 13, 15, 17$ and $(\Delta = 10J, U = 19.85J)$ (blue), $(\Delta = 3J, U = 4.75J)$ (red) and system sizes $L = 12, 14, 16$ for $(\Delta = 1J, U = 4.75J)$ (green). The dashed lines show the analytic prediction for the non-interacting steady-state imbalance Eq. (4.7). Same numerical data as shown in panel (a) of Fig. 4.8.

In the presence of weak interactions localization has been predicted to survive in the presence of small additional disorder or harmonic confinement due to Stark MBL, leading to a finite steady-state imbalance [76, 157, 253]. Here, we find that after an initial decay at intermediate times a plateau of the imbalance develops, which persists for long evolution times up to 700τ (Fig. 4.14a) in the strongly-interacting regime. A comparison with ED simulations (inset Fig. 4.13a) in a clean system, i.e., without spin-dependent tilt and harmonic confinement, with the same tilt and interaction strengths and for a Néel-ordered initial CDW (as opposed to the random-spin initial state realized in the experiment) further highlights that the non-vanishing imbalance appears not as a result of experimental imperfections at least for the experimentally relevant observation times.

Moreover, this robust steady-state value survives over a wide range of parameters (Fig. 4.14b). As a function of the tilt it qualitatively follows the behavior of the non-interacting system, but shows consistently lower steady-state values.

For very small values of the tilt, one expects the interactions between particles result in a dephasing of the local coherent dynamics that give rise to Wannier-Stark localization in the non-interacting limit and hence lead to vanishing imbalances. Instead, Fig. 4.14c shows a finite steady-state value for $\Delta_{\downarrow} = 1.1J$ that it is largely independent of the interaction strength. Nevertheless, we numerically found that the imbalance decays to zero for evolution times on the order of $10^4\tau$ when considering a Néel-ordered singlon CDW initial state for a clean system, which we reproduce in Fig. 4.13c. This trace further agrees with the finite imbalance measured at $\sim 200\tau$. Moreover, the observed inversion

of the spin-resolved imbalance for the experimental results $\mathcal{I}^\downarrow < \mathcal{I}^\uparrow$ (although $\Delta_\downarrow > \Delta_\uparrow$) is explained by the non-monotonic dependence of the stationary imbalance on the tilt for $\Delta_\sigma < 2J$ as shown in Fig. 4.14a.

For intermediate values of the tilt $\Delta/J \simeq 3$ we find a clear interaction dependence of the stationary value (Fig. 4.14b), which is similar for both spins and is well reproduced by numerical simulations. The imbalance is symmetric around $U = 0$ due to the dynamical symmetry between attractive and repulsive interactions (Section 4.2.2) when $(\Delta_\downarrow - \Delta_\uparrow) \ll J$. The global minimum appearing at intermediate interactions corresponds to the resonant regime $|U| \simeq 2\Delta$, which dominates over the $|U| \simeq \Delta$ due to the CDW structure of the initial states. The precise value of the resonance is slightly shifted (see Fig. 4.14d), in agreement with our perturbative computation in Section 4.3.1 (dashed line in fig3d). For large interactions and weak spin-dependence $(\Delta_\downarrow - \Delta_\uparrow) \ll J$, we expect the system to then recover the non-interacting regime (see Appendix C).

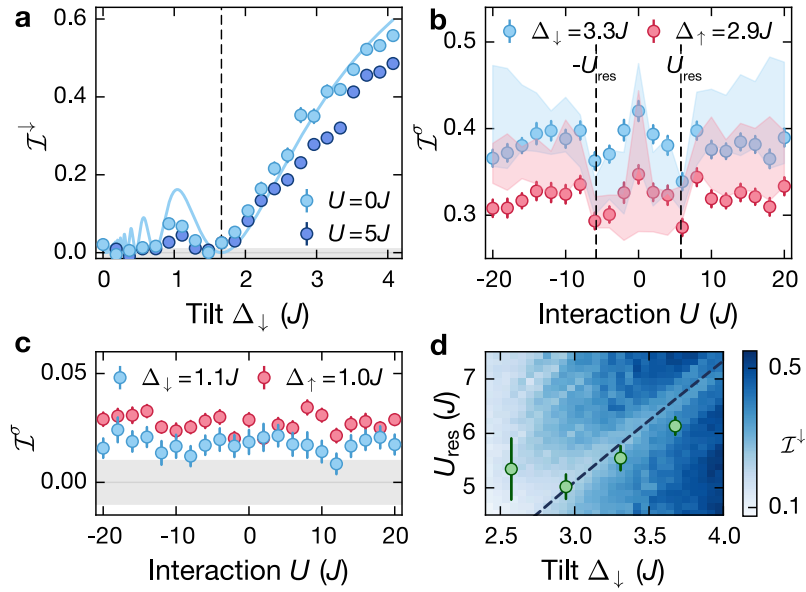


Figure 4.14.: **Long-time dynamics close to resonance $U \simeq 2\Delta$.** **a** Imbalance versus Δ_\downarrow measured at $U = 0J$ (spin-polarized, light blue) and $U = 5J$ (spin-resolved measurement, dark blue). Each data point is averaged over ten equally spaced times in a time window between 70τ and 100τ ($U = 0J$) and 340τ and 370τ ($U = 5J$). The solid line shows the analytic prediction for \mathcal{I}^\downarrow [Eq. (4.7)] and the dashed line indicates the first root of the Bessel function at $\Delta_\downarrow \approx 1.5J$. **b** Spin-resolved imbalance versus interaction strength for $\Delta_\downarrow = 3.30(3)J$. The shaded trace is an ED simulation and the width indicates the 1σ standard deviation. Each numerical and experimental point is averaged over ten time steps equally spaced between 170τ and 200τ . **c** Spin-resolved imbalance versus interaction strength at $\Delta_\downarrow = 1.10(1)J$. Each point is averaged over the same time steps as in (b). **d** Resonances extracted from interaction scans for $U > 0$ as in (d) for different tilt values (see Supplementary Material in Ref. [3]). The color plot shows ED calculations for the same parameters as in the experiment, but with $\omega_h = 0$, for $L = 13$ sites. The dashed line indicates the analytic prediction for the resonance $U_{\text{res}} \simeq 2\Delta_\downarrow - 8J^2/(3\Delta_\downarrow)$. The grey shaded area in (a),(c) indicates the calibrated detection resolution. In all panels error bars denote the SEM. This figure has been taken from Ref. [3].

While the experimentally investigated regimes are far from the range of applicability

of our perturbative arguments, the experimental results are consistent with them and quantitatively agree with the numerical results for the tilted 1D Fermi-Hubbard model, including neither a spin-dependent tilt nor a harmonic trap. In fact, such irregularities are expected to contribute to prevent the system from thermalizing at the observational times.

In the limit of large tilts $\Delta \gg J, |U|$, we found an approximate dipole-conserving Hamiltonian $H_{\text{eff}}^{\text{dip}}$ which to third order in perturbation theory on $\lambda = J/\Delta$, is strongly fragmented. This is seemingly consistent with the observed non-ergodic behavior. Yet, higher-order processes $\mathcal{O}(\lambda^4)$, relevant for $\Delta \simeq 3J$, are expected to melt the CDW within the experimentally studied timescales. These higher-order processes as well as the dominant off-diagonal contribution, however, require the production of doublons, which is penalized by the on-site interaction U which we found leads to a significant slowdown of the dynamics (see Fig. 4.7). This could explain the robustness of the steady-state value observed in the experiment.

On resonance, $|U_{\text{res}}| = 2\Delta$, we derived an effective Hamiltonian $\hat{H}_{\text{eff}}^{\text{res}}$ conserving the dipole moment, the doublon number or the sum of the two. This Hamiltonian is fragmented which leads to a finite steady-state value within the relevant fragment. However, unlike in the previous regime, doublons can be formed without energy penalties, leading to a faster initial decay of the imbalance and a lower steady-state value. For finite λ or longer evolution times, higher-order hopping processes will mix different fragments hence enabling additional dynamics. These processes are expected to eventually melt the CDW completely, although the required timescales may be very large. Locating such a resonant point (at finite Δ) requires fine-tuning which translates to the generic presence of a finite off-resonant diagonal contribution comparable to higher-order contributions that could potentially “shield” this non-ergodic behavior. While in the experiment we find robust steady-state values even for rather low values of the tilt ($\Delta \simeq 3J$) up to evolution times of about 700τ (Fig. 4.13a), our numerical results Fig. 4.13b suggest that the imbalance will eventually vanish at longer times.

Finally, we emphasize that in none of our numerical simulations for the clean system, a finite value of the imbalance goes along with a logarithmic growth of the half-chain entanglement entropy (see Fig. 4.8c). Even for large $U \simeq 2\Delta = 20J$, the entropy quickly reaches the Page value within the relevant Krylov sector whose size grows exponentially with system size, hence leading to a volume law scaling. Therefore, the observed phenomena cannot be explained by the phenomenon of Stark MBL.

4.6. Conclusions and discussion

In this chapter, we have explained how the phenomenon of Hilbert space fragmentation can be explored in current experimental setups, identifying ultracold atoms in optical lattices as a powerful tool to realized different regimes. While we entirely focused on dynamics constrained by the coupling of an external field to the charge degrees of freedom, the possibility of tuning a spin-dependent tilt allows to explore many other scenarios, which combine charge and spin dynamics. Moreover, we have demonstrated both experimentally and numerically non-ergodic behavior in the tilted 1D Fermi-Hubbard model over a wide range of parameters at the relevant observation times. We have found numerical evidence that at least in certain regimes this non-ergodic behavior is explained by an emergent Hilbert-space fragmentation, where higher-order terms become ineffective to spread correlations. Concurrently and after the publication of these results, several works studied the phenomenology of Stark MBL including two experimental studies based on trapped ions [273] and superconducting circuits [274]. Relevant to our previous discussion is the construction of dynamical l-bits [275], and hence of l-bits, in the large tilt regime. Un-

derstanding their existence and consequences derived from those at the resonant regimes, is a question worth exploring. Nevertheless, many other questions related to the current chapter still remain unanswered.

For future studies it would be interesting to systematically investigate the initial-state dependence of the dynamics. This is a characteristic feature of Hilbert-space fragmentation that could also shed light to the difference between the standard disorder-induced and Stark MBL. A first step on this direction has been already taken in Ref. [4], which studied the evolution of different families of initial states in the presence of stronger tilts than the ones considered in this chapter. In fact, it would be conceptually interesting to reconcile the phenomenon of Stark MBL and Hilbert-space fragmentation, by systematically studying the impact of weak disorder or residual harmonic confinement on the long-time dynamics. This is expected to be dominated by a competition with the higher-order perturbative processes that drive thermalization in the clean limit. This question would benefit from recent experimental developments as the quantum gas microscope [152, 153], which performing on-site measurements and manipulations allows to investigate the evolution of other local observables from specific initial states; and the possibility to perform randomized measurements, to study the evolution of the n th-order Renyi entropies [276] in the regimes of interest. The combination of these two developments would let us explore the rich dynamics of fragmented models, which include fragments with integrable, non-integrable as well as other constrained behavior, answering e.g., questions about their transport properties.

Moreover, adding periodic modulation as an additional ingredient, other strongly-fragmented models, scarred models and time crystals could be engineered [277–279] or drive-induced localization could be investigated [280, 281] as well as the robustness of Stark MBL. Furthermore, an extension to 2D could serve as benchmark for the robustness of Hilbert-space fragmentation in the presence of multipolar conservation laws [6, 181, 282] or bath-coupling [283]. Finally, it will be also interesting to further explore the connection between lattice gauge theories and the phenomenon of Hilbert-space fragmentation which could be addressed experimentally in a similar model [284]. We comment more on this in Chapter 7.

Part III.

Spatially-modulated symmetries

5. New families of modulated symmetries in 1D

Unconventional symmetries, like for example multiple-moment conservation and continuous as well as discrete subsystem symmetries, are gaining a lot of attention due to the unexpected and rich phenomena they can lead to. These include new equilibrium phases of matter with novel low-energy features like for example fracton phases [52, 54–57, 60], subsystem SPTs [285], fractal symmetries and criticality [286, 287], fractal spin liquids [288] etc, as well as unusual non-equilibrium properties such as sub-diffusive transport [6, 178, 289–293] and Hilbert space fragmentation [1, 181]. And while a priori artificial, we just found out that for example the dipole moment is approximately conserved in experimentally accessible setups and relevant physical scenarios.

The common underlying idea is the non-trivial *spatial modulation* of the corresponding conserved quantities, namely $\mathcal{Q}_{\{\alpha_{\mathbf{r}}\}} = \sum_{\mathbf{r}} \alpha_{\mathbf{r}} q_{\mathbf{r}}$, where $q_{\mathbf{r}}$ is some local charge at location \mathbf{r} . Similarly, in the case of discrete symmetries that can be expressed as tensor product of local unitaries $S = \otimes_{\mathbf{r}} U^{\alpha_{\mathbf{r}}}$ where $\alpha_{\mathbf{r}} = 0, 1$. As such, they fail to commute with spatial translations. For example, in the case of multipole conservation $\alpha_{\mathbf{r}}$ is a polynomial of the spatial coordinates $r_i = x, y, z$, while for subsystem symmetries $\alpha_{\mathbf{r}}$ takes non-zero values only on a spatial submanifold.

In this and in the following chapter, we inquire about the possible modulated continuous symmetries a (local) Hamiltonian can have, and extend the notion of spatial modulation to more general cases of $\alpha_{\mathbf{r}}$. We show that such symmetries appear in some simple, locally interacting systems, and give various examples in both one (1D), two (2D) and three (3D) dimensions. The symmetries we identify come in two main flavors that can occur simultaneously. One type is exponentially-modulated and leads to localized modes at the boundaries of the system and to infinitely long-lived boundary correlations, resembling the physics of strong zero modes [184]. The other type corresponds to the conservation of certain momentum-components of a local observable. Interestingly, in 2D and 3D we find various models where long-lived modes exist along some closed hypersurfaces in momentum-space; resembling systems with Bose surfaces [294–298] and the UV/IR-mixing phenomenon [299–301]. We will discuss the effect of these symmetries on the system’s dynamics and show that they lead to unusual features in correlations functions, such as long-lived spatial oscillations on microscopic scales.

5.1. Cellular automaton dynamics

We will consider stochastic block cellular automaton dynamics, which allow for large-scale numerical simulations, although all of our models can be mapped to quantum models that realize the same set of symmetries. We consider a chain of classical discrete spins that take values $s_x \in \{-S, \dots, S\}$ on each site $x = 0, \dots, N - 1$. Equivalently we could consider local positive values $n_x \in \{0, \dots, 2S + 1\}$ representing the occupation number of a site. The dynamics is generated by local gates G_x , acting in a finite neighbourhood of site x , mimicking finite-range interactions. The effect of a gate of range $\ell + 1$ is described by a set of integers n_i such that when applying $G_x = \{n_i\}$, the spins are updated as $s_{x+i} \rightarrow s_{x+i} \pm n_i$ with $i \in \{0, \dots, \ell - 1\}$, which can be understood as mimicking spin ladder operators. These updates are randomly applied among those configurations for which $|s_{x+i} \pm n_i| \leq S$, such

that the corresponding transition rates between two different local configurations \mathbf{s}, \mathbf{s}' are symmetric, i.e., $\gamma_{\mathbf{s} \rightarrow \mathbf{s}'} = \gamma_{\mathbf{s}' \rightarrow \mathbf{s}}$ ¹. This ensures that detailed balance is satisfied with respect to the “infinite temperature” (uniformly random) ensemble, which is therefore a stationary state of this stochastic process. At each application either (i) $s_{x+i} \rightarrow s_{x+i} + n_i$ is applied or (ii) its inverse, $s_{x+i} \rightarrow s_{x+i} - n_i$, or (iii) no update is made. For each time step, we randomly pick a non-overlapping complete covering of the (1D or 2D) lattice by the gates $G_{\mathbf{x}}$. For a model in 1D with gates acting on 2ℓ sites, we pick randomly an integer $m \in \{0, \dots, \ell - 1\}$ and apply all other non-overlapping gates on sites $x = m \pmod{\ell}$. Similarly, in 2D with gates of size $\ell \times \ell$ we pick two integers $m_x, m_y \in \{0, \dots, \ell - 1\}$ and shift the gates accordingly. A (discrete) evolution till time t then consists on the application of t consecutive layers of gates.

5.2. Models and symmetries

To classify the families of all possible continuous global conserved quantities a system can have is certainly a hard problem. Instead, we first consider a family of 1D models to introduce the notion of modulated symmetries and only later on, we will briefly revisit the more general question. Without loss of generality we consider a family of models labeled by positive integers $q \geq 1, p \geq 0$, defined by the gates

$$G_x^{(p,q)} = \{n_0, n_1, n_2\} = \{q, -p, q\}, \quad (5.1)$$

acting on a three-site block centered around x . This particular choice of family of systems will allow us to “factorize” and separate different families of symmetries, but our results will apply to more general systems. We first notice that for $2q \neq p$, these models do not conserve the total charge $\mathcal{Q} = \sum_j s_j$ or any of its higher moments. Nevertheless, there still exist some global conserved quantities, which we now construct.

Consider the general ansatz $\mathcal{Q}_{\{\alpha_j\}} \equiv \sum_j \alpha_j s_j$. Then $\mathcal{Q}_{\{\alpha_j\}}$ is a conserved quantity for the evolution generated by $G^{(q,p)}$ if and only if $\{\alpha_j\}$ fulfills the recurrence relation

$$q\alpha_{j+2} - p\alpha_{j+1} + q\alpha_j = 0. \quad (5.2)$$

As a linear recurrence, Eq. (5.2) equation admits a general solution in terms of the roots r_1, r_2 of the associated characteristic equation (obtained by substituting $\alpha_x = r^x$ into Eq. (5.2))

$$r^2 - \frac{p}{q}r + 1 = 0 \text{ with solutions } r_{1/2} = \frac{p}{2q} \pm \sqrt{\left(\frac{p}{2q}\right)^2 - 1}. \quad (5.3)$$

A general solution of Eq. (5.2) can then be written as $\alpha_j = a(r_1)^j + b(r_2)^j$ if the roots are not degenerate ($r_1 \neq r_2$) or $\alpha_j = a(r_1)^j + bj(r_2)^j$ if $r_1 = r_2$. Moreover, these can be parametrized by the initial conditions α_0, α_1 , or equivalently, one can fix the boundary conditions α_0, α_{N-1} , which implies that the model Eq. (5.1) has at most two linearly-independent conserved quantities of this kind. Note that if q divides p then $\mathcal{Q}_{\{\alpha_j\}}$ has an integer spectrum and thus generates a representation of $U(1)$. Otherwise $\mathcal{Q}_{\{\alpha_j\}}$ will pick up sums of powers of p/q and the symmetry transformation is then a unitary representation² of the additive group \mathbb{R} . As the second order polynomial in Eq. (5.3) is palindromic (self-reciprocal) [302], its two roots r_1, r_2 are inverses of each other, $r_2 = 1/r_1$. Thus, three different scenarios can occur, depending on the ratio p/q :

¹Note that this implementation differs from that used in previous works [6, 178, 291, 292], where all local updates consistent with symmetry requirements were allowed. However, the conclusions do not depend on this choice.

²Imposing integer spectrum requires a system size dependent normalization of the conserved quantity $\mathcal{Q}_{\{\alpha_j\}} \rightarrow q^L \mathcal{Q}_{\{\alpha_j\}}$.

5.2.1. Dipole conservation

If $2q = p$ then $r_2 = r_1 = 1$, which leads to a general solution of the form $\alpha_j = a_0 + a_1 j$; this reproduces the conservation of charge and dipole moment. Although we will explicitly construct models conserving higher m -moments of the charge ($Q^{(n)} = \sum_j j^n s_j$, with $n \leq m$), which require longer-range gates, it is worth to already mention that in those cases, one will find that $r = 1$ is a $(m + 1)$ -fold degenerate root. Then, α_j will include the contribution $\sum_{n=0}^m a_n j^n$. In fact, $r = 1$ will be the only root for the shortest-range gates compatible with conserving the first m moments of the charge: The characteristic polynomial is given by $(r - 1)^{m+1}$, which corresponds to the linear recurrence relation $\sum_{j=0}^{m+1} (-1)^j \binom{m+1}{j} \alpha_j = 0$ that at least requires local terms of size $m + 2$. The associated gates are then given by $\{n_j = \pm(-1)^j \binom{m+1}{j}\}_{j=0}^{m+1}$, which correspond to the coefficients of a finite difference Δ^{m+1} of order $m + 1$, a relation we will make use of in the following section.

5.2.2. Quasi-periodic modulation

If $2q > p$, then Eq. (5.3) has two complex solutions $e^{\pm i k^*}$ with $k^* = \arccos(\frac{p}{2q})$ ³. A general solution of Eq. (5.2) then takes the form $\alpha_j = a e^{i k^* j} + b e^{-i k^* j} = A \cos(k^* j + \phi)$ with constants a, b (equivalently, A, ϕ) fixed by α_0, α_1 ⁴. Thus, although the total charge is not conserved, some finite momentum component of it is. However, while the recursion relation can always be solved in a system with open boundary conditions (OBC), the corresponding momentum mode might not exist in a finite system with periodic boundaries (PBC). Indeed, we could search directly for a conserved quantity of the form $s_k \equiv \sum_j e^{i k j} s_j$, by plugging the ansatz $\alpha_j = e^{i k j}$ into Eq. (5.2), which then becomes $\chi(k) \equiv \cos(k) - \frac{p}{2q} = 0$. Notice that the discrete Fourier transform of the recurrence relation is given by $e^{i k} \chi(k) \tilde{\alpha}_k = 0$. However, we should also require that $\alpha_j = \alpha_{j+N}$ for all sites j , i.e., that k is a multiple of $\frac{2\pi}{N}$. Thus, a necessary condition for a solution $k = k^*$ to exist is that k^* is at least a rational multiple of π . According to Niven's theorem [304], this is the case if and only if $\frac{p}{2q} \in \{0, \frac{1}{2}, 1\}$ or equivalently $k^* \in \{0, \pm\frac{\pi}{3}, \pm\frac{\pi}{2}\}$. In this case, the modulation k^* is commensurate, having a finite periodicity on the lattice, and the symmetry is exact for some finite system sizes that are integer multiples of its period ($\frac{2\pi}{k^*}$). For example, when $k^* = \pm\frac{\pi}{3}$ and for any choice α_0, α_1 , the general solution takes the form $\alpha_x = \{\alpha_0, \alpha_1, \alpha_1 - \alpha_0, -\alpha_0, -\alpha_1, \alpha_0 - \alpha_1\} \bmod(6)$ which repeats with period six. Thus the choices $\alpha_0 = 1, \alpha_1 = 0$ and $\alpha_0 = 0, \alpha_1 = 1$ correspond to staggered sublattice symmetries. The case $k^* = \pm\frac{\pi}{2}$ leads to a similar structure.

In the more general case, however, k^* is not a rational multiple of π , the modulation is quasi-periodic, and the conserved quantity does not exist for any finite system with PBC. Nevertheless, for sufficiently large systems the distance between momenta in the reciprocal lattice goes as $2\pi/N$, and there will be momentum modes that are almost conserved, and the symmetry re-emerges in the thermodynamic limit.

5.2.3. Exponentially localized

The final scenario is $2q < p$ for which $r_{1,2}$ are real, positive and non-degenerate. This implies $r_1 > 1$ and $r_2 = 1/r_1 < 1$, leading to two conserved quantities exponentially localized at the two boundaries of the system (for OBC). Thus, it is more appropriate to instead label solutions by the two endpoints, α_0 and α_{N-1} , rather than α_0 and α_1 . Let

³This can be generalized to longer-range gates using results from Ref. [303].

⁴Notice that because of the spatial inversion symmetric gate G_x in Eq. (5.1), if a momentum k^* of the spin is conserved, so is $-k^*$.

5.3. General construction and analogous quantum models

us denote by \mathcal{Q}_ℓ (\mathcal{Q}_r) the charge localized at the left (right) boundary of the system with boundary conditions $\alpha_0^\ell = 1, \alpha_{L-1}^\ell = 0$ ($\alpha_0^r = 0, \alpha_{N-1}^r = 1$). Their exact form is given by

$$\alpha_x^{k=\ell,r} = \frac{1}{r^{N-1} - r^{-(N-1)}} \left[(\alpha_{N-1}^k - \alpha_0^k r^{-(N-1)}) r^x + (\alpha_0^k r^{N-1} - \alpha_{N-1}^k r^{-x}) \right], \quad (5.4)$$

with $r > 1$ the largest root of the associated characteristic equation. In the limit of large N , this takes the asymptotic form

$$\alpha_x^\ell \approx r^{-x}, \quad \text{and} \quad \alpha_x^r \approx r^{x-(N-1)},$$

decaying exponentially towards the bulk. Note that in this case, it is not possible to satisfy the recursion relation with PBC.

The form of these exponential symmetries might suggest that the number of symmetry sectors scales exponentially with system size, and thus that the presence of a single exponential symmetry can lead to (an exponential) fragmentation. However, this is not the case for the symmetries we just constructed as we know there is an extensive number of gates preserving this symmetry which connect many different configurations with the same total charge. In particular, given an exponential symmetry of the form $\mathcal{Q} = \sum_{j=0}^{N-1} r_*^j s_j$, two configurations $\{s_j\}$ and $\{s'_j\}$ belong to the same symmetry sector if and only if r_* is a solution of the polynomial equation $\sum_{j=0}^{N-1} r^j (s_j - s'_j) = 0$. From here one can infer that the number of configurations $\{s'_j\}$ with the same charge as $\{s_j\}$ is given by the number of polynomials of degree $N - 1$ with integer coefficients $s_j - s'_j$ which have r_* as a root.

Hence, the construction we just presented is restricted to spatial modulations that can appear as solutions of the recurrence relation Eq. (5.2), and therefore to those whose associated roots are algebraic numbers⁵. This in particular implies that we will not obtain conserved quantities like for example $\alpha_x = e^x, \pi^x$, since e and π are both transcendental. In fact, it is not at all clear whether one can construct a local Hamiltonian with these transcendental modulations: Being r transcendental implies that no polynomial $\sum_{j=0}^{N-1} x^j (s_j - s'_j)$ exists which has r as a root, and therefore that not two distinct configurations can have the same value of this modulated charge. In this situation, the spectrum of \mathcal{Q} would be exponentially large providing an example of fragmentation with a single global conserved quantity, although the associated bond algebra (in the formulation of Ref. [166]) might be completely trivial⁶.

5.3. General construction and analogous quantum models

5.3.1. General parametrization of size-3 gates

The family of gates introduced in Eq. (5.1) led to particular useful properties when classifying the possible modulated symmetries. First of all, we considered a particular sign structure of the gates with both q, p being positive. Allowing for p to become negative such that

$$G_x^{(p,q)} = \{n_0, n_1, n_2\} = \{q, p, q\}, \quad (5.5)$$

translates into $r_1, r_2 < 0$ (where still $r_1 \cdot r_2 = 1$). This simply leads to an additional staggering of the associated charges. In particular: For $|p/(2q)| = 1$ one finds $\alpha_j = (a_0 + a_1 j)(-1)^j$ and $\alpha_j = (-1)^j (a(r_1)^j + b(r_2)^j)$ in the other two scenarios. For example, in the case of commensurate modulation this corresponds to the additional solutions with $\frac{p}{2q} \in \{0, \pm\frac{1}{2}, \pm 1\}$.

⁵A number is said to be algebraic if there exists a polynomial equation with integer coefficients for which this is a solution.

⁶I thank Sanjay Moudgalya for an interesting discussion about these ideas.

In general, a gate acting on three consecutive sites can be parametrized as

$$G_x^{(b,p,q)} = \{n_0, n_1, n_2\}. \quad (5.6)$$

Its associated recurrence relation takes the form

$$n_2\alpha_{j+2} + n_1\alpha_{j+1} + n_0\alpha_j = 0, \quad (5.7)$$

with roots

$$r_{1,2} = -\frac{n_1}{2n_2} \pm \frac{1}{2n_2} \sqrt{n_1^2 - 4n_0n_2}, \quad (5.8)$$

for $n_2 \neq 0$ of the corresponding characteristic equation. Since the equation is no longer palindromic, r_1, r_2 won't in general be the inverse of each other and can take the general form $Re^{i\theta}$, thus combining exponential and quasi-periodic symmetries. For non-degenerate roots this leads to $\alpha_j = (R_1)^j e^{i\theta_1 j} + (R_2)^j e^{i\theta_2 j}$, while if $n_1^2 = 4n_0n_2$ a double degenerate root exists with $r_{1,2} = -n_1/(2n_2)$ such that $\alpha_j = (-\frac{n_1}{2n_0})^j (a + bj)$. For example, for $n_0 = 4, n_1 = -4, n_2 = 1$ this leads to the conservation of the first moment of an exponential localized symmetry $\mathcal{Q}_{\alpha_j} = \sum_j (a + bj)2^j s_j$ at the right boundary (note that this choice does not correspond to a inversion symmetric gate).

The previous construction can be extended to longer-range gates which will lead to higher-order recurrence relations with associated characteristic polynomials of higher degree. This can help to avoid possible non-generic results for particular models and also get rid of strong Hilbert space fragmentation even for small spin representations S .

5.3.2. Longer-range gates

The two previous sections introduced some specific 3-local gates which apart from fulfilling the goal of introducing these new families of modulated symmetries, can be used as building blocks to construct longer-range gates, although such longer-range models are perfectly valid on its own and do not need to follow the construction presented here.

Consider the family of size-3 gates, $G^{(n_0, n_1, n_2)}$ in Eq. (5.6), determined by the strings of numbers $\{n_i\} = (n_0, n_1, n_2)$ acting on sites $(x, x + 1, x + 2)$ with associated characteristic equation $n_0 + n_1 r + n_2 r^2 = 0$. Let us start constructing range-4 gates from range-3 ones and address the general case afterwards. Adding up strings corresponding to two overlapping range-3 gates we find

$$\frac{\begin{pmatrix} (n_0, n_1, n_2, 0) \\ \pm(0, n_0, n_1, n_2) \end{pmatrix}}{(n_0, n_1 \pm n_0, n_2 \pm n_1, \pm n_2)}, \quad (5.9)$$

such that the resulting gate $G_x = \{n_i\} = \{n_0, n_1 \pm n_0, n_2 \pm n_1, \pm n_2\}$ acts on sites $(x, x + 1, x + 2, x + 3)$. The associated recurrence relation takes the form

$$n_0\alpha_j + (n_1 \pm n_0)\alpha_{j+1} + (n_2 \pm n_1)\alpha_{j+2} \pm n_2\alpha_{j+3} = 0, \quad (5.10)$$

with characteristic equation

$$n_0 + (n_1 \pm n_0)r + (n_2 \pm n_1)r^2 \pm n_2r^3 = 0. \quad (5.11)$$

Generically, such a combination results in a characteristic equation which contains additional roots to those we started from. Indeed, due to the linearity of Eq. (5.10), these include the roots of $n_0 + n_1 r + n_2 r^2$, i.e., independent solutions corresponding to each of the original gates, as can be clearly seen by factorizing Eq. (5.10) in the form

$$(n_0 + n_1 r + n_2 r^2)(r \pm 1) = 0. \quad (5.12)$$

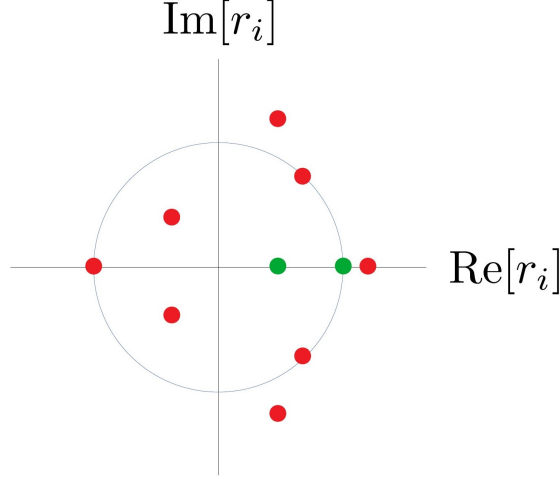


Figure 5.1.: **Modulated symmetries in 1D.** A possible distribution of roots $\{r_i\}_{i=0}^{\ell-1}$ of the characteristic equation $\sum_{i=0}^{\ell-1} n_i r^i = 0$ associated to a set of local gates $G_x^\ell = \{n_i\}_{i=0}^{\ell-1}$ of size ℓ . Red (green) dots correspond to single (double) degenerate roots and the circumference has radius equals to one.

In this case, we find the additional solution $r = \pm 1$. However, a cellular automaton (or quantum Hamiltonian) evolution including range-3 but also range-4 gates, will only host those symmetries corresponding to the common set of solutions, i. e. those for which $b + pr + qr^2 = 0$.

In general, given two gates $\{n'_{\mathbf{r}}\}, \{n''_{\mathbf{r}}\}$ with a common conserved quantity $\mathcal{Q} = \sum_j r^j s_j$, their element-wise combination, $\{n_{\mathbf{r}}\} \equiv \{n'_{\mathbf{r}} \pm n''_{\mathbf{r}}\}$, also features the same symmetry. Indeed, the resulting recurrence equation $\sum_{\mathbf{r}} (n'_{\mathbf{r}} \pm n''_{\mathbf{r}}) \alpha_{\mathbf{r}} = 0$ is satisfied if both $\sum_{\mathbf{r}} n'_{\mathbf{r}} \alpha_{\mathbf{r}}$ and $\sum_{\mathbf{r}} n''_{\mathbf{r}} \alpha_{\mathbf{r}}$ vanish. This translates into the characteristic polynomial associated to $\{n_{\mathbf{r}}\}$ being factorized as $(x - r)P(x)$, where $P(x)$ can have additional roots. Nevertheless, additional solutions might arise from a cancellation between the two terms, as it was the case of our previous example.

In general, given a system specified by a set of gates $G_x^\ell = \{n_i\}_{i=0}^{\ell-1}$ of size ℓ , we find the associated conserved quantities $\mathcal{Q}_{\{\alpha_j\}} = \sum_j \alpha_j s_j$, by solving the linear recurrence equation $\sum_{i=0}^{\ell-1} n_i \alpha_{j+i} = 0$ for every site j compatible with the boundary conditions. A general solution can be written in terms of the roots $\{r_i\}_{i=1}^{\ell-1}$ of the associated characteristic equation $\sum_{i=0}^{\ell-1} n_i r^i = 0$, as $\alpha_j = \sum_{i=0}^{\ell-1} a_i(j) (r_i)^j$ where $a_i(j)$ will be a power of the coordinate j for degenerate roots. Moreover, since the characteristic polynomial has real coefficients, every complex root r_i appears together with its complex conjugate \bar{r}_i . In particular, if r_i is not imaginary and it is degenerate, then so is its complex conjugate. Fig. 5.1 shows a possible distribution of roots $\{r_i\}$.

5.3.3. Quantum Hamiltonians and strong zero modes

Although we focused on classical cellular automata, each of our models can be easily related to a corresponding quantum Hamiltonian, by mapping a gate G_x , characterized by integers $\{n_{\mathbf{a}}\}$, to a local Hamiltonian

$$\hat{H}_{G_x} = \sum_j \left[J_j \bigotimes_a (\hat{S}_{j+a}^{\text{sgn}(n_a)})^{|n_a|} + \text{H.c.} \right] + V(\{\hat{S}_j^z\}), \quad (5.13)$$

with $\text{sgn}[\cdot] \in \{+, -\}$ the sign function, \hat{S}^\pm the spin ladder operators acting on a local Hilbert space with dimension $2S \geq \max(\{n_a\})$ and $V(\{\hat{S}_j^z\})$ is a general term diagonal

in the local z -basis. These quantum Hamiltonians possess the same set of symmetries as their classical counterparts which are generated by

$$\hat{Q}_{\{\alpha_j\}} = \sum_j \alpha_j \hat{S}_j^z \text{ s.t. } e^{i\beta \hat{Q}_{\{\alpha_j\}}} \hat{S}_i^\pm e^{-i\beta \hat{Q}_{\{\alpha_j\}}} = e^{\pm i\beta \alpha_i} \hat{S}_i^\pm. \quad (5.14)$$

These can also include additional \mathbb{Z}_2 symmetries like $R_x = \prod_j e^{i\pi \hat{S}_j^x}$ (depending on the choice of V) and $R_y = \prod_j e^{i\pi \hat{S}_j^y}$ (depending on the particular gate G_x and V). Indeed, $R_x \hat{S}^\pm R_x = \hat{S}^\mp$ and then the Hamiltonian is invariant under R_x if V is built up from even products in \hat{S}^z operators.

In particular, these conservation laws anticommute with the exponentially localized symmetries $\mathcal{Q}^{\ell,r}$ leading to a degenerate many-body spectrum and thus featuring the same phenomenology as the strong zero modes introduced by Paul Fendley [184] (leading to finite boundary autocorrelations as we find at the end of this chapter). The defining properties of a strong zero mode (SZM) $\hat{\Psi}$ were already discussed in Table 3.2 in Chapter 3. First of all, such modes are localized near an edge of the system. Moreover, SZM become exact symmetries in the limit of infinite chains, unlike $\mathcal{Q}^{\ell,r}$ which are exact for any finite system. Apart from this, the other major differences to standard SZM are: Firstly, the lack of a normalization condition similar to $\hat{\Psi}^\dagger \hat{\Psi} = 1$ for fermionic SZM (and $\hat{\Psi}^n = 1$ for some n in the case of spin systems), which ensures the SZM is well-defined within a given phase. This condition appears to be ‘‘highly non-trivial and fundamental’’ [185] to ensure a non-zero radius of convergence in the perturbative construction of such modes. However, as stated in Ref. [185] this condition could be relaxed in the definition, although it holds for all previous constructions of SZM. In fact, unlike $\hat{\Psi}$, the ‘strong zero modes’ we constructed are continuous symmetries with an extensive spectrum. Thus the fact that $\mathcal{Q}^{\ell,r}$ anticommutes with R_x only leads to a pairing among two symmetry sectors of $\mathcal{Q}^{\ell,r}$ with opposite charges. Nonetheless, the charges we constructed yield the same phenomenology of standard SZM, but for interacting non-integrable systems, unlike most of the previous literature on the topic. The price is dealing with rather less natural Hamiltonians, which however, allows for generalizations to higher dimensions as we will find in the following chapter.⁷

Analogously, we can introduce bosonic systems (or fermionic as long as we consider sufficiently large local Hilbert space dimension) with the same family of modulated symmetries, where a modulation of the local density \hat{n}_j is conserved instead of that for the total magnetization. These are given by

$$\hat{H}_{G_x} = \sum_j \left[J_j \otimes_a (\hat{b}_{j+a}^{\#(n_a)})^{|n_a|} + \text{H.c.} \right] + V(\{\hat{n}_j\}), \quad (5.15)$$

attaching a creation operator when $n_a > 0$, i.e., $\#(n_a) = \dagger$, and annihilation operator otherwise ($\#(n_a) = 1$). In this case, the conserved quantity reads $\hat{Q}_{\{\alpha_j\}} = \sum_j \alpha_j \hat{n}_j$ which generates the phase transformations $\hat{b}_j \rightarrow e^{-i\beta \alpha_j} \hat{b}_j$ and $\hat{b}_j^\dagger \rightarrow e^{i\beta \alpha_j} \hat{b}_j^\dagger$. The low-temperature behavior of such systems is related to the recently introduced Bosonic-Luttinger liquids [298], which admits a quasi-long range order phase characterized by two-coupled Luttinger liquids. The results will be published elsewhere.

5.3.4. Dipole and higher-moment conserving systems

In Section 5.2.1 we already found how to obtain the shortest range models conserving the first m moments of the charge. Here we provide an alternative recursive construction

⁷I thank Paul Fendley and Fabian Essler for very insightful discussions about strong zero modes during my visit in November 2021.

5.3. General construction and analogous quantum models

to generate longer-range terms, applicable to both gates and local Hamiltonian terms, which give us additional insights into the dynamics of such systems. Although for convenience we formulate it in terms of quantum Hamiltonians, the analogous construction directly translates into the gate formulation using the inverse of the mapping introduced in Eq. (5.13).

We start from a simple Hamiltonian of the form $\hat{H} = \hat{H}_{\ell=2}^{(0)} + \hat{H}_z$, with $\hat{H}_{\ell=2}^{(0)} = \sum_x (\hat{S}_x^+ \hat{S}_{x+1}^- + \text{H.c.})$ hosting local XY-type terms of range $\ell = 2$ that conserve the total charge $Q^{(0)} = \sum_x \hat{S}_x^z$, and \hat{H}_z containing arbitrary local terms diagonal in the \hat{S}^z -basis.⁸ The \hat{S}_x^\pm , \hat{S}_x^z are spin operators in a given representation S . Here, an elementary term $h_2^{(0)}(x) \equiv \hat{S}_x^+ \hat{S}_{x+1}^-$ can be interpreted as the creation of a dipole against some background. A new term that additionally conserves the dipole moment $Q^{(1)} = \sum_x x \hat{S}_x^z$ can then be obtained by simply multiplying this operator with its hermitian conjugate at some shifted position, e.g. $h_3^{(1)}(x) = \left(h_2^{(0)}(x)\right)^\dagger h_2^{(0)}(x+1)$, yielding $\hat{H}_3^{(1)} = \sum_x \hat{S}_x^- \left(\hat{S}_{x+1}^+\right)^2 \hat{S}_{x+2}^- + \text{H.c.}$, the model we already encountered in Chapter 2. Then, we can interpret $\left(h_2^{(0)}(x)\right)^\dagger, h_2^{(0)}(x)$ as raising/lowering operators for dipoles, in a similar manner as ladder operators for \hat{S}^z . The above recursion can be iterated to obtain models conserving arbitrary moments of the charge

$$Q^{(m)} = \sum_x x^m \hat{S}_x^z. \quad (5.16)$$

Formally, we consider a m^{th} moment conserving Hamiltonian of range ℓ in the form $\hat{H}_\ell^{(m)} = \sum_x h_\ell^{(m)}(x) + \text{h.c.}$, whose local terms can be expanded as

$$h_r^{(m)}(x) = \bigotimes_{a=0}^{\ell-1} \left(\hat{S}_{x+a}^{\text{sgn}[\sigma_m(a)]} \right)^{|\sigma_m(a)|}, \text{ with } \sigma_m(a) \in \mathbb{Z}, \quad (5.17)$$

where by definition $\sigma_m(0) \neq 0$, $\sigma_m(\ell-1) \neq 0$. For the XY-terms, $\sigma_0(0) = -\sigma_0(1) = 1$. Again, arbitrary terms diagonal in \hat{S}^z could be added to Eq. (5.17) without affecting the conservation laws. Analogous to the argument above, given $h_\ell^{(m-1)}(x)$, we can then construct a $(\ell+r)$ -range term that additionally conserves the m^{th} moment by imposing the recursive relation

$$\sigma_m(a) = -\sigma_{m-1}(a) + \sigma_{m-1}(a-r), \quad (5.18)$$

on the exponents of the spin ladder operators. Eq. (5.18) reflects the construction of $\hat{H}_{\ell+r}^{(m)}$ via shifting an elementary m -pole by r sites. These elementary m -pole configurations have vanishing lower moments and a spatially independent m^{th} moment, similar to usual charges. However, their number is not conserved.

Eq. (5.18) can be rephrased as a discrete lattice derivative of spacing r , $\sigma_m(a) = -\Delta_x [\sigma_{m-1}](a)$, which implies $\sigma_m(a) = (-\Delta_x)^m [\sigma_0](a)$. Interpreting σ_0 -terms, associated to $h_2^{(0)}(x)$, as a finite difference with spacing $\ell = 1$, $(-\Delta_x)[f](x) = \sum_a \sigma_0(x+a) f(a)$ with some lattice function $f(a)$, the exponents $\sigma_m(a)$ effectively correspond to a lattice discretization of the $(m+1)^{\text{st}}$ derivative

$$(-\Delta_x)^{m+1}[f](x) = \sum_a \sigma_m(a) f(x+a), \quad (5.19)$$

rediscovering our earlier construction in terms of recurrence relations.

Using the spin commutation relations and Eq. (5.19), we see that $[Q^{(n)}, h_r^{(m)}(x)] \propto \sum_a \sigma_m(a) (x+a)^n = (-\Delta_x)^{m+1}[x^n] = 0$ for $n \leq m$, i.e. all moments $Q^{(n \leq m)}$ are indeed

⁸In particular, this can render the model non-integrable.

conserved. The same holds for longer range Hamiltonians, using alternative discretization schemes of the involved derivatives. We note that this is a discretized version of the field theory construction in Ref.[305].

5.4. Hydrodynamics for multipole-conserving systems

In Section 1.1.3 we argued that in the presence of conserved quantities, the dynamics leading to the global equilibrium state are dominated by the transport of the corresponding densities, smoothing out inhomogeneities of the initial state [98, 101, 102]. In general, continuous symmetries provide long-lived modes that dominate the dynamics at long times. Recent works investigated how hydrodynamics applies in the presence of less conventional symmetries like multipole and subsystem symmetries [178, 289–292] (including Ref. [6] which we present in this section) providing different derivations of the hydrodynamic behavior of such systems and leading to sub-diffusive transport. Particularly relevant is the experimental work of Ref. [113] for a two-dimensional Fermi-Hubbard model tilted along one of the lattice directions. Here, an initial density wave of interacting fermions along the tilted direction with wavelength λ , was observed to exponentially decay as $\sim \exp(-k^4 t)$ in the presence of a strong tilt, and was understood in terms of a classical hydrodynamic model (see Fig. 5.2) whose predictions for the decay of charge correlations agree with dipole-moment conservation in 1D. The linear potential couples directly to the center of mass $\sum_x x \hat{n}_x$ (see also [306]) and can thus be thought of as inducing an effective dipole conservation on long length scales.

In this section, we revisit this behavior focusing on the late-time transport of dipole- and higher-moment conserving 1D systems in the absence of strong Hilbert space fragmentation by including longer-range interactions and higher spin representations. We find anomalously slow, subdiffusive transport of the underlying charges, described by a cascade of exponents depending on the highest conserved moment. We further develop a general analytic hydrodynamic approach, valid for arbitrary conserved multipole moments that is in full agreement with our numerical results using cellular automaton dynamics and consistent to our findings with the quantum Hamiltonian evolution. Finally, we discuss experimental characteristics of higher-moment conservation, consistency of the results with exact quantum Hamiltonian evolution for dipole-conserving spin chains, and the relevance of energy and momentum conservation.

5.4.1. Generalized Fick's law

To understand how this slow anomalous diffusion can emerge as a classical hydrodynamic description of the late-times quantum evolution, we consider the Heisenberg evolution equation of the charge density \hat{S}_x^z for the previously introduced models. This yields

$$\frac{d}{dt} \hat{S}_x^z = \frac{i}{\hbar} [\hat{H}_r^{(m)}, \hat{S}_x^z] = - \sum_a \sigma_m(a) \Omega_{x+a}^{(m)} \equiv (-\Delta_x)^{m+1} \Omega_x^{(m)}, \quad (5.20)$$

with the operator $\Omega_x^{(m)} = -\frac{i}{\hbar} (h_r^{(m)}(x) - \text{H.c.})$, which takes the form of a generalized ‘multipole current’ of m -poles. $\Omega_x^{(m)}$ corresponds to the one-dimensional version of the generalized rank- $(m+1)$ tensor currents appearing in fractonic systems [290, 307]). This form of the time evolution applies to arbitrary Hamiltonians conserving the m^{th} moment of the charge, with microscopic details only entering $\Omega_x^{(m)}$. Imposing a continuity equation for the charge density, $\frac{d}{dt} \hat{S}_x^z = (-\Delta_x) J_x^{(m)}$, we obtain the form of the charge current $J_x^{(m)} = (-\Delta_x)^m \Omega_x^{(m)}$. In the formulation of Ref. [290] this corresponds to $J_i = \partial_{j_1} \cdots \partial_{j_m} J_{ij_1 \cdots j_m}$

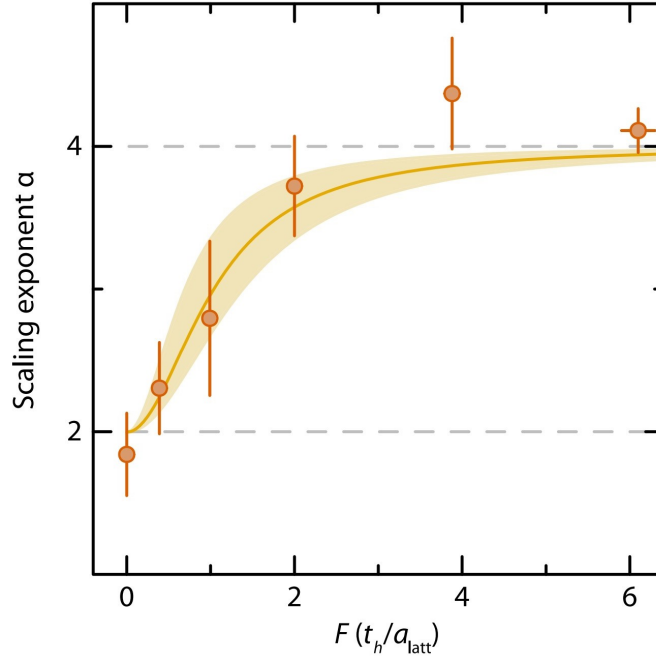


Figure 5.2.: **Experimental diffusive-to-subdiffusive crossover.** Extracted scaling exponent α for $\tau \propto \lambda^\alpha$ from the time-decay of initial density waves $n(x, t) = \bar{n} + A_0 e^{-t/\tau} \sin(\frac{2\pi}{\lambda}x + \phi(t))$ with fixed wavelength λ as a function of the tilt (orange circles). As the tilt is increased from $F a_{\text{latt}}/t_h = 0$ to $F a_{\text{latt}}/t_h = 6$, the relaxation of initial density waves crosses over from diffusive ($\alpha = 2$) to subdiffusive behavior with $\alpha = 4$. The shaded curve is a prediction from the hydrodynamic model presented in the supplementary material of Ref. [113] from where this figure has also been taken. Here t_h is the hopping energy and a_{latt} is the lattice spacing.

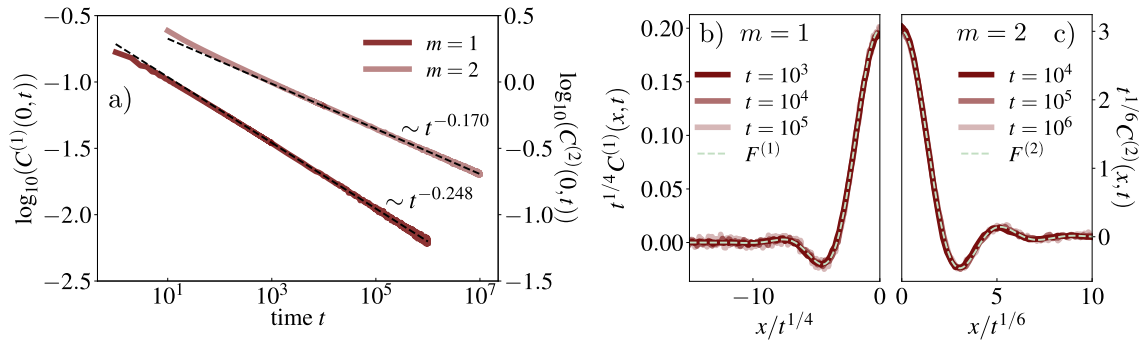


Figure 5.3.: **Hydrodynamics.** **a)** Return probability $C^{(m)}(0, t)$ for dipole- and quadrupole conservation. The long time behavior approaches an m -dependent algebraic decay $\sim t^{-1/2(m+1)}$. The numerical values of the exponents were extracted from fits over the latter three time decades (dashed lines). **b)+c)** Scaling collapse for $m = 1$ and $m = 2$ according to the long wavelength description Eq. (5.24). In addition to the numerical data, the fundamental solution of Eq. (5.24) (dashed line) is shown. The system size is $L = 10^4$ and correlations were averaged over at least 10^3 random initial states in all panels. The numerical results were obtained by Johannes Feldmeier as published in Ref. [6].

relating the conventional charge current J_i to the multipole one $J_{ij_1 \dots j_m}$, which ensures the conservation of the multipole moment [293]. Hence, it is the latter which appears to be relevant to understand the transport properties of the system [290]. This e.g., results in the familiar $J_x^{(0)} = \Omega_x^{(0)}$ in the case of only-charge conserving systems, leading to the diffusive case.

To arrive at a closed equation, we consider a sufficiently coarse grained version of the expectation value of the charge density $s(x, t)$, in the limit of long wavelengths ($\Delta_x \rightarrow \partial_x$) assuming large enough variation lengths in space, such that $\frac{\partial}{\partial t} s(x, t) = (-\partial_x)^{m+1} \langle \Omega_x^{(m)} \rangle$. To obtain a closed equation for $s(x, t)$, we follow the hydrodynamic paradigm and assume that we can relate the multipole current to the derivatives of the charge density via a gradient expansion, keeping only the lowest term allowed (see e.g. Ref. [102]). We therefore expand

$$\langle \Omega_x^{(m)} \rangle = -D (\partial_x)^{l(m)} s(x, t), \quad (5.21)$$

and our task is to find the *lowest*, meaning most relevant in the renormalization group sense as detailed in Appendix D.2, possible $l(m) \in \mathbb{N}$ such that $D \neq 0$ is consistent with the conservation of all moments $Q^{(n \leq m)}$.

For charge-conserving interacting quantum systems ($m = 0$), known to generically exhibit diffusive transport at late times in the absence of momentum conservation [99, 103–110], we should obtain Fick's law $\langle \Omega_x^{(0)} \rangle = \langle J_x^{(0)} \rangle = -D \partial_x s(x, t)$, i.e. $l(0) = 1$, resulting in the usual diffusion equation for $s(x, t)$. However, general solutions of the diffusion equation break higher-moment conservation (see Ref.[308] for an extended discussion and the role of boundary conditions). This is seen most easy for the example of a melting domain wall, which exhibits a net current of charge, violating dipole conservation.

To generalize Fick's law when higher moments of the charge are conserved, we notice that in a closed system (in the absence of sinks or sources) with open boundary conditions, the m-pole current $\langle \Omega_x^{(m)} \rangle_{e.q.} = \langle \Omega_x^{(m)} \rangle(t \rightarrow \infty) = 0$ vanishes at equilibrium, which implies that the equilibrium charge distribution is given by

$$s(x, t)_{eq.} = a_0 + a_1 x + \dots + a_{l(m)-1} x^{l(m)-1} = \sum_{k=0}^{l(m)-1} a_k x^k. \quad (5.22)$$

On the other hand, since all first m moments of the charge $Q^{(n \leq m)}$ are conserved, the equilibrium configuration is completely characterized by the first m moments of the initial configuration, which corresponds to $m + 1$ quantities. Moreover, any non-vanishing initial higher moment $Q^{(n > m+1)}$ will decay in time hence inducing a non-zero current. E.g., if only total charge is conserved, a local gradient of charge induces a current that compensates it. Hence $l(m) \geq m + 1$. All together, this implies that $l(m) = m + 1$, and the natural generalization of Fick's law is then given by $\langle \Omega_x^{(m)} \rangle = -D (\partial_x)^{m+1} s(x, t)$, namely, the dynamics balances out inhomogeneities of the m^{th} derivative of the charge density. A way to interpret this result is as follows: A uniform shift $s(x, t) \rightarrow s(x, t) + \mu_k x^k$ for any choice of μ_k 's, maps one equilibrium configuration to another that has different moments of the charge, and thus $\langle \Omega_x^{(m)} \rangle$ should remain unchanged. For example, uniformly tuning the chemical potential, does not lead to local charge gradients, then keeping the current unchanged. This in particular implies that $\langle \Omega_x^{(m)} \rangle$ needs to be at least proportional to $(\partial_x)^{m+1} s(x, t)$

Inserting this relation back into the evolution equation for the charge density, we finally arrive at the generalized hydrodynamic equation

$$\partial_t s(x, t) + D(-1)^{m+1} (\partial_x)^{2(m+1)} s(x, t) = 0, \quad (5.23)$$

valid for systems conserving all multipole moments up to and including m . In Appendix D.2 we show that this equation captures the relevant contributions at long distances and late times. Within linear response, the spin-spin correlator $C^{(m)}(x, t) = \langle s(x, t)s(0, 0) \rangle_c$ behaves as the Green's function of this equation of motion [98] and takes the scaling form

$$C^{(m)}(x, t) = \frac{1}{(Dt)^{1/2(m+1)}} F^{(m)}\left[\frac{x^{2(m+1)}}{t}\right], \quad (5.24)$$

where the position x only enters through the ratio $x^{2(m+1)}/t$, the function $F^{(m)}$ can be written in terms of generalized hypergeometric functions (see e.g., Ref. [309]) and the dynamical exponent is $2(m+1)$.

Alternative derivations of Eq. (5.23) were presented in Ref. [290] and also in Ref. [178] for the specific case of dipole conservation. The latter provided the following reasoning: The fundamental process that moves charges is the one that displaces equal amount of charge from location x to $x \pm dx$, as this conserves the dipole moment. It is the gradient in the density of these processes, call it $p(x, t)$, that will induce a local charge current $j \propto -\nabla p$. In fact, p is our coarse grained multipole current $\langle \Omega^{(1)} \rangle$. To relate it with the density of charges s , one assumes that the system evolves driven by the maximization of local entropy such that $p \propto \delta S$. Assuming now that the local entropy density only depends on $s(x, t)$ at that position, such that one can expand in orders of the local charge density; and that the global equilibrium state corresponds to a uniform density distribution $s(x, t) \approx \bar{s}$, one then finds $p(x, t) \propto -\nabla^2 s(x, t)$. All together, one finds $j \propto \nabla^3 s$, which plugging into the continuity equation for s , gives Eq. (5.23) with $m = 1$. This derivation could then be generalized to the conservation of higher moments, which requires: expanding the local entropy δS to higher orders in the density, and identify the relevant fundamental process. For example, when $m = 2$ (see construction in Section 5.3.4), this is given by the displacement of charge from $x - 2dx$ and x to $x - dx$, and from $x + dx$ to x and $x + 2dx$ ⁹.

5.4.2. Quantum model with dipole conservation

As a consistency check of the hydrodynamic theory we just derived for the evolution of the charge density, we simulate the dynamics of a specific quantum model featuring dipole conservation. We choose the smallest local Hilbert space dimension $S = 1/2$ such that we can reach as large system sizes as possible using exact diagonalization. In particular, we consider the charge and dipole-conserving Hamiltonian given by

$$\hat{H} = \hat{H}_4^{(1)} + \hat{H}_5^{(1)}, \quad (5.25)$$

with open boundary conditions, where

$$\hat{H}_4^{(1)} = - \sum_{j=1}^{N-3} [\hat{S}_j^+ \hat{S}_{j+1}^- \hat{S}_{j+2}^- \hat{S}_{j+3}^+ + \text{h.c.}], \quad (5.26)$$

and

$$\hat{H}_5^{(1)} = - \sum_{j=1}^{L-4} [\hat{S}_j^+ \hat{S}_{j+1}^- \hat{S}_{j+3}^- \hat{S}_{j+4}^+ + \text{h.c.}], \quad (5.27)$$

where N indicates the length of the chain and we fix the largest symmetry sector with $\langle \sum_x \hat{S}_x^z \rangle = \langle \sum_j j \hat{S}_j^z \rangle = 0$. Within this sector, Hamiltonian \hat{H} in Eq. 5.25 has been shown to be ergodic and only weakly fragmented [253].

⁹I thank Alan Morningstar author of Ref. [178] for explaining me in detail the reasoning and assumptions of their derivation.

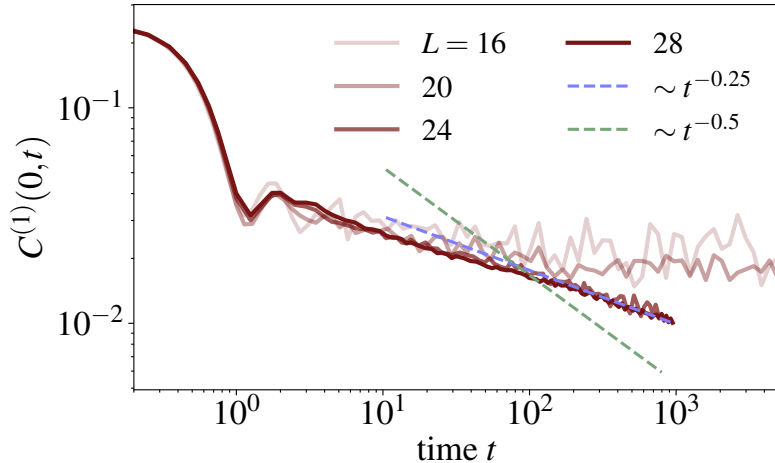


Figure 5.4.: Spin autocorrelation $C^{(1)}(t)$ in the center of the chain, defined in Eq. 5.28, for several $N \in \{16, 20, 24, 28\}$. $C^{(1)}(t)$ decays to zero algebraically $C^{(1)}(t) \sim t^{-\alpha}$, with α consistent with a subdiffusive relaxation $\alpha \approx 1/4$. The dashed-lines $\sim t^{-0.5}$ and $\sim t^{-0.25}$ are guides for the eye. The numerical results were obtained by Giuseppe De Tomasi as published in Ref. [6].

We study the evolution of the spin-spin correlator

$$C^{(1)}(t) = \langle \hat{S}_{N/2}^z(t) \hat{S}_{N/2}^z(0) \rangle_c, \quad (5.28)$$

where $\langle \cdot \rangle = \frac{1}{\mathcal{N}} \text{Tr}[\cdot]$ is the normalized infinite-temperature trace, with \mathcal{N} the dimension of the Hilbert space sector $\langle \sum_j \hat{S}_j^z \rangle = \langle \sum_j j \hat{S}_j^z \rangle = 0$. Figure 5.4 shows $C^{(1)}(t)$ for several system sizes $N \in \{16, 20, 24, 28\}$.

For small system sizes $N \in \{16, 20\}$, $C^{(1)}(t)$ has been computed using exact diagonalization, and for $N \in \{24, 28\}$ using Chebyshev polynomials¹⁰ techniques for the time evolution where the trace has been evaluated stochastically [311, 312]. As expected, after a short time propagation ($t \sim O(1)$) at which local degrees of freedom become entangled, $C^{(1)}(t)$ relaxes to zero algebraically $C^{(1)}(t) \sim t^{-\alpha}$. This relaxation, in contrast to ordinary diffusive systems, where $C^{(0)}(0, t) \sim t^{-1/2}$ [101], to the equilibrium value is subdiffusive with $\alpha < 1/2$ and it is in agreement with our hydrodynamic description, although in the presence of energy conservation. The observed decay appears to be consistent with the subdiffusive exponent $\alpha = 1/4$ for ergodic dipole conserving Hamiltonians (blue dash-line in Fig. 5.4).

However, observing the scaling collapse of the spatial correlation function and obtaining a better fit of the algebraic decay for such small system sizes is out of reach. Alternative approaches could be simulating the system using: the time evolving block decimation (TEBD) or time-dependent variational principle (TDVP) algorithms for matrix product states, which however are limited to short times [313]; or perhaps using the dissipation-assisted operator evolution (DAOE) method introduced in Ref. [314].

Nevertheless, after the completion of this work, a non-equilibrium field theory approach was pursued [315] to approximate the quantum dynamics of a specific bosonic dipole-conserving model¹¹, which confirmed subdiffusive decay of spin correlations and the scaling form of spatial correlations within the 2-particle irreducible effective action approach,

¹⁰This numerical simulations were performed by Giuseppe De Tomasi and published in Ref. [6]. The method of Chebyshev polynomials is explained in Ref. [310].

¹¹Although particle statistics are not expected to play a role in the long-time dynamics for sufficiently generic dipole-conserving system, this choice facilitates the field theory formulation.

and approximation of the full quantum dynamics. In fact, the authors of this work generalized the hydrodynamic formulation we discuss before, to include energy conservation. This results in a coupled hydrodynamic theory with crossed terms appearing in the gradient expansion of the dipole and energy currents leading to two independent modes: (i) the subdiffusive energy-charge mode we already encounter, and (ii) a diffusive energy-only mode which can be probed for initial configurations with homogeneous filling fractions and highly localized energy inhomogeneities.

5.4.3. Numerical results with cellular automaton dynamics

In this section we further, and more systematically, validate our hydrodynamic theory for an already classical system, using the block cellular automaton dynamics introduced in Section 5.1. In particular, we numerically compute the connected¹² spin-spin correlator $C^{(m)}(j, t) = \overline{s_j(t)s_0(0)}$ where site 0 is placed at the central site. Here, $\overline{(\dots)}$ denotes the average over a uniform distribution of initial configurations and (m-pole conserving) circuit realizations, thus probing the propagation of spontaneous fluctuations on top of an “infinite temperature” equilibrium state. Using this formulation, the correlation function acquires the simple expression

$$C^{(m)}(j, t) = \overline{s_j(t)s_0(0)} = \frac{1}{\mathcal{N}} \sum_{s(0)} s_0(0) \overline{s_j(t)}^{\text{r.t.}}, \quad (5.29)$$

where \mathcal{N} is the total number of allowed configurations and $\overline{s_j(t)}^{\text{r.t.}}$ denotes the average over random trajectories starting from the initial configuration $s(0)$. Notice that this is a classical (stochastic) evolution, which does not conserve the total energy.

In Fig. Fig. 5.3 (a) we observe that the late time dynamics follows an algebraic decay which we numerically estimate to be $C^{(1)}(0, t) \sim t^{-0.248} \approx t^{-1/4}$ in the dipole-conserving model, and $C^{(2)}(0, t) \sim t^{-0.170} \approx t^{-1/6}$ for the conservation of quadrupole moment. In general, Eq. 5.24 predicts $C^{(m)}(0, t) \sim t^{-1/2(m+1)}$.

Moreover, figure 5.3 (b,c) shows full agreement between analytical and numerical results of the spatial correlation function for $m = 1, 2$ upon fitting the only free parameter D , i.e., the generalized diffusion constant. In particular, as demonstrated in Fig. 5.3 (b,c), $C^{(m)}(j, t)$ accurately follows the scaling collapse predicted by Eq. (5.24). For $m = 0$, Eq. (5.23) reduces to the usual diffusion equation and $C^{(0)}(x, t)$ is a Gaussian probability distribution describing the movement of an initially localized excitation through the system [101, 316]. For $m \geq 1$, as shown in Fig. 5.3 and more generally clear from a vanishing second moment $\langle x^2 \rangle_{C^{(m)}} = \int dx x^2 C^{(m)}(x, t) = 0$ ¹³, $C^{(m)}(x, t)$ cannot be interpreted as a probability distribution. Instead, the associated oscillations in the profile of $C^{(m)}(x, t)$ form a characteristic signature of higher-moment conservation that can potentially also be observed in quench experiments of domain wall initial states, see Fig. 5.5 (b). In addition, we notice that the central peak of $C^{(m)}(x, t)$ in Fig. 5.3 (b,c) is well approximated by a Gaussian $\exp(-x^2/\sigma^2(t)) / \sqrt{\pi\sigma^2(t)}$ with $\sigma(t) = (Dt)^{1/2(m+1)}$. The additional dressing density modulations can be understood heuristically if we interpret this Gaussian distribution as describing the movement of an excitation through the system which is part of a m -pole. Conservation of $Q^{(m>0)}$ implies that a surrounding cloud of opposite charge has to be dragged along: E.g., when $m = 1$ a moving (+)-charge will have (-)-charge attached, leading to a negative contribution into the correlation.

Moreover, our derivation also predicts the expected equilibrium distribution Eq. (5.22) in closed systems, where the corresponding constants $a_k = a_k(Q^{(n \leq m)})$ are uniquely fixed

¹²Notice that $\overline{s_0(0)} = 0$ and thus the disconnected part vanishes.

¹³This can be proven by writing $\int dx x^2 C^{(m)}(x, t) = \int dk e^{-Dk^2(m+1)t} \int dx x^2 e^{-ikx}$ and using $\int dx x^2 e^{-ikx} \propto \delta''(k)$.

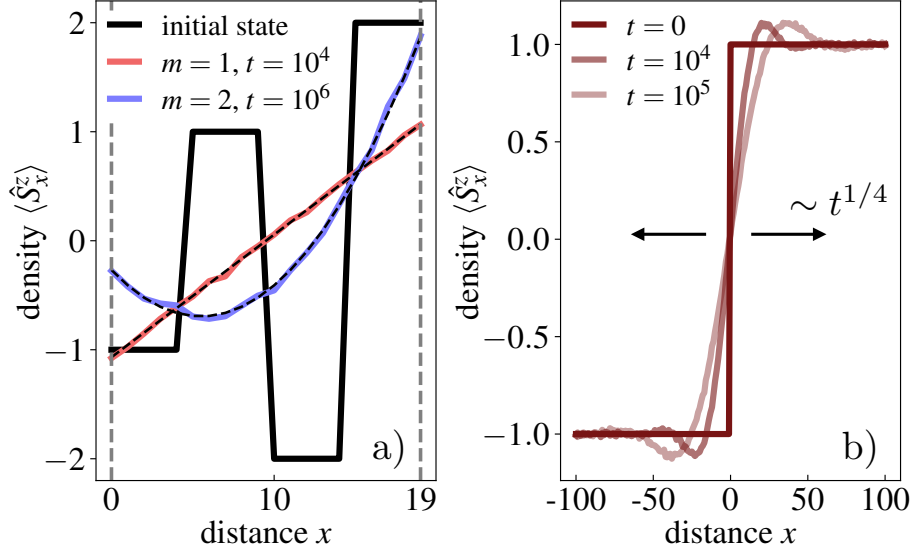


Figure 5.5.: **Implications of higher moment conservation.** **a)** In a finite size system with open boundary conditions (gray dashed lines), the charge density relaxes to an equilibrium distribution that is a polynomial of order m (here: $S = 3$). The black dashed lines are the analytical predictions from Eq. (5.22). **b)** The melting of a domain wall in a dipole conserving system for sufficiently large spin (here: $S = 2$) appears as the cumulative distribution function of $C^{(1)}(x, t)$, with characteristic charge density oscillations. The numerical results were obtained by Johannes Feldmeier as published in Ref. [6].

by the charge moments $Q^{(n \leq m)}$ of the initial state. In particular we need to require $Q^{(n)} = \sum_{k=0}^m a_k \sum_{j=1}^N j^{n+k}$ for all $n = 0, \dots, m$. On the one hand, we know that the sum $\sum_{j=1}^N j^{n+k}$ scales as $\mathcal{O}(N^{n+k+1})$, while on the other, $Q^{(n)}$ can take values that scale as $\mathcal{O}(N^{n+1})$ with system size N . Thus, the coefficients a_k should grow as $|a_k| \sim \mathcal{O}(N^{-k})$. Because of the system size scaling, the non-uniformity of the equilibrium distribution becomes only manifest in observables that involve macroscopic distances like for example $\langle \hat{S}_N^z \rangle - \langle \hat{S}_0^z \rangle \sim a_0 N + a_1 + \mathcal{O}(1/N)$. The prediction Eq. (5.22) can be verified numerically in small systems by monitoring the charge distribution resulting from a fixed initial state at very late times. Fig. 5.5 (a) shows a chosen initial charge distribution (black line) in a system of size $N = 20$, as well as the late time distributions obtained from evolving the system using both dipole- (red line) and quadrupole-conserving (blue line) automata. The resulting distributions are in very good agreement with the predicted polynomials (shown with dashed lines) of Eq. (5.22), validating our approach. Therefore we conclude that our hydrodynamic theory correctly captures the long-time dynamics of systems with charge and dipole conservation, although in the absence of energy conservation.

Before closing this section, we notice that while usually, the hydrodynamic description of a system conserving $m + 1$ quantities is given by a set of $m + 1$ coupled equations for the associated densities and currents [98, 101, 114], the present systems are described by a *single* equation Eq. (5.23) for the charge density constrained by the conservation of its higher moments. This is due to the hierarchical structure of the conservation laws Eq. (5.16) that specify all $Q^{(m)}$ in terms of the fundamental charges of the theory.

5.5. General “hydrodynamic” approach with modulated symmetries: Quasi-periodic symmetries

Not all models we have introduced conserved the total charge (and then neither of its higher-moments) and thus the spin density is not the relevant long-wavelength degree of freedom for which a hydrodynamic theory should be written. Nevertheless, these modes can still be probed via the physically relevant and accessible “infinite temperature” spin-spin correlations $C(\mathbf{r}, t) \equiv s_{\mathbf{r}}(t)s_{\mathbf{0}}(0)$ that we considered in the previous sections. This approach has the advantage of capturing the behavior of the three types of models we discussed (including dipole and higher-moment conservation) and being easily generalized to higher dimensions.

Consider the periodically modulated symmetries corresponding to conserved momentum components of the total spin. These can be identified by the vanishing of some characteristic function, $\chi(\mathbf{k}) = 0$. To understand the dynamical consequences, we will assume a description in the spirit of linear hydrodynamics, which provides a closed linear equation of motion for the relevant slow degrees of freedom. In momentum space, this can be written as

$$\partial_t \delta_{\mathbf{k}}(t) = -\omega(\mathbf{k})\delta_{\mathbf{k}}(t), \quad (5.30)$$

where $\delta_{\mathbf{k}}(t)$ is the Fourier transform of some coarse grained version of the local spin density. The key difference from more usual hydrodynamic descriptions is that we cannot simply expand the “imaginary frequency” $\omega(\mathbf{k})$ near $\mathbf{k} \approx \mathbf{0}$. Instead, we have to take into account the slow modes at finite momenta originating from the modulated symmetries.

To obtain $\omega(\mathbf{k})$, we require that: (i) $\omega(\mathbf{k}) \geq 0$ leading to physically meaningful solutions, (ii) $\omega(\mathbf{k}) = 0 \Leftrightarrow \chi(\mathbf{k}) = 0$ to exactly capture the conserved momenta modes corresponding to the relevant slow degrees of freedom, and (iii) $\omega(\mathbf{k})$ is analytic around these points. This latter condition rules out $\omega(\mathbf{k})$ being an odd power of $|\chi(\mathbf{k})|$. A natural approximation that satisfies all these requirements and should correctly capture the leading order behavior in the regimes where $\omega(\mathbf{k}) \approx 0$ is $\omega(\mathbf{k}) \sim |\chi(\mathbf{k})|^2$. Let’s emphasize that this relation only holds for momenta \mathbf{k} close to the conserved modes at which $\chi(\mathbf{k}) = 0$. In principle, $\omega(\mathbf{k})$ could have an imaginary part. However, for the systems we consider this possibility is ruled out by inversion symmetry: Consider Eq. (5.30). Under spatial inversion $\delta_{\mathbf{k}} \rightarrow \delta_{-\mathbf{k}}$, mapping Eq. (5.30) to $\partial_t \delta_{-\mathbf{k}}(t) = -\omega(\mathbf{k})\delta_{-\mathbf{k}}(t)$, which is equivalent to $\partial_t \delta_{\mathbf{k}}(t) = -\omega(-\mathbf{k})\delta_{\mathbf{k}}(t)$. Hence $\omega(\mathbf{k}) = \omega(-\mathbf{k})$. Moreover, since $s_{\mathbf{r}}$ is real, it implies that $\delta_{-\mathbf{k}} = \delta_{\mathbf{k}}^*$. Hence, taking the conjugate of Eq. (5.30), and comparing with the equation for $\delta_{-\mathbf{k}}$ leads to $\omega(\mathbf{k})^* = \omega(-\mathbf{k})$. From here, we deduce that $\omega(\mathbf{k})$ is real ($\omega(\mathbf{k})^* = \omega(\mathbf{k})$) and even function of \mathbf{k} . Nevertheless, it would be interesting to understand if such terms can appear in other scenarios. One can check that the approximation $\omega(\mathbf{k}) \sim |\chi(\mathbf{k})|^2$ correctly captures the known behavior in a variety of models, including those with dipole conservation and subsystem symmetries (see Appendix E.2 for a general discussion).

As we saw before, within linear response, the spin-spin correlator behaves as the Green’s function of this equation of motion [98], $C(\mathbf{r}, t) = \int d^d k e^{i\mathbf{k}\cdot\mathbf{r} - \omega(\mathbf{k})t}$. When evaluating at $\mathbf{r} = \mathbf{0}$, we can rewrite this as

$$C(\mathbf{r} = \mathbf{0}, t) = \int_0^\infty d\omega \rho(\omega) e^{-\omega t}. \quad (5.31)$$

The long-time decay ($t \rightarrow \infty$) is therefore determined by the density of states (DOS), $\rho(\omega)$, near $\omega \approx 0$ [317].

Consider $G^{(p,q)}$ with $2q > p$. To evaluate the DOS we calculate $N(\omega)$, the number of states in the frequency range $[0, \omega]$ (i. e., $N(\omega)$ is the area of the region in the Brillouin zone (BZ) delineated by the condition $\omega(\mathbf{k}) \leq \omega$) and then take a derivative, $\rho(\omega) = \frac{dN(\omega)}{d\omega}$. For example, if only charge is conserved $\omega(k) = k^2$ and the DOS scales as $\rho(\omega) \sim \omega^{-1/2}$ leading

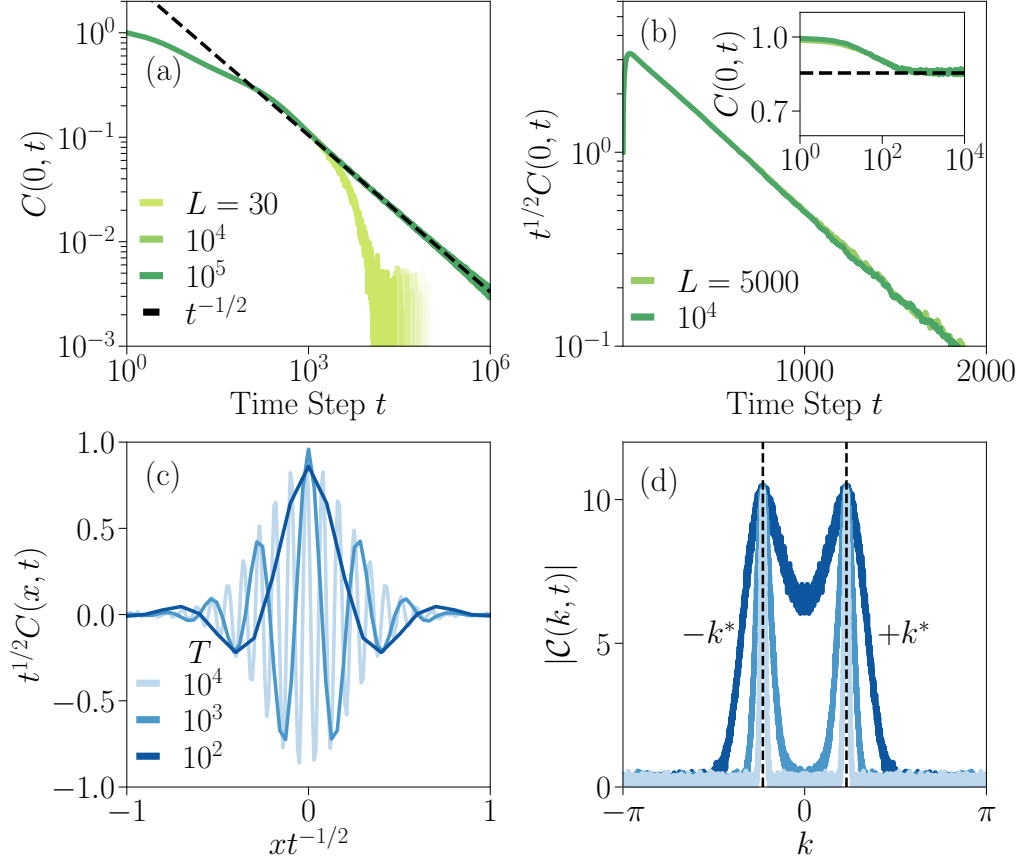


Figure 5.6.: **Dynamics in 1D.** Evolution of the spin-spin correlator $C(x, t)$ for the 1D models in Eq. (5.1). (a) $C(0, t)$ for quasi-periodic symmetries with $S = 5$ and $(p, q) = (3, 2)$. (b) exponentially-localized symmetries with $S = 10$ and $(p, q) = (3, 1)$. The inset shows the boundary correlation which is lower bounded by Mazur’s bound (black dashed line). (c-d) Spatial correlations for the model in panel (a): “Dressed” scaling collapse of $C(x, t)$ (c) and its spatial Fourier transform $\mathcal{C}(k, t)$, which becomes increasingly peaked at $k = \pm k^*$ (d). These numerical results were obtained together with Julius Lehman as published in Ref. [5].

to diffusive behavior. In the case of quasi-periodic symmetries, we have $\omega(k^* + \delta k) \sim \delta k^2$ near the conserved momentum k^* , and then $N(\omega) = \int_{k_{\min}}^{k_{\max}} dk = \int_{-\sqrt{\omega}}^{\sqrt{\omega}} d\delta k = 2\sqrt{\omega}$. This gives rise to a DOS $\rho(\omega) \sim \omega^{-1/2}$ which yields a diffusive scaling, $C(0, t) \sim t^{-1/2}$ upon inserting in into Eq. (5.31). This is consistent with our numerical results for $(p, q) = (3, 2)$ shown in Fig. 5.6a, and for longer-range gate. Fig. 5.7 shows numerical data for a stochastic evolution combining layers of range-3 gates with layers of range-4 ones and $(p, q) = (3, 2)$. In both simulations, we chose S sufficiently large such that the system is not strongly fragmented (see discussion at the end of the chapter).

Nevertheless, since this choice of $p/(2q)$ is incommensurate for any system size, this is not an exact symmetry for PBC, and then $C(0, t)$ is expected to decay exponentially at sufficiently late times that scale with system size (see data for $L = 30$ in Fig. 5.6a). The situation changes for dipole-conservation ($2q = p$). In this case, $k^* = 0$, so the leading contribution vanishes and we instead have $\omega(k) \sim k^4$, recovering the known sub-diffusive scaling $C(0, t) \sim t^{-1/4}$ that we found in the previous section [6, 113, 178, 289, 290].

The role of finite-momenta modes becomes much more apparent when we consider the

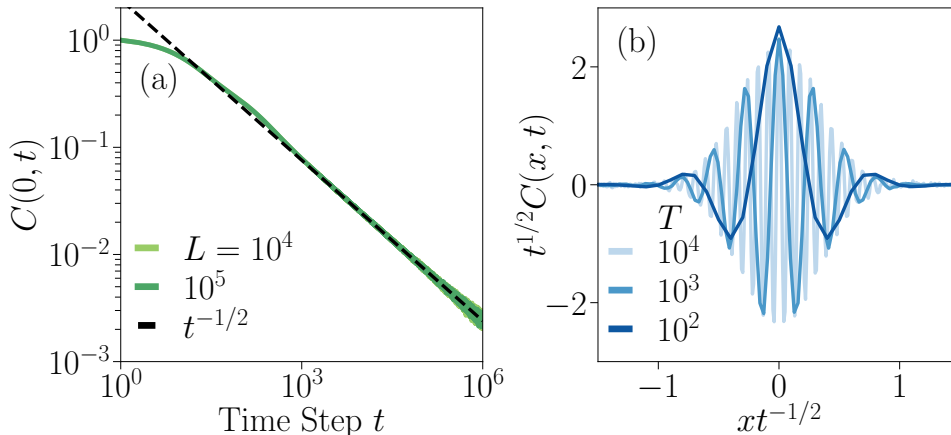


Figure 5.7.: **Longer-range gates.** Evolution of the spin-spin correlator $C(x, t)$ for $S = 10$ combining size-3 and size-4 gates with $(p, q) = (3, 2)$. (a) Evolution of the auto-correlation function $C(0, t)$. (b) Spatial correlations. These numerical results were obtained together with Julius Lehmann as published in Ref. [5].

spatial structure of the correlations. Taking into account the slow modes around $k \approx \pm k^*$, we obtain

$$C(x, t) \approx \Re \left[\int_{-\infty}^{\infty} dk e^{ikx} e^{-Dt(k-k^*)^2} \right] \sim \cos(k^*x) \frac{1}{t^{1/2}} \mathcal{N} \left(\frac{x^2}{t} \right), \quad (5.32)$$

where D is some phenomenological diffusion constant, and \mathcal{N} denotes a Gaussian function, i.e., diffusive behavior modulated by a factor that oscillates at the microscopic scale $1/k^*$. This behavior is numerically verified in Fig. 5.6(c,d). Additional details on the numerical implementation can be found in Appendix D. The influence of finite (lattice-scale) momentum components in the BZ on long-time / large-distance correlations can be seen as an infinite temperature manifestation of UV/IR-mixing in these models [299–301]. The reason for its appearance is precisely the fact that we are not considering the relevant long-wave length degrees of freedom but rather the microscopic (ultraviolet) ones. A more standard approach would require expanding $s(x) \sim e^{ik^*x} \delta_{k^*}(x) + e^{-ik^*x} \delta_{-k^*}(x)$ and construct a hydrodynamic theory for $\delta_{\pm k^*}(x)$. Nevertheless, at the moment it is not clear how to generalize this construction to higher dimensions and thus we focus on the behavior of the infinite-temperature correlations $C(x, t)$.

5.6. Exponentially-localized symmetries and Mazur's bound

We can also apply our approximation to models with exponentially localized symmetries. In this case, $\omega(k) \sim |\chi(k)|^2$ is finite everywhere, which indicates an exponential decay of correlations. Nevertheless, there can be a correction coming from the large density of states near the minimum of $\omega(k)$. To see this, consider again the model Eq. (5.1), but this time with $2q < p$. The dispersion has a minimum at $k = 0$ and expanding around it we find $\omega(k) \approx (\frac{1}{2}k^2 - k_0^2)^2$, with $k_0^2 \equiv \frac{2q-p}{2q} < 0$. Integrating over k we find the long-time asymptotic form $C(0, t) \sim e^{-k_0^2 t} / \sqrt{t}$. The numerical results for $(p, q) = (3, 1)$ with $S = 10$ shown in Fig. 5.6b for $t^{1/2}C(0, t)$ are consistent with this scaling for bulk correlations. Once again, we chose S sufficiently large to speed up the dynamics and avoid strong fragmentation of the configuration space. However, the exponentially localized symmetries have a strong effect on the dynamics near the boundary, leading to infinitely long-lived correlations. This can be proven using Mazur's inequality [116] introduced in Chapter 1 whose value is shown with a dashed line in the inset of Fig. 5.6b.

We recall from Chapter 1 that the main requirement to use this bound for the time-average of a correlation function is proving that such value is non-negative. These include thermal averages for both quantum and classical systems and also, the time-average expectation value of the spin-spin correlator $\langle s_{\mathbf{r}}(t)s_{\mathbf{r}}(0) \rangle$ governed by the cellular automaton dynamics introduced in this chapter (see proof in Appendix D).

In particular, this means that we can apply Mazur bound to boundary correlators in the presence of exponentially-localized symmetries. Without loss of generality, we focus on the left boundary $\langle s_{\ell}(t)s_{\ell}(0) \rangle$, since the exact same result applies to the right one via spatial inversion around the center of the chain:

$$C_{\ell} \equiv \lim_{T \rightarrow \infty} \frac{1}{T} \int_0^T dt \langle s_{\ell}(t)s_{\ell}(0) \rangle \geq \sum_{\alpha, \beta} \langle s_{\ell}, Q_{\alpha} \rangle (K^{-1})_{\alpha, \beta} \langle Q_{\beta}, s_{\ell} \rangle \equiv M_{\ell},$$

where $\langle \cdot \rangle$ on the right hand side of the inequality corresponds to the uniform distribution over configuration space, which can be understood as an 'infinite temperature' ensemble. In particular, from the equation $\langle s_i s_j \rangle = \frac{S(S+1)}{3} \delta_{i,j}$ one can compute the remainder averages. Recall that the bound M_{ℓ} simplifies whenever the set of conserved quantities $\{Q_{\alpha}\}$ are orthogonal with respect to $\langle \cdot, \cdot \rangle$ such that $K_{\alpha, \beta} \propto \delta_{\alpha, \beta}$. In our case there exists (at least) two such conserved quantities Q_{ℓ}, Q_r localized at the left and right boundaries respectively. Although we can get exact formulas for a finite system of size N using Eq. (5.4), we are interested in the limit of long chains $N \rightarrow \infty$, where the conserved quantities take the asymptotic form

$$Q_{\ell} \approx \sum_{j=0}^{N-1} r^{-j} s_j, \quad \text{and} \quad Q_r \approx \sum_{j=0}^{N-1} r^{j-(N-1)} s_j,$$

with $r > 1$ the largest root. This simplifies the expression for M_{ℓ} since in the limit $N \rightarrow \infty$ Q_{ℓ}, Q_r become orthogonal, $\langle Q_{\ell}, Q_r \rangle \rightarrow N/r^N$. Together with $\langle Q_{\ell}, Q_{\ell} \rangle, \langle Q_r, Q_r \rangle \approx \langle (s_x)^2 \rangle \frac{r^2}{r^2-1}$, the Mazur bound becomes

$$M_{\ell} \approx \frac{\langle s_{\ell}, Q_{\ell} \rangle^2}{\langle Q_{\ell}, Q_{\ell} \rangle} + \frac{\langle s_{\ell}, Q_r \rangle^2}{\langle Q_r, Q_r \rangle} = \langle (s_x)^2 \rangle \frac{r^2 - 1}{r^2} \left[(\alpha_0^{\ell})^2 + (\alpha_0^r)^2 \right] = \langle (s_x)^2 \rangle \left(1 - \frac{1}{r^2} \right),$$

with $\langle (s_x)^2 \rangle = S(S+1)/3$ for a given local spin S , and the same value for the boundary correlations on the right edge. This implies that the presence of exponentially localized symmetries, leads to infinitely long-lived correlations at the boundaries of a 1D system. In particular, for the model studied in Fig. 5.6b $q = 2, p = 3$, whose largest root is $r = (3 + \sqrt{5})/2$ leading to $M_{\ell, r} / \langle (s_x)^2 \rangle \approx 0.85$.

5.7. Discussion and outlook

We have uncovered new families of spatially modulated symmetries in one spatial dimension with quasi-periodic and exponentially localized charges as well as re-discovered dipole and higher-moment conservation from a different perspective. While the parametrization introduced in Section 5.2 splits these symmetries apart, they can be simultaneously present in the same local model. The derivation in terms of recurrence relations also provides a reverse-engineering approach where one can obtain the (classical or quantum) model associated to a given spatial modulation, defined as the (potentially degenerate) root of a characteristic polynomial with associated recurrence relation. Then the integer coefficients of this recurrence translate into powers of ladder operators located at the site dictated by the recurrence.

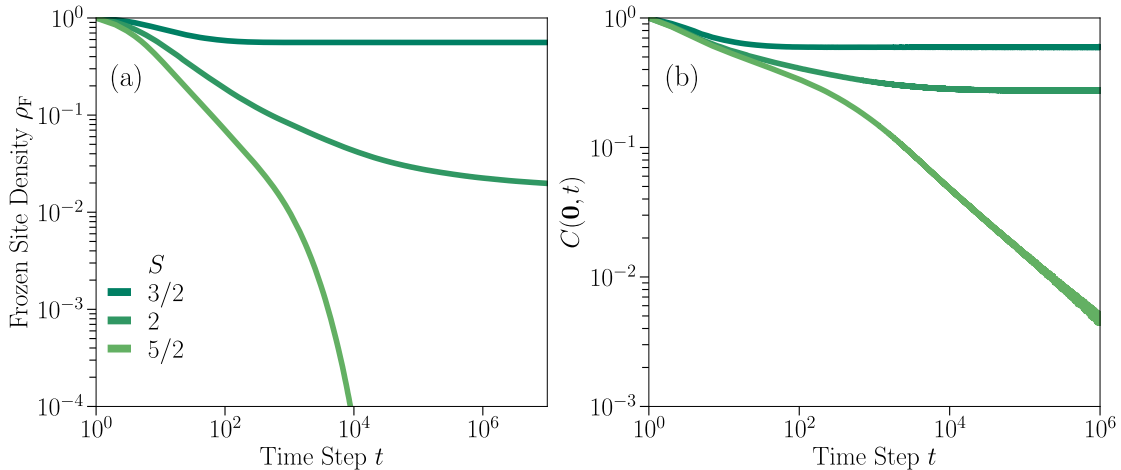


Figure 5.8.: **Fragmentation of 1D models.** Cellular automaton evolution of the frozen site density ρ_F (panel a) and the autocorrelation function $C(0, t)$ for the 1D models introduced in Eq. 5.5 with $(p, q) = (3, 2)$ with periodic boundary conditions. The system size in both plots is $N = 99999$. The quantity ρ_F was introduced in Ref. [318] and quantifies the number of frozen sites in a typical evolution, i.e., sites that remain unchanged for all times $\leq t$. A non-zero stationary value of ρ_F is expected to signal strong fragmentation and coincides with non-vanishing correlations. These numerical results were obtained by Julius Lehmann and have not been published.

Once these symmetries were presented, we focused on their effect on the long-time behavior of spin correlations, assuming no strong fragmentation of the configuration (or Hilbert) space which could turn our hydrodynamic theory not valid. While it has been studied in detailed when strong fragmentation can occur for dipole-conserving systems (see Chapter 2 and Chapter 3), no such analysis has been performed neither for higher-moment conserving systems nor for systems with quasi-periodic and exponentially-localized symmetries. In particular, the analysis for the latter could be eased by considering periodic boundary conditions were neither the exponentially localized nor most quasi-periodic quantities are exactly conserved. For example, Fig. 5.8 shows not yet published results for the long-time behavior of the frozen site density ρ_F (defined in the caption) and the auto-correlation function $C(0, t)$ for $(p, q) = (3, 2)$, corresponding to an incommensurate modulation, for periodic boundary conditions. The numerical results show non-vanishing values of ρ_F and $C(0, t)$ at the longest times for the smallest compatible $S = 3/2$, which appears to hold also for $S = 2$, although additional analysis is required. This signals non-ergodic behavior for sufficiently small spin representations S that can be associated to strong fragmentation of the configuration space even in the absence of exact symmetries.

Analogous to 1D systems with dipole conservation, quasi-periodic symmetries can be approximately realized in the strong detuning limit of experimental realizations of the interacting Aubry-André model [37, 319], which will also include particle number conservation. An alternative is to consider the Ising chain in the presence of a modulated transverse field and a uniform longitudinal one. This derivation will be published in a future work.

For dipole and higher-moment conservation we have provided a more detailed construction of the hydrodynamic theory and validate its consistency with the quantum Hamiltonian dynamics. In addition to the subdiffusive decay of autocorrelations, we have identified oscillations in the spatial density profile both for delta and domain wall initial conditions as characteristic properties of higher-moment conservation, which could be in principle

detectable in quantum quench experiments. As in Ref. [113], this scenario could be experimentally realized in the strong tilt regime of either a 2d system tilted along one of the coordinate directions and preparing a domain-wall like initial configuration, or a 1D chain. Nevertheless, this still requires a thorough analysis which considers experimental details and limitations as well as the fact that dipole moment is not exactly conserved. In fact, as we already found in the previous chapter, the behavior of tilted systems in experimentally observable time-scales appear to strongly depend on the dimensionality of the system as well as on the configuration of the initial state, leading to both non-ergodic behavior at observable times even for low values of the tilt [3, 273] as well as thermalizing dynamics [113]. In this context, understanding how the microscopically conserved dipole moment [235], granting a meaningful description in terms of dipole-conserving processes and thus fragmentation, becomes only relevant at long wavelengths, which still leads to a subdiffusive hydrodynamic mode, is an open interesting question. Moreover, the hydrodynamics of dipole-conserving systems in the presence of momentum conservation has been investigated in Ref. [293]. It has been found that linear hydrodynamics (that we discussed in this chapter) becomes unstable, leading to an anomalous scaling with dynamical exponent $z \approx 2.5$.

6. Modulated symmetries in 2D

So far we studied the consequences for the dynamics to conserve certain unconventional quantities in one-dimensional lattice systems. We found three different behaviors of the spin-spin correlations depending on the type of spatial modulation: (i) Polynomial, which corresponds to higher-moment conservation leading to subdiffusion; (ii) quasi-periodic modulation, which we found to behave diffusively although with additional oscillations at the scale of the lattice scaling associated to the conservation of finite modes of the spin; and (iii) exponentially localized charges which while have no effect on the bulk, lead to finite boundary correlations for open boundary conditions.

Higher dimensions open the door to completely new families of conserved quantities lying between global, i.e., including an extensive number of sites (on the lattice) and local symmetries, which only act on a local region. These for example correspond to the conservation of magnetization along a line or a plane on a 3D lattice, or even to discrete symmetry transformations supported on a fractal structures, as it is the case for the Neumann-Moore's [320] and Haah's models [53] as well as for related constructions [321]. In fact, previous works have already studied the dynamics of higher-dimensional systems conserving *all* multipole-moment components of a certain order [290], and systems hosting U(1) subsystem symmetries [290–292], including a careful analysis of fragmented structure in the presence of those [322].

The goal of this chapter is to understand these results from the recurrence relation approach and identify new spatially modulated symmetries. As in the previous chapter, we use the formulation in terms of classical block cellular automaton dynamics specified by a set of local gates $G_{\mathbf{r}}$ acting on the neighborhood of a given site \mathbf{r} . Firstly in Section 6.1, we consider a specific 2D lattice model for which we are able to construct an extensive number of conserved quantities which are localized at the boundary of the system. Using Mazur's bound, we numerically show that these lead to finite boundary correlations, which in turn provides a route to construct strong zero modes in higher-dimensional systems. This is part of an ongoing project whose results be published in the future.

We will then consider systems with quasi-periodic conserved quantities in Section 6.2. Here a subextensive, and thus infinite in the thermodynamic limit, number of conserved modes can appear taking the form of lines and surfaces of conserved momenta. These give rise to exotic forms of sub-diffusive behavior with a rich spatial structure influenced by lattice-scale features. They include systems with charge and higher-moment conservation as well as subsystem symmetries, but are not restricted to them.

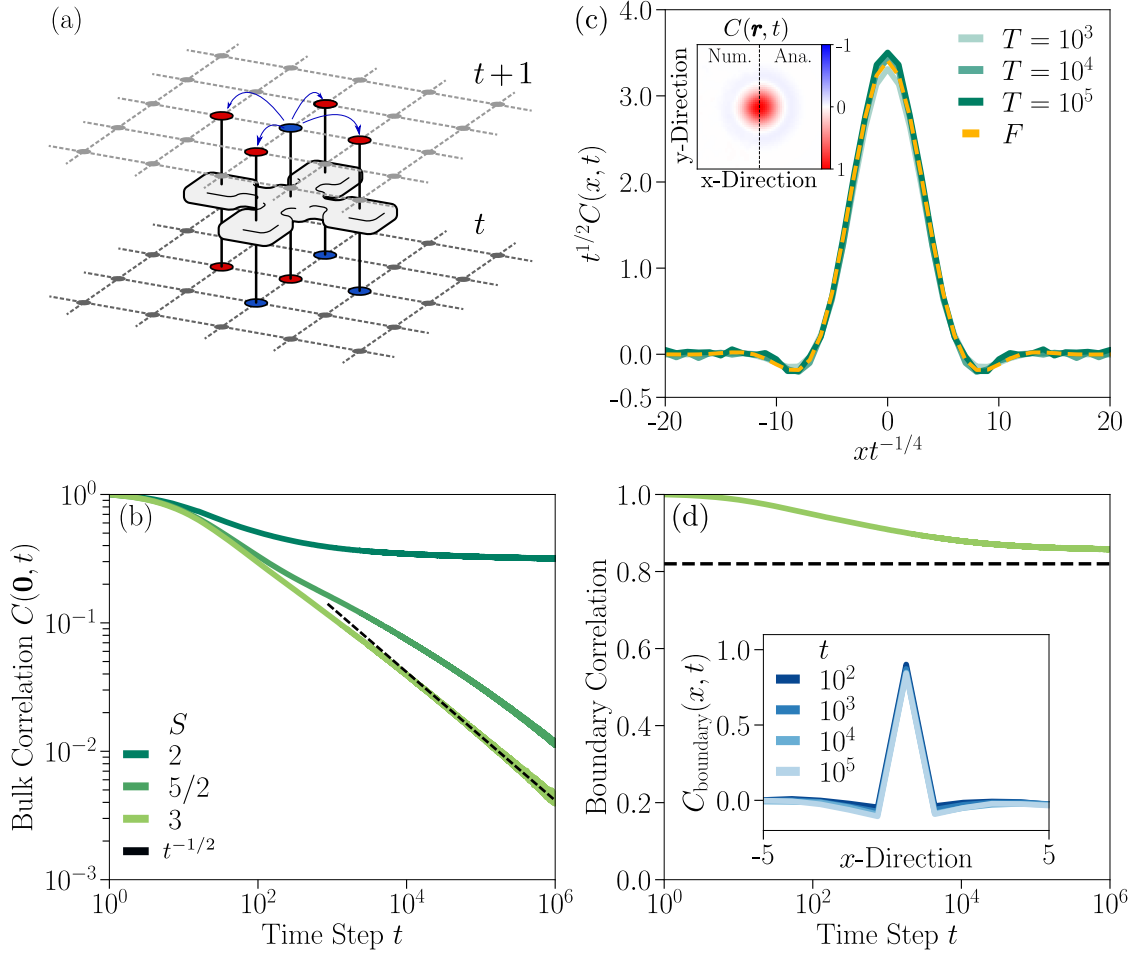


Figure 6.1.: **Discrete Laplacian model.** (a) Schematics of a local gate corresponding to Eq. (6.1). (b) Evolution of the spin autocorrelation $C(\mathbf{0}, t)$ in the bulk shown for $N = 249$ and $S = 2, 5/2, 3$. The plot also includes a guide-for-the-eye line with $t^{-1/2}$. $C(\mathbf{0}, t)$ decays for $S > 2$ but it saturates to a finite value for $S = 2$. **Inset:** Spatial correlation $C(x; t = 2000)$ for $S = 3$ and linear system size $L = 200$ (left half Num.) in comparison to the analytic solution in Eq. (6.3) (right half Ana.). Both plots are normalized to the interval $[0, 1]$. (c) Scaling collapse of the spatial profile along the x -axis using the scaling form Eq.(6.3) (shown in dashed-yellow) for $S = 3$ and $N = 300$. The prediction closely matches the numerical data. (d) Boundary correlations for $S = 3$ and $N = 300$. Numerical simulations are converged in system size at the longest time. The black dashed line shows Mazur's bound numerically evaluated using Eq. (6.26). **Inset:** Spatial profile of the boundary correlations with respect to the central boundary site. These numerical results were obtained by Julius Lehmann and are yet not published.

6.1. The discrete Laplacian model

We start by considering a microscopic model with local gates $G_{x,y}$ acting on a 3×3 block of a 2D square lattice centered around a site with coordinates (x, y) . The gate is again specified by a set of integers and illustrated in Fig. 6.1, such that $G_{x,y} : s_{x+i,y+j} \rightarrow s_{x+i,y+j} \pm n_{i,j}$, with

$$G_{x,y}^{\boxplus} = \{n_{0,0}, n_{0,1}, n_{0,-1}, n_{1,0}, n_{-1,0}\} = \{+4, -1, -1, -1, -1\} \quad (6.1)$$

for $S \geq 2$. This gate symmetrically distributes charges among the four neighboring sites linked with a central site of coordinates (x, y) . This model can be pictured as two copies of the one-dimensional dipole-conserving gates $G_{2,1}$ Eq. (5.1) acting along orthogonal directions. It has several global U(1) symmetries: It conserves both the total charge $\mathcal{Q}^{(0)} = \sum_{\mathbf{r}} s_{\mathbf{r}}$ and its dipole moments $\mathcal{Q}_x^{(1)} = \sum_{\mathbf{r}} x s_{\mathbf{r}}$, $\mathcal{Q}_y^{(1)} = \sum_{\mathbf{r}} y s_{\mathbf{r}}$, as well as some quadratic moments $\mathcal{Q}_{xy}^{(2)} = \sum_{\mathbf{r}} x y s_{\mathbf{r}}$, $\mathcal{Q}_{x^2-y^2}^{(2)} = \sum_{\mathbf{r}} (x^2 - y^2) s_{\mathbf{r}}$, but not $\mathcal{Q}_{x^2+y^2}^{(2)} = \sum_{\mathbf{r}} (x^2 + y^2) s_{\mathbf{r}}$.

For $S = 2$, one can show that the spin correlations $C(\mathbf{r}, t)$ saturate to a finite value in the thermodynamic limit due to strong fragmentation. This is numerically shown in Fig. 6.1(b) where the spin autocorrelation appears to saturate even at times $t = 10^6$ with no observable shift for with system size. The analytical proof of this fact will be published in a future work. However, for $S > 2$ correlations decay algebraically as governed by the slow-modes associated to the previous U(1) charges. In particular, the charge $s(\mathbf{r}, t)$ is transported across the system following the generalized diffusion equation derived in Ref. [290]

$$\partial_t s(\mathbf{r}, t) + D (\partial_x^2 + \partial_y^2)^2 s(\mathbf{r}, t) = 0, \quad (6.2)$$

with D a generalized diffusion constant. Even though some quadratic moments are conserved, Eq. (6.2) only involves fourth-order spatial derivatives in $s(\mathbf{r}, t)$, instead of the naively expected sixth order ones for the maximal quadratic algebra [66] which includes $\mathcal{Q}_{x^2+y^2}$. From Eq. (6.2) we find that $C(\mathbf{r}, t)$ takes the scaling form

$$C(\mathbf{r}, t) = \frac{1}{(Dt)^{\frac{1}{2}}} F\left(\frac{r^4}{Dt}\right), \quad (6.3)$$

with F a function only of the ratio r^4/t where $r = \sqrt{x^2 + y^2}$. Thus, we expect a rotationally symmetric distribution of $C(\mathbf{r}, t)$ as well as a power law decay of bulk autocorrelations $C(\mathbf{0}, t) \sim t^{-1/2}$ at long times.

Fig. 6.1(b) includes numerical results for $C(\mathbf{r}, t)$ with $S > 2$ and system size $L = 249$. Data is converged in system size at the longest times shown in the plot. After an initial non-universal transient regime, which becomes shorter for increasing S , the autocorrelation function approaches $C(\mathbf{0}, t) \propto t^{-1/2}$ for every $S > 2$, with microscopic details only entering the diffusion constant D . Moreover, in Fig. 6.1c we study the spatial correlations $C(\mathbf{r}, t)$. We verify the scaling behavior of Eq. (6.3) by performing a scaling collapse of $C(\mathbf{r}, t)$, displaying good quantitative agreement with the analytical prediction. This displays the characteristic oscillating spatial charge modulation in the presence of higher-moment conservation, which is analogous to the 1D dipole-conserving systems we encounter in the previous chapter. This is also clearly shown in the inset, which compares numerical and analytical results for the spatial distribution after 2000 times steps, $C(\mathbf{r}, t = 2000)$, obtained for $S = 3$ and system size $L = 200$. This explicitly shows the rotational symmetry of $C(\mathbf{r}, t)$.

Therefore, the global conserved quantities we identified are sufficient to predict the late-time dynamics of the bulk correlator $C(\mathbf{r}, t)$ in the absence of strong fragmentation. Does it then mean that we can rule out the existence of other spatially-modulated symmetries? As we find out there exist sub-extensively many other modulated symmetries whose total number scales with the linear system size N . While they did not play a role in the bulk, they can lead to infinite long-lived correlations at the boundary.

6.1.1. Solving the recurrence relation

To detect additional modulated conserved quantities $\mathcal{Q}_{\{\alpha_{\mathbf{r}}\}} = \sum_{\mathbf{r}} \alpha_{\mathbf{r}} s_{\mathbf{r}}$, we look for non-trivial solutions of the associated two-dimensional recurrence relation

$$\sum_{i,j} n_{i,j} \alpha_{x+i,y+j} = 0, \quad (6.4)$$

satisfied at every lattice site with coordinates (x, y) . In particular, for the model with gates $G_{x,y}^{\boxplus}$ in Eq. (6.1) on a square lattice $\mathcal{L} = B \cup D$ of size $(N+2) \times (N+2)$, we want to solve the following recurrence relation for points in the bulk $D = \{(i, j) \in \{1, \dots, N\}^2\}$

$$4\alpha_{i,j} - \alpha_{i+1,j} - \alpha_{i-1,j} - \alpha_{i,j+1} - \alpha_{i,j-1} = 0, \quad (6.5)$$

given a set of boundary values $\alpha_{i,j}^B$, i.e. the $4N$ values $\alpha_{0,j}, \alpha_{N+1,j}, \alpha_{i,0}, \alpha_{i,N+1}$ with $i, j = 1, \dots, N$. Notice that degrees of freedom at the corner sites $(0, 0), (N+1, N+1), (0, N+1), (N+1, 0)$ are not acted upon by any gate $G_{x,y}^{\boxplus}$, and hence are decoupled from the rest of the system. This precisely corresponds to a solution of the following discrete problem with Dirichlet boundary conditions

$$\begin{cases} \alpha_{i,j} = \frac{1}{4} (\alpha_{i+1,j} + \alpha_{i-1,j} + \alpha_{i,j+1} + \alpha_{i,j-1}) & \text{for } (i, j) \in D, \\ \alpha_{i,j} = \alpha_{i,j}^B & \text{for } (i, j) \in B, \end{cases} \quad (6.6)$$

where the value at site (i, j) is given by the average value of the (four) neighboring sites. A function satisfying this property is called *discrete harmonic*, and in fact our equation is a discrete version of the Laplace equation with Dirichlet boundary conditions. Hence the name for the model. This property leads to two important corollaries that become useful to address the problem analytically [323]:

1. A (discrete) harmonic function defined on \mathcal{L} reaches its maximum M and minimum m values at the boundary B . In particular, if $\alpha_{i,j}^B \in \{0, 1\}$ then $\alpha_{i,j}$ is bounded and non-negative $0 \leq \alpha_{i,j} \leq 1$ for all points in the bulk.
2. Using the previous result, it follows that the solution is *unique*: given two (discrete) harmonic functions f, g on \mathcal{L} such that $f = g$ on B , then $f(x) = g(x)$ for all $x \in \mathcal{L}$.

The second property is particularly useful as it ensures that for any choice of boundary conditions a solution $\alpha_{i,j}$ exists and is unique, which translates into a conserved quantity whose spatial modulation is specified by $\alpha_{i,j}$. This apparently innocent result allows us to construct sub-extensively many (scaling with the linear system size N) conserved quantities for any finite lattice, and study the localization properties of such quantities in the thermodynamic limit. Otherwise either none or infinitely many solutions can exist, making difficult to even numerically find solutions to the problem.

Analogously to the continuum case, we can solve Eq. (6.6) via separation of variables, i.e., $\alpha_{i,j} = F(i)G(j)$. Let us explicitly follow the main procedure which will teach us something about the structure of the solutions. Using this ansatz the recurrence relation becomes

$$4F(i)G(j) = (F(i+1) + F(i-1))G(j) + F(i)(G(j+1) + G(j-1)). \quad (6.7)$$

After dividing by $F(i)G(j)$ (assuming $\alpha_{i,j}$ does not vanish in the bulk) we find

$$4 = \frac{F(i+1) + F(i-1)}{F(i)} + \frac{G(j+1) + G(j-1)}{G(j)}. \quad (6.8)$$

This implies that each term on the right hand side is a constant function of its argument and hence, they satisfy the one-dimensional recurrence relations

$$\begin{cases} F(i+1) - 2F(i) + F(i-1) = \lambda F(i), \\ G(j+1) - 2G(j) + G(j-1) = -\lambda G(j), \end{cases} \quad (6.9)$$

along the horizontal and vertical lattice directions respectively, for certain values of $\lambda \in \mathbb{R}$ which are fixed by the boundary conditions. To proceed we notice that being Eq. (6.5) linear, the Dirichlet problem can be solved adding up the solutions of four different Dirichlet problems with vanishing boundaries conditions except at a given boundary. This means that a general solution can be written as

$$\alpha_{i,j} = \alpha_{i,j}^1 + \alpha_{i,j}^2 + \alpha_{i,j}^3 + \alpha_{i,j}^4, \quad (6.10)$$

with the different contributions solving the boundary problems

$$\begin{cases} \#1 : G(0) = G(N+1) = 0 \text{ and } F(0) = 0, \text{ with } \alpha_{N+1,j}^1 = f_2(j) \\ \#2 : G(0) = G(N+1) = 0 \text{ and } F(N+1) = 0, \text{ with } \alpha_{0,j}^2 = f_1(j) \\ \#3 : F(0) = F(N+1) = 0 \text{ and } G(0) = 0, \text{ with } \alpha_{i,N+1}^3 = g_1(j) \\ \#4 : G(0) = G(N+1) = 0 \text{ and } G(N+1) = 0, \text{ with } \alpha_{i,0}^4 = g_2(j). \end{cases} \quad (6.11)$$

For example, solving problem #1 leads to $G_n(j) = \sin(k_y^n j)$ and $F_n(i) = \sinh(\kappa_x^n i)$ with $k_y^n = n\pi/(N+1)$ for $n \in [0, N+1] \cap \mathbb{Z}$. This also restricts the values of $0 < \lambda < 4$ to those satisfying $\cos(k_x^n) = 1 - \lambda_n/2$, and in turn $\cosh(\kappa_x^n) = 1 + \lambda_n/2$. Hence, we have found the fundamental solutions $A_n \sinh(\kappa_x^n i) \sin(k_y^n j)$, which by linear superposition lead to the general solution of problem #1

$$\alpha_{i,j}^1 = \sum_{n=0}^{N+1} A_n \sinh(\kappa_x^n i) \sin(k_y^n j), \quad (6.12)$$

where the coefficients A_n are fixed by

$$f_2(j) = \sum_{n=0}^{N+1} A_n \sinh(\kappa_x^n (N+1)) \sin(k_y^n j), \quad (6.13)$$

i.e., proportional to the Fourier coefficients of $f_2(j)$.

Solving the three remaining problems, which again involve products of sinusoidal and hyperbolic functions, one can find a general solution of Eq.(6.6) for any choice of boundary functions. This implies that the fundamental solutions $\sinh(\kappa_x^n i) \sin(k_y^n j)$, $\sinh(\kappa_x^n [i - (N+1)]) \sin(k_y^n j)$, $\sin(k_x^n i) \sin(\kappa_y^n j)$, $\sin(k_x^n i) \sinh(\kappa_y^n [j - (N+1)])$ with $n = 0 \dots, N+1$ form a basis for solutions of Eq. (6.6), showing that the number of independent symmetries scales with the linear system size. This approach not only gives us the fundamental solutions from where to obtain any other one, but also allows us to explicitly find particular spatial modulations that connect to the quasi-periodic and exponential modulations we encountered in the previous chapter. In general, we can solve Eqs. (6.9) finding the roots of the associated characteristic polynomials $r^2 - (2 \pm \lambda)r + 1 = 0$ which take the values

$$\begin{cases} x_{1,2} = \frac{2+\lambda}{2} \pm \frac{\sqrt{\lambda(\lambda+4)}}{2}, \\ y_{1,2} = \frac{2-\lambda}{2} \mp \frac{\sqrt{\lambda(\lambda-4)}}{2}, \end{cases} \quad (6.14)$$

for the first and second equations respectively. As the characteristic polynomial are palindromic, the two roots are inverse of each other. Whether these are real ($\eta_{x,y}$) or pure complex phases ($e^{ik_{x,y}}$) is determined by the sign of the discriminants $\Delta_x = \lambda(\lambda+4)$, $\Delta_y = \lambda(\lambda-4)$: If $\Delta_{x,y} > 0$, the corresponding solution can be written in terms of hyperbolic or exponential functions; while $\Delta_{x,y} < 0$ correspond to sinusoidal or complex exponential modulations.

We can split the solutions into three main types: (i) $\lambda = 0$ contains all multipole conserved quantities we already identified except for the $x^2 - y^2$ quadratic moment. As this solution does not factorize in horizontal and vertical directions, but rather as $\alpha_{x,y} = (x+y)(x-y)$, we can only recover it by superposing many fundamental solutions. Alternatively, these could be explicitly found when writing the recurrence relation in terms of center of mass $s = i+j$ and relative $r = i-j$ coordinates, i.e., $\alpha_{i,j} = F(s)G(r)$. The second case (ii) corresponds to exponential (hyperbolic) solutions, which are localized near the corners of the 2D lattice when $|\lambda| > 4$. These can be directly found solving Eq.(6.5) with the ansatz $\alpha_{i,j} = (\eta_x)^i (\eta_y)^j$. Finally, the third case (iii) corresponds to the product of sinusoidal and hyperbolic solutions along orthogonal directions, like e.g., $\alpha_{i,j} = (\eta_x)^i e^{-ik_y j}$. Thus, while solutions with a finite momentum mode along one of the lattice directions exist (for $|\lambda| < 4$), these are exponentially damped along the orthogonal direction and do not contribute to spin correlations in the bulk, similarly to what happened in 1D (see Section 5.6). Moreover, we can also rule out solutions of the form $\alpha_{i,j} \sim e^{ik_x i} e^{ik_y j}$ which would have led to conserved finite modes in the bulk correlations ¹.

Nevertheless, these solutions (or rather linear combinations of) could lead to finite boundary correlations. To study this possibility, we follow the more direct approach of Ref. [324] that gives the general solution of Eq. (6.6) explicitly in terms of the boundary conditions. This reads

$$\alpha_{i,j} = \sum_{a=1}^N \alpha_{a,N+1}^B T_{a,N}(i,j) + \sum_{a=1}^N \alpha_{a,0}^B T_{a,1}(i,j) + \sum_{b=1}^N \alpha_{0,b}^B T_{1,b}(i,j) + \sum_{b=1}^N \alpha_{N+1,b}^B T_{1,b}(i,j), \quad (6.15)$$

where each sum runs over each of the boundaries with values $\alpha_{i,j}^B$. The kernel function $T_{a,b}(i,j)$ is given by the double sum

$$T_{a,b}(i,j) \equiv \frac{1}{(N+1)^2} \sum_{r=1}^N \sum_{s=1}^N \frac{\sin(\frac{ir\pi}{N+1}) \sin(\frac{js\pi}{N+1}) \sin(\frac{ar\pi}{N+1}) \sin(\frac{bs\pi}{N+1})}{1 - \frac{1}{2} \cos(\frac{r\pi}{N+1}) - \frac{1}{2} \cos(\frac{s\pi}{N+1})}, \quad (6.16)$$

with $a, b, i, j = 1, \dots, N$. In fact, $T_{a,b}(i,j)$ solves the linear recurrence equation

$$T_{a,b}(i,j) - \frac{1}{4} (T_{a,b}(i+1,j) + T_{a,b}(i-1,j) + T_{a,b}(i,j+1) + T_{a,b}(i,j-1)) = \delta_{(a,b),(i,j)}, \quad (6.17)$$

and hence corresponds to a fundamental solution of the discrete Laplace operator with vanishing boundary conditions. In particular, Eq. (6.15) can be understood as the convolution between the Green function $T_{a,b}(i,j)$ and the boundary values $\alpha_{i,j}^B$.

6.1.2. Finite boundary correlations and Mazur's bound

From here we can now construct $4(N+1)$ linearly independent conserved quantities

$$Q^{\mathbf{r}0} = \sum_{i,j} \alpha_{i,j}^{\mathbf{r}0} s_{i,j} \quad (6.18)$$

¹Alternatively, we could have plugged this ansatz into Eq. (6.5) and realize that the resulting equation $2 = \cos(k_x) + \cos(k_y)$, can only be solved for $k_x = k_y = 0$.

labeled by $\mathbf{r}_0 = (i_0, j_0)$. We order these charges by the location of the site \mathbf{r}_0 , starting from the lower left corner, corresponding to $\mathbf{r}_0 = (0, 0)$, and continuing in clock-wise direction along the boundary: $(0, 0) \rightarrow (0, N+1) \rightarrow (N+1, N+1) \rightarrow (N+1, 0)$. These correspond to solutions $\alpha_{i,j}^{\mathbf{r}_0}$ with vanishing boundary values everywhere except at the site with coordinates $\mathbf{r}_0 = (i_0, j_0)$: $\alpha_{i,j}^{\mathbf{B}} = \delta_{i,i_0} \delta_{j,j_0}$. For \mathbf{r}_0 at the corners of the lattice, $\alpha_{i,j}^{\mathbf{r}_0} = \delta_{i,i_0} \delta_{j,j_0}$, i.e., the charge at the corner is completely decoupled from the rest of the system and hence it is trivially conserved. In the following, we focus on the remainder $4N$ conserved quantities. For these, $\alpha_{i,j}^{\mathbf{r}_0}$ is also bounded in the bulk (as a result of the second corollary we discussed) $0 \leq \alpha_{i,j}^{\mathbf{r}_0} \leq 1$ and coincides with $T_{a,b}(i, j)$ after taking $(a, b) = (i_0, j_0)$. We dubbed these canonical conserved quantities.

Our aim is to investigate whether boundary correlations are finite for any (spin representation) S in the thermodynamic limit. In particular whether the time average autocorrelation is finite

$$\lim_{T \rightarrow \infty} \frac{1}{T} \int_0^T dt \langle s_{x,y}(t) s_{x,y}(0) \rangle \geq M_{S_{x,y}^z}, \quad (6.19)$$

for sites (x, y) located close to the boundary. To show that autocorrelations are finite one can use Mazur's bound, and check whether it is sufficient including the single localized charge for which \mathbf{r}_0 coincides with the coordinates of the point at which we want to evaluate it. In fact, this was the procedure we followed in Chapter 3 when we only needed to use the left- and right-most SLIOMs to prove finite boundary correlations. Fig. 6.2 shows the spatial dependence of two solutions $\alpha_{i,j}^{\mathbf{r}_0}$ where $(i_0, j_0) = (0, N)$ (panel a) and $(i_0, j_0) = (0, \frac{N}{2})$ (panel b), corresponding to a point near the corner and at the central point of the left boundary respectively. The figure shows the spatial decay of the solutions when moving towards the bulk into different directions. In both cases, we find that these are not exponentially but rather power-law localized at the boundaries of the system. In particular, $\alpha_{i,j}$ decays inversely proportional with the distance when located at the center of the boundary (panel b). Hence, one cannot prove finite-boundary correlations considering a single canonical charge. Alternatives to this approach require: Either considering several of the canonical charges in the computation of Mazur's bound (potentially a linear in N number of them), or to look for a choice of boundary conditions which lead to more localized solutions in the bulk. In the following, we pursue the first strategy and defer the second for a future work [325]. For the latter, we can show that it is possible to construct solutions that decay with any power of the distance ($r^{-(n+1)}$) by combining a finite number (n) of canonical charges.

We notice that while linearly independent, these conserved quantities are not orthogonal with respect to the uniform distribution in configuration space:

$$\langle \mathcal{Q}^{\mathbf{r}_0}, \mathcal{Q}^{\mathbf{r}'_0} \rangle = \frac{S(S+1)}{3} \sum_{i,j} \alpha_{i,j}^{\mathbf{r}_0} \alpha_{i,j}^{\mathbf{r}'_0}, \quad (6.20)$$

and thus, to calculate Mazur's bound we need to use the general expression we presented in Chapter 1, namely

$$M_{S_{x,y}^z} \equiv \sum_{\mathbf{r}_0, \mathbf{r}'_0} \langle s_{x,y}, \mathcal{Q}^{\mathbf{r}_0} \rangle (K^{-1})_{\mathbf{r}_0, \mathbf{r}'_0} \langle \mathcal{Q}^{\mathbf{r}'_0}, s_{x,y} \rangle. \quad (6.21)$$

Here K is the (positive definite) non-diagonal $4N \times 4N$ matrix with elements $K_{\mathbf{r}_0, \mathbf{r}'_0} = \langle \mathcal{Q}^{\mathbf{r}_0}, \mathcal{Q}^{\mathbf{r}'_0} \rangle$. In particular, using the explicit expression $\alpha_{i,j}^{\mathbf{r}_0} = \delta_{i,i_0} \delta_{j,j_0} + T_{a,b}(i, j)$ for (a, b) fixed by \mathbf{r}_0 , these are given by

$$K_{\mathbf{r}_0, \mathbf{r}'_0} = \frac{S(S+1)}{3} \sum_{i,j=0}^{N+1} \alpha_{i,j}^{\mathbf{r}_0} \alpha_{i,j}^{\mathbf{r}'_0} = \delta_{\mathbf{r}_0, \mathbf{r}'_0} + \sum_{i,j=1}^N T_{a,b}(i, j) T_{a',b'}(i, j), \quad (6.22)$$

where the diagonal entries correspond to the normalization of the conserved quantities. Finally, using that

$$\langle s_{x,y}, \mathcal{Q}^{\mathbf{r}'_0} \rangle = \frac{S(S+1)}{3} \alpha_{x,y}^{\mathbf{r}'_0}, \quad (6.23)$$

we obtain the general expression for Mazur's bound

$$M_{S_{x,y}^z} = \frac{S(S+1)}{3} \sum_{\mathbf{r}_0, \mathbf{r}'_0} \alpha_{x,y}^{\mathbf{r}_0} \cdot (K^{-1})_{\mathbf{r}_0, \mathbf{r}'_0} \cdot \alpha_{x,y}^{\mathbf{r}'_0}, \quad (6.24)$$

which can be evaluated at any point (x, y) of the lattice. Nevertheless, it simplifies when evaluated it at a boundary site

$$M_{S_{\mathbf{r}_0}^z} = \frac{S(S+1)}{3} (K^{-1})_{\mathbf{r}_0, \mathbf{r}_0}, \quad (6.25)$$

or alternatively, when computing the average boundary auto-correlation

$$\lim_{T \rightarrow \infty} \frac{1}{T} \int_0^T dt \frac{1}{4N} \sum_{\mathbf{r}_0 \in B} \langle s_{\mathbf{r}_0}(t) s_{\mathbf{r}_0}(0) \rangle = \frac{S(S+1)}{3} \frac{1}{4N} \text{tr}(K^{-1}). \quad (6.26)$$

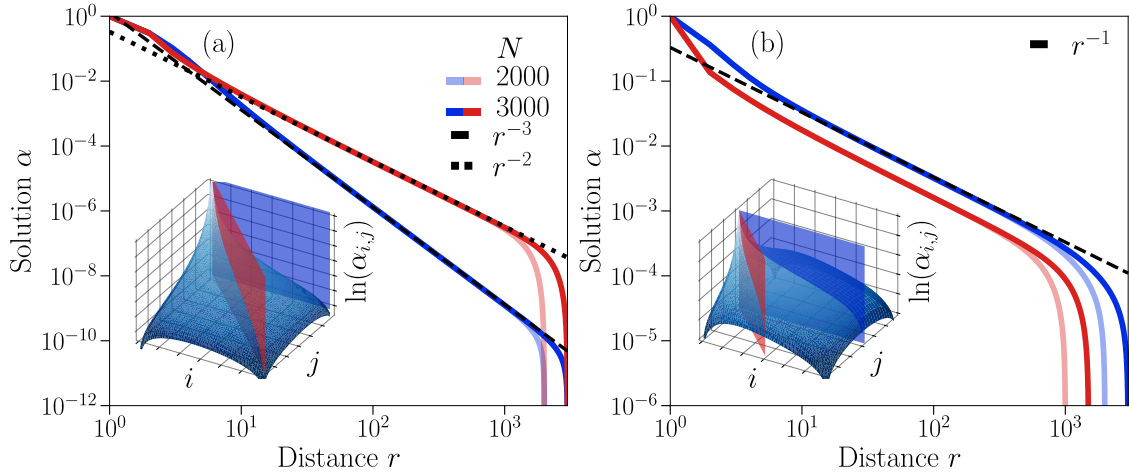


Figure 6.2.: **Localization properties of the “canonical” conserved quantity.** Dependence of the coefficients $\alpha_{i,j}^{\mathbf{r}_0}$ when moving towards the bulk along two different directions marked by the cutting planes in each of the insets: $\mathbf{r}_0 = (0, 0)$ in panel a, and $\mathbf{r}_0 = (0, N/2)$ in b. This figure was obtained by Julius Lehmann.

Therefore, being able to analytically show that indeed the (time-average) boundary correlations saturate to a finite value for any S in the thermodynamic limit completely relies on the structure of $T_{a,b}(i, j)$ through the matrix K . A first attempt could be to use the largest eigenvalue of K , to lower bound $M_{S^z}^B \geq 1/\lambda_{\max}$. However, one can numerically find that λ_{\max} scales with N and hence this bound goes to zero in the thermodynamic limit. A second option is to look at the region close to a corner, e.g., the one with coordinates $(0, 0)$. From our solution of the recurrence relation using separation of variables, we know that solutions of the form $\alpha_{i,j} = (\eta_x)^i (\eta_y)^j$ exist. In particular, there exist solutions with $|\eta_x|, |\eta_y| < 1$, which then are *exponentially* localized at this corner. Evaluating Mazur's bound at a site with coordinates (x, y) close to the corner and including only this conserved quantity one finds

$$M_{S_{x,y}^z} = \frac{S(S+1)}{3} \frac{(\alpha_{x,y})^2}{\sum_{i,j} (\alpha_{i,j})^2} \rightarrow \frac{S(S+1)}{3} (\eta_x)^{2x} (\eta_y)^{2y} (1 - (\eta_x)^2) (1 - (\eta_y)^2) \quad (6.27)$$

in the limit $N \rightarrow \infty$. The largest bound can then be found optimizing the expression on the right hand side over the set of solutions of the equation

$$(\eta_x)^2 \eta_y + \eta_y + \eta_x (\eta_y)^2 + \eta_x = 4\eta_x \eta_y, \quad (6.28)$$

restricted to the domain $|\eta_x|, |\eta_y| < 1$. Therefore as long as the site (x, y) is at finite distance from the corner, Mazur's bound will be finite, which in turn shows that the time-average boundary correlation saturates to a finite value.

Our numerical simulations indeed suggest that boundary auto-correlations are finite in the thermodynamic limit and at infinite times. Fig. 6.1d shows numerical results (green continuous line) for the boundary correlations $C_{\text{bound}}(\mathbf{r}, t)$ evaluated at the central site $\mathbf{r} = (0, \frac{N}{2})$ for $S = 3$. While bulk correlations (Fig. 6.1b) follow the hydrodynamic prediction given in Eq. (6.3), $C_{\text{bound}}(\mathbf{r}, t)$ appears to saturate to a finite value at the longest time scales of our simulations. This coincides with the averaged boundary value as defined in Eq. (6.26). We also emphasize that these results are converged in system size and hold for larger S .

Using the explicit expression for the matrix elements of K in Eq. (6.22), we numerically evaluate Mazur's bound at the center of the left boundary (Eq. (6.25)). Moreover, since we are interested in the limit $N \rightarrow \infty$, we only include those conserved quantities that are localized at left boundary, then reducing the linear dimension of K from $4N$ to N . Fig. 6.3 shows the scaling of $M_{S^z}^{(0, \frac{N}{2})}$ with system size for N taking values between 50 and 300, which appears to converge to a finite value just below 0.82. In Fig. 6.1d, we plot the value of Mazur's bound for $N = 300$ (black dashed line), which approximates quantitatively well the saturation value obtained in numerical simulations. At the moment we are working out an analytical proof to show that Mazur's bound is indeed finite for every point at the boundary (besides the corners), although certain caveats still need to be resolved, apart from additional subtleties that appeared in the thermodynamic limit. This requires utilizing the structure of $K_{\mathbf{r}_0, \mathbf{r}'_0}$.

Moreover, the inset of Fig. 6.1d shows that the spatial correlations *at the boundary*, namely, $\langle s_{(0,y)}(t) s_{(0, \frac{N}{2})}(0) \rangle$, are localized at the central point with no observable drift at late times. This suggests that one could construct a single conserved quantity that is responsible for this effect, which should be more sharply localized than the canonical charges. As we will prove in the future publication [325] together with Julius Lehmann, Tibor Rakovszky and Frank Pollmann, this is indeed the case.

Before closing this section, we notice that the previous construction can be extended to other lattices as well as to higher dimensions, as long as the solutions of the corresponding linear recurrence equation $\alpha_{\mathbf{r}}$, are discrete harmonic functions. This is the case when for a lattice specified by $\mathcal{G} = \{V, E\}$ with vertices V and links E , then the recurrence can be written as

$$\alpha_v = \frac{1}{|\mathcal{N}_v|} \sum_{v' \in \mathcal{N}_v} \alpha_{v'}, \quad (6.29)$$

where \mathcal{N}_v is the set of sites connected to v and $|\mathcal{N}_v|$ its number. In this case, for a given choice of boundary conditions, a unique solution exists, which corresponds to a conserved quantity. See Ref. [325] for additional details.

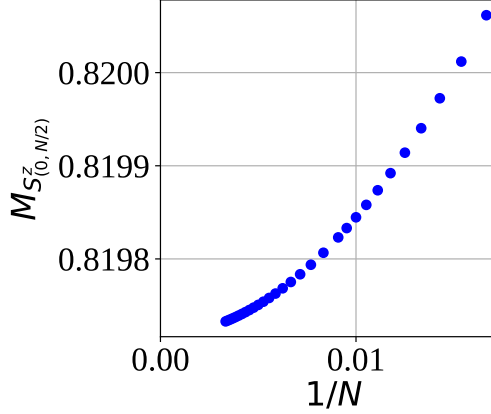


Figure 6.3.: **Finite-size scaling of Mazur's bound.** Scaling with system size (N) of Mazur's bound in Eq. (6.25) via numerical evaluation.

6.2. Subsystem symmetries in momentum space

In the previous section, we found that while the late-time dynamics of the spin-correlations in the bulk is governed by the hydrodynamic mode $\mathbf{k} \rightarrow 0$, which in turn is constrained by the conservation of its higher-moments, boundary correlations do not decay due to the presence of extensively many conserved quantities that are localized at the edges of the system. This generalizes the phenomenology associated to exponentially localized symmetries that we uncovered in the previous chapter. In this section we explore a new possibility: The existence of spatially-modulated symmetries which lead to new finite-mode contributions that govern the late-dynamics of spin correlations. This is the higher-dimensional analog of the quasi-periodic symmetries we already encountered in 1D, with the striking possibility that they can now take the form of lines and surfaces of conserved momenta instead of being isolated points in the Brillouin zone (BZ). This leads to a rich variety of sub-diffusive behaviour with the spatial structure influenced by lattice-scale features.

We set the stage by constructing a model which features these symmetries. In this microscopic model, local gates $G_{x,y}$ act on a 4×4 block of a 2D square lattice in the vicinity of the site with coordinates x, y , and are specified by a set of integers, such that $G_{x,y} : s_{x+i,y+j} \rightarrow s_{x+i,y+j} \pm n_{i,j}$. One can think of it as the expanded version of the model we analyzed in the previous chapter. These gates are given by

$$G = \{n_{0,0}, n_{0,3}, n_{3,0}, n_{3,3}, n_{1,1}, n_{1,2}, n_{2,1}, n_{2,2}\} = \{1, 1, 1, 1, -1, -1, -1, -1\}, \quad (6.30)$$

whose action is illustrated in Fig. 6.4a. This model has the same global U(1) symmetries as before. Nevertheless, it also conserves the staggered magnetization along all rows and columns i.e., $\mathcal{S}_{x_0} = \sum_y (-1)^y s_{x_0,y}$, $\mathcal{S}_{y_0} = \sum_x (-1)^x s_{x,y_0}$ which are example of subsystem symmetries. However, these do not exhaust the set of modulated symmetries of the model. As before, we need to solve the associated recurrence relation

$$\alpha_{i,j} + \alpha_{i+3,j} + \alpha_{i,j+3} + \alpha_{i+3,j+3} - \alpha_{i+1,j+1} - \alpha_{i+2,j+1} - \alpha_{i+2,j+2} - \alpha_{i+1,j+2} = 0, \quad (6.31)$$

for all $i, j = 0, \dots, N-2$ on a square lattice of size $(N+2) \times (N+2)$. Once again, one can try to solve the equation by separation of variables $\alpha_{i,j} = F(i)G(j)$. However, this choice does not simplify the recurrence. Instead, we need to factorize it as $\alpha_{i,j} = F(s)G(r)$ with $s = i + j$ and $r = i - j$ for a lattice compatible with this parametrization (a rectangular

lattice rotated 45 degrees.) Doing so one finds

$$\begin{aligned} & F(s+3)[G(r-3) - G(r-1) - G(r+1) + G(r+3)] + \\ & [F(s+6) - F(s+4) - F(s+2) + F(s)]G(r) = 0, \end{aligned} \quad (6.32)$$

which simplifies into solving two one-dimensional linear recurrence equations

$$\begin{cases} G(r-3) - G(r-1) - G(r+1) + G(r+3) = \lambda G(r), \\ F(s+6) - F(s+4) - F(s+2) + F(s) = -\lambda F(s+3), \end{cases} \quad (6.33)$$

for $\lambda \in \mathbb{R}$. Even then, classifying possible solutions is not as simple as in the previous section, as now the associated characteristic polynomials $x^6 - x^4 \mp \lambda x^3 - x^2 + 1 = 0$ have degree six, with no closed formula for its associated roots as a function of λ ². More importantly, as explicitly shown in expression Eq. (6.31), solutions of this recurrence equation are not discrete harmonic functions in the bulk, i.e., the value of $\alpha_{i,j}$ on a site is not the average of values at neighboring sites. This implies that the associated Dirichlet problem (with sufficiently many fixed boundary values) may have no solution or that this is not unique. Nevertheless, one can always find boundary values for which a unique solution exists: First, we can fix the three upper- and left-most rows and columns respectively, and solve the recurrence (with open boundary conditions) recursively. Then fix the boundary values according to the obtained solution. Alternatively, we can consider a particular ansatz for $\alpha_{i,j}$ which solves the recurrence for every gate $G_{x,y}$ compatible with the lattice for OBC, and fix the values of $\alpha_{i,j}$ at the sites which do not overlap with any gate. This will provide an exact solution and give us useful information about its spatial dependence.

We start with $\alpha_{i,j} = e^{ik_x i} e^{ik_y j}$, the 2D analog of the quasi-periodically modulated symmetries we encountered in the previous chapter. The recurrence relation Eq. (6.31) then reduces to finding the (real) roots (k_x, k_y) of

$$\begin{aligned} \chi(\mathbf{k}) &\equiv \sum_{i,j} n_{a,b} e^{i(k_x i + k_y j)} \propto \cos(k_x/2) \cos(k_y/2) \times \\ &\times [\cos(k_x) + \cos(k_y) - 2 \cos(k_x) \cos(k_y)] = 0. \end{aligned} \quad (6.34)$$

The solutions of $\chi(\mathbf{k}) = 0$ are highlighted in green in Fig. 6.4b. The conservation of total charge corresponds to the mode \mathfrak{s}_0 at $\mathbf{k} = (0,0)$, while the staggered subsystem symmetries $\mathcal{S}_x, \mathcal{S}_y$ show up as the lines with $k_y = \pi$ and $k_x = \pi$ respectively. Moreover, we find a set of contour lines (forming a closed loop in the Brillouin zone) along which the second line of Eq. (6.34) vanishes. As we explained in the previous chapter, each of these corresponds to an exact symmetry for OBC, whose total number scales with the linear system size $\mathcal{O}(N)$ (see Appendix E.3). However, most points along these lines are not realized exactly in a finite system with PBC, but become exact symmetries only in the thermodynamic limit, leading to an (infinite dimensional) emergent symmetry group.

Before closing this section, we notice that based on the solution of the discrete Laplacian model using separation of variables, we also expect to find solutions of the form $\alpha_{i,j} = \eta_x^i e^{ik_y j}$, $e^{ik_x i} \eta_y^j$, with $\eta_x, \eta_y \in \mathbb{R}$. Plugging these Ansätze in Eq. (6.31) we get

$$\alpha_{i,j} = \eta_x^i e^{ik_y j} : (\eta_x^{3/2} + \eta_x^{-3/2}) \cos\left(\frac{3}{2}k_y\right) = (\eta_x^{1/2} + \eta_x^{-1/2}) \cos\left(\frac{1}{2}k_y\right), \quad (6.35)$$

$$\alpha_{i,j} = e^{ik_x i} \eta_y^j : (\eta_y^{3/2} + \eta_y^{-3/2}) \cos\left(\frac{3}{2}k_x\right) = (\eta_y^{1/2} + \eta_y^{-1/2}) \cos\left(\frac{1}{2}k_x\right), \quad (6.36)$$

²This would enter the arena of Galois theory.

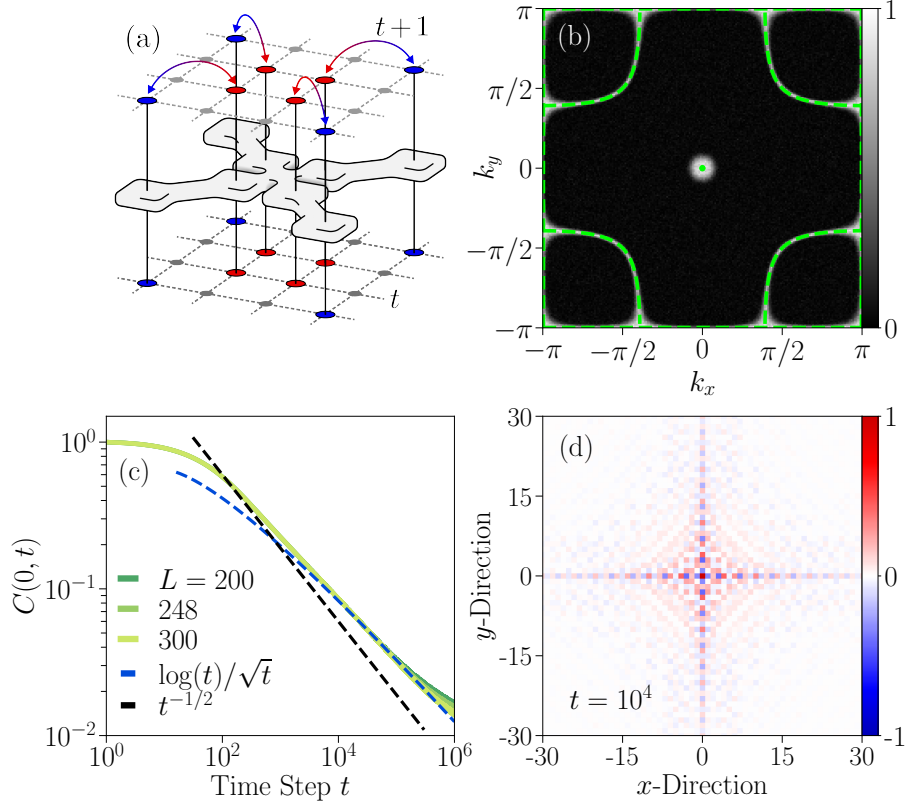


Figure 6.4.: **Finite-momentum modes in 2D.** (a) Schematics of a local gate corresponding to Eq. (6.30). (b) Correlation function $\mathcal{C}(\mathbf{k}, t)$ within the Brillouin zone at $t = 10^4$. The solution of Eq. (6.34) is shown in a green (dashed) line. (c) The autocorrelation decays as $C(0, t) \sim \log(t)/\sqrt{t}$. (d) Correlations $C(\mathbf{x}, t)$ are concentrated along the two axes and show oscillations on lattice scales that survive for long times. These numerical results were obtained by Julius Lehmann as published in Ref. [5].

which in fact admit non-trivial solutions. As we already discussed in the previous section, we expect them to have no effect on bulk correlations, but potentially on the boundary dynamics. Preliminary numerical results indicate that this is the case. However, we currently miss a strategy to find a lower bound for those systems whose recurrence relations are not discrete harmonic functions.

6.2.1. Symmetries in real space

Straight lines in the BZ correspond, upon inverse discrete Fourier transform, to symmetry operators that act along columns or rows on the lattice. In particular, the staggered subsystem symmetries $\mathcal{S}_x, \mathcal{S}_y$ correspond to the inverse Fourier transform of solutions lying along the $k_x, k_y = \pi$ lines in momentum space

$$\mathcal{S}_{y_0} \equiv \sum_x (-1)^x s_{x, y_0} = \frac{1}{N} \sum_{k_y} e^{-iy_0 k_y} \mathcal{J}_{\pi, k_y}, \quad (6.37)$$

$$\mathcal{S}_{x_0} \equiv \sum_y (-1)^y s_{x_0, y} = \frac{1}{N} \sum_{k_x} e^{-ix_0 k_x} \mathcal{J}_{k_x, \pi}. \quad (6.38)$$

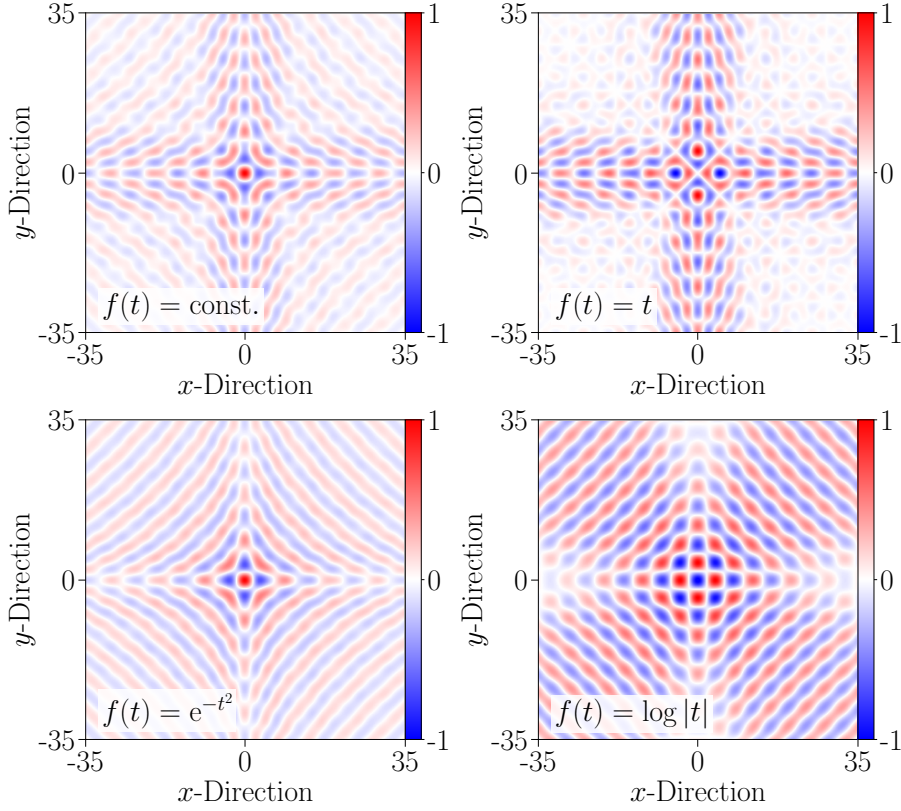


Figure 6.5.: Real-space modulations $\alpha(\mathbf{r})$ of conserved quantities from performing the integral in Eq. (6.44) for different choices of $f(t)$.

These can also be written in the following form

$$\mathcal{S}_{y_0} = \frac{1}{N^2} \sum_{x,y} \alpha(\mathbf{r}; y_0) s_{x,y}, \quad (6.39)$$

(and analogous for \mathcal{S}_{x_0}) with the modulation given by the inverse Fourier transform of the function $f(\mathbf{k}) = e^{-ik_y y_0}$

$$\alpha(\mathbf{r}) = \sum_{\mathbf{k} \in \{(k_x = \pi, k_y)\}} e^{i\mathbf{k} \cdot \mathbf{r}} f(\mathbf{k}), \quad (6.40)$$

taking values along the lines $k_x = \pi$ ($k_y = \pi$). Without loss of generality, and evaluating at $y_0 = 0$, this implies that \mathcal{S}_{y_0} appears as the “equally weighted” inverse Fourier transform along the one-dimensional manifold of solutions of $\chi(\mathbf{k}) = 0$ corresponding to $k_x = \pi$. This result is quite natural: Along these straight lines, one finds the most localized object in real space (i.e., a Kronecker delta) via the 1D inverse Fourier transform of the constant function.

A natural question is whether one could similarly construct a subsystem symmetry from the inverse Fourier transform of conserved modes along some closed loop in the BZ, such as the ones we encountered in Fig. 6.4b. Here, we will argue that this is in general not the case: the quantities that can be constructed in this case decay asymptotically as $\|\mathbf{r}\|^{-1/2}$ at large distance along almost all directions in space, implying that they are spread out around the entire system.

To build some intuition, consider a simple example where the conserved momenta are along a circle in momentum space. In particular let us consider a continuum model invariant under the shift symmetry $\phi(x) \rightarrow \phi(x) + \alpha(x)$ with $\alpha(x)$ satisfying $(\Delta + 1)\alpha(x) =$

0 where $\Delta = \partial_x^2 + \partial_y^2$. In fact, this corresponds to the free part of the 2D UV theory in Ref. [298], and is invariant under $\alpha_{\mathbf{k}}(x) = \cos(\mathbf{k} \cdot \mathbf{x})$ for any \mathbf{k} with unit norm ($\|\mathbf{k}\| \equiv \sqrt{k_x^2 + k_y^2} = 1$) and corresponding conserved quantity $N_{\mathbf{k}}$. Since this set can be easily parametrized in polar coordinates, one can exactly compute the inverse Fourier transform. A naive guess to find the most localized quantity in real space is to consider the constant function $f(\mathbf{k}) = 1$ with support on this set. The result can be obtained via the line integral

$$\alpha(\mathbf{r}) = \int_{S^1} ds e^{i\mathbf{k}(s) \cdot \mathbf{r}} = 2\pi \mathcal{J}_0(\|\mathbf{r}\|), \quad (6.41)$$

where \mathcal{J}_0 is a zeroth order Bessel function of the first kind. This leads to a conserved quantity “localized” around $\mathbf{r} = \mathbf{0}$ with asymptotic behavior (i.e., in the limit $\|\mathbf{x}\| \gg 1$) given by $\alpha(\mathbf{r}) \sim \frac{1}{\sqrt{\|\mathbf{r}\|}} \cos(\|\mathbf{x}\| - \frac{\pi}{4})$.

In fact, the asymptotic behavior is generic and applies even if we consider the inverse Fourier transform of some more generic function along the circle. Let us fix a direction $\mathbf{r}/\|\mathbf{r}\|$ and write $\mathbf{k} \cdot \mathbf{r} = r \cos \theta$ along the unit circle in \mathbf{k} -space. Let us take an arbitrary function $f(\theta)$ that we wish to Fourier transform. In the limit $r \rightarrow \infty$, we can evaluate this by a stationary phase approximation, which gives

$$\int_0^{2\pi} d\theta f(\theta) e^{ir \cos \theta} \sim \sqrt{\frac{2\pi}{r}} \left(e^{i(r-\frac{\pi}{4})} f(0) + e^{-i(r-\frac{\pi}{4})} f(\pi) \right), \quad (6.42)$$

where we dropped terms that decay faster than $r^{-1/2}$. The leading term might vanish if $f(\theta)$ happens to be zero at both $\theta = 0$ and π ; however, for any particular choice of f , this will only happen for a few specific directions; in almost all directions we have a decay $r^{-1/2}$ to leading order.

While the circular shape simplified the calculation, this discussion is quite general. What we needed is that for any choice of direction, $\hat{\mathbf{r}} \equiv \mathbf{r}/\|\mathbf{r}\|$ there is some isolated points along the loop of conserved momenta where $\hat{\mathbf{r}}$ is normal to the loop; the integral can then be evaluated in a stationary phase approximation at these points which lead to the same $r^{-1/2}$ decay.

As an example of how this works, let us consider the model in Eq. (6.30) in detail. We want to evaluate the line integral

$$\int_{\mathcal{C}} ds e^{i\mathbf{k}(s) \cdot \mathbf{r}} f(s) = \int_{\mathcal{C}} ds e^{irg(s)} f(s) \quad (6.43)$$

for some function f , along the “loop” \mathcal{C} within the BZ, defined by the equation $\cos(k_x) + \cos(k_y) - 2 \cos(k_x) \cos(k_y) = 0$, and with $g(s) \equiv \mathbf{k}(s) \cdot \hat{\mathbf{r}}$. As before, the asymptotics will be dominated by saddle points of $g(s)$, i.e., points along the loop where $\hat{\mathbf{r}} \cdot \mathbf{k}'(s) = 0$ such that $\hat{\mathbf{r}}$ is normal to the loop. Apart from non-generic behavior along certain directions, in general, the result decays as $r^{-1/2}$.

Apart from their slow asymptotic decay, the real-space conserved quantities constructed from the inverse Fourier transform also exhibit a rich spatial structure, involving short-scale oscillations similar to the circular case considered above. To address this question we notice that \mathcal{C} splits into four arcs \mathcal{C}_i each of them lying within one of the four quadrants of the BZ, such that Eq. (6.43) can be written as

$$\sum_{i=1}^4 \int_{\mathcal{C}_i} ds e^{i\mathbf{k}(s) \cdot \mathbf{r}} f(s) = \int_{\mathcal{C}_1} ds \cos(k_x(s)x) \cos(k_y(s)y) f(s).$$

In particular, \mathcal{C}_1 lies in the first quadrant with $k_x, k_y > 0$, and takes the form of an hyperbola $XY = 1$ with $X = 1 - 2 \cos(k_x)$, $Y = 1 - 2 \cos(k_y)$. We therefore parametrize it

6.2. Subsystem symmetries in momentum space

via $X = e^t$, and $Y = e^{-t}$, with t taking values in $|t| \leq \log(3)$. In this new parametrization the modulation $\alpha(\mathbf{r})$ reads

$$\int_{-\log(3)}^{\log(3)} dt \|\mathbf{k}'(t)\| \cos(k_x(t)x) \cos(k_y(t)y) f(t), \quad (6.44)$$

where $\|\mathbf{k}'(t)\| = \sqrt{(k'_x(t))^2 + (k'_y(t))^2}$.

In Fig. 6.5, we plot a few different results obtained by numerically evaluating the integral (6.44) for different choices of $f(t)$.

Finally, we note that even in cases that evade our stationary phase analysis, the spatial decay of the resulting real-space functions still tends to remain slow. In particular, integrating over a square $[-k, k] \times [-k, k]$ in momentum space gives

$$\frac{1}{4} \int_{-k}^k dk_x \int_{-k}^k dk_y e^{i(k_x x + k_y y)} = \frac{\sin(kx) \cos(ky)}{x} + \frac{\sin(ky) \cos(kx)}{y},$$

so that the decay is merely enhanced to r^{-1} .

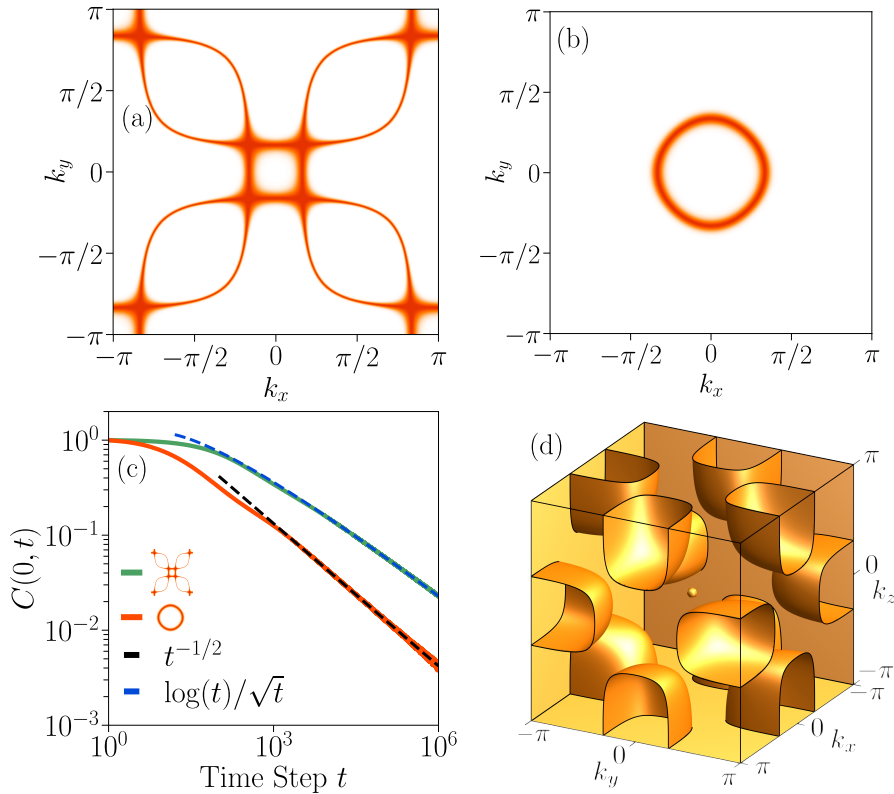


Figure 6.6.: **Generalizations with (quasi)-periodic symmetries.** (a,b) Examples of 2D systems which do not conserve total charge whose local gates are given by Eq. (6.50) and Eq. (6.51) respectively. The figures show $e^{-|\chi(\mathbf{k})|^2}$. (c) Numerical results for $C(\mathbf{0}, t)$: Model in panel (a) (red line) decays as $C(\mathbf{0}, t) \sim \log(t)/\sqrt{t} + O(t^{1/2})$, while model in panel (b) follows $C(\mathbf{0}, t) \sim t^{-1/2}$ respectively. Data was computed for $S = 10$ (green line) and $S = 3$ (red line) and system size $N = 300$. (d) 3D generalization of the 2D model in Eq. (6.30). The figure shows the solutions of $\chi(\mathbf{k}) = 0$.

6.2.2. Hydrodynamic description: Long-time scaling of correlations

As we already saw in Section 5.5 of the previous chapter, the asymptotic decay of correlations

$$C(\mathbf{r} = \mathbf{0}, t) = \int_0^\infty d\omega \rho(\omega) e^{-\omega t}, \quad (6.45)$$

is governed by the density of states (DOS) $\rho(\omega)$ near $\omega \approx 0$. For this model, $\rho(\omega)$ picks up contributions from various parts of the BZ: As already noted, it vanishes at the origin as well as along the lines shown in Fig. 6.4b. Recall that to evaluate the DOS we calculate $N(\omega)$, the number of states in the frequency range $[0, \omega]$ (i. e., $N(\omega)$ is the area of the region in the BZ delineated by the condition $\omega(k_x, k_y) \leq \omega$) and then take a derivative, $\rho(\omega) = \frac{dN(\omega)}{d\omega}$. In this case, the dispersion relation reads

$$\begin{aligned} \omega(k_x, k_y) &\sim |\chi(k_x, k_y)|^2 = \cos^2(k_x/2) \cos^2(k_y/2) \times \\ &\times [\cos(k_x) + \cos(k_y) - 2 \cos(k_x) \cos(k_y)]^2, \end{aligned} \quad (6.46)$$

valid for (k_x, k_y) close to the conserved momentum modes. We split up $N(\omega)$ into a sum of contributions from different regions of the BZ which we evaluate independently.

1) $\mathbf{k} \approx \mathbf{0}$ — Near the origin (a root of the second line of Eq. (6.46)), the dispersion is dictated by the multipole symmetries alone. It has an expansion $\omega(\mathbf{k}) \approx k^4 + \mathcal{O}(k^5)$ where $k \equiv \sqrt{k_x^2 + k_y^2}$. This is spherically symmetric and has the sub-diffusive scaling that one expects based on the fact that the model conserves dipole moments. This gives $N(\omega) \sim \int_0^{\omega^{1/4}} dk k \sim (\omega^{1/4})^2$ and a DOS $\rho(\omega) \sim \omega^{-1/2}$.

2) $k_x, k_y \approx \pi$ — At the corner of the BZ, the two lines of conserved momenta $k_x = \pi$ and $k_y = \pi$ meet (roots of the first line in Eq. (6.46)). Expanding around this point, we find $\omega(\mathbf{k}) \approx q_x^2 q_y^2$, where $k_i = \pi - q_i$. This situation is similar to the case of U(1) subsystem symmetries that was considered in Ref. [291], which has the same dispersion near the origin. There the two subsystem symmetries were related to the total magnetization along every row and column in the 2D lattice. This gives rise to a logarithmic correction to the DOS. The computation goes as follows: We write

$$N(\omega) = \int_{\omega(\mathbf{k}) \leq \omega} dq_x dq_y = \int_{q_x^{\min}}^{q_x^{\max}} dq_x q_y(q_x), \quad (6.47)$$

where $|q_x^{\min}|, |q_x^{\max}|$ are bounded such that the Taylor expansion around $k_x = \pi, k_y = \pi$ holds. Thus, $q_x^{\min} q_x^{\max} = \omega^{1/2}$ and we obtain

$$N(\omega) = a\omega^{1/2} + b\omega^{-1/2} \log(\omega) \sim \omega^{1/2} \log(\omega) \quad (6.48)$$

for small ω and for a, b real constants that depend on the cutoff q_x^{\max} .

3) $k_x \approx \pi, k_y \approx k^*$ — There is another similar point where the $k_x = \pi$ line of conserved momenta crosses the loop of conserved modes; this happens when $k_y = k^*$ where $\cos k^* = 1/3$. In fact, there are four such points in total, $(k_x, k_y) = (\pi, k^*), (\pi, -k^*), (k^*, \pi), (-k^*, \pi)$, each with identical contributions to the DOS. Expanding around one of these points, we again find $\omega(\mathbf{k} + \delta\mathbf{k}) \approx \delta k_x^2 \delta k_y^2$, so these also lead to the same contribution, $N(\omega) \sim \omega^{1/2} \log(\omega)$.

4) $k_x \approx \pi$, $k_y \not\approx k^*, \pi$ — Along the line $k_x = \pi$, but away from the aforementioned crossing points (call this distance ϵ), we have $\omega(\mathbf{k}) \approx q_x^2 f(k_y)$, where $f(k_y) = \cos^2(k_y/2)(3 \cos(k_y) - 1)$ depends on k_y and is finite everywhere in this regime. $N(\omega)$ is therefore

$$N(\omega) = \int_{\omega(\mathbf{k}) \leq \omega} dq_x dk_y \sim \int_{|k^*| + \epsilon}^{\pi - \epsilon} dk_y \frac{\omega^{1/2}}{\sqrt{f(k_y)}} \sim \omega^{1/2}, \quad (6.49)$$

which is approximately the area of a rectangle of width $\mathcal{O}(\omega^{1/2})$ and length $\mathcal{O}(1)$. This gives $N(\omega) \sim \omega^{1/2}$ and similarly for the line $k_y \approx \pi$.

5) The loop — Intuitively, the contribution of the loop is similar to the previous case: $N(\omega)$ counts the area of a ‘fattened’ loop, extended to a size $\sim \omega^{1/2}$ in the direction transverse to it and one expects a contribution of size $N(\omega) \sim \omega^{1/2}$. A more detailed calculation not included in this thesis, confirms this expectation.

All together — Most of the contributions scale $N(\omega) \sim \omega^{1/2}$ to leading order for small ω . The exception are the five points where different lines of conserved momenta cross, at which $N(\omega)$ has an additional logarithmic enhancement. These latter contributions dominate at the smallest frequencies, leading to $N(\omega) \sim \omega^{1/2} \log(\omega) + \mathcal{O}(\omega^{1/2})$. Taking a derivative, we get $\rho(\omega) \sim \omega^{-1/2} \log(\omega) + \mathcal{O}(\omega^{-1/2})$ and plugging this into Eq. (6.45) gives an autocorrelation $C(\mathbf{0}, t) \sim t^{-1/2} \log(t) + \mathcal{O}(t^{-1/2})$, which we numerically confirm in Fig. 6.4c.

The finite momentum contributions also lead to spatial oscillations of $C(\mathbf{x}, t)$ at short scales (see Fig. 6.4d), which can be clearly identified in its Fourier transform $\mathcal{C}(\mathbf{k}, t)$ shown in Fig. 6.4b, concentrated along the solutions of $\chi(\mathbf{k}) = 0$. Another consequence is that $C(\mathbf{r}, t)$ does not have full rotational but only the discrete rotational invariance of the gate, and concentrates around the two coordinate axes.

6.2.3. Generalization and extension to higher dimensions

Many other models which exhibit conserved momenta along various shapes in the BZ exist, including ones that do not conserve the total charge $\mathcal{Q} = \sum_{\mathbf{r}} s_{\mathbf{r}}$, and thus none of its multipole-moments. A couple of examples are shown in Fig. 6.6(a,b) as well as in Appendix E.1. Fig. 6.6a corresponds to a model with 5×5 local gates specified by the array of integers

$$n_{i,j} = \begin{pmatrix} -2 & 0 & 3 & 0 & -2 \\ 0 & -2 & 0 & -2 & 0 \\ 3 & 0 & 2 & 0 & 3 \\ 0 & -2 & 0 & -2 & 0 \\ -2 & 0 & 3 & 0 & -2 \end{pmatrix}, \quad (6.50)$$

while 3×3 gates were used to construct the model in Fig. 6.6b

$$n_{i,j} = \{n_{0,0}, n_{0,1}, n_{0,-1}, n_{1,0}, n_{-1,0}\} = \{+3, -1, -1, -1, -1\}. \quad (6.51)$$

This can be understood as a deformation of the discrete Laplacian model in Eq. (6.1) after replacing $4 \rightarrow 3$. Thus solutions of the recurrence relation are not longer in the kernel of the discrete Laplacian but rather eigenfunctions with non-vanishing eigenvalue, i.e.,

$$\alpha_{i,j} - \frac{1}{4}(\alpha_{i+1,j} + \alpha_{i-1,j} + \alpha_{i,j+1} + \alpha_{i,j-1}) = \frac{1}{4}\alpha_{i,j}, \quad (6.52)$$

resembling the eigenvalue problem $(\partial_x^2 + \partial_y^2)\alpha(x, y) = \lambda\alpha(x, y)$ in the continuum. Its characteristic function reads

$$\chi(\mathbf{k}) = 2(\cos(k_x) + \cos(k_y)) - 3, \quad (6.53)$$

whose solutions lie in the single loop that is close to a circle of unit radius, i.e., $\chi(\mathbf{k}) \approx k_x^2 + k_y^2 - 1$.

In general this construction can be reversed to construct models whose conserved momentum modes lie along particular paths and can be easily extended to higher dimensions. E.g., we can consider a 3D natural generalization of Eq. (6.30). The corresponding gate acts on a $4 \times 4 \times 4$ cube, moving charges between the inner 8 sites and the outer 8 corners. In this case one finds exact conserved quantities lying in intersecting 2D manifolds in momentum space as we show in Fig. 6.6d.

All these symmetries lead to different late-time scalings of the correlations, depending on the details of $|\chi(\mathbf{k})|$. The decay is at least as slow as $C(\mathbf{0}, t) \sim t^{-1/2}$, coming from the fact that expanding the dispersion along a co-dimension 1 hypersurface (a line in 2D or a surface in 3D) is formally similar to an expansion in one dimension. However, the actual behavior can be much slower than this. While the details of these shapes should show up in the spatial structure of $C(\mathbf{r}, t)$, the decay at $\mathbf{r} = \mathbf{0}$ is dictated by a few relevant features that enter into the calculation of $\rho(\omega)$. Similarly to the previous analysis for model Eq. (6.30), we can split up the calculation of $\rho(\omega)$ into two contributions: continuous lines and singular points (such as crossing points between two lines).

Along the lines, $N(\omega)$ is the area of a strip given by broadening the line to include points with $\omega(\mathbf{k}) \leq \omega$. The width of this strip depends on the expansion of ω along the transverse direction. Taylor expanding around a point \mathbf{k} on the contour of this line, we can write the leading order term as $\chi(\mathbf{k} + \delta\mathbf{k}) \approx (a\delta k_x + b\delta k_y)^m$, where $a, b \in \mathbb{R}$ generically depend on \mathbf{k} . We call m the *multiplicity* of the line: the simplest possibility, realized in the model (6.30), is $m = 1$ which gives $N(\omega) \sim \omega^{1/2}$ and thus $C(\mathbf{0}, t) \sim t^{-1/2}$. This is for example the case for the model specified by Eq. E.7 (see orange line in Fig. 6.6c). However, higher multiplicities are possible, as in the model shown on the left of Table 1 in Appendix E.1, where near the $k_x = 0$ axis, we have $\omega(\mathbf{k}) \sim k_y^4$ (and vice versa). In general, we then get $N(\omega) \sim \omega^{1/2m}$ which leads to a contribution $C(\mathbf{0}, t) \sim t^{-1/2m}$ in the autocorrelation.

An enhanced contribution to the DOS can arise from *singular points*, where the leading order Taylor expansion of $\chi(\mathbf{k})$ does not have the form $(a\delta k_x + b\delta k_y)^m$. This can occur for various reasons: (i) at isolated points, (ii) at a meeting point of multiple branches of the curve, or (iii) if the form of the expansion changes at a point along the curve. In our list of singular points, (iv) we also include points where two or more lines touch: while in this case we do have an expansion of the above form, with $m > 1$, the value of m changes discontinuously as we move away from the touching point.

Without loss of generality, we can write the leading term in the Taylor expansion of the characteristic function around a point as [326]

$$\chi(\mathbf{k} + \delta\mathbf{k}) \approx \prod_i (a_i \delta k_x + b_i \delta k_y)^{m_i}, \quad (6.54)$$

where the coefficients a_i, b_i might be complex in general. When a_i/b_i is real, we can picture the corresponding term as the tangent of the curve at the meeting point \mathbf{k} , each appearing with some multiplicity m_i . $m_i > 1$ might occur because the line in question itself has a non-trivial multiplicity, or because two different lines share the same tangent, i.e. when they have a touching point at \mathbf{k} . Terms where a_i/b_i is complex are singularities that do not arise from the meeting of contour lines; an extreme example is an isolated singular point (such as $\mathbf{k} = \mathbf{0}$ for Eq. (6.34)).

In general, contributions from singular points can lead to three different scalings of $N(\omega)$ depending on the ratio between the total multiplicity $m = \sum_i m_i$ and the largest m_i in expression (6.54)

- if $2m_i < m$ or \mathbf{k} is an isolated point then $N(\omega) \sim \omega^{1/m}$,

- if $2m_i = m$ then $N(\omega) \sim \omega^{1/m} \log(\omega)$,
- if $2m_i > m$ then $N(\omega) \sim \omega^{1/2m_i}$,

to leading order. Notice that the condition $2m_i > m$ is equivalent to $m_i > \sum_{j \neq i} m_j$, such that one tangent line dominates over all the others. In this case, the DOS has an entirely different power law than what the naive dimension counting $\omega \sim k^{2m}$ would suggest; consequently correlations have a slower decay $C(\mathbf{0}, t) \sim t^{-1/2m_i}$. A simple situation where this occurs is a point where two lines have a touching point. The details of this general analysis and its application to other 2D models are provided in Appendix E.1.

6.3. Conclusions and outlook

In this chapter we have generalized the notion of spatially-modulated symmetries from 1D to higher-dimensions. These include already known examples, like U(1) subsystem symmetries and the conservation of multipole moments of the charge. On the one hand, the existence of not only a finite but an infinite number of symmetries, opens the possibility to construct conserved quantities with intricate spatial structure, which can lead to (provable) finite boundary correlations. We also found that these can lead to a whole hierarchy of subdiffusive behavior with complicated spatial correlations.

However, while we uncovered some of the ins and outs and consequences of such a rich structure, many open questions have appeared on the way. A natural question is how to construct a complete hydrodynamic description, which could be used to predict the long-time behavior of the spin-spin correlations, including the spatial structure. One could decompose the spin density as $s(\mathbf{r}) \sim \sum_{\{\mathbf{k} | \chi(\mathbf{k})=0\}} \mathbf{e}^{i\mathbf{k} \cdot \mathbf{r}} \mathfrak{s}_{\mathbf{k}}(\mathbf{r})$, and construct a hydrodynamic theory for the relevant long-wavelength degrees of freedom $\mathfrak{s}_{\mathbf{k}}(\mathbf{r})$'s, which could be further constrained by the conservation of higher-moments of the charge. Although addressing a different question, this approach is similar to the expansion of the UV boson (fermion) in terms of low-energy degrees of freedom lying close to the Bose (Fermi) surface (see e.g., Ref. [298]). In fact, this is the reason such lattice-scale oscillations are observed in the spin correlations. However, the situation can become rather complicated in two and higher spatial dimensions, where infinitely many momenta lie along different intricate shapes in the BZ. The derivation of an appropriate hydrodynamic description is then an interesting challenge that I would like to pursue in a future work. On the same line of thought, generalizing the analysis of the decay of spin correlations to 3D remains open. This now requires considering surfaces intersecting with other surfaces as well as with one-dimensional manifolds.

Moreover, we focused on the effects of such symmetries on classical “infinite temperature” dynamics. However, the presence of these symmetries can have also strong effects on the low-temperature physics of the associated quantum models. Analogous to the previous chapter, a model with local gates $G_{\mathbf{r}} = n_{i,j}$ can be mapped to a local quantum Hamiltonian where each integer $n_{i,j}$ is mapped to a raising/ lowering (or creation/ annihilation) operator depending on the sign of $n_{i,j}$ which acts on a site (i, j) , $|n_{i,j}|$ times. Such systems are related to the previously studied models with Bose surfaces [294–298, 301] and to the current effort to understand the proper formulation of quantum field theories as appearing in the continuum limit of systems with unconventional symmetries, which in turn relates to the phenomenon of ‘UV/IR’-mixing [299, 300, 327]. In fact, motivated by some of these works, I find interesting the question of how to properly gauging such symmetries.

Our construction of localized symmetries at the boundaries of the system also opens up a new exciting possibility: Systems with strong zero modes [184] in more than 1D. In fact these systems can include additional \mathbb{Z}_2 symmetries, which anticommutes with *all* the modulated ones [325]. Understanding whether the existing definition of strong zero

mode [184] is compatible with these charges (which are not exponentially localized at the boundary of the system), or possible connections to topologically ordered systems, are also questions worth exploring.

7. Conclusions and outlook

In this thesis, we discussed several topics ranging from classical to quantum dynamics, focusing on the role of symmetries and the notion of symmetry itself. To do so we combined two main tools: Simple toy models that allowed us to have a deep understanding of the system in question, and extensive numerical calculations that allowed us to validate our understanding and overcome potential analytical limitations. Our main goals were to elucidate the constraints that assuming an unconventional symmetry enforces on the system dynamics with special focus on quantum thermalization, and using this knowledge, explain experimental observations and theoretically explore new scenarios. In the following, we summarize the main conclusions reached in this thesis and discuss possible future research directions. We expand some of those that were already suggested at the end of each chapter, and provide a bird's-eye survey of relevant open questions. I believe the results discussed in this thesis will serve as a solid ground to pursue them and to expand our understanding on the role of symmetries on the behavior of classical and quantum systems in- and out-of-equilibrium.

7.1. Part I: Hilbert space fragmentation

Summary. In the first half of Part I, we focused on systems with charge and dipole conservation. We showed that this combination leads to an extensive fragmentation of the Hilbert space, which in turn can lead to a breakdown of thermalization. For a one-dimensional spin-1 minimal model, we found that the infinite temperature auto-correlation saturated to a finite value, showcasing non-thermal behavior. We identified the absence of thermalization as a consequence of the *strong fragmentation* of the Hilbert space into exponentially many invariant subspaces in the local S^z basis, arising from the interplay of dipole conservation and local interactions. We then extended the model and found that this perturbation leads to a *weak fragmentation*: the system still has exponentially many invariant subspaces, but they are no longer sufficient to avoid thermalization for typical initial states. More generally, for any finite range of interactions, we showed that the system is still fragmented leading to (exponentially many) non-thermal eigenstates appearing throughout the entire spectrum. We then compared our results to charge and dipole moment conserving random unitary circuit models. This led us to the conclusion that indeed, the same fragmented structure is found in other implementations of the dynamics with the same symmetries, highlighting that the fragmented structure is completely specified by the local dynamics.

In Chapter 3 we then found the second main conclusion of this part, namely, that the existence of an extensive number of non-local but yet *statistically localized integrals of motion* (SLIOMs) is a sufficient condition for fragmentation to arise. We identified such conserved quantities in the relevant dipole-conserving model (as well in other related systems), which allowed us to analytically characterize the complete fragmented structure. At this stage we found the extremely rich dynamics fragmented models can offer, with different fragments displaying completely distinct phenomenology including thermalizing and non-thermalizing behavior. This corresponds to the third important conclusion of this part. Moreover, armed with the SLIOMs, we were able to show that these systems host *strong zero modes* (SZM), leading to finite boundary magnetization and an exact

degeneracy of the many-body spectrum in the presence of an additional (anticommuting) symmetry. From here, we also analytically confirmed the finite saturation value of spin correlations for the strongly-fragmented minimal model with dipole conservation.

Outlook. As we thoroughly discussed in Section 3.5.3, one could argue that SLIOMs should also be resolved when studying thermalization properties of the system. In this restricted setting, one can then find (exponentially large) subspaces where ETH holds [2, 260], and even study the MBL phase transition [7, 328]. Nevertheless, one can also find equally meaningful counter-arguments to avoid resolving such non-local conserved quantities (see Section 3.5.3), as for example, whether then projectors on energy eigenstates should also be accounted for. Hence, a certain level of ambiguity lies on specifying what entitles a conserved quantity to be fixed when studying quantum thermalization in a many-body system. Resolving this could shed some light on previous discussions appearing in the literature [42, 204, 205] and in general on the role of conservation laws when investigating the ETH and quantum thermalization.

In the following, we discuss other open questions that emerged when studying the phenomenon of Hilbert space fragmentation.

- **Lattice gauge theories.** On a lattice, gauge invariance translates into the existence of extensively many *local conserved quantities* — Gauss law. This splits up the Hilbert space into (exponentially many) super-selection sectors which correspond to different physical scenarios. Hence, the system is usually assumed to belong to a specific super-selection sector. However, recent studies discussed the possibility of considering initial states which have weight on all possible superselection sectors. This was shown to lead to localized dynamics where an effective disorder potential would emerge as a result of combining different background charges [38, 39, 141].

While LGT could be labeled as “locally” fragmented due to the extensive number of conserved quantities, their local support clearly differs from that of SLIOMs and hence the structure is rather different. Thus, it would be useful to precisely relate the fragmentation arising in the models we introduced in Chapter 2 to those for lattice gauge theories [38, 39]. Can we understand certain lattice gauge theories as a limiting case of fragmentation? In particular, one could understand certain fragmented models as a “linear combination” of LGT where the non-local conserved quantities responsible for fragmentation, are generated via non-local combinations (and products thereof) of (now broken) localized Gauss laws. Moreover, simple LGT have been shown [329] to be equivalent to the PXP Hamiltonian which was utilized to explain the experimental observations in Ref. [43], which we know can be related to dipole-conserving spin chains (see Section 3.3). Thus, it is a relevant question to understand how these three different phenomena relate to each other.

- **Continuum theories.** The phenomenon of fragmentation has been so far addressed in lattice models with a finite dimensional local Hilbert space (see reviews [221, 330])). However, it is unclear whether this phenomenon can occur for either lattice models with infinite-dimensional Hilbert spaces, or alternatively, for theories in the continuum. For the former, we developed the understanding that replacing the local spin degrees of freedom in the dipole-conserving models considered in Chapter 2, by an infinite-dimensional local Hilbert space (unbounded from both above and below), would not lead to fragmentation. However, a general statement about this impossibility is still missing. On the other hand, whether a continuum theory can showcase fragmentation and how to technically deal with it, could become relevant when addressing the low-energy physics of fragmented systems, specially those whose

fragmented structure is not analytically known. This could relate to the ongoing effort to properly formulate the continuum theory description of certain lattice models in presence of subsystem symmetries [297, 299–301].

- **Quantum correlations.** The examples of Hilbert space fragmentation that appeared in this thesis occurred with respect to a many-body basis which involves no (neither long nor short) quantum entanglement. In particular, that was the reason to utilize classical cellular automaton in order to study certain features that arise as a direct consequence of this fragmented structure [6, 291, 292, 331, 332]. However, it is not clear the role that quantum correlations play in these systems, and whether these can lead to effects that depart from the “classical” behavior. On the one hand, it would be interesting to understand whether for example, similarly to Ref. [333], one can make use of the constraints to prepare highly entangled many-body states from simple initial product ones. A different approach to understand the role of quantum correlations was pursued in Ref. [166], which introduced a family of models showcasing strong quantum fragmentation, i.e., strong fragmentation in an entangled basis, together with a general formalism in terms of commutant algebras (see the more extended discussion of Section 3.5.1). The authors concluded that quantum fragmentation appears when the commutant algebra is non-Abelian, hence providing a potential — not yet exploited— constructive way to obtain other quantum fragmented models. While it is still unclear whether one can extend the construction of Ref. [166] to weakly quantum fragmented systems, it would be interesting to follow a similar path that the one taken in Chapter 2, and study the difference between strong and weak quantum fragmentation. In particular, understand whether quantum correlations can change the universal properties of the freezing transition study in Ref. [178] for dipole-conserving systems.

7.2. Part II: Experimental realization in tilted interacting systems

Summary. In Part II we turned our attention to the experimental realization of fragmented Hamiltonians. With this aim and inspired by actual experimental setups, we considered a one-dimensional system of interacting particles in the presence of a tilted (i.e., linearly growing) potential that couples to the center of mass of the system. We found that in the strong tilted regime, the physics can be approximated by an effective dipole-conserving Hamiltonian that resembles those we encountered in Part I. We also explored other parameters regimes where the dynamics was governed by a kinetic constrained Hamiltonian which to a finite-evolution time features the phenomenon of Hilbert space fragmentation. Hence, it is possible to explore the physics of Hilbert space fragmentation in the lab, which turns into the first main conclusion of this part. At the same time, this system has been predicted to be many-body localized for sufficiently strong tilts in the presence of interactions (Stark MBL [76, 157]) when an additional weak disorder or a residual harmonic potential is present, hence coexisting with the approximate dipole-conserving regime. The extraordinary level of control of current experimental setups for which the system can be assumed to be isolated for really long times (of the order of 700 tunneling times in units of the hopping rate), permits to address these questions experimentally, going beyond current computational techniques. In particular, this is achieved by an interacting (degenerate) fermionic gas of ultracold atoms trapped in an optical lattice in the presence of a gradient magnetic field, which implements the linear potential [3, 4]. The experimental results show evidence that even for intermediate values of the tilt and close to a resonance between the tilt and the interaction strength, the system appears to retain

memory of the initial state. Using the effective dipole-conserving Hamiltonian, together with energetic and perturbative arguments, we provided a physical argument that would explain such non-ergodic behavior at finite observational times. However, whether such non-ergodic behavior corresponds to a transient pre-thermal regime, or indeed lasts to infinite times still requires additional work. Nonetheless, the second main conclusion of this part is the use of ultracold atoms as a powerful tool to realize different dynamical regimes whose dynamics are governed by kinetically constrained systems.

Outlook. These novel theoretical and experimental results could be used to address relevant open questions that remain unanswered.

- **Initial state dependence.** In this thesis we discussed an experimentally feasible approach to study phenomena that appears as a consequence of a fragmented Hilbert space. Although a first proof of principle was put forward in Ref. [4], it would be interesting to systematically study the dependence on the initial state and the time scales for which the fragmented effective Hamiltonian is a good approximation. Moreover, this analysis could shed light on the nature of Stark MBL in comparison to the standard disorder-induced MBL [34, 130, 132], and the role of additional experimental contributions that depart from the ideal model. In fact, as we discussed in Section 4.6, such questions could significantly benefit from recent experimental developments as the quantum gas microscope [152, 153], which performing on-site measurements and manipulations allows to investigate the evolution of other local observables from specific initial states; and the possibility to perform randomized measurements, to study the evolution of the n th-order Renyi entropies (see review [276]) in the regimes of interest. The combination of these two developments would let us explore the rich dynamics of fragmented models, which include fragments with integrable, non-integrable as well as other constrained behavior, answering questions regarding their restricted transport and thermalization properties, hence exploring Krylov-restricted thermalization [260]. These tools would also allow to characterize the regimes where Stark MBL is expected, by even studying the information propagation using the evolution of the experimentally measurable Renyi entropies.
- **1D to 2D crossover.** How does Stark MBL depend on the spatial dimension? The authors of Ref. [113] studied the time decay of different initial density wave configurations in a 2D optical lattice (i.e., confined to two spatial dimensions) in the presence of a tilted potential that was aligned along one of the coordinate directions. The authors found that the system did thermalize for different initial wavelengths, although in a subdiffusive manner for sufficiently long ones that could be described in terms of a classical hydrodynamic theory [98, 102]. This was built from the assumption that the system has reached local equilibrium, related to the absence of tilt in the orthogonal direction. Instead, the experimental results of Ref. [3] (and partially discussed in Chapter 4) for a tilted one-dimensional system showed non-ergodic behavior for very long times. Therefore, a natural question is how to reconcile these two results. Among other important points, this requires understanding the dependence of the observed results on the prepared initial states, e.g., whether the 2D system thermalizes at the observational times when preparing a charge density wave configuration analogous to the 1D setting of Ref. [3]; and also on the tilt direction. In particular, certain “misalignment” between the tilt and the lattice has been argued to induce dipole (and potentially quadrupole) conservation in 2D [181]. Moreover, it would also be interesting to understand the transient regime where the microscopically dipole-moment, approximately conserved for sufficiently strong tilts, becomes only “macroscopically” conserved at long distances.

7.3. Part III: Modulated symmetries in 2D

Summary. In Part III we extended the family of spatially-modulated symmetries, which includes multipole-moment and subsystem symmetries as particular examples. Appearing as solutions of discrete recurrence relations, we uncovered new instances that in one-dimension included (quasi)-periodic modulations of a local density, exponentially localized symmetries at the boundary of the system and combinations thereof. In higher dimensions, the number of such symmetries can scale with the linear system size and be combined to give rise to much richer structure. We showed that these can take the form of lines and surfaces of conserved momenta, extending quasi-periodic symmetries from one to higher dimensions; or lead to infinitely many charges localized at the boundaries of the system. In particular, we could exactly obtain the latter by phrasing the problem in terms of discrete harmonic functions. These novel conserved quantities provide long-lived modes that govern the late-time dynamics of certain observables. In particular, we developed a hydrodynamic theory to predict the late-time dynamics of spin-spin correlations. For charge and multipole-moment conservation, this led to a generalized diffusion equation where charge is sub-diffusively transported while preserving its higher-moments. Instead, in the absence of charge conservation or in the presence of finite momentum modes, we obtained exotic forms of sub-diffusive behavior whose scaling is controlled by the particular geometry of conserved modes in the Brillouin zone, and a rich spatial structure influenced by lattice-scale features. On the other hand, symmetries localized at the boundary gave rise to finite boundary correlations, which instead vanished in the bulk of the system. As in Part I, we found that in the presence of an additional anti-commuting symmetry, the quantum many-body spectrum is at least two-fold degenerate, hence providing a novel approach to construct SZM beyond one dimension.

Outlook. The relative novelty of the new classes of spatially-modulated symmetries presented in this thesis, leads to many open questions. In this context, the most pressing one is to understand the level of fine-tuning of the models we discussed. For example, what minimal mathematical structure we need to impose to realize such symmetries, or whether to which extend and circumstances they can be approximately conserved to observe similar phenomena. In the following, we provide some other future directions that naturally emerge as a result of this thesis.

- **Strong zero modes.** In this thesis we discussed two different generalizations of SZM, which in short are approximately conserved quantities which are localized at the edges of the system [184, 186]. The first appeared as the boundary SLIOMs in systems with strong fragmentation (Chapter 3), which pretty much fell under the existing definition of SZM appearing in Ref. [184, 185], except from the fact these are exact and are only exponentially localized with respect to the Frobenius norm. The second appeared as particular instances of spatially-modulated symmetries in one (Chapter 5) and higher spatial dimensions (Chapter 6). Moreover, unlike standard SZM, we already noticed that such conserved quantities have an extensive spectrum, and are exactly conserved for all system sizes. Hence, while both lead to finite boundary correlations and an at least, two fold degeneracy of the many-body spectrum, it is not clear these can be considered the same beast. Reconciling these apparently similar manifestations by revisiting the existent definition of SZM would be a fruitful path to deepen our understanding of strongly interacting systems.
- **Hydrodynamic theory.** In Chapters 5 and 6, we provided a general protocol to predict the late-time decay of spin auto-correlations. We referred to this as *hydrodynamic description*, since it was inspired by linear hydrodynamics, i.e., we

assumed a close linear equation relating the time derivative of the correlation function with itself. However, as we also discussed, a proper hydrodynamic formulation of the theory should have dealt with the relevant long-wave length degrees of freedom associated to the (potentially infinite) many conserved modes [98, 101]. This would allow us not only to probe the system, but have a complete understanding of the underlying physics, including the coupling between different hydrodynamic modes, possible instabilities of the resulting hydrodynamic theory [293], and perhaps to realize systems that approximately rather than exactly have the same conserved modes.

- **Bose surfaces.** We focus on the role of spatially-modulated symmetries at infinite temperature, averaging over all compatible configurations. However, such symmetries could play even a greater role at low-temperatures. The intricate shapes of conserved momenta that we found in Chapter 6 reminds of the Bose (and Fermi) surfaces studied before in the literature [294–298], which even not being exactly conserved, appear to give a robust phase of matter at low-temperature. Moreover, the proper effective field theory derivation of these models is a topic of current research [299, 300], which is expected to deepen our understanding of quantum field theory as well as its potential limitations. On the other hand, models with symmetries localized at the boundary of the system reminds of topological phases of matter where gapless modes circulate along the boundaries in two and higher spatial dimensions. In the line of Ref. [334], which managed to relate certain higher order topological insulators and fracton systems, it is still an open question to understand the precise relation between those topological orders and the systems with localized boundary symmetries we introduced in this thesis.
- **Experimental realization.** We started this thesis noticing that dipole-conservation was a rather unconventional symmetry, which we would not have expected to find in Nature. However, in Chapter 4 we found out that these become useful to describe systems in the presence of a strong tilted field [3, 113, 181, 251, 260]. With a similar spirit, I wonder whether other spatially-modulated symmetries, *a priori* unconventional, could become pertinent to understand the physics of other experimentally relevant regimes. This appears to be the case for 1D systems with quasi-periodic symmetries of the general form $\Delta \sum_j \cos(kj + \varphi) \hat{n}_j$ for any (detuning) strength Δ and phase off-set φ . Such quasi-periodic local potentials can be experimentally realized in ultracold atoms, allowing for a high level of tunability of the parameters k , Δ and ϕ [37, 319]. Therefore, analogous to the discussion in Chapter 4 and in the presence of interactions, the strong detuning regime can be approximately described by a system with modulated symmetries¹. In fact, these systems have been already experimentally studied [37, 319] in the context of MBL. In the absence of interactions, this is known as Aubry-André model [336] and it has been shown to give rise to a localized-to-delocalized phase transition as a function of Δ [336–338]. Similarly, it is believed that when interactions are present, the system becomes localized for sufficiently strong detuning [37, 319, 339–341]. However, our previous derivation appears to suggest that one can find certain resonant processes that eventually can delocalize the system. A more careful analysis is still required to answer this question.
- **The notion of symmetry.** In Chapter 5 and Chapter 6, we introduced a way to construct novel microscopic models with spatially-modulated symmetries. However,

¹Notice, that the resulting effective Hamiltonians will also have particle number conservation. Nevertheless, one can avoid this circumstance starting from e.g., the transverse field Ising model [335].

these were restricted to appear as solutions of linear recurrence relations, and thus as linear combinations of powers of algebraic numbers. Essentially, these gave rise to two main classes of modulations: hyperbolic and sinusoidal. For example, this derivation cannot capture spatial modulations of the form $\alpha_j = \pi^j$ or $\alpha_j = \log(j)$. The ultimate question we would like to address is: What are the possible symmetries a system can have? It is clear that answering this question requires imposing meaningful physical limitations. For example, we should require the system to lead to non-trivial dynamics as otherwise, such system would trivially conserve any quantity. E.g., can a given symmetry sector for the quantity $\sum_j \pi^j S_j^z$ being non-trivial? Locality also appears to be relevant in the discussion. Answering this question is an endeavor worth to follow.

Many interesting ideas are still waiting to be explored. This thesis represents a step forward in this direction.

Appendices

A. Additional results for dipole-conserving chains

In this appendix we gather additional numerical evidence which support the results presented in Chapter 2. We start by numerically identifying the largest symmetry sector ($(q, p) \approx (0, 0)$ with $(q, p) = (0, 0)$ for particular system sizes) in Section A.1 and showing the distributions of fragments sizes and operators weights when restricted to it. We then provide additional numerical results for the finite-size scaling of spin auto-correlations, as well as for the scaling of frozen states, the Mazur bound and the dimension of the largest fragment within the symmetry sector $(q, p) = (0, 0)$ (Section A.2). Finally, we provide in Section A.3 numerical results for the operator spreading of a local charge density operator $S_0^z(t)$, which gives another measure of localization. This contributes to showing the distinction between the strongly- and weakly-fragmented cases.

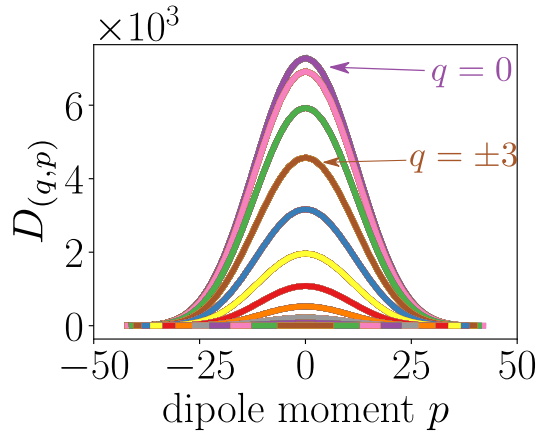


Figure A.1.: Distribution of dimensions $D_{(q,p)}$ for the $\mathcal{H}_{(q,p)}$ invariant subspaces. Each curve corresponds to a subspace with fixed charge q .

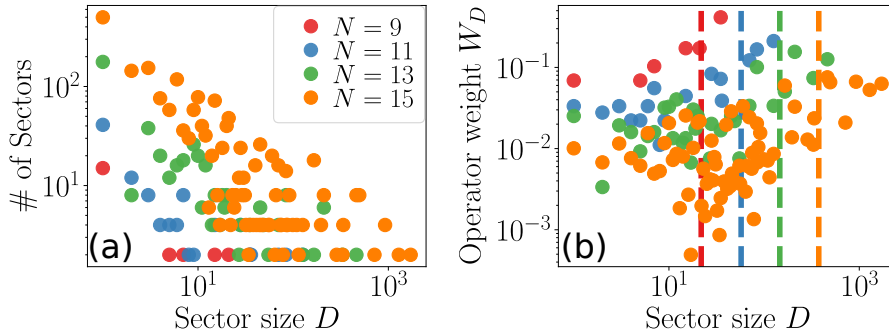


Figure A.2.: (a) Distribution of sector sizes D with $\mathcal{H}_i \subset \mathcal{H}_{(0,0)}$ for the Hamiltonian H_3 . (b) operator weight distribution W_D . Both plots are similar to the full distributions shown in the main text. The vertical dashed lines in (b) indicates the average sector size, which grows exponentially in system size, but is nevertheless exponentially smaller than the largest sector.

A.1. Largest charge and dipole symmetry sector

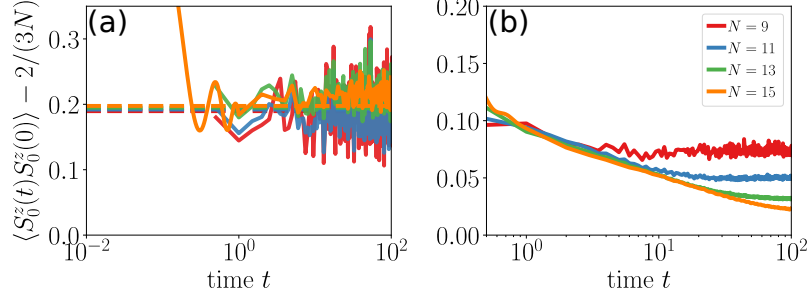


Figure A.3.: Finite size scaling for the auto-correlation function $\langle S_0^z(t)S_0^z(0) \rangle$ at infinite temperature in the full Hilbert space after subtracting the thermal value. Panel (a) shows a finite value for the auto-correlation under the evolution of H_3 in Eq. (2.1). The dashed lines show the lower bound in Eq. (A.1). (b) The auto-correlation function decays to zero with system size once the longer range-interaction H_4 in Eq. (2.2) is added to H_3 .

A.1. Largest charge and dipole symmetry sector

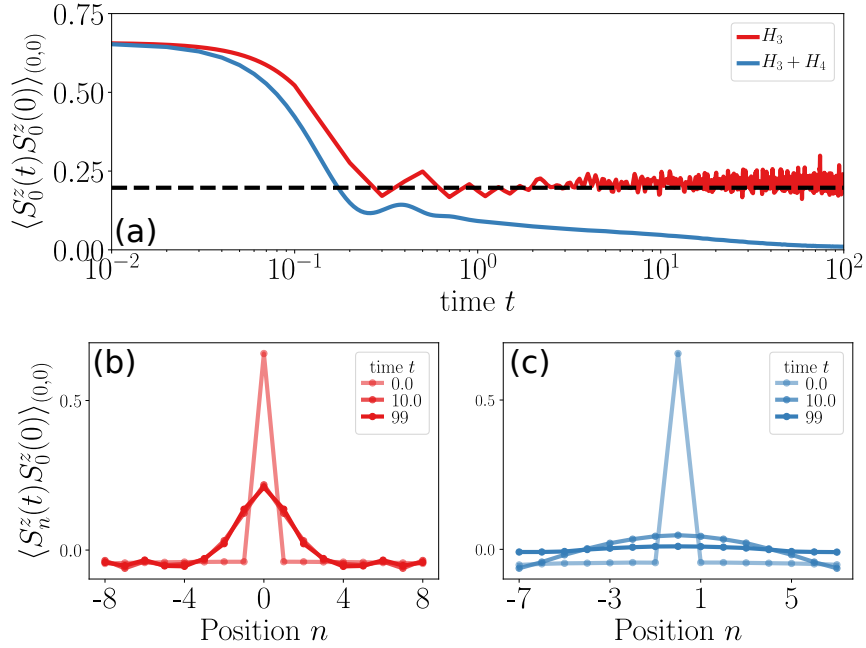


Figure A.4.: (a) Auto-correlation function (upper panel) $\langle S_0^z(t)S_0^z(0) \rangle_{(0,0)}$ in the symmetry sector $q = p = 0$ at infinite temperature for H_3 (red curve) and $H_3 + H_4$ (blue curve) for $N = 15$. Spatially resolved correlation functions for (b) H_3 and (c) $H_3 + H_4$.

While analytical formulae for the size of a symmetry sector with a given total charge q can be obtained for a given spin representation S in terms of binomial coefficients, the counting becomes quite cumbersome when restricted to a given global dipole moment p . This counting can be re-formulated as the number of possible restricted compositions (i.e., partitions of a number where the order of the summands matters) of length N where each summand can only take $2S+1$ values, for which I am not aware of an analytical expression. Instead, we numerically obtain these counting for several system sizes. Fig. A.1(b) shows the size of the symmetry sectors with different global quantum numbers q and p for spin representation $S = 1$ and system size $N = 13$. Note that this distribution is independent

Appendix A. Additional results for dipole-conserving chains

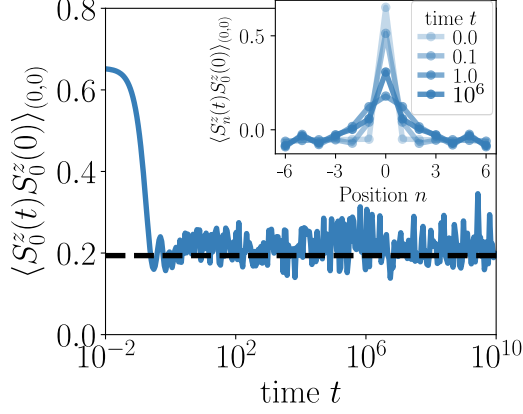


Figure A.5.: Evolution of the auto-correlation function $\langle S_0^z(t)S_0^z(0) \rangle_{(0,0)}$ for the Hamiltonian H_3 and system size $N = 13$, where longer time scales $t \sim 10^{10}$ can be numerically reached. We observe the same qualitative behavior as in Fig. 2.1.

of the specific Hamiltonian under study. Each curve corresponds to a fixed value of the charge quantum number q . The dimension $D_{(q,p)}$ decreases with increasing absolute value of the charge. The distributions for $+q$ and $-q$ coincide due to time reversal invariance, the way we have chosen the reference site n_0 , and labeling the sites in the chain. A different labeling of sites, would simply shift the mean value of both distributions symmetrically with respect $p = 0$. We also observe that the distribution attains a maximum at the $(0,0)$ -sector, as claimed in the main text. In addition, we obtain symmetric distributions because P changes sign under inversion, while Q is invariant.

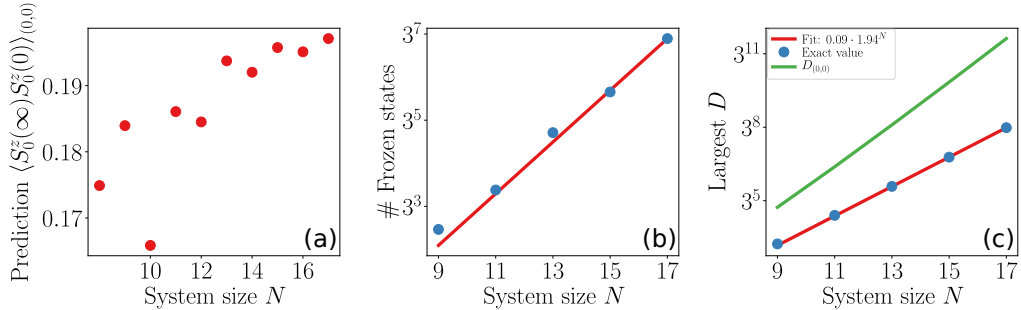


Figure A.6.: Scaling within the $q = p = 0$ sector for Hamiltonian H_3 . (a) Scaling of the lower bound $\lim_{T \rightarrow \infty} 1/T \int_0^T dt \langle S_0^z(t)S_0^z(0) \rangle_{(0,0)}$ with system size. (b) Scaling of the number of frozen states. (c) Scaling of the largest sector dimension (blue dots) in comparison to the dimension of the $(0,0)$ sector (green line).

Finally, we show the sector size and the operator weight distributions with $W_D \equiv \sum_{D_i=D} \text{tr}(Z_i^2) / \left(\sum_D \sum_{D_i=D} \text{tr}(Z_i^2) \right)$ for invariant subspaces within the largest (q,p) -sector, i.e., $q = p = 0$. Fig. A.2(a) shows qualitatively the same sector size distribution as in Fig. 2.3(c) in the full Hilbert space. Fig. A.2(b) also reflects the main properties of the operator weight distribution, featuring a wide distribution with significant weight on small sectors.

A.2. Finite-size scaling of the autocorrelator

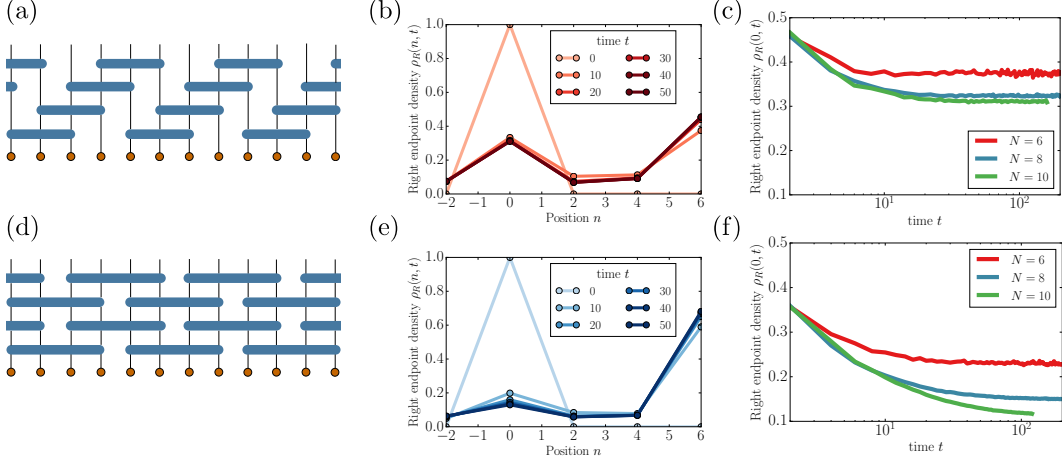


Figure A.7.: Operator spreading of $S_0^z(t)$ for random circuits with gate sizes $l = 3$ and 4. Panels (a) and (d) show the circuit geometries, slightly modified from the ones in the main text in order to ease numerical calculations. (b) and (e) show the profile of right endpoint weights $\rho_R(n, t)$ at different times for a 10-site chain, for $l = 3$ and $l = 4$ respectively. Both have a peak near the origin, but in the former case it is much larger and stops decaying after a few time steps, while in the latter case it keeps decaying to longer times. Finite size flow of the size of the peaks as a function of time, shown in (c) and (f) indicates that while for $l = 3$ the system saturates to a finite value, this is not the case for $l = 4$, where the long-time value scales to zero for large system sizes.

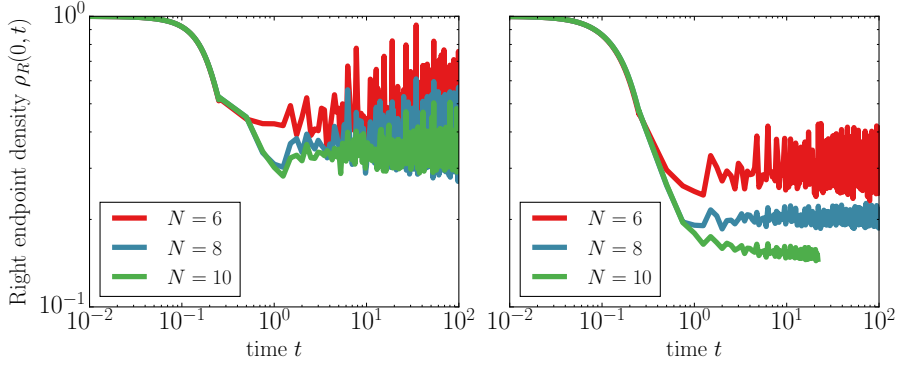


Figure A.8.: Height of the peak in ρ_R of $S_0^z(t)$ obtained for Hamiltonians H_3 (left) and $H_3 + H'_4$ (right).

A.2. Finite-size scaling of the autocorrelator

In this section we present in more detail the finite size scaling of the auto-correlation function and its lower bound.

First, we discuss the scaling of the auto-correlation function $\langle S_0^z(t)S_0^z \rangle$ at infinite temperature in the full Hilbert space in Fig. A.3 for both the minimal model H_3 in Eq. (2.1) and the combined Hamiltonian $H_3 + H_4$. On the one hand, the minimal model realizes a finite saturation value at long times which slightly grows with system size as can be seen in Fig. A.3(a). On the other hand, when the combined Hamiltonian $H_3 + H_4$ is considered, the auto-correlation decays to zero with system size. This agrees with the discussion in the main text, where it was argued that for longer range Hamiltonians, the system thermalizes

and the correlation decays to zero at long times in the thermodynamic limit.

Moreover, as we discussed in the main text, not only the auto-correlation function in the full Hilbert space shows a non-thermal (thermal) behavior for H_3 ($H_3 + H_4$). We can also realize this behavior within a specific restricted symmetry sector. In Figs. A.4(a) we show the behavior of the auto-correlation function $\langle S_0^z(t)S_0^z \rangle_{(0,0)}$ in the largest (q,p) -symmetry sector, $q = p = 0$, and size $N = 15$ showing the same qualitative behavior: a finite saturation value at long times for H_3 (panel (a)) and thermalization for the combined Hamiltonian $H_3 + H_4$ (panel (b)). Note that since charge is conserved and we evaluate the correlation within the $q = 0$ sector, $\sum_n \langle S_n^z(t)S_0^z(0) \rangle = 0$ at all times and thus the surface under the peak must add up to zero.

Moreover, in Fig. A.5, we show the persistence of the non-thermalizing behavior for H_3 at longer times $t = 10^{10}$ for smaller system size $N = 13$ and within the $(0,0)$ -sector. The space resolved correlation function is also shown in the inset showing the absence of thermalization even at long time scales.

In Fig. A.6(a) we show the scaling of the lower bound $C_0^z(\infty)$ in Eq. (2.5) with system size N restricted to the $(0,0)$ symmetry sector of H_3 . In this case the lower bound takes the form

$$\lim_{T \rightarrow \infty} \frac{1}{T} \int_0^T dt \langle S_0^z(t)S_0^z(0) \rangle_{(0,0)} \geq \frac{1}{D_{(0,0)}} \sum_{\mathcal{H}_i \subset \mathcal{H}_{(q,p)}} \frac{1}{D_i} [\text{tr}(Z_i)]^2. \quad (\text{A.1})$$

We observe that the value increases with N and realize an even-odd dependence on N decreasing with system size. In addition, Figs. A.6(b-c) show, respectively, how the number of frozen states and the size of the largest invariant subspace within the $(0,0)$ symmetry sector grow with system size. Since the largest sector does not scale with the size of the entire Hilbert space, the lower dimensional sectors become thermodynamically important. Compare for example with a spin 1/2 chain with charge conservation only. The dimension of the full Hilbert space is 2^N and the largest (zero charge) subspace scales as $\sqrt{1/N} \cdot 2^N$; hence, the exponents are the same up to logarithmic corrections.

A.3. Operator spreading of $S_0^z(t)$

Here we consider another measure of localization, that contains complementary information about the Heisenberg picture evolution of the charge density operator $S_0^z(t)$ compared to its auto-correlation function. In particular we look at how S_0^z spreads out in the space of all possible operators, becoming a complicated superposition of many operators, and how its spatial support grows in time.

In order to do this, we first need to introduce a local basis in the space of operators acting on a single site of the spin chain. For the spin-1 models we consider, such a basis consists of 9 linearly independent operators that span the entire space of on-site operators. A possible choice is given by the 8 Gell-Mann matrices, together with the identity $\mathbb{1}$. Let us denote these as λ^a for $a = 0, \dots, 8$, where $\lambda^0 \equiv \mathbb{1}$. A basis of operators on the entire chain is then given by products of such local basis elements of the form $\lambda^{\mathbf{a}} \equiv \bigotimes_{n=-N/2}^{N/2} \lambda_n^{a_n}$, labeled by a list of N indices $\{a_n\}$. These operator strings form an orthonormal basis in the Hilbert space of operators with respect to the Frobenius inner product $\langle A, B \rangle \equiv \text{tr}(A^\dagger B)/3^L$ where A and B are two arbitrary operators, and \dagger is the adjoint operation.

Given such a basis, one can always expand the time evolved operator as

$$S_0^z(t) = \sum_{\mathbf{a}} c_{\mathbf{a}}(t) \lambda^{\mathbf{a}}. \quad (\text{A.2})$$

A.3. Operator spreading of $S_0^z(t)$

The coefficients $c_{\mathbf{a}}(t)$ characterize how $S_0^z(t)$ spreads out in the space of all possible operators. In particular, focusing on spatial spreading, it is useful to classify the basis strings $\lambda^{\mathbf{a}}$ according to their right endpoints (assuming open boundary conditions), i.e., the rightmost site n such that $\lambda^{a_n} \neq \mathbb{1}$ but $\lambda^{a_{m>n}} = \mathbb{1}$. Denoting this site by $\text{RHS}(\mathbf{a})$ we can define the *right endpoint density* of S_0^z at time t as [342–344]

$$\rho_R(n, t) \equiv \sum_{\text{RHS}(\mathbf{a})=n} |c_{\mathbf{a}}(t)|^2. \quad (\text{A.3})$$

At time $t = 0$ this is a delta function at the initial position of the operator, $\rho_R(n, 0) = \delta_{n0}$. During time evolution, as the support of $S_0^z(t)$ increases, $\rho_R(n, t)$ moves to the right, ballistically for generic clean systems. At the same time, its value near the origin decays to zero, exponentially when symmetries are not present [343], and as a power law when the operator is a conserved density [107, 345]. A possible alternative measure of localized behavior is therefore to look at the spreading of the right endpoint density and look for a finite weight remaining near the origin at infinite times, even in the thermodynamic limit.

We first consider the evolution of $\rho_R(t)$ in random circuits, first with 3- and then with 4-site gates. In order to evaluate $\rho_R(n, t)$ we represent $S_0^z(t)$ as a matrix product operator [346] (MPO) and apply the random gates to that to evolve it in time. In order to simplify the calculations, we consider slightly modified circuit geometries (shown in Fig. A.7(a),(d)), which allow us to use the well known time-evolving block decimation (TEBD) algorithm, after blocking pairs of sites together [268].

Our numerics only allow us to access small systems of size $N = 6, 8, 10$. To compute the spreading of $\rho_R(n, t)$, we place an operator S^z on the third site from the left end of the system and calculate $\rho_R(n, t)$ at different positions and times. For a circuit made out of 3-site gates, we find a persistent peak near the original position, whose size decays only slightly with system size (Fig. A.7(a)-(c)). For the circuit with gate-size $\ell = 4$ on the other hand, we observe a much smaller peak, which keeps decreasing until finite size effects kick in, similar to the behavior observed for the autocorrelator in the main text, and consistent with the prediction that in the thermodynamic limit the peak would eventually disappear (Fig. A.7(d)-(f)). We also observe a larger peak at the rightmost site, where most of the operator weight accumulates at long times.

The same difference in behavior between 3-site and 4-site interactions is also present in the Hamiltonian case. For H_3 we find that the peak in $\rho_R(0, t)$ is almost independent of system size, in agreement with the non-ergodic behavior observed in the autocorrelator in the main text. This is shown in the left panel of Fig. A.8. This behavior changes, however, once we add 4-site terms to the Hamiltonian. In particular we consider the perturbation

$$H'_4 = - \sum_{n \in 2\mathbb{Z}} \left[S_n^+ S_{n+1}^- S_{n+2}^- S_{n+3}^+ + \text{H.c.} \right]. \quad (\text{A.4})$$

This is the same as in Eq. (2.2), except that only terms with even n are present. This is done in order to simplify numerical calculations (making the Hamiltonian nearest neighbor after blocking pairs of neighboring sites together). We expect that if $H_3 + H'_4$ does not exhibit a persistent peak in ρ_R , then neither should $H_3 + H_4$, therefore it is enough to show its absence in the former case. This is indeed what we find as shown in the right panel of Fig. A.8

B. More in-depth look into SLIOMs

In this appendix we gather various results, that while we omitted in Chapter 3, contribute to a deeper understanding of the SLIOMs and their effect on the dynamics. In Section B.1, we refine our definition of SLIOMs and discuss the construction of related conserved quantities even for periodic boundary conditions. We then provide several formulae for the computation of Haar random averages in Section B.2, and include the computation of the average filling fraction of defects and of the uncertainties for the distributions discussed in Section 3.1.2. The rest of the sections gather additional numerical results concerning: the width of the distribution of diagonal matrix elements $S_{L/2}^z S_{L/2+1}^z$ (Section B.3), a lower bound of spatial correlations for the $t - J_z$ model with open boundaries using the Mazur bound (Section B.4), the scaling of these quantities for periodic boundary conditions (Section B.5), and finally the scaling of the saturation value of the half-chain entanglement entropy at long times (Section B.6). In this appendix we use L to refer to the size of the system.

B.1. A more refined definition of SLIOMs

While in Sec. 3.1.2 we gave a definition of SLIOMs, sufficient for the $t - J_z$ Hamiltonian, it is worthwhile to elaborate further on the structure of the SLIOMs we encountered in this work and how precisely localization appears for them.

In the case discussed in Sec. 3.1.2, a very useful property was that the terms appearing in the definitions of the SLIOMs \hat{q}_k squared to projectors $\mathcal{O}_i^{k\dagger} \mathcal{O}_i^k = \hat{\mathcal{P}}_i^k$ (using the convention in Eq. (3.2)). These projectors were then used to define the spatial distribution over i that we analyzed in the main text. However, one could consider a slightly more general version of the $t - J_z$ model, where the fermions carry a higher spin, $S > 1/2$. In that case, $(S_i^z)^2$ is no longer equal to the projector \tilde{n}_i , and the interpretation becomes less clear.

In this more general case, we can still use the definition of \hat{q}_k introduced in the main text:

$$\hat{q}_k = \sum_i \hat{\mathcal{P}}_i^k S_i^z. \quad (\text{B.1})$$

Note that the conserved quantity splits up into a projector ($\hat{\mathcal{P}}_i^k$) onto certain configurations and an associated ‘charge’ (S_i^z), and that in our discussion of the statistical localization it was in fact only the projector part that played a role. Note that this is analogous to the structure we observed for the local dipole moments defined for the Hamiltonian H_3 in Eq. (3.22), i.e., a sum of projectors multiplied by an associated ‘charge’ (in that case, the dipole moment between two subsequent defects). In both cases, the statistical localization is a property of the projectors, rather than the charges.

This suggests the following general definition of SLIOMs that encompasses all the cases encountered in our manuscript:

$$\hat{q} = \sum_{i_1, i_2, \dots, i_n} \hat{\mathcal{Q}}_{i_1 i_2 \dots i_n} C_{i_1 i_2 \dots i_n}. \quad (\text{B.2})$$

Here, $\hat{\mathcal{Q}}_{i_1 i_2 \dots i_n}$ is a projection onto configurations where the sites i_1, \dots, i_n are occupied by a particular combination of particles, while $C_{i_1 i_2 \dots i_n}$ is some charge (in the cases we

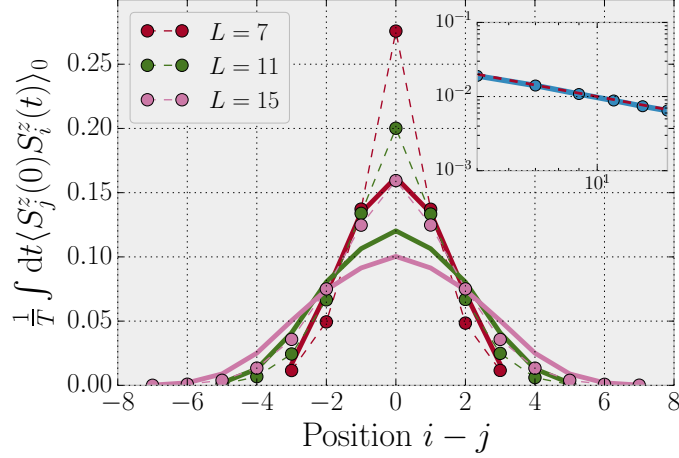


Figure B.1.: **Time averaged correlations vs. their conjectured values.** The dots (connected by narrow dashed lines) show the long-time average (averaged between times $t = 50$ and $t = 100$) of the correlator $\langle S_j^z(t)S_i^z \rangle_{\beta=0}$, while the solid lines represent $C_{ij}(\infty)$, defined by the formula (B.13). This is a lower bound near the origin, but becomes smaller than the numerical value in the tails (i.e., the observed distribution is actually *narrower* than the prediction). However, the two curves approach each other as system size is increased. This is shown by the inset, where the blue dotted curve represents $\sum_i \left[\frac{1}{T} \int_{50}^{100} dt \langle S_j^z(t)S_i^z \rangle_{\beta=0} - C_{ij}(\infty) \right]^2$ as a function of L , approximately decreasing as $1/L$ (red dashed line).

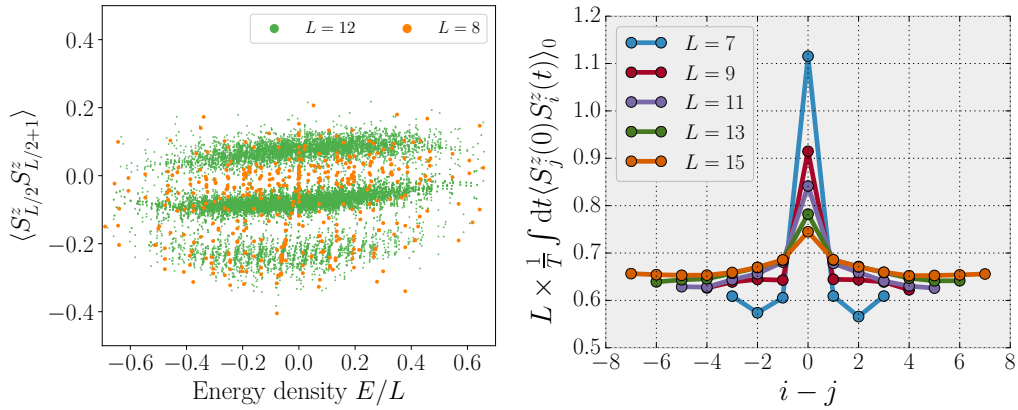


Figure B.2.: **Thermalization in the $t - J_z$ model with closed boundaries** Left: expectation values of nearest neighbor antiferromagnetic correlations in eigenstates for $N_F = L/2$, $S_{\text{tot}}^z = 0$ for different system sizes. The distribution has a width that does not decrease with system size. Right: time average (between times 50 and 100) of the spatially resolved spin-spin correlations at infinite temperature. While there is a small peak around the origin remaining for the available system sizes, the correlations mostly spread out over the whole chain and take values $\propto 1/L$, unlike the case of an open chain shown in Fig. 3.3(c).

consider, usually an integer) associated to this configuration. One can then consider the distribution of the expectation value (in some appropriately chosen ensemble of typical states) $\langle \hat{Q}_{i_1 i_2 \dots i_n} \rangle$. This is now a distribution on $[1, L]^n$ (where we have assumed a 1D system) and one can examine how it is localized on this potentially larger dimensional space.

The $t - J_z$ model with arbitrary spin corresponds (for a given fermion indexed by k) to the choice $n = 1$, $\hat{Q}_i = \hat{P}_i^k$ and $C_i = S_i^z$. The sign of a defect in H_3 again corresponds to taking $n = 1$, but now with \hat{Q}_i a projector onto having the k -th defect on site i and again $C_i = S_i^z$ (in the original spin-1 language). Both of these cases are partially localized, to regions of size $O(\sqrt{L})$, in the single coordinate i . The localized dipole moments, on the other hand, correspond to $n = 2$, with \hat{Q}_{ij} projecting onto configurations with a pair of defects on sites i, j with no other defect in-between. The expectation value $\langle \hat{Q}_{ij} \rangle$ in this case is exponentially localized in the relative coordinate $j - i$ as discussed in the main text. The associated charge is now the dipole moment $C_{ij} = P_{ij} \equiv \sum_{\ell=i}^{j-1} \ell S_\ell^z$.

This general definition also allows us to talk about conserved quantities for the $t - J_z$ model with periodic boundaries (see also App. B.5), even though in this case they are no longer localized. With periodic boundaries, we no longer have a way of labeling fermions individually (e.g. the first fermion can become the last by travelling around the boundary). Nevertheless, we still have a conservation of the total spin pattern and could use the general form (B.2) with $n = N_F$ to define conserved quantities associated to this. Let us take $\hat{Q}_{i_1 \dots i_{N_F}}$ to be the projector onto states where the N_F fermions occupy the sites i_1, \dots, i_{N_F} and let σ be a cyclic permutation of the indices i_1, i_2, \dots, i_{N_F} . Then the following choices all correspond to conserved quantities:

$$\begin{aligned} C_{i_1 \dots i_{N_F}}^{(1)} &= \sum_{\sigma} S_{\sigma(i_1)}^z, \\ C_{i_1 \dots i_{N_F}}^{(2)} &= \sum_{\sigma} S_{\sigma(i_1)}^z S_{\sigma(i_2)}^z, \\ C_{i_1 \dots i_{N_F}}^{(3)} &= \sum_{\sigma} S_{\sigma(i_1)}^z S_{\sigma(i_2)}^z S_{\sigma(i_3)}^z, \\ &\vdots \\ C_{i_1 \dots i_{N_F}}^{(N_F)} &= \sum_{\sigma} S_{\sigma(i_1)}^z S_{\sigma(i_2)}^z S_{\sigma(i_3)}^z \dots S_{\sigma(i_{N_F})}^z. \end{aligned}$$

$C^{(1)}$ is just the total magnetization $S_{i_1}^z + \dots + S_{i_{N_F}}^z$. $C^{(2)}$ measures the AFM ordering of the spins in squeezed space, etc. Note that they are not all independent, for example $C^{(N_F)}$, which measures the overall spin parity, is completely determined by $C^{(1)}$.

Nevertheless, while one can write conserved quantities for the periodic case, they are qualitatively very different from the SLIOMs of the open chain. The main difference is that in this case, with periodic boundaries, the conserved quantities do not factorize into products of 1-particle charges (SLIOMs with $n = 1$). Instead, for a typical state, they involve a sum over all extensively many particles, and thus any notion of localization is lost.

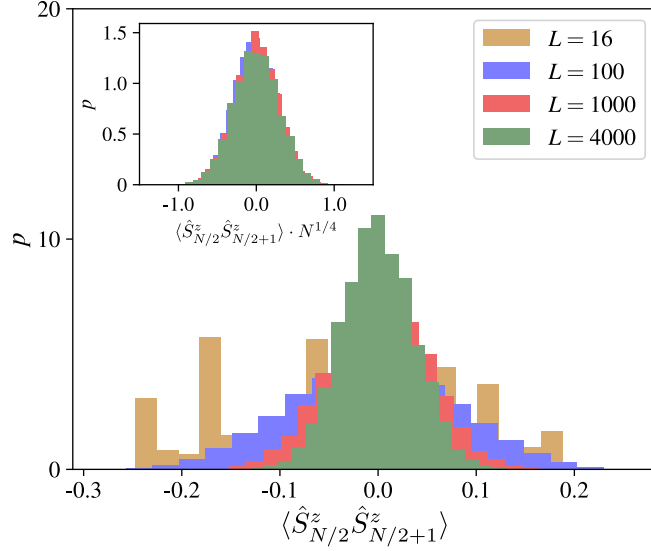


Figure B.3.: Distribution of $\langle S_{L/2}^z S_{L/2+1}^z \rangle$ uniformly sampled after fixing a random spin pattern. This numerical simulation was performed by Johannes Feldmeier.

B.2. Averaging over ensembles of random states

Here we briefly summarize the relevant formulae for averaging over both Haar random states, as well as random states restricted to a fixed $U(1)$ symmetry sector.

B.2.1. Haar average and variance

A Haar random state $|\psi\rangle$ can be written as $|\psi\rangle = U|0\rangle = \sum_i U_{\alpha 0} |\alpha\rangle$, where U is a unitary matrix chosen from the Haar ensemble and $|0\rangle$ is an arbitrary basis element from a complete orthonormal basis $\{|\alpha\rangle\}$. The average of an observable \hat{O} is then

$$\mathbb{E}_{\text{Haar}}[\langle \psi | \hat{O} | \psi \rangle] = \sum_{\alpha, \beta} O_{\alpha\beta} \mathbb{E}_{\text{Haar}}[U_{\alpha 0}^* U_{\beta 0}] = \frac{\text{tr}(\hat{O})}{D}, \quad (\text{B.3})$$

where D is the Hilbert space dimension and we have used the fact that

$$\mathbb{E}_{\text{Haar}}[U_{\alpha 0}^* U_{\beta 0}] = \frac{\delta_{\alpha\beta}}{D}. \quad (\text{B.4})$$

To get the variance over the Haar distribution, we are going to need to average over higher moments of the unitary U . In particular we have to evaluate

$$\mathbb{E}_{\text{Haar}}[\langle \psi | \hat{O} | \psi \rangle^2] = \sum_{\alpha\beta\mu\nu} O_{\alpha\beta} O_{\mu\nu} \mathbb{E}_{\text{Haar}}[U_{\alpha 0}^* U_{\beta 0} U_{\mu 0}^* U_{\nu 0}], \quad (\text{B.5})$$

which is given by the formula

$$\mathbb{E}_{\text{Haar}}[U_{\alpha 0}^* U_{\beta 0} U_{\mu 0}^* U_{\nu 0}] = \frac{\delta_{\alpha\beta} \delta_{\mu\nu} + \delta_{\alpha\nu} \delta_{\beta\mu}}{D(D+1)}. \quad (\text{B.6})$$

Using this, one finds that the variance is

$$\mathbb{E}_{\text{Haar}}[\langle \psi | \hat{O} | \psi \rangle^2] - \mathbb{E}_{\text{Haar}}[\langle \psi | \hat{O} | \psi \rangle]^2 = \frac{1}{D+1} \left[\frac{\text{tr}(\hat{O}^2)}{D} - \left(\frac{\text{tr}(\hat{O})}{D} \right)^2 \right]. \quad (\text{B.7})$$

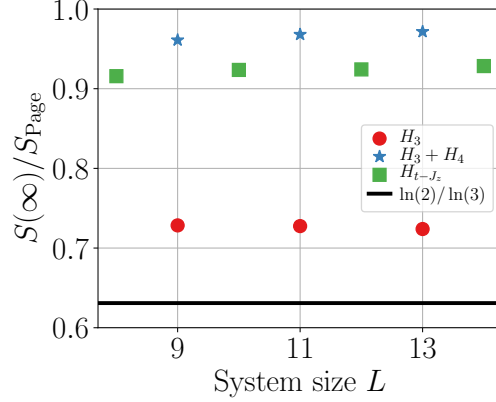


Figure B.4.: **Scaling of the saturation value of the entanglement entropy with system size.** We show the ratio of the saturation value of the entanglement entropy $S(\infty)$ and the Page value $S_{\text{Page}} = \ln(3)L/2 - 1/2$, for H_3 (red circles), $H_3 + H_4$ (blue stars) and H_{t-J_z} (green squares).

The particular cases we considered in the main text correspond to projection operators, $\hat{O}^2 = \hat{O}$. In this case, defining the probability $p = \text{tr}(\hat{O})/D$ we get

$$\mathbb{E}_{\text{Haar}}[\langle \psi | \hat{O} | \psi \rangle^2] - \mathbb{E}_{\text{Haar}}[\langle \psi | \hat{O} | \psi \rangle]^2 = \frac{p - p^2}{D + 1}, \quad (\text{B.8})$$

which is suppressed by a factor of D compared to p itself.

B.2.2. Fixed U(1) symmetry sectors

In order to consider random states with a fixed eigenvalue under some U(1) symmetry, we should to consider a unitary U that commutes with the symmetry operator. That is, we take U to be block diagonal in the symmetry basis, with each block an independent Haar random unitary. In this case, we can average over the block separately. Denoting the U(1) quantum numbers by N , we then get a generalization of the previous formula,

$$\mathbb{E}_{\text{U}(1)}[U_{\alpha\alpha'}^* U_{\beta\beta'}] = \sum_N \frac{P_{\alpha\beta}^{(N)} P_{\alpha'\beta'}^{(N)}}{D_N}, \quad (\text{B.9})$$

where $P^{(N)}$ is a projector onto the symmetry sector with N , and $D_N \equiv \text{tr}(P^{(N)})$ is the corresponding dimension.

The ensemble of random states is defined by $|\psi\rangle = U|0\rangle$ where the basis state $|0\rangle$ is chosen to have a fixed quantum number N . This picks out a single projector from the above sum to give

$$\mathbb{E}_{\text{U}(1)}[\langle \psi | \hat{O} | \psi \rangle] = \frac{\text{tr}(\hat{O}P^{(N)})}{D_N}. \quad (\text{B.10})$$

In the cases we consider, \hat{O} and $P^{(N)}$ are both diagonal projectors in the same local product basis. $\text{tr}(\hat{O}P^{(N)})$ is therefore simply given by counting the number of configurations that are in the intersection, satisfying both $\hat{O} = 1$ and $P^{(N)} = 1$.

In an analogous manner, one could calculate variances over this ensemble. The result is the same as for the Haar random case, but with $D \rightarrow D_N$ and the δ functions in Eq. (B.6)

replaced by matrix elements of $P^{(N)}$. Consequently, the variance becomes

$$\mathbb{E}_{\mathcal{U}(1)}[\langle \psi | \hat{O} | \psi \rangle^2] - \mathbb{E}_{\text{Haar}}[\langle \psi | \hat{O} | \psi \rangle]^2 = \frac{1}{D_N + 1} \left[\frac{\text{tr}(\hat{O}P^{(N)}\hat{O}P^{(N)})}{D_N} - \left(\frac{\text{tr}(\hat{O}P^{(N)})}{D_N} \right)^2 \right]. \quad (\text{B.11})$$

As mentioned above, we are interested in cases where \hat{O} and $P^{(N)}$ are both projectors, diagonal in the same basis. Therefore $\hat{O}P^{(N)}$ is also a projector, $\hat{O}P^{(N)}\hat{O}P^{(N)} = \hat{O}P^{(N)}$, and the variance is now suppressed by a factor of $D_N + 1$, still exponentially large in system size for typical symmetry sectors.

B.2.3. Computation of the average number of defects

As an application, in this section we compute the average filling fraction of defects $\langle \nu_d \rangle$. To do so, let us compute $\mathbb{E}_{\text{Haar}}[\langle \psi | N^d | \psi \rangle]$ appearing in Eq. (3.21). Using Eq. (B.3) we find that

$$\mathbb{E}_{\text{Haar}}[\langle \psi | N^d | \psi \rangle] = \frac{1}{2} \sum_{k=1}^L \frac{\text{tr}[(\hat{q}_{k+1})^2(1 + \hat{q}_k \hat{q}_{k+1})]}{3^L}. \quad (\text{B.12})$$

Now we split the computation in two steps. First, let us compute each of the terms individually:

$$\frac{1}{3^L} \text{tr}[(\hat{q}_{k+1})^2] = \frac{1}{3^L} \sum_{i,j} \text{tr}[\hat{\mathcal{P}}_i^{k+1} \hat{\mathcal{P}}_j^{k+1} S_i^z S_j^z] = \frac{1}{3^L} \sum_i \text{tr}[\hat{\mathcal{P}}_i^{k+1} (S_i^z)^2] = \sum_i p_{\text{Haar}}(i; k+1),$$

where we have used that for $i < j$ the trace vanishes due to $\text{tr}(S_j^z) = 0$ and p_{Haar} is defined in Eq. (3.7). Now, combining this with the fact that $\hat{\mathcal{P}}_i^k \hat{\mathcal{P}}_i^{k+1} = 0$, the second term vanishes:

$$\frac{1}{3^L} \text{tr}[\hat{q}_k (\hat{q}_{k+1})^3] = \frac{1}{3^L} \sum_{i,j} \text{tr}[\hat{\mathcal{P}}_i^k \hat{\mathcal{P}}_j^{k+1} S_i^z S_j^z] = \frac{1}{3^L} \sum_i \text{tr}[\hat{\mathcal{P}}_i^k \hat{\mathcal{P}}_i^{k+1} (S_i^z)^2] = 0.$$

Thus, for a Haar random state with filling fraction $\nu = 2/3$, and using the fact that $\sum_k p_{\text{Haar}}(i; k+1) = \nu$, we obtain that the typical filling fraction of defects is

$$\langle \nu_d \rangle = \frac{1}{L} \mathbb{E}_{\text{Haar}}[\langle \psi | N^d | \psi \rangle] = \frac{1}{2L} \sum_{k=1}^L \sum_i p_{\text{Haar}}(i; k+1) = \frac{1}{L} \sum_i \frac{\nu}{2} = \frac{1}{3}.$$

Intuitively, this comes from the fact that any given charge has equal probability of having the same vs. opposite sign as the nearest charge on the left, making the probability of finding a defect on a particular site $\nu/2 = 1/3$.

B.3. Finite-size scaling of Fig. 3.4

We show numerical evidence that the width of the distribution in Fig. 3.4 scales with system size as $L^{-1/4}$ for sufficiently large system sizes. To do so, we assume that the fragment associated to any spin pattern configuration is ergodic, and approximate energy eigenstates (in the middle of the spectrum) by an equal weight superposition of all possible hole positions with a given spin pattern. One can then use Monte-Carlo techniques to sample the expectation value $\langle S_{L/2}^z S_{L/2+1}^z \rangle$ evaluated on these eigenstates. This results in a probability distribution for $\langle S_{L/2}^z S_{L/2+1}^z \rangle$ as shown in Fig. B.3 for different system sizes. The inset shows evidence that the width scales as $L^{-1/4}$, due to the scaling-collapse of the distribution for $L^{1/4} \langle S_{L/2}^z S_{L/2+1}^z \rangle$ with system size.

B.4. Spatially resolved autocorrelations at long times

As noted in the main text (see Eq. (3.10)), Mazur's inequality provides a strict lower bound on autocorrelations $\langle S_j^z(t)S_j^z \rangle$ in terms of the conserved quantities of the system. However, to understand the spatial spreading of spin density S_j^z , it is also interesting to consider correlations between different sites of the form $\langle S_j^z(t)S_i^z \rangle$, for which the same lower bound does not exist. Here we provide a conjecture for the long-time average of these correlations in the thermodynamic limit of the $t - J_z$ model and show some supporting numerics.

While one cannot lower bound the correlations between different sites in the same way as autocorrelators, one could in principle calculate their time average if one had access to a *complete* orthogonal set of 3^L conserved quantities (a basis of all operators diagonal in the eigenbasis of H_{t-J_z}). Given such an orthogonal set $\{\hat{I}_a\}_{a=1}^{3^L}$, one can prove [170] that the time average becomes

$$\lim_{T \rightarrow \infty} \frac{1}{T} \int dt \langle S_j^z(t)S_i^z \rangle_{\beta=0} = \sum_a \frac{\langle S_j^z \hat{I}_a \rangle_{\beta=0} \langle S_i^z \hat{I}_a \rangle_{\beta=0}}{\langle \hat{I}_a^2 \rangle_{\beta=0}}. \quad (\text{B.13})$$

The formula (B.13) requires knowledge of exponentially many conserved quantities, which is much more than the information contained in only the SLIOMs \hat{q}_k defined in Eq. (3.6). Our conjecture is that in the limit $L \rightarrow \infty$ the correct time average is given by restricting the sum on the right hand side to the set $\{\hat{q}_k\}$, ignoring other conserved quantities, i.e.

$$\sum_k \frac{\langle S_j^z \hat{q}_k \rangle_{\beta=0} \langle S_i^z \hat{q}_k \rangle_{\beta=0}}{\langle \hat{q}_k^2 \rangle_{\beta=0}} \equiv C_{ij}(\infty). \quad (\text{B.14})$$

Indeed, this conjecture is supported by the observation that the quantities $C_{ij}(\infty)$ are all positive and they sum up to the correct value, $\sum_j C_{ij}(\infty) = 2/3 = \sum_j \langle S_j^z(t)S_i^z \rangle_{\beta=0}$. This means that the contribution coming from all remaining terms ($\hat{I}_a \neq \hat{q}_k$) in the sum (B.13) have to be such that their sum over i vanishes. Our conjecture amounts to saying that they in fact all individually vanish in the thermodynamic limit.

This conjecture is supported by our small scale numerics, which show that the difference between the two distributions decreases with L . In particular, we can define the mean square distance of the two,

$$\sum_i \left[\frac{1}{T} \int dt \langle S_j^z(t)S_i^z \rangle_{\beta=0} - C_{ij}(\infty) \right]^2. \quad (\text{B.15})$$

We find (see in particular the inset of Fig. B.1) that this quantity decreases with system size, approximately as $1/L$. Note that the distribution $C_{ij}(\infty)$ has a width $\propto \sqrt{L}$, such that our conjecture implies that for a finite open chain the charge remains trapped in a region much smaller than the entire system as discussed also in the main text.

B.5. $t - J_z$ model with closed boundaries

Our discussion of the $t - J_z$ model in the main text focused on a chain with open boundaries. This allowed us to label fermions by an integer k , starting from one of the endpoints, leading to the definition of SLIOMs in Eq. (3.6). Here we detail how the situation changes when periodic boundary conditions are taken.

In the periodic case, the conserved spin pattern is only well defined modulo cyclic translations around the chain, allowing for additional matrix elements between certain sectors that are disconnected for the open chain. Nevertheless, this only reduces the number of disconnected sectors by at most a factor of $1/L$, such that there are still exponentially

Appendix B. More in-depth look into SLIOMs

many invariant subspaces and the dimension of the largest one still scales asymptotically as $\sim 2^L$. The Hilbert space is therefore still strongly fragmented and should therefore violate ETH. Indeed, repeating the same calculation as in Fig. 3.4(b) for the closed chain, we again find a wide distribution of diagonal matrix elements of $S_{L/2}^z S_{L/2=1}^z$. This is shown in Fig. B.2(a). Approximating eigenstates by an equal weight superposition of hole positions in this case suggests that the width of the distribution asymptotically decreases with system size as $L^{-1/2}$ in the thermodynamic limit (recall, that for open chains the narrowing was slower, $\sim L^{-1/4}$).

The difference between open and closed boundaries becomes even more explicit when we consider the conserved quantities that label the disconnected sectors. In particular, the SLIOMs defined in Eq. (3.6) are no longer conserved, since fermions can now circle around the boundaries. Indeed, while the whole of the spin pattern is still conserved, talking about the spin of individual fermions is no longer meaningful and consequently, the spatial localization associated to the conserved quantities breaks down. This explains the different asymptotic scaling in the width of the distribution of diagonal matrix elements. It also shows up when considering the late-time behavior of correlations of the form $\langle S_j^z(t) S_i^z \rangle_{\beta=0}$. Unlike the case with open boundaries, where these spread out only over a region of size \sqrt{L} (see Fig. 3.3(c)), for a closed chain the spread out over the entire chain, saturation to a value of $O(1/L)$. This is shown in Fig. B.2(b).

Note that for the Hamiltonian H_3 in Eq. (3.16) the situation is quite different. While labeling individual defects also loses meaning with periodic boundaries, the regions surrounded by neighboring defects are still well defined and have the same $O(1)$ size as with open boundaries. This is consistent with the localized behavior (i.e., infinitely long-lived autocorrelations) *in the bulk*, discussed in Sec. 3.2.2.

B.6. Saturation value of the entanglement entropy

In this appendix we compare the scaling of the saturation value of the entanglement entropy ($S(\infty)$) with initial (Haar) random product states (not in the z basis), for the models studied in the main text. For completeness, we also show the scaling for the dipole-conserving Hamiltonian $H_3 + H_4$ with

$$H_4 = - \sum_n \left[S_n^+ S_{n+1}^- S_{n+2}^- S_{n+3}^+ + \text{H.c.} \right], \quad (\text{B.16})$$

which is only weakly fragmented and saturates close to the Page value [118], $S_{\text{Page}} = \ln(3)L/2 - 1/2$, up to a constant offset.

In Fig. B.4, we show the scaling of $S(\infty)$ with system size for H_3 (red circles), $H_3 + H_4$ (blue stars) and H_{t-J_z} (green squares). The scaling (for the small system sizes the simulations were performed) suggests that for the $t - J_z$ model $S(\infty)$ will approach S_{Page} in the thermodynamic limit, while it remains only a fraction of it for H_3 .

B.6. Saturation value of the entanglement entropy

C. Effective description in the strong interacting limit

In this short appendix we obtain the effective Hamiltonian in the limit $|U| \gg J, \Delta$ with $||U| - n\Delta| \neq 0$ for any $n \in \mathbb{N}$ to avoid possible resonances [347]. In this limit, the number of doublons N_{doub} is effectively conserved up to times that scale exponentially in the interaction strength U [235, 255]. Dealing with initial singlon configurations, we have $N_{\text{doub}} = 0$ and assume a negligible fraction of dynamically-generated doublons after the quench. In this limit, the effective Hamiltonian provides non-trivial dynamics at first order in perturbation theory

$$\begin{aligned} \hat{H}_{\text{eff}}^U = & -J \sum_{i,\sigma} [(1 - \hat{n}_{i,\bar{\sigma}}) \hat{c}_{i,\sigma}^\dagger \hat{c}_{i+1,\sigma} (1 - \hat{n}_{i+1,\bar{\sigma}}) + \text{h.c.}] \\ & + \Delta \sum_{i,\sigma} i \hat{n}_{i,\sigma}. \end{aligned} \quad (\text{C.1})$$

Note that the dynamics generated by this Hamiltonian conserves the configuration of spins $|\{\sigma_1, \dots, \sigma_N\}\rangle$, with $\sigma_i = \{\uparrow, \downarrow\}$ and the total particle number N . The last term in Eq. (C.1) equally couples to both spin degrees of freedom and the many-body states expressed in the particle-number basis factorize in terms of N free Wannier-Stark localized spinless fermions with many-body wave function $|\{i_1, \dots, i_N\}\rangle$, with $i_i \in \{-\frac{L}{2}, \dots, 0, \dots, \frac{L}{2}\}$ and fixed spin configuration $|\{\sigma_1, \dots, \sigma_N\}\rangle$ [196]. As a result the effective Hamiltonian [Eq. (C.1)] takes the form

$$\hat{H}_{\text{eff}}^U = -J \sum_i (\hat{c}_i^\dagger \hat{c}_{i+1} + \text{h.c.}) + \Delta \sum_i i \hat{n}_i. \quad (\text{C.2})$$

This has to be compared with the non-interacting Hamiltonian in Eq. (4.1) for $N = N_\uparrow + N_\downarrow$ spinful fermions, which for a one-body observable like the imbalance gives exactly the same result. Higher-order terms at finite U do not conserve the spin configuration $|\{\sigma_1, \dots, \sigma_N\}\rangle$. The leading terms in second-order perturbation are spin-exchange and longer-range hopping terms, as well as nearest-neighbors interactions $-2J^2/U \sum_{i,\sigma} \hat{n}_{i,\sigma} \hat{n}_{i+1,\bar{\sigma}}$, which lead to an interaction-induced decay of the imbalance to lower values compared to the non-interacting case at sufficiently long times ($t \sim U/J^2$).

The experimental setup has a weak spin-dependent tilt ($\Delta_\downarrow - \Delta_\uparrow \approx 0.3J < J$), hence, the previous discussion provides a good approximation for sufficiently strong U . Only in the limit $\Delta_\downarrow - \Delta_\uparrow > J$, the effective Hamiltonian in Eq. (C.1) does not map onto spinless fermions, because it depends on the spin configuration. This implies that the non-quadratic interaction terms, appearing in the hopping, have to be taken into account. This corresponds to two Stark ladders with different slopes constraining the mobility within each other.

D. Implementation of cellular automaton dynamics and Mazur bound

In this appendix we start by providing additional details about the numerical implementation of the cellular automaton evolution in Chapters 5 and 6, and show that Mazur’s bound [116] can be applied to the correlation functions, as for example defined in Eq. (5.29), of the stochastic evolution we studied (Section D.3). This relies on showing that its infinite-time-average value is non-negative.

D.1. Details on the implementation of cellular automaton dynamics

As discussed in the main text, at each application of a local gate we choose randomly (with probabilities 1/3 each) between three possibilities: applying $G_{\mathbf{x}}$, applying its inverse, or doing nothing. In the first two cases, the update is applied only if it does not lead to a violation of the local constraint $|s_{\mathbf{r}}| \leq S$ on any site, otherwise we leave the configuration unchanged. These updates are randomly applied among those configurations for which $|s_{x+i} \pm n_i| \leq S$, such that the corresponding transition rates between two different local configurations \mathbf{s}, \mathbf{s}' are symmetric, i.e., $T_{\mathbf{s} \rightarrow \mathbf{s}'} = T_{\mathbf{s}' \rightarrow \mathbf{s}}$. This ensures that detailed balance is satisfied with respect to the “infinite temperature” (uniformly random) ensemble, which is therefore a stationary state of this stochastic process. Note that this implementation differs from that used in previous works [6, 178, 291, 292], where all local updates consistent with symmetry requirements were allowed. Thus, certain direct transitions in the latter implementation require multiple updates in the former.

At each time step, we randomly pick a non-overlapping complete covering of the (1D or 2D) lattice by the gates $G_{\mathbf{x}}$. For a model in 1D with gates acting on 2ℓ sites, we pick randomly an integer $m \in \{0, \dots, \ell - 1\}$ and apply all gates on sites $x = m \pmod{\ell}$. Similarly, in 2D with gates of size $\ell \times \ell$ we pick two integers $m_x, m_y \in \{0, \dots, \ell - 1\}$ and shift the gates accordingly. Moreover, for periodic boundary conditions we choose system sizes that are multiple of ℓ .

When considering periodic boundary conditions, we average not only over randomly initial configurations but also over different lattice sites. Being the system translational invariant, the spin-spin correlation only depends on the relative distance, i. e. $\langle s_{\mathbf{x}_2}(t) s_{\mathbf{x}_1}(0) \rangle_c = \langle s_{\mathbf{x}_1 - \mathbf{x}_2}(t) s_{\mathbf{0}}(0) \rangle_c$. We do this by centering every site and computing the correlations relative to this new central site $\mathbf{x} = \mathbf{0}$. Using this procedure, we can increase the number of averaged measurements by the size of the volume of the system.

Finally, Tables D.1 and D.2 provide details on the choice of boundary conditions (PBC and OBC standing for periodic and open boundary conditions respectively) and the number of random initial configurations (Number Initial States) the data has been averaged over.

D.1. Details on the implementation of cellular automaton dynamics

Figure	Label	Number Initial States	Boundary Conditions
5.6(a)	30	12550	PBC
	10^4	3000	
	10^5	1000	
5.6(b)	5000	5000	OBC
	10^4	4000	
5.6(c)/(d)	10^2	2000	PBC
	10^3		
	10^4		
5.8(a)/(b)	10^6	1000	PBC
6.1(b)/(d)	10^6	2000	OBC
6.1(c)	10^5	3000	PBC
6.4(c)	200	1000	PBC
	248		
	300		
6.4(b)/(d)	10^4	1000	PBC

Table D.1.: Boundary conditions and number of random initial states used for the data shown in the respective figures and labels of the main text.

Figure	Label	Number Initial States	Boundary Conditions
E.4(a)	Eq. (E.5)	1000	PBC
	Eq. (E.7)		
E.4(b)	10^4	1000	PBC
	10^5		
5.7(a)	10^4	6500	PBC
	10^5	1000	
5.7(b)	10^2	2000	PBC
	10^3		
	10^4		

Table D.2.: Boundary conditions and number of random initial states used for the data shown in the respective figures and labels of the supplement material.

D.2. Scaling analysis of the generalized diffusion equation

We provide a general scaling analysis demonstrating that the expansion of the multipole current in terms of derivatives of the charge density employed in the main text, indeed captures the relevant contributions at late times and for long wavelengths. Let us start with the hydrodynamic equation for the coarse-grained charge density $s(x, t)$ of a system conserving all multipole moments $Q^{(n \leq m)}$

$$\begin{aligned} \frac{\partial}{\partial t} s(x, t) - (-\partial_x)^{m+1} \langle \Omega_x^{(m)} \rangle &= \\ &= \frac{\partial}{\partial t} s(x, t) + D (-1)^{m+1} (\partial_x)^{2(m+1)} s(x, t) = 0. \end{aligned} \quad (\text{D.1})$$

Here, we have used the expansion of the multipole current given by $\langle \Omega_x^{(m)} \rangle \approx -D (\partial_x)^{m+1} s(x, t)$ as discussed in the main text. The goal is to determine the relevance of taking into account additional contributions $\langle \Omega_x^{(m)} \rangle = \langle \Omega_x^{(m)} \rangle (\partial_x^j s(x, t))^i$ with $i, j \in \mathbb{N}$.

We do so following the scheme laid out in Ref. [99, 100]. While the continuity equation for the charge is exact, the multipole current is subject to fluctuations or noise $\xi(x, t)$, i.e. $\langle \Omega_x^{(m)} \rangle \rightarrow \langle \Omega_x^{(m)} \rangle + \xi(x, t)$, such that Eq. (D.1) becomes

$$\frac{\partial}{\partial t} s(x, t) + D (-1)^{m+1} (\partial_x)^{2(m+1)} s(x, t) = (-\partial_x)^{m+1} \xi(x, t). \quad (\text{D.2})$$

These fluctuations are assumed to be uncorrelated

$$\langle \xi(x, t) \xi(x', t') \rangle = \eta \delta(x - x') \delta(t - t'), \quad (\text{D.3})$$

whose amplitude (η) are tied to the correlation functions of the charge density at equilibrium [99, 100]. Moreover, $\langle \xi(x, t) \rangle = 0$ since otherwise this would yield a persistent current. Eq. (D.2) and Eq. (D.3) define a fixed point relative to which we can investigate the effect of other possible terms. Consider a scale transformation $x \rightarrow \tilde{x} = x/\lambda$ with $\lambda > 1$. We say that a quantity F has a scaling dimension n if under this transformation $F \rightarrow F\lambda^n$. Assuming that the generalized diffusion constant is scale invariant, i.e. $[D] = 0$, and demanding that Eq. (D.2) is a fixed point under this rescaling, then fixes the scaling dimensions of $t, \xi, s(x, t)$: Firstly, we obtain $[t] = -2(m+1)$ from the left hand side of Eq. (D.2). Second, Eq. (D.3) implies $[\xi] = m + 3/2$. Note that $[\eta] = 0$, as η is fixed by D due to its relation via equilibrium fluctuations [100]. Finally, Eq. (D.2) yields $[s(x, t)] = 1/2$. Given these scaling dimensions, we can assess whether additional terms included in the expansion of $\langle \Omega_x^{(m)} \rangle$, are relevant (positive scaling dimension), irrelevant (negative one) or marginal (vanishing scaling dimension), and moreover, whether they are consistent with multipole conservation laws.

We see that including terms $\langle \Omega_x^{(m)} \rangle \sim \alpha_{i,j} (\partial_x)^j s(x, t)^i$ in Eq. (D.1) leads to a scaling dimension $[\alpha_{i,j}] = m + 1 - j + \frac{1}{2}(1 - i)$ of the corresponding coefficient $\alpha_{i,j}$. In general all terms for which $2(m+1-j) < i - 1$ are irrelevant, which include terms with $j > m + 1, i \geq 1$ as well as $j = m + 1, i > 1$.

How about potentially relevant/marginal terms with $j \leq m + 1$ and $1 \leq i \leq 2(m + 1 - j) + 1$? For $j = m + 1$ we are led back to the term used in Eq. (D.1). All other relevant/marginal terms necessarily have $j < m + 1$, and thus *fewer* derivatives than the number of $m + 1$ independent constants necessary to characterize equilibrium. Following the argument used in the main text, integrating the associated condition $\langle \Omega_x^{(m)} \rangle_{eq.} = 0$ of a vanishing multipole current in equilibrium does hence not provide sufficiently many freely adjustable parameters for the equilibrium charge distribution. In other words, for

terms with $j < m + 1$ it is always possible to find initial states such that the conservation of some $Q^{(n \leq m)}$ is broken.

Overall, we find that the expansion $\langle \Omega_x^{(m)} \rangle \approx -D(\partial_x)^{m+1}s(x, t)$ used in the main text captures the unique, most scaling relevant term consistent with all multipole conservation laws.

D.3. Non-negativity of autocorrelations

Let us write out in more detail what we mean by the autocorrelation that we want to calculate:

$$C_{\mathbf{r}}(t) \equiv \frac{1}{D} \sum_{\mathbf{s}(0)} s_{\mathbf{r}}(0) \langle s_{\mathbf{r}}(t) \rangle_{\mathbf{s}(0)}. \quad (\text{D.4})$$

Here, we are sampling all initial configurations $\mathbf{s}(0)$ and D is the total number of configurations ($D = (2S + 1)^N = 5^N$ for an N -site lattice of spin- S d.o.f.). $\mathbf{s}(t)$ denotes the time-evolved configuration and the brackets denote averaging over the random trajectories. In other words, $\langle s_{\mathbf{r}}(t) \rangle_{\mathbf{s}(0)} = \sum_{\mathbf{s}} p_{\mathbf{s}(0)}(\mathbf{s}, t) s_{\mathbf{r}}$, where $p_{\mathbf{s}(0)}(\mathbf{s}, t)$ is the probability distribution over spin configurations for a fixed initial condition $\mathbf{s}(0)$. In terms of the transition probability matrix T — connecting two spin configurations with a certain rate— it can be written as $p_{\mathbf{s}(0)}(\mathbf{s}, t) = (T^t)_{\mathbf{s}, \mathbf{s}(0)}$. Ultimately, we are interested in the time-averaged correlations $\overline{C}_{\mathbf{r}} \equiv \lim_{\tau \rightarrow \infty} \frac{1}{\tau} \sum_{t=0}^{\tau} C_{\mathbf{r}}(t)$

The space of all spin configurations falls apart into a large number of different connected components. Let us decompose the correlation into contributions coming from different sectors:

$$C_{\mathbf{r}}(t) = \frac{1}{D} \sum_{\mathcal{C}} \sum_{\mathbf{s}(0) \in \mathcal{C}} s_{\mathbf{r}}(0) \langle s_{\mathbf{r}}(t) \rangle_{\mathbf{s}(0)}. \quad (\text{D.5})$$

Let us now focus on $\langle s_{\mathbf{r}}(t) \rangle_{\mathbf{s}(0)}$ for a particular initial configuration belonging to a sector \mathcal{C} . Restricted to the sector, the dynamics is by definition irreducible. It is also reversible: $T_{\mathbf{s}\mathbf{s}'} = T_{\mathbf{s}'\mathbf{s}}$. With these two conditions, there is a unique stationary distribution, which is uniform over all $\mathbf{s} \in \mathcal{C}$. We therefore reach the uniform distribution $p_{\mathcal{C}}(\mathbf{s}) \equiv \lim_{\tau \rightarrow \infty} \frac{1}{\tau} \sum_{t=0}^{\tau} p_{\mathbf{s}(0)}(\mathbf{s}, t) = \frac{1}{D(\mathcal{C})}$, where $D(\mathcal{C})$ is the number of configurations belonging to \mathcal{C} .

Let $D_q(\mathcal{C})$ denote the number of configurations in \mathcal{C} which has $s_{\mathbf{r}} = q$ (notice that $\sum_q D_q(\mathcal{C}) = D(\mathcal{C})$). Then the time-averaged expectation value is $\overline{\langle s_{\mathbf{r}}(t) \rangle_{\mathbf{s}(0)}} = \sum_q q \frac{D_q(\mathcal{C})}{D(\mathcal{C})} \equiv \bar{q}(\mathcal{C})$. This is independent of $\mathbf{s}(0)$ within the same \mathcal{C} so we get

$$\sum_{\mathbf{s}(0) \in \mathcal{C}} s_{\mathbf{r}}(0) \overline{\langle s_{\mathbf{r}}(t) \rangle_{\mathbf{s}(0)}} = \bar{q}(\mathcal{C}) \sum_q q D_q(\mathcal{C}) = D(\mathcal{C}) \bar{q}(\mathcal{C})^2. \quad (\text{D.6})$$

Plugging this back into Eq. (D.5), we get that $\overline{C}_{\mathbf{r}} = \sum_{\mathcal{C}} \frac{D(\mathcal{C})}{D} \bar{q}(\mathcal{C})^2 \geq 0$, with all terms being non-negative.

E. Survey of results for spatially-modulated symmetries

In this appendix we gather various results for spatially-modulated symmetries in two and higher-dimensions, expanding our discussion in Chapter 6. We start by constructing other examples of microscopic systems with modulated symmetries in Section E.1. We then provide the analytics supporting the general theory whose main results are summarized in Section 6.2.2. This predicts the late-time decay of the spin auto-correlation function in the presence of quasi-periodic symmetries (see Section E.2). In Section E.3, we show that for open boundary conditions, the number of solutions of a two-dimensional recurrence scales with the linear system size (as implicitly contained in the main text). In Section 6.2.1 we discussed the possibility of combining the set of conserved modes lying along any closed loop in momentum space, to construct a subsystem symmetry in real space.

E.1. Further examples of systems with periodically modulated symmetries

In this section we show some additional examples of 2D and 3D models with quasi-periodic symmetries. The 2D models consist of size-5 gates $G_{\mathbf{r}} = \{n_{i,j}\}$ with $i, j \in \{-2, \dots, +2\}$, acting on a neighbourhood of a site \mathbf{r} . $n_{i,j}$ are identified with the entries of a 5×5 matrix. The first set of models, shown in Table E.1, conserve all moments of the charge including the octupole one, i.e., $\sum_{x,y} x^n y^m s_{x,y}$ with $n + m \leq 3$. Imposing these symmetries leads to the general matrix expression

$$n_{i,j} = \begin{pmatrix} a & b & c & b & a \\ b & g & h & g & b \\ c & h & m & h & c \\ b & g & h & g & b \\ a & b & c & b & a \end{pmatrix}. \quad (\text{E.1})$$

Different choices of the parameters a, \dots, m will in general correspond to different quasi-periodic modulated symmetries. In terms of these parameters, $\chi(\mathbf{k})$ takes the form

$$\begin{aligned} \chi(\mathbf{k}) \propto & 4a \cos(2k_x) \cos(2k_y) + 4b(\cos(k_x) \cos(2k_y) + \cos(2k_x) \cos(k_y)) + 2c(\cos(2k_x) \\ & + \cos(2k_y)) + 4g \cos(k_x) \cos(k_y) + 2h(\cos(k_x) + \cos(k_y)) + m. \end{aligned} \quad (\text{E.2})$$

Dropping the requirement of D_4 symmetric gates (and instead considering skew-centrosymmetric gates), while still preserving all quadratic moments, included $\mathcal{Q}_{x^2+y^2}$, leads to the general matrix expression

$$n_{i,j} = \begin{pmatrix} a & b & c & -f & -a \\ f & g & h & -g & -b \\ c & h & 0 & -h & -c \\ b & g & -h & -g & -f \\ a & f & -c & -b & -a \end{pmatrix}, \quad (\text{E.3})$$

E.1. Further examples of systems with periodically modulated symmetries

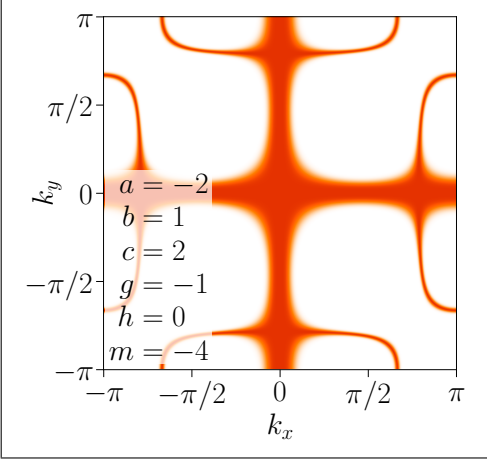
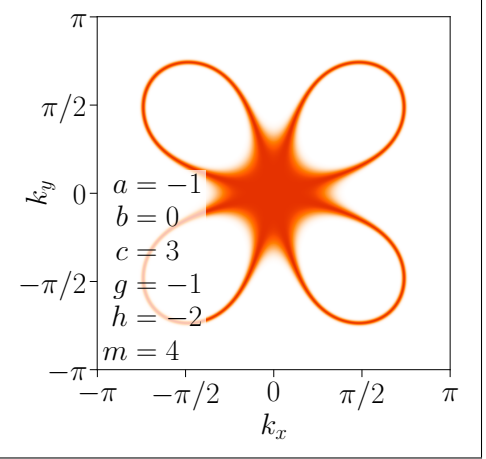
Characteristic $\chi(\mathbf{k})$	
	
Leading order of $\omega(\mathbf{k} \approx \mathbf{0})$	
$(25k_x^2 k_y^2)^2$	$(k_x^4 + k_y^4 - 17k_x^2 k_y^2)^2$

Table E.1.: Examples of 2D systems with quasi-periodic symmetries and 3-pole conservation. The plot shows $e^{-|\chi(\mathbf{k})|^2}$, with the analytical expression for $\chi(\mathbf{k})$ given in Eq. (E.2). The corresponding parameters are specified in the panel.

with

$$\chi(\mathbf{k}) \propto 2a \sin(2k_x) \cos(2k_y) + b(\sin(k_x - 2k_y) + \sin(2k_x + k_y)) + c(\sin(2k_x) - \sin(2k_y)) + f(\sin(2k_x - k_y) + \sin(k_x + 2k_y)) + 2g \sin(k_x) \cos(k_y) + h(\sin(k_x) - \sin(k_y)). \quad (\text{E.4})$$

Results for models of this type are shown in Table E.2.

In Fig. 6.6a of the main text, we also gave an example of a model which does not conserve the total charge $\mathcal{Q} = \sum_{\mathbf{r}} s_{\mathbf{r}}$, and thus any of its higher-moments, but realize non-trivial finite mode contributions. This model corresponds to the 5×5 local gates

$$n_{i,j} = \begin{pmatrix} -2 & 0 & 3 & 0 & -2 \\ 0 & -2 & 0 & -2 & 0 \\ 3 & 0 & 2 & 0 & 3 \\ 0 & -2 & 0 & -2 & 0 \\ -2 & 0 & 3 & 0 & -2 \end{pmatrix}, \quad (\text{E.5})$$

with associated characteristic equation

$$\chi(\mathbf{k}) = 4 \cos(k_x) \cos(k_y) - 3(\cos(2k_x) + \cos(2k_y)) + 4 \cos(2k_x) \cos(2k_y) - 1. \quad (\text{E.6})$$

Here, we also introduce a second model with 3×3 local gates given by

$$n_{i,j} = \begin{pmatrix} 0 & 1 & 0 \\ 1 & -3 & 1 \\ 0 & 1 & 0 \end{pmatrix}, \quad (\text{E.7})$$

and characteristic function

$$\chi(\mathbf{k}) = 2(\cos(k_x) + \cos(k_y)) - 3. \quad (\text{E.8})$$

whose solutions lie in a single loop (see Fig. E.1). In the following section we will obtain the long-time behavior of $C(\mathbf{r}, t)$ for these.

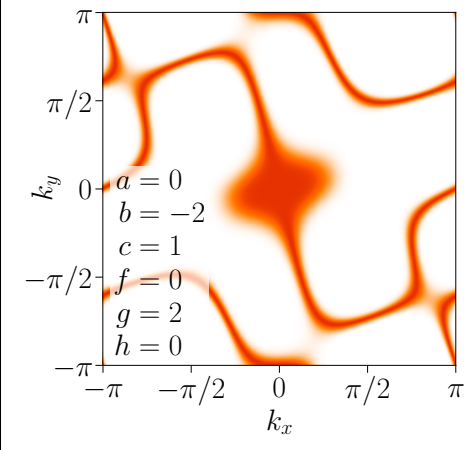
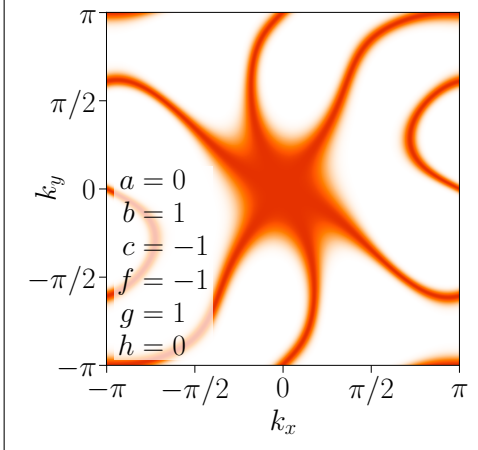
Characteristic $\chi(\mathbf{k})$	
 <p> $a = 0$ $b = -2$ $c = 1$ $f = 0$ $g = 2$ $h = 0$ </p>	 <p> $a = 0$ $b = 1$ $c = -1$ $f = -1$ $g = 1$ $h = 0$ </p>
Leading order of $\omega(\mathbf{k} \approx \mathbf{0})$	
$(k_x^3 + 2k_x^2k_y + 4k_xk_y^2 - k_y^3)^2$	$(k_x^3 - 2k_x^2k_y - k_xk_y^2 + k_y^3)^2$

Table E.2.: Examples of 2D systems with quasi-periodic symmetries. The plot shows $e^{-|\chi(\mathbf{k})|^2}$, with the analytical expression for $\chi(\mathbf{k})$ given in Eq. (E.4). The corresponding parameters are specified in the panel.

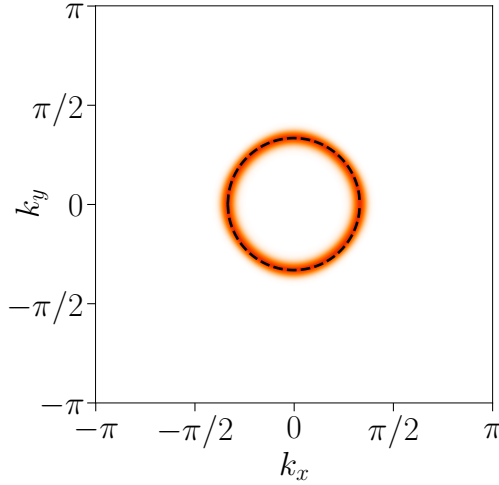


Figure E.1.: 2D system without total charge conservation. The figure shows $e^{-|\chi(\mathbf{k})|^2}$ (orange) and solutions of $\chi(\mathbf{k}) = 0$ (black dashed line) with the analytical expression for $\chi(\mathbf{k})$ given in Eq. (E.8).

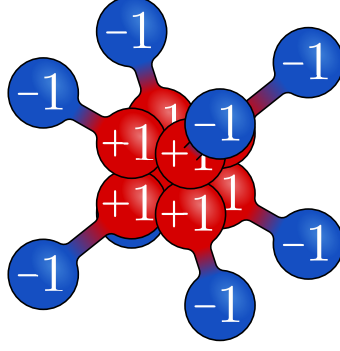


Figure E.2.: Structure of the three-dimensional gate whose characteristic's zeros ($\chi(\mathbf{k}) = 0$) are shown in Fig. 6.6b. It is constructed from two Eq. (6.30) gates superimposed on the diagonal planes.

Finally, we turn to a 3D model, which is a natural generalization of Eq. (6.30). The corresponding gate acts on a $4 \times 4 \times 4$ cube, moving charges between the inner 8 sites and the outer corners; this is illustrated in Fig. E.2. The resulting characteristic equation is given by

$$\begin{aligned} \chi(\mathbf{k}) = & 16 \cos\left(\frac{k_x}{2}\right) \cos\left(\frac{k_y}{2}\right) \cos\left(\frac{k_z}{2}\right) \times \\ & \times [4 \cos(k_x) \cos(k_y) \cos(k_z) - \\ & - 2(\cos(k_x) \cos(k_y) + \cos(k_y) \cos(k_z) + \cos(k_x) \cos(k_z)) \\ & + \cos(k_x) + \cos(k_y) + \cos(k_z) - 1] e^{i\frac{k_x+k_y+k_z}{2}}. \end{aligned} \quad (\text{E.9})$$

The zeros of this function were sketched in Fig. 6.6b of the paper.

E.2. General theory for the decay of autocorrelations in 2D

Here we discuss how the presence of conserved momentum modes in 2D affects the decay of the spin-spin autocorrelation. As we argued in the main text, the long time behavior is dominated by the density of states at low frequencies, via Eq. (5.31), which can be determined from the dispersion relation $\omega(\mathbf{k}) \sim |\chi(\mathbf{k})|^2$. We first discuss the details of this calculation for the model (6.30) and then provide some general considerations applicable to arbitrary dispersion relations.

E.2.1. General considerations

As we saw in Fig. 6.6a, and in the previous section, there are many other examples of conserved momentum modes arranged along various shapes in the BZ. While the details of these shapes should show up in the spatial structure of $C(\mathbf{r}, t)$, the $\mathbf{r} = \mathbf{0}$ autocorrelation is dictated by a few relevant features that enter into the calculation of $\rho(\omega)$. Similarly to the example above, we will split up the calculation of $\rho(\omega)$ into two contributions: continuous lines and singular points (such as crossing points between two lines).

Along the lines, $N(\omega)$ is the area of a strip given by broadening the line to include points with $\omega(\mathbf{k}) \leq \omega$; The width of this strip depends on the expansion of ω along the transverse direction. Taylor expanding around a point \mathbf{k} on the contour, we can write the leading order term as $\chi(\mathbf{k} + \delta\mathbf{k}) \approx (a\delta k_x + b\delta k_y)^m$, where $a, b \in \mathbb{R}$ generically depend on \mathbf{k} . We call m the *multiplicity* of the line: the simplest possibility, realized in the model (6.30), is $m = 1$ which gives $N(\omega) \sim \omega^{1/2}$ and thus $C(\mathbf{0}, t) \sim t^{-1/2}$. However, higher multiplicities are possible, as in the model shown on the left of Table E.1, where near the $k_x = 0$ axis,

Appendix E. Survey of results for spatially-modulated symmetries

we have $\omega(\mathbf{k}) \sim k_y^4$ (and vice versa). In general, we then get $N(\omega) \sim \omega^{1/2m}$ which leads to a contribution $C(\mathbf{0}, t) \sim t^{-1/2m}$ in the autocorrelation.

An enhanced contribution to the DOS can arise from *singular points*, where the leading order Taylor expansion of $\chi(\mathbf{k})$ does not have the form $(a\delta k_x + b\delta k_y)^m$. This can occur for various reasons: at isolated points, at a meeting point of multiple branches of the curve, or if the form of the expansion changes at a point along the curve. In our list of singular points, we also include points where two or more lines touch: while in this case we do have an expansion of the above form, with $m > 1$, the value of m changes discontinuously as we move away from the touching point.

Without loss of generality, we can write the leading term in the Taylor expansion of the characteristic function around a point as [326]

$$\chi(\mathbf{k} + \delta\mathbf{k}) \approx \prod_i (a_i \delta k_x + b_i \delta k_y)^{m_i}, \quad (\text{E.10})$$

where the coefficients a_i, b_i might be complex in general. When a_i/b_i is real, we can picture the corresponding term as the tangent of the curve at \mathbf{k} , each appearing with some multiplicity m_i . $m_i > 1$ might occur because the line in question itself has a non-trivial multiplicity, or because two different lines share the same tangent, i.e. when they have a touching point at \mathbf{k} . Terms where a_i/b_i is complex are singularities that do not arise from the meeting of contour lines; an extreme example is an isolated singular point (such as $\mathbf{k} = \mathbf{0}$ for Eq. (6.34)) where all tangent lines are complex. For another example of complex roots, consider $\mathbf{k} = \mathbf{0}$ in the left panel of Table E.2.

Using polar coordinates, $(\delta k_x, \delta k_y) \equiv (k \cos \theta, k \sin \theta)$ we can rewrite Eq. (E.10) as $\chi(\mathbf{k} + \delta\mathbf{k}) \approx k^m f(\theta)$, where $m \equiv \sum_i m_i$ is the total multiplicity of the singular point. Consider now the set of points defined by the condition $\omega(k, \theta) \sim |\chi(k, \theta)|^2 = k^{2m} |f(\theta)|^2 = \omega$; this is equivalent to $k = k_\omega(\theta) = \omega^{1/2m} |f(\theta)|^{-1/m}$. The state counting then becomes

$$N(\omega) \sim \int_{\omega(\mathbf{k}) \leq \omega} d^2k = \int_0^{2\pi} d\theta \int_0^{k_\omega(\theta)} dk k = \frac{\omega^{1/m}}{2} \int_0^{2\pi} d\theta |f(\theta)|^{-2/m}. \quad (\text{E.11})$$

The integrand in Eq. (E.11) diverges along the tangent lines, $\theta = \theta_i$, defined by $a_i \cos \theta_i + b_i \sin \theta_i = 0$. We can split the integral into regions close to these angles and regions away from them, as illustrated in Fig. E.3; for the latter, the integrand is finite and we are simply left with a contribution that scales as $N(\omega) \sim \omega^{1/m}$.

The contribution from regions close to $\theta \approx \theta_i$ depends on how $f(\theta)$ vanishes at this point, which is set by the multiplicity m_i : $f(\theta_i + \delta\theta) \sim \delta\theta^{m_i} + \mathcal{O}(\delta\theta^{m_i+1})$. Close to the tangent line, we thus have $\int_{\theta_i}^{\theta_i + \Delta\theta_i} d\theta (\theta - \theta_i)^{-2m_i/m}$ (here $\Delta\theta_i$ is some small angle beyond which the leading order Taylor expansion is no longer valid) If $2m_i < m$ then the integral converges and we are left with $N(\omega) \sim \omega^{1/m}$. If $2m_i \geq m$ it diverges at $\omega \rightarrow 0$ and we need to regularize it.

To regularize the integral, note that our initial Taylor expansion of $\chi(\mathbf{k})$ is only valid within some neighborhood of the singular point we consider. In particular, we should restrict ourselves to a disc of some small radius, $k \leq \Delta k$, around this point and count low-frequency states only within this circle. This means that the part of the integral (E.11) near θ_i should be further decomposed into two parts: those θ for which $k_\omega(\theta) \leq \Delta k$ and those where $k_\omega(\theta) > \Delta k$; this is again illustrated in Fig. E.3. The point separating the two cases is defined by $\Delta k^{2m} |f(\theta_i + \delta\theta_i^*)|^2 \sim \Delta k^{2m} (\delta\theta_i^*)^{2m_i} = \omega$ which implies $\delta\theta_i^* \sim \omega^{1/2m_i} / \Delta k^{m/m_i}$. We thus replace the contribution from $\theta \approx \theta_i$ with a sum of two terms:

$$\int_{\theta_i}^{\theta_i + \Delta\theta_i} k_\omega^2(\theta) d\theta \rightarrow \Delta k^2 \int_{\theta_i}^{\theta_i + \delta\theta_i^*} d\theta + \int_{\theta_i + \delta\theta_i^*}^{\theta_i + \Delta\theta_i} k_\omega^2(\theta) d\theta. \quad (\text{E.12})$$

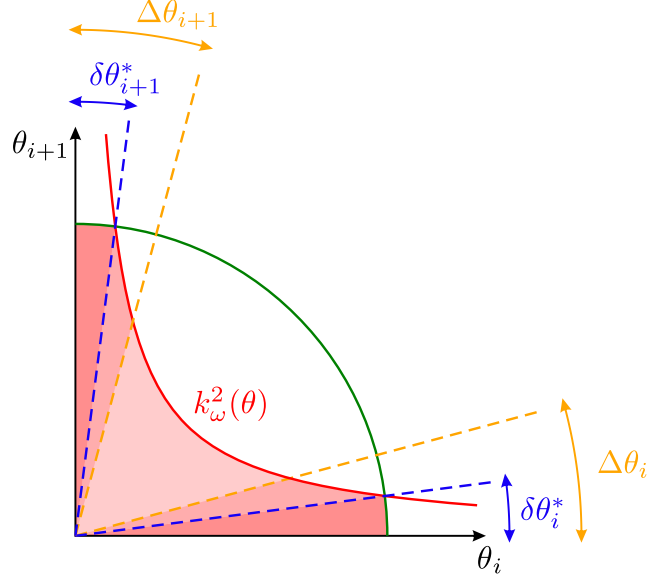


Figure E.3.: Evaluating the integral over angles in Eq. (E.11). We evaluate a contribution from the region between two subsequent zeros of $f(\theta)$, θ_i and θ_{i+1} which we take to be the x and y axes for simplicity. We are interested in the area bounded by the curve $k_\omega^2(\theta)$ (red line) which diverges at $\theta_{i,i+1}$; to regularize we restrict to within a circle of radius Δk (green line). This splits the area into three parts, shown in different shades of red. This figure was created by Tibor Rakovszky and published in Ref. [5].

The first is simply the area of the circular segment between θ_i and $\theta_i + \delta\theta_i^*$, which gives $N(\omega) \sim \Delta k^2 \delta\theta_i^* \sim \omega^{1/2m_i}$. The second behaves differently depending on whether $2m_i = m$ or $2m_i > m$:

$$\omega^{\frac{1}{m}} \int_{\delta\theta_i^*}^{\Delta\theta} \frac{d\theta}{\theta^{2m_i/m}} \sim \begin{cases} \omega^{\frac{1}{m}} \log(\omega) & 2m_i = m \\ \omega^{\frac{1}{2m_i}} + \mathcal{O}(\omega^{\frac{1}{m}}) & 2m_i > m \end{cases}.$$

To summarize we find three distinct cases:

- if $2m_i < m$ then $N(\omega) \sim \omega^{1/m}$,
- if $2m_i = m$ then $N(\omega) \sim \omega^{1/m} \log(\omega)$,
- if $2m_i > m$ then $N(\omega) \sim \omega^{1/2m_i}$,

to leading order. Remembering that $m = \sum_i m_i$, the condition $2m_i > m$ is equivalent to $m_i > \sum_{j \neq i} m_j$, such that one tangent line dominates over all the others.

The first of these possibilities is realized at the origin in Fig. 6.6a and in the right panel of Tables E.1 and E.2. In these cases m is simply the number of lines that cross; for example, the dispersion of Fig. 6.6a leads to $C(\mathbf{0}, t) \sim t^{-1/4}$. The second case was realized at the crossing points in the model (6.30), with $m_1 = m_2 = 1$. This is also the case near the origin in the left figure of Table E.1 where $m_1 = m_2 = 2$. In some sense, the most interesting is the last possibility. In this case, the DOS has an entirely different power law than what the naive dimension counting $\omega \sim k^{2m}$ would suggest; consequently correlations have a slower decay $C(\mathbf{0}, t) \sim t^{-1/2m_i}$. A simple situation where this occurs is a point where two lines have a touching point.

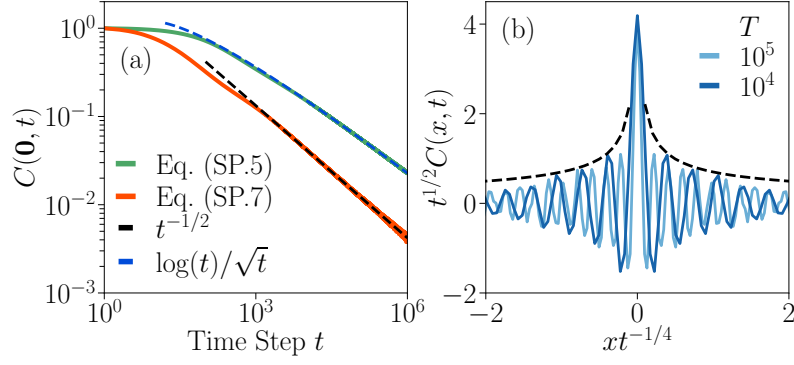


Figure E.4.: **Examples of 2D models lacking charge conservation.** (a) Autocorrelation decay $C(\mathbf{0}, t)$ for gates in Eq. (E.7) (red line) and Eq. (E.5) (green line). (b) Approximate scaling collapse for model in Eq. (E.7).

E.2.2. Applications to models in Fig. 6.6a

Let us first consider the model specified by the set of gates in Eq. (E.7) and associated set of slow modes specified by Eq. (E.8), which lie along a single-loop. Since no momentum \mathbf{k} along this loop is a singular point, e.g., there are no crossings, the multiplicity of the line is simply $m = 1$. This then leads to $N(\omega) \sim \omega^{1/2}$, i.e., the area of a ‘fattened’ loop of transversal size $\omega^{1/2}$, giving an autocorrelation decay $C(\mathbf{0}, t) \sim t^{-1/2}$, as numerically verified in Fig. E.4a (see red line). In fact, approximating the set of solutions by a circle of radius k_* we can get a closed expression for $C(\mathbf{r}, t)$ as the Hankel transform of $e^{-(k^2 - k_*^2)^2 t}$

$$C(\mathbf{r}, t) = 2\pi \int_0^\infty dk k \mathcal{J}_0(kr) e^{-(k^2 - k_*^2)^2 t}, \quad (\text{E.13})$$

with \mathcal{J}_0 the zeroth order Bessel function of the first kind. While for $k_* = 0$, this has a closed analytical expression given by a Meijer G-function, this does not appear to be the case for k_* . Thus, we consider the limit $t \rightarrow \infty$ where only momenta $k \approx k_*$ contribute, such that we obtain the leading order term

$$C(\mathbf{r}, t) \sim \frac{\mathcal{J}_0(k_* r)}{\sqrt{t}}, \quad (\text{E.14})$$

resembling our findings in 1D, with the sinusoidal dressing replaced by a different oscillatory function. This approximate behavior is numerically verified in Fig. E.4b (black dashed line). We will further discuss this model in Section 6.2.1.

On the other hand, the set of slow modes associated to the second model in Eq. (E.5) (see left half of Fig. 6.6a), lie along two loops centered at $(\pi, 0)$ and $(0, \pi)$. These intersect at eight different points along the $k_y = \pm k_x$ lines given by $\{(\pm\frac{\pi}{6}, \pm\frac{\pi}{6}), (\pm\frac{5\pi}{6}, \pm\frac{5\pi}{6})\}$. As each independent loop has simple multiplicity ($m_i = 1$), this corresponds to the case $2m_i = m = \sum_i m_i = 2$, and thus we expect a long-time scaling of the autocorrelation given by $C(\mathbf{0}, t) \sim \log(t)/\sqrt{t} + \mathcal{O}(t^{-1/2})$. This prediction is numerically verified in Fig. E.4a (see blue line).

E.3. Counting the number of independent modulated symmetries

We would like to count the number of independent modulated symmetries corresponding to independent solutions of the two-dimensional recurrence equation Eq. (6.4). To do so, let us consider a finite system of linear size L and open boundary conditions (OBC), such that

E.3. Counting the number of independent modulated symmetries

all solutions of the recurrence relation correspond to exact symmetries. Imposing periodic boundary conditions (PBC), leads to the additional constraints $\alpha_{i+L,j} = \alpha_{i,j+L} = \alpha_{i,j}$ for all i, j , which then depends on the system size.

Let us first consider a particular example, and only later extend the resulting counting to the general case. Consider the recurrence relation

$$4\alpha_{i,j} - \alpha_{i-1,j} - \alpha_{i+1,j} - \alpha_{i,j-1} - \alpha_{i,j+1} = 0, \quad (\text{E.15})$$

which is a two-dimensional second-order linear equation in both x and y directions. This e.g., is the associated equation to the set of 3×3 local gates

$$G = \{n_{0,0}, n_{-1,0}, n_{1,0}, n_{0,1}, n_{0,-1}\} = \{4, -1, -1, -1, -1\},$$

Obtaining an analytical exact solution for a 2D recurrence relation, requires either to obtain the corresponding generating function, or rewriting the system as a Sylvester equation [324]. In both cases, and even with the full solution at hand, it is still rather involving to extract information from it. Alternatively, one can recursively solve $\alpha_{i,j} = f(\alpha_{m,n})$ with $m \neq i, n \neq j$, after fixing a minimal set of initial (or boundary [324]) conditions. For example, Eq. (E.15) can be expressed as

$$\alpha_{i+1,j} = 4\alpha_{i,j} - \alpha_{i-1,j} - \alpha_{i,j+1} - \alpha_{i,j-1}, \quad (\text{E.16})$$

such that it is sufficient to fix the values along the first two left columns $\alpha_{0,j}, \alpha_{1,j}$, and the rows at the bottom $\alpha_{i,0}$ and top $\alpha_{i,L}$ of the lattice, to obtain the value of any $\alpha_{i,j}$ corresponding to an exact conservation law. This implies that one needs to fix $D = 4(L-2)$ initial conditions. These correspond to the entries of $\alpha_{0,j}, \alpha_{1,j}, \alpha_{i,0}$ and $\alpha_{i,L}$ after taken care of the corner values which do not enter into the solution of the recurrence relation Eq. (E.15). In general, given a two dimensional recurrence relation, one needs to fix $D = \mathcal{O}(L)$ values.

However, not every choice of initial conditions corresponds to a linearly independent conserved quantity. Let us collect $\alpha_{0,j}, \alpha_{1,j}$ and $\alpha_{i,0}$ into a vector \mathbf{v}_0 with D entries. Then, any choice of initial conditions can be written as a linear combinations of elements of the canonical basis \mathbf{e}_i with zeros in every entry except the i th one. This was also the case in 1D: There we encountered a second-order recurrence relation which requires fixing (α_0, α_1) (or equivalently (α_0, α_{L-1})). Thus, the set of initial conditions is a two-dimensional vector space with canonical basis vectors: $\mathbf{e}_1 \equiv (1, 0)$ and $\mathbf{e}_2 \equiv (0, 1)$.

In 2D, this implies that there exist a subextensive number of linearly independent conserved quantities $D = \mathcal{O}(L)$. Indeed, this scaling is consistent with the fact that factorizable solutions of the form $\alpha_{i,j} = (r_x)^i (r_y)^j$, lead to one-dimensional manifolds parametrized by r_x, r_y . An example of this was shown in Fig. 6.4b and Fig. 6.6, but it also holds for the exponential localized solutions of Eq. (E.15).

We emphasize that for the previous computation any such choice corresponds to an exact symmetry. Nevertheless, in the case of PBC, neither exponential symmetries nor most modes are exactly realized; moreover, we also note that if \mathbf{k} is a conserved mode, so is $-\mathbf{k}$.

Bibliography

- [1] **Pablo Sala**, Tibor Rakovszky, Ruben Verresen, Michael Knap, and Frank Pollmann. Ergodicity breaking arising from Hilbert Space Fragmentation in Dipole-Conserving Hamiltonians. *Physical Review X*, 10(1), Feb 2020. ISSN 2160-3308. doi: 10.1103/physrevx.10.011047. URL <http://dx.doi.org/10.1103/PhysRevX.10.011047>.
- [2] Tibor Rakovszky, **Pablo Sala**, Ruben Verresen, Michael Knap, and Frank Pollmann. Statistical localization: From strong fragmentation to strong edge modes. *Physical Review B*, 101(12), Mar 2020. ISSN 2469-9969. doi: 10.1103/physrevb.101.125126. URL <http://dx.doi.org/10.1103/PhysRevB.101.125126>.
- [3] Sebastian Scherg, Thomas Kohlert, **Pablo Sala**, Frank Pollmann, Bharath Hebbe Madhusudhana, Immanuel Bloch, and Monika Aidelsburger. Observing non-ergodicity due to kinetic constraints in tilted Fermi-Hubbard chains. *Nature Communications*, 12(1), Jul 2021. ISSN 2041-1723. doi: 10.1038/s41467-021-24726-0. URL <http://dx.doi.org/10.1038/s41467-021-24726-0>.
- [4] Thomas Kohlert, Sebastian Scherg, **Pablo Sala**, Frank Pollmann, Bharath Hebbe Madhusudhana, Immanuel Bloch, and Monika Aidelsburger. Experimental realization of fragmented models in tilted Fermi-Hubbard chains, 2021. URL <https://arxiv.org/abs/2106.15586>.
- [5] **Pablo Sala**, Julius Lehmann, Tibor Rakovszky, and Frank Pollmann. Dynamics in systems with modulated symmetries. 2021. URL <https://arxiv.org/abs/2110.08302>.
- [6] Johannes Feldmeier, **Pablo Sala**, Giuseppe De Tomasi, Frank Pollmann, and Michael Knap. Anomalous diffusion in dipole- and higher-moment-conserving systems. *Physical Review Letters*, 125(24), Dec 2020. ISSN 1079-7114. doi: 10.1103/physrevlett.125.245303. URL <http://dx.doi.org/10.1103/PhysRevLett.125.245303>.
- [7] Giuseppe De Tomasi, Daniel Hetterich, **Pablo Sala**, and Frank Pollmann. Dynamics of strongly interacting systems: From Fock-space fragmentation to many-body localization. *Physical Review B*, 100(21), Dec 2019. ISSN 2469-9969. doi: 10.1103/physrevb.100.214313. URL <http://dx.doi.org/10.1103/PhysRevB.100.214313>.
- [8] Immanuel Bloch, Jean Dalibard, and Wilhelm Zwerger. Many-body physics with ultracold gases. *Rev. Mod. Phys.*, 80:885–964, Jul 2008. doi: 10.1103/RevModPhys.80.885. URL <https://link.aps.org/doi/10.1103/RevModPhys.80.885>.
- [9] Colin D. Bruzewicz, John Chiaverini, Robert McConnell, and Jeremy M. Sage. Trapped-ion quantum computing: Progress and challenges. *Applied Physics Reviews*, 6(2):021314, Jun 2019. doi: 10.1063/1.5088164. URL <https://doi.org/10.1063/1.5088164>.
- [10] Antoine Browaeys and Thierry Lahaye. Many-body physics with individually controlled rydberg atoms. *Nature Physics*, 16(2):132–142, Jan 2020. doi: 10.1038/s41567-019-0733-z. URL <https://doi.org/10.1038/s41567-019-0733-z>.

- [11] Mari Carmen Bañuls, Rainer Blatt, Jacopo Catani, Alessio Celi, Juan Ignacio Cirac, Marcello Dalmonte, Leonardo Fallani, Karl Jansen, Maciej Lewenstein, Simone Montangero, Christine A. Muschik, Benni Reznik, Enrique Rico, Luca Tagliacozzo, Karel Van Acoleyen, Frank Verstraete, Uwe-Jens Wiese, Matthew Wingate, Jakub Zakrzewski, and Peter Zoller. Simulating lattice gauge theories within quantum technologies. *The European Physical Journal D*, 74(8), aug 2020. doi: 10.1140/epjd/e2020-100571-8. URL <https://doi.org/10.1140%2Fepjd%2Fe2020-100571-8>.
- [12] Christian W. Bauer, Zohreh Davoudi, A. Baha Balantekin, Tanmoy Bhattacharya, Marcela Carena, Wibe A. de Jong, Patrick Draper, Aida El-Khadra, Nate Gemelke, Masanori Hanada, Dmitri Kharzeev, Henry Lamm, Ying-Ying Li, Junyu Liu, Mikhail Lukin, Yannick Meurice, Christopher Monroe, Benjamin Nachman, Guido Pagano, John Preskill, Enrico Rinaldi, Alessandro Roggero, David I. Santiago, Martin J. Savage, Irfan Siddiqi, George Siopsis, David Van Zanten, Nathan Wiebe, Yukari Yamauchi, Kübra Yeter-Aydeniz, and Silvia Zorzetti. Quantum simulation for high energy physics, 2022. URL <https://arxiv.org/abs/2204.03381>.
- [13] Adam R. Brown, Hrant Gharibyan, Stefan Leichenauer, Henry W. Lin, Sepehr Nezami, Grant Salton, Leonard Susskind, Brian Swingle, and Michael Walter. Quantum gravity in the lab: Teleportation by size and traversable wormholes, 2019. URL <https://arxiv.org/abs/1911.06314>.
- [14] Sepehr Nezami, Henry W. Lin, Adam R. Brown, Hrant Gharibyan, Stefan Leichenauer, Grant Salton, Leonard Susskind, Brian Swingle, and Michael Walter. Quantum gravity in the lab: Teleportation by size and traversable wormholes, part ii, 2021. URL <https://arxiv.org/abs/2102.01064>.
- [15] M. Gring, M. Kuhnert, T. Langen, T. Kitagawa, B. Rauer, M. Schreitl, I. Mazets, D. Adu Smith, E. Demler, and J. Schmiedmayer. Relaxation and prethermalization in an isolated quantum system. *Science*, 337(6100):1318–1322, 2012. doi: 10.1126/science.1224953. URL <http://science.sciencemag.org/content/337/6100/1318>.
- [16] Sebastian Hild, Takeshi Fukuhara, Peter Schauß, Johannes Zeiher, Michael Knap, Eugene Demler, Immanuel Bloch, and Christian Gross. Far-from-equilibrium spin transport in heisenberg quantum magnets. *Phys. Rev. Lett.*, 113:147205, Oct 2014. doi: 10.1103/PhysRevLett.113.147205. URL <https://link.aps.org/doi/10.1103/PhysRevLett.113.147205>.
- [17] R. C. Brown, R. Wyllie, S. B. Koller, E. A. Goldschmidt, M. Foss-Feig, and J. V. Porto. Two-dimensional superexchange-mediated magnetization dynamics in an optical lattice. *Science*, 348(6234):540–544, 2015. ISSN 0036-8075. doi: 10.1126/science.aaa1385. URL <http://science.sciencemag.org/content/348/6234/540>.
- [18] Adam M. Kaufman, M. Eric Tai, Alexander Lukin, Matthew Rispoli, Robert Schittko, Philipp M. Preiss, and Markus Greiner. Quantum thermalization through entanglement in an isolated many-body system. *Science*, 353(6301):794–800, 2016. doi: 10.1126/science.aaf6725. URL <http://science.sciencemag.org/content/353/6301/794>.
- [19] Yijun Tang, Wil Kao, Kuan-Yu Li, Sangwon Seo, Krishnanand Mallayya, Marcos Rigol, Sarang Gopalakrishnan, and Benjamin L. Lev. Thermalization near integrability in a dipolar quantum newton’s cradle. *Phys. Rev. X*, 8:021030, May 2018. doi: 10.1103/PhysRevX.8.021030. URL <https://link.aps.org/doi/10.1103/PhysRevX.8.021030>.

Bibliography

- [20] Tiff Brydges, Andreas Elben, Petar Jurcevic, Benoît Vermersch, Christine Maier, Ben P. Lanyon, Peter Zoller, Rainer Blatt, and Christian F. Roos. Probing rényi entanglement entropy via randomized measurements, apr 2019. URL <https://doi.org/10.1126%2Fscience.aau4963>.
- [21] L. D’Alessio, Y. Kafri, A. Polkovnikov, and M. Rigol. From quantum chaos and eigenstate thermalization to statistical mechanics and thermodynamics. *Advances in Physics*, 65(3):239–362, 2016. doi: 10.1080/00018732.2016.1198134. URL <https://doi.org/10.1080/00018732.2016.1198134>.
- [22] Christian Gogolin and Jens Eisert. Equilibration, thermalisation, and the emergence of statistical mechanics in closed quantum systems. *Reports on Progress in Physics*, 79(5):056001, 2016. URL <http://stacks.iop.org/0034-4885/79/i=5/a=056001>.
- [23] Florian Meinert, Michael Knap, Emil Kirilov, Katharina Jag-Lauber, Mikhail B. Zvonarev, Eugene Demler, and Hanns-Christoph Nägerl. Bloch oscillations in the absence of a lattice. *Science*, 356(6341):945–948, 2017. ISSN 0036-8075. doi: 10.1126/science.aah6616. URL <https://science.sciencemag.org/content/356/6341/945>.
- [24] J. von Neumann. Beweis des ergodensatzes und des h-theorems in der neuen mechanik. *Zeitschrift für Physik*, 57(1):30–70, sep 1929. doi: 10.1007/BF01339852. URL <https://doi.org/10.1007/BF01339852>.
- [25] J. von Neumann. Proof of the ergodic theorem and the h-theorem in quantum mechanics. *The European Physical Journal H*, 35(2):201–237, sep 2010. doi: 10.1140/epjh/e2010-00008-5. URL <https://doi.org/10.1140%2Fepjh%2Fe2010-00008-5>.
- [26] Luigi Amico, Rosario Fazio, Andreas Osterloh, and Vlatko Vedral. Entanglement in many-body systems. *Rev. Mod. Phys.*, 80:517–576, May 2008. doi: 10.1103/RevModPhys.80.517. URL <https://link.aps.org/doi/10.1103/RevModPhys.80.517>.
- [27] Michael A. Nielsen and Isaac L. Chuang. *Quantum Computation and Quantum Information: 10th Anniversary Edition*. Cambridge University Press, 2010. doi: 10.1017/CBO9780511976667.
- [28] John Preskill. Lecture notes on quantum computation (chapter 4). URL <http://theory.caltech.edu/~preskill/ph219/>.
- [29] J. M. Deutsch. Quantum statistical mechanics in a closed system. *Phys. Rev. A*, 43:2046–2049, Feb 1991. doi: 10.1103/PhysRevA.43.2046. URL <https://link.aps.org/doi/10.1103/PhysRevA.43.2046>.
- [30] M. Srednicki. Chaos and quantum thermalization. *Phys. Rev. E*, 50(2):888–901, August 1994. doi: 10.1103/PhysRevE.50.888. URL <https://link.aps.org/doi/10.1103/PhysRevE.50.888>.
- [31] Marcos Rigol, Vanja Dunjko, and Maxim Olshanii. Thermalization and its mechanism for generic isolated quantum systems. *Nature*, 452:854–8, 05 2008. doi: 10.1038/nature06838. URL <https://doi.org/10.1038%2Fnature06838>.
- [32] J.W. Gibbs. *Elementary Principles in Statistical Mechanics*. Schribner’s sons, 1902.
- [33] Hyungwon Kim, Tatsuhiko N. Ikeda, and David A. Huse. Testing whether all eigenstates obey the eigenstate thermalization hypothesis. *Phys. Rev. E*, 90:052105, Nov

2014. doi: 10.1103/PhysRevE.90.052105. URL <https://link.aps.org/doi/10.1103/PhysRevE.90.052105>.
- [34] D.M. Basko, I.L. Aleiner, and B.L. Altshuler. Metal–insulator transition in a weakly interacting many-electron system with localized single-particle states. *Annals of Physics*, 321(5):1126–1205, 2006. ISSN 0003-4916. doi: <https://doi.org/10.1016/j.aop.2005.11.014>. URL <http://www.sciencedirect.com/science/article/pii/S0003491605002630>.
- [35] Rahul Nandkishore and David A. Huse. Many-body localization and thermalization in quantum statistical mechanics. *Annual Review of Condensed Matter Physics*, 6(1):15–38, 2015. doi: 10.1146/annurev-conmatphys-031214-014726. URL <http://dx.doi.org/10.1146/annurev-conmatphys-031214-014726>.
- [36] Ehud Altman and Ronen Vosk. Universal dynamics and renormalization in many-body-localized systems. *Annual Review of Condensed Matter Physics*, 6(1):383–409, 2015. doi: 10.1146/annurev-conmatphys-031214-014701. URL <https://doi.org/10.1146/annurev-conmatphys-031214-014701>.
- [37] M. Schreiber, S. S. Hodgman, P. Bordia, H. P. Lüschen, M. H. Fischer, R. Vosk, E. Altman, U. Schneider, and I. Bloch. Observation of many-body localization of interacting fermions in a quasirandom optical lattice. *Science*, 349(6250):842, 2015. doi: 10.1126/science.aaa7432. URL <http://www.sciencemag.org/content/349/6250/842.abstract>.
- [38] A. Smith, J. Knolle, D. L. Kovrizhin, and R. Moessner. Disorder-free localization. *Phys. Rev. Lett.*, 118:266601, Jun 2017. doi: 10.1103/PhysRevLett.118.266601. URL <https://link.aps.org/doi/10.1103/PhysRevLett.118.266601>.
- [39] Marlon Brenes, Marcello Dalmonte, Markus Heyl, and Antonello Scardicchio. Many-body localization dynamics from gauge invariance. *Phys. Rev. Lett.*, 120:030601, Jan 2018. doi: 10.1103/PhysRevLett.120.030601. URL <https://link.aps.org/doi/10.1103/PhysRevLett.120.030601>.
- [40] M. van Horssen, E. Levi, and J. P. Garrahan. Dynamics of many-body localization in a translation-invariant quantum glass model. *Phys. Rev. B*, 92(10):100305, September 2015. doi: 10.1103/PhysRevB.92.100305. URL <https://link.aps.org/doi/10.1103/PhysRevB.92.100305>.
- [41] Zhihao Lan, Merlijn van Horssen, Stephen Powell, and Juan P. Garrahan. Quantum slow relaxation and metastability due to dynamical constraints. *Phys. Rev. Lett.*, 121:040603, Jul 2018. doi: 10.1103/PhysRevLett.121.040603. URL <https://link.aps.org/doi/10.1103/PhysRevLett.121.040603>.
- [42] Naoto Shiraishi and Takashi Mori. Systematic construction of counterexamples to the eigenstate thermalization hypothesis. *Phys. Rev. Lett.*, 119:030601, Jul 2017. doi: 10.1103/PhysRevLett.119.030601. URL <https://link.aps.org/doi/10.1103/PhysRevLett.119.030601>.
- [43] Hannes Bernien, Sylvain Schwartz, Alexander Keesling, Harry Levine, Ahmed Omran, Hannes Pichler, Soonwon Choi, A Zibrov, Manuel Endres, Markus Greiner, Vladan Vuletic, and Mikhail D. Lukin. Probing many-body dynamics on a 51-atom quantum simulator. *Nature*, 551, 07 2017. doi: 10.1038/nature24622. URL <https://doi.org/10.1038/nature24622>.

Bibliography

- [44] C. J. Turner, A. A. Michailidis, D. A. Abanin, M. Serbyn, and Z. Papić. Weak ergodicity breaking from quantum many-body scars. *Nature Physics*, 14(7):745–749, July 2018. ISSN 1745-2481. doi: 10.1038/s41567-018-0137-5. URL <https://www.nature.com/articles/s41567-018-0137-5>.
- [45] Soonwon Choi, Christopher J. Turner, Hannes Pichler, Wen Wei Ho, Alexios A. Michailidis, Zlatko Papić, Maksym Serbyn, Mikhail D. Lukin, and Dmitry A. Abanin. Emergent $su(2)$ dynamics and perfect quantum many-body scars. *Phys. Rev. Lett.*, 122:220603, Jun 2019. doi: 10.1103/PhysRevLett.122.220603. URL <https://link.aps.org/doi/10.1103/PhysRevLett.122.220603>.
- [46] Cheng-Ju Lin and Olexei I. Motrunich. Exact quantum many-body scar states in the rydberg-blockaded atom chain. *Physical Review Letters*, 122(17), apr 2019. doi: 10.1103/physrevlett.122.173401. URL <https://doi.org/10.1103/2Physrevlett.122.173401>.
- [47] Sanjay Moudgalya, Stephan Rachel, B. Andrei Bernevig, and Nicolas Regnault. Exact excited states of nonintegrable models. *Physical Review B*, 98(23), dec 2018. doi: 10.1103/physrevb.98.235155. URL <https://doi.org/10.1103/2Physrevb.98.235155>.
- [48] Sanjay Moudgalya, Nicolas Regnault, and B. Andrei Bernevig. Entanglement of exact excited states of affleck-kennedy-lieb-tasaki models: Exact results, many-body scars, and violation of the strong eigenstate thermalization hypothesis. *Phys. Rev. B*, 98:235156, Dec 2018. doi: 10.1103/PhysRevB.98.235156. URL <https://link.aps.org/doi/10.1103/PhysRevB.98.235156>.
- [49] E. Noether. Invariante variationsprobleme. *Nachrichten von der Gesellschaft der Wissenschaften zu Göttingen, Mathematisch-Physikalische Klasse*, 1918:235–257, 1918. URL <http://eudml.org/doc/59024>.
- [50] David A. Huse, Rahul Nandkishore, and Vadim Oganesyan. Phenomenology of fully many-body-localized systems. *Phys. Rev. B*, 90:174202, Nov 2014. doi: 10.1103/PhysRevB.90.174202. URL <http://link.aps.org/doi/10.1103/PhysRevB.90.174202>.
- [51] Maksym Serbyn, Z. Papić, and Dmitry A. Abanin. Local conservation laws and the structure of the many-body localized states. *Phys. Rev. Lett.*, 111:127201, Sep 2013. doi: 10.1103/PhysRevLett.111.127201. URL <http://link.aps.org/doi/10.1103/PhysRevLett.111.127201>.
- [52] Claudio Chamon. Quantum glassiness in strongly correlated clean systems: An example of topological overprotection. *Phys. Rev. Lett.*, 94:040402, Jan 2005. doi: 10.1103/PhysRevLett.94.040402. URL <https://link.aps.org/doi/10.1103/PhysRevLett.94.040402>.
- [53] Jeongwan Haah. Local stabilizer codes in three dimensions without string logical operators. *Phys. Rev. A*, 83:042330, Apr 2011. doi: 10.1103/PhysRevA.83.042330. URL <https://link.aps.org/doi/10.1103/PhysRevA.83.042330>.
- [54] M. Pretko, X. Chen, and Y. You. Fracton phases of matter. *International Journal of Modern Physics A*, 35(06):2030003, 2020. doi: 10.1142/S0217751X20300033. URL <https://doi.org/10.1142/S0217751X20300033>.

- [55] R. M. Nandkishore and M. Hermele. Fractons. *Annual Review of Condensed Matter Physics*, 10(1):295–313, 2019. doi: 10.1146/annurev-conmatphys-031218-013604. URL <https://doi.org/10.1146/annurev-conmatphys-031218-013604>.
- [56] Sagar Vijay, Jeongwan Haah, and Liang Fu. A new kind of topological quantum order: A dimensional hierarchy of quasiparticles built from stationary excitations. *Physical Review B*, 92(23), Dec 2015. ISSN 1550-235X. doi: 10.1103/physrevb.92.235136. URL <http://dx.doi.org/10.1103/PhysRevB.92.235136>.
- [57] Sagar Vijay, Jeongwan Haah, and Liang Fu. Fracton topological order, generalized lattice gauge theory, and duality. *Phys. Rev. B*, 94:235157, Dec 2016. doi: 10.1103/PhysRevB.94.235157. URL <https://link.aps.org/doi/10.1103/PhysRevB.94.235157>.
- [58] Timothy H. Hsieh and Gábor B. Halász. Fractons from partons. *Phys. Rev. B*, 96:165105, Oct 2017. doi: 10.1103/PhysRevB.96.165105. URL <https://link.aps.org/doi/10.1103/PhysRevB.96.165105>.
- [59] Gábor B. Halász, Timothy H. Hsieh, and Leon Balents. Fracton topological phases from strongly coupled spin chains. *Phys. Rev. Lett.*, 119:257202, Dec 2017. doi: 10.1103/PhysRevLett.119.257202. URL <https://link.aps.org/doi/10.1103/PhysRevLett.119.257202>.
- [60] Michael Pretko. Subdimensional particle structure of higher rank $u(1)$ spin liquids. *Phys. Rev. B*, 95:115139, Mar 2017. doi: 10.1103/PhysRevB.95.115139. URL <https://link.aps.org/doi/10.1103/PhysRevB.95.115139>.
- [61] M. Pretko. The Fracton Gauge Principle. *ArXiv e-prints*, July 2018.
- [62] Michael Pretko. Higher-spin witten effect and two-dimensional fracton phases. *Phys. Rev. B*, 96:125151, Sep 2017. doi: 10.1103/PhysRevB.96.125151. URL <https://link.aps.org/doi/10.1103/PhysRevB.96.125151>.
- [63] D. J. Williamson, Z. Bi, and M. Cheng. Fractonic matter in symmetry-enriched $U(1)$ gauge theory. *Phys. Rev. B*, 100:125150, Sep 2019. doi: 10.1103/PhysRevB.100.125150. URL <https://link.aps.org/doi/10.1103/PhysRevB.100.125150>.
- [64] Daniel Bulmash and Maissam Barkeshli. Generalized $U(1)$ Gauge Field Theories and Fractal Dynamics. *arXiv e-prints*, art. arXiv:1806.01855, June 2018.
- [65] D. Marcos, P. Widmer, E. Rico, M. Hafezi, P. Rabl, U.-J. Wiese, and P. Zoller. Two-dimensional lattice gauge theories with superconducting quantum circuits. *Annals of Physics*, 351:634–654, December 2014. doi: 10.1016/j.aop.2014.09.011.
- [66] Andrey Gromov. Towards classification of fracton phases: The multipole algebra. *Physical Review X*, 9(3), Aug 2019. ISSN 2160-3308. doi: 10.1103/physrevx.9.031035. URL <http://dx.doi.org/10.1103/PhysRevX.9.031035>.
- [67] Abhinav Prem, Jeongwan Haah, and Rahul Nandkishore. Glassy quantum dynamics in translation invariant fracton models. *Phys. Rev. B*, 95:155133, Apr 2017. doi: 10.1103/PhysRevB.95.155133. URL <https://link.aps.org/doi/10.1103/PhysRevB.95.155133>.
- [68] Michael Pretko. Finite-temperature screening of $u(1)$ fractons. *Phys. Rev. B*, 96:115102, Sep 2017. doi: 10.1103/PhysRevB.96.115102. URL <https://link.aps.org/doi/10.1103/PhysRevB.96.115102>.

Bibliography

- [69] Claudio Castelnovo and Claudio Chamon. Topological quantum glassiness. *Philosophical Magazine*, 92(1-3):304–323, 2012. doi: 10.1080/14786435.2011.609152. URL <https://doi.org/10.1080/14786435.2011.609152>.
- [70] E. H. Rezayi and F. D. M. Haldane. Laughlin state on stretched and squeezed cylinders and edge excitations in the quantum hall effect. *Phys. Rev. B*, 50:17199–17207, Dec 1994. doi: 10.1103/PhysRevB.50.17199. URL <https://link.aps.org/doi/10.1103/PhysRevB.50.17199>.
- [71] E. J. Bergholtz and A. Karlhede. Quantum hall system in tao-thouless limit. *Physical Review B*, 77(15), Apr 2008. ISSN 1550-235X. doi: 10.1103/physrevb.77.155308. URL <http://dx.doi.org/10.1103/PhysRevB.77.155308>.
- [72] Emil J. Bergholtz, Masaaki Nakamura, and Juha Suorsa. Effective spin chains for fractional quantum hall states. *Physica E: Low-dimensional Systems and Nanostructures*, 43(3):755 – 760, 2011. ISSN 1386-9477. doi: <https://doi.org/10.1016/j.physe.2010.07.044>. URL <http://www.sciencedirect.com/science/article/pii/S1386947710004340>. NanoPHYS 09.
- [73] Zheng-Yuan Wang, Shintaro Takayoshi, and Masaaki Nakamura. Spin-chain description of fractional quantum hall states in the jain series. *Phys. Rev. B*, 86:155104, Oct 2012. doi: 10.1103/PhysRevB.86.155104. URL <https://link.aps.org/doi/10.1103/PhysRevB.86.155104>.
- [74] Masaaki Nakamura, Zheng-Yuan Wang, and Emil J. Bergholtz. Exactly solvable fermion chain describing a $\nu = 1/3$ fractional quantum hall state. *Phys. Rev. Lett.*, 109:016401, Jul 2012. doi: 10.1103/PhysRevLett.109.016401. URL <https://link.aps.org/doi/10.1103/PhysRevLett.109.016401>.
- [75] T. Hartmann, F. Keck, H. J. Korsch, and S. Mossmann. Dynamics of Bloch oscillations. *New J. Phys.*, 6:2–2, January 2004. ISSN 1367-2630. doi: 10.1088/1367-2630/6/1/002. URL <https://doi.org/10.1088/1367-2630/6/1/002>.
- [76] M. Schulz, C. A. Hooley, R. Moessner, and F. Pollmann. Stark Many-Body Localization. *Phys. Rev. Lett.*, 122(4):040606, January 2019. doi: 10.1103/PhysRevLett.122.040606. URL <https://link.aps.org/doi/10.1103/PhysRevLett.122.040606>.
- [77] L. D’Alessio and M. Rigol. Long-time Behavior of Isolated Periodically Driven Interacting Lattice Systems. *Physical Review X*, 4(4), Dec 2014. ISSN 2160-3308. URL <http://dx.doi.org/10.1103/PhysRevX.4.041048>.
- [78] E. T. Jaynes. Information theory and statistical mechanics. *Phys. Rev.*, 106:620–630, May 1957. doi: 10.1103/PhysRev.106.620. URL <https://link.aps.org/doi/10.1103/PhysRev.106.620>.
- [79] T. Mori, T. N. Ikeda, E. Kaminishi, and M. Ueda. Thermalization and prethermalization in isolated quantum systems: a theoretical overview. *Journal of Physics B: Atomic, Molecular and Optical Physics*, 51(11):112001, may 2018. doi: 10.1088/1361-6455/aabcbf. URL <https://doi.org/10.1088/1361-6455/aabcbf>.
- [80] J. Eisert, M. Friesdorf, and C. Gogolin. Quantum many-body systems out of equilibrium. *Nature Physics*, 11(2):124–130, feb 2015. doi: 10.1038/nphys3215. URL <https://doi.org/10.1038/nphys3215>.
- [81] David Huse. Summer school: Dynamics and disorder in quantum many body systems far from equilibrium, 2019.

- [82] R. V. Jensen and R. Shankar. Statistical behavior in deterministic quantum systems with few degrees of freedom. *Phys. Rev. Lett.*, 54:1879–1882, Apr 1985. doi: 10.1103/PhysRevLett.54.1879. URL <https://link.aps.org/doi/10.1103/PhysRevLett.54.1879>.
- [83] M V Berry. Regular and irregular semiclassical wavefunctions. *Journal of Physics A: Mathematical and General*, 10(12):2083–2091, dec 1977. doi: 10.1088/0305-4470/10/12/016. URL <https://doi.org/10.1088/0305-4470/10/12/016>.
- [84] Mark Srednicki. The approach to thermal equilibrium in quantized chaotic systems. *Journal of Physics A: Mathematical and General*, 32(7):1163–1175, jan 1999. doi: 10.1088/0305-4470/32/7/007. URL <https://doi.org/10.1088/0305-4470/32/7/007>.
- [85] G. P. Berman and F. M. Izrailev. The fermi–pasta–ulam problem: Fifty years of progress. *Chaos: An Interdisciplinary Journal of Nonlinear Science*, 15(1):015104, mar 2005. doi: 10.1063/1.1855036. URL <https://doi.org/10.1063/1.1855036>.
- [86] Matthew B. Hastings and Tohru Koma. Spectral gap and exponential decay of correlations. *Communications in Mathematical Physics*, 265(3):781–804, apr 2006. doi: 10.1007/s00220-006-0030-4. URL <https://doi.org/10.1007/s00220-006-0030-4>.
- [87] Tony Jin. Equilibration of quantum cat states. *SciPost Phys.*, 9:4, 2020. doi: 10.21468/SciPostPhys.9.1.004. URL <https://scipost.org/10.21468/SciPostPhys.9.1.004>.
- [88] Giulio Biroli, Corinna Kollath, and Andreas M. Läuchli. Effect of rare fluctuations on the thermalization of isolated quantum systems. *Phys. Rev. Lett.*, 105:250401, Dec 2010. doi: 10.1103/PhysRevLett.105.250401. URL <https://link.aps.org/doi/10.1103/PhysRevLett.105.250401>.
- [89] Noah Linden, Sandu Popescu, Anthony J. Short, and Andreas Winter. Quantum mechanical evolution towards thermal equilibrium. *Phys. Rev. E*, 79(6):061103, June 2009. doi: 10.1103/PhysRevE.79.061103.
- [90] Naoto Shiraishi and Keiji Matsumoto. Undecidability in quantum thermalization. *Nature Communications*, 12(1), aug 2021. doi: 10.1038/s41467-021-25053-0. URL <https://doi.org/10.1038/s41467-021-25053-0>.
- [91] James R. Garrison and Tarun Grover. Does a single eigenstate encode the full hamiltonian? *Physical Review X*, 8(2), apr 2018. doi: 10.1103/physrevx.8.021026. URL <https://doi.org/10.1103/physrevx.8.021026>.
- [92] Takashi Mori. Weak eigenstate thermalization with large deviation bound, 2016.
- [93] Giacomo De Palma, Alessio Serafini, Vittorio Giovannetti, and Marcus Cramer. Necessity of eigenstate thermalization. *Physical Review Letters*, 115(22), nov 2015. doi: 10.1103/physrevlett.115.220401. URL <https://doi.org/10.1103/physrevlett.115.220401>.
- [94] Fritz Haake. *Quantum Signatures of Chaos*. Springer-Verlag, Berlin, Heidelberg, 2006. ISBN 3540677232.
- [95] O. Bohigas, M. J. Giannoni, and C. Schmit. Characterization of chaotic quantum spectra and universality of level fluctuation laws. *Phys. Rev. Lett.*, 52:1–4, Jan

Bibliography

1984. doi: 10.1103/PhysRevLett.52.1. URL <https://link.aps.org/doi/10.1103/PhysRevLett.52.1>.
- [96] MV Berry. Chaos and the semiclassical limit of quantum mechanics (is the moon there when somebody looks?). In *Quantum Mechanics: Scientific perspectives on divine action*, pages 41 – 54. Vatican Observatory CTNS publications, 2001. Other: Eds R J Rusell, P Clayton, K Wegter-McNelly and J Polkinghorne.
- [97] N Schuch, M M Wolf, K G H Vollbrecht, and J I Cirac. On entropy growth and the hardness of simulating time evolution. *New Journal of Physics*, 10(3):033032, mar 2008. doi: 10.1088/1367-2630/10/3/033032. URL <https://doi.org/10.1088/2F1367-2630%2F10%2F3%2F033032>.
- [98] Dieter Forster. *Hydrodynamic fluctuations, broken symmetry, and correlation functions*. CRC Press, 2018.
- [99] Jonathan Lux, Jan Müller, Aditi Mitra, and Achim Rosch. Hydrodynamic long-time tails after a quantum quench. *Physical Review A*, 89(5), May 2014. ISSN 1094-1622. doi: 10.1103/physreva.89.053608. URL <http://dx.doi.org/10.1103/PhysRevA.89.053608>.
- [100] J. Lux. *Fluctuations in and out of Equilibrium: Thermalization, quantum measurements and Coulomb disorder*. PhD thesis, 2016.
- [101] P. M. Chaikin and T. C. Lubensky. *Principles of Condensed Matter Physics*. Cambridge University Press, 1995. doi: 10.1017/CBO9780511813467.
- [102] Benjamin Doyon. Lecture Notes On Generalised Hydrodynamics. *SciPost Phys. Lect. Notes*, page 18, 2020. doi: 10.21468/SciPostPhysLectNotes.18. URL <https://scipost.org/10.21468/SciPostPhysLectNotes.18>.
- [103] S. Mukerjee, V. Oganesyan, and D. Huse. Statistical theory of transport by strongly interacting lattice fermions. *Phys. Rev. B*, 73:035113, Jan 2006. doi: 10.1103/PhysRevB.73.035113. URL <https://link.aps.org/doi/10.1103/PhysRevB.73.035113>.
- [104] A Bohrdt, C B Mendl, M Endres, and M Knap. Scrambling and thermalization in a diffusive quantum many-body system. *New Journal of Physics*, 19(6):063001, 2017. URL <http://stacks.iop.org/1367-2630/19/i=6/a=063001>.
- [105] E. Leviatan, F. Pollmann, J. H. Bardarson, D. A. Huse, and E. Altman. Quantum thermalization dynamics with Matrix-Product States, 2017.
- [106] T. Rakovszky, F. Pollmann, and C. W. von Keyserlingk. Diffusive Hydrodynamics of Out-of-Time-Ordered Correlators with Charge Conservation. *Phys. Rev. X*, 8:031058, Sep 2018. doi: 10.1103/PhysRevX.8.031058. URL <https://link.aps.org/doi/10.1103/PhysRevX.8.031058>.
- [107] V. Khemani, A. Vishwanath, and D. A. Huse. Operator spreading and the emergence of dissipative hydrodynamics under unitary evolution with conservation laws. *Phys. Rev. X*, 8:031057, Sep 2018. doi: 10.1103/PhysRevX.8.031057. URL <https://link.aps.org/doi/10.1103/PhysRevX.8.031057>.
- [108] D. E. Parker, X. Cao, A. Avdoshkin, T. Scaffidi, and E. Altman. A Universal Operator Growth Hypothesis. *Phys. Rev. X*, 9:041017, Oct 2019. doi: 10.1103/PhysRevX.9.041017. URL <https://link.aps.org/doi/10.1103/PhysRevX.9.041017>.

- [109] S. Gopalakrishnan and R. Vasseur. Kinetic Theory of Spin Diffusion and Superdiffusion in XXZ Spin Chains. *Phys. Rev. Lett.*, 122:127202, Mar 2019. doi: 10.1103/PhysRevLett.122.127202. URL <https://link.aps.org/doi/10.1103/PhysRevLett.122.127202>.
- [110] A. Schuckert, I. Lovas, and M. Knap. Nonlocal emergent hydrodynamics in a long-range quantum spin system. *Phys. Rev. B*, 101:020416, Jan 2020. doi: 10.1103/PhysRevB.101.020416. URL <https://link.aps.org/doi/10.1103/PhysRevB.101.020416>.
- [111] C. Zu, F. Machado, B. Ye, S. Choi, B. Kobrin, T. Mittiga, S. Hsieh, P. Bhattacharyya, M. Markham, D. Twitchen, A. Jarmola, D. Budker, C. R. Laumann, J. E. Moore, and N. Y. Yao. Emergent hydrodynamics in a strongly interacting dipolar spin ensemble. *Nature*, 597(7874):45–50, sep 2021. doi: 10.1038/s41586-021-03763-1. URL <https://doi.org/10.1038/s41586-021-03763-1>.
- [112] M. K. Joshi, F. Kranzl, A. Schuckert, I. Lovas, C. Maier, R. Blatt, M. Knap, and C. F. Roos. Observing emergent hydrodynamics in a long-range quantum magnet, 2021. URL <https://arxiv.org/abs/2107.00033>.
- [113] Elmer Guardado-Sanchez, Alan Morningstar, Benjamin M. Spar, Peter T. Brown, David A. Huse, and Waseem S. Bakr. Subdiffusion and heat transport in a tilted two-dimensional fermi-hubbard system. *Physical Review X*, 10(1), Feb 2020. ISSN 2160-3308. doi: 10.1103/physrevx.10.011042. URL <http://dx.doi.org/10.1103/PhysRevX.10.011042>.
- [114] LD Landau and EM Lifshitz. Fluid mechanics. Volume 6 of Course of Theoretical Physics, 2nd English ed. Translated from the Russian by JB Sykes, WH Reid, 1987.
- [115] Juan Maldacena, Stephen H. Shenker, and Douglas Stanford. A bound on chaos. *Journal of High Energy Physics*, 2016(8), aug 2016. doi: 10.1007/jhep08(2016)106. URL [https://doi.org/10.1007/jhep08\(2016\)106](https://doi.org/10.1007/jhep08(2016)106).
- [116] P. Mazur. Non-ergodicity of phase functions in certain systems. *Physica*, 43(4):533–545, 1969. ISSN 0031-8914. doi: [https://doi.org/10.1016/0031-8914\(69\)90185-2](https://doi.org/10.1016/0031-8914(69)90185-2). URL <http://www.sciencedirect.com/science/article/pii/0031891469901852>.
- [117] Abhishek Dhar, Aritra Kundu, and Keiji Saito. Revisiting the Mazur bound and the Suzuki equality. *Chaos, Solitons & Fractals*, 144:110618, mar 2021. doi: 10.1016/j.chaos.2020.110618. URL <https://doi.org/10.1016/j.chaos.2020.110618>.
- [118] D. N. Page. Average entropy of a subsystem. *Phys. Rev. Lett.*, 71:1291–1294, Aug 1993. URL <https://link.aps.org/doi/10.1103/PhysRevLett.71.1291>.
- [119] S.C. Morampudi, A. Chandran, and C.R. Laumann. Universal entanglement of typical states in constrained systems. *Physical Review Letters*, 124(5), Feb 2020. ISSN 1079-7114. doi: 10.1103/physrevlett.124.050602. URL <http://dx.doi.org/10.1103/PhysRevLett.124.050602>.
- [120] Giuseppe De Tomasi and Ivan M. Khaymovich. Multifractality meets entanglement: Relation for nonergodic extended states. *Physical Review Letters*, 124(20), May 2020. ISSN 1079-7114. doi: 10.1103/physrevlett.124.200602. URL <http://dx.doi.org/10.1103/PhysRevLett.124.200602>.

Bibliography

- [121] Hyungwon Kim and David A. Huse. Ballistic spreading of entanglement in a diffusive nonintegrable system. *Physical Review Letters*, 111(12), sep 2013. doi: 10.1103/physrevlett.111.127205. URL <https://doi.org/10.1103%2Fphysrevlett.111.127205>.
- [122] Pasquale Calabrese and John Cardy. Evolution of entanglement entropy in one-dimensional systems. *Journal of Statistical Mechanics: Theory and Experiment*, 2005(04):P04010, apr 2005. doi: 10.1088/1742-5468/2005/04/p04010. URL <https://doi.org/10.1088%2F1742-5468%2F2005%2F04%2Fp04010>.
- [123] Vincenzo Alba and Pasquale Calabrese. Entanglement and thermodynamics after a quantum quench in integrable systems. *Proceedings of the National Academy of Sciences*, 114(30):7947–7951, jul 2017. doi: 10.1073/pnas.1703516114. URL <https://doi.org/10.1073%2Fpnas.1703516114>.
- [124] Vincenzo Alba and Pasquale Calabrese. Entanglement dynamics after quantum quenches in generic integrable systems. *SciPost Physics*, 4(3), mar 2018. doi: 10.21468/scipostphys.4.3.017. URL <https://doi.org/10.21468%2Fscipostphys.4.3.017>.
- [125] Pasquale Calabrese. Entanglement spreading in non-equilibrium integrable systems. *SciPost Phys. Lect. Notes*, page 20, 2020. doi: 10.21468/SciPostPhysLectNotes.20. URL <https://scipost.org/10.21468/SciPostPhysLectNotes.20>.
- [126] Jean-Sébastien Caux and Jorn Mossel. Remarks on the notion of quantum integrability. *Journal of Statistical Mechanics: Theory and Experiment*, 2011(2):02023, Feb 2011. doi: 10.1088/1742-5468/2011/02/P02023.
- [127] Enej Ilievski, Marko Medenjak, Tomaž Prosen, and Lenart Zadnik. Quasilocal charges in integrable lattice systems. *Journal of Statistical Mechanics: Theory and Experiment*, 2016(6):064008, jun 2016. doi: 10.1088/1742-5468/2016/06/064008. URL <https://doi.org/10.1088%2F1742-5468%2F2016%2F06%2F064008>.
- [128] B. Sutherland. *Beautiful Models: 70 Years Of Exactly Solved Quantum Many-body Problems*. World Scientific Publishing Company, 2004. ISBN 9789813102149. URL <https://books.google.fr/books?id=ze87DQAAQBAJ>.
- [129] P. W. Anderson. Absence of diffusion in certain random lattices. *Phys. Rev.*, 109:1492–1505, Mar 1958. doi: 10.1103/PhysRev.109.1492. URL <https://link.aps.org/doi/10.1103/PhysRev.109.1492>.
- [130] I. V. Gornyi, A. D. Mirlin, and D. G. Polyakov. Interacting Electrons in Disordered Wires: Anderson Localization and Low-T Transport. *Physical Review Letters*, 95(20), nov 2005. doi: 10.1103/physrevlett.95.206603. URL <https://doi.org/10.1103%2Fphysrevlett.95.206603>.
- [131] Jens H. Bardarson, Frank Pollmann, and Joel E. Moore. Unbounded Growth of Entanglement in Models of Many-Body Localization. *Phys. Rev. Lett.*, 109(1):017202, July 2012. doi: 10.1103/PhysRevLett.109.017202.
- [132] Rahul Nandkishore and David A. Huse. Many-body localization and thermalization in quantum statistical mechanics. *Annual Review of Condensed Matter Physics*, 6(1):15–38, mar 2015. doi: 10.1146/annurev-conmatphys-031214-014726. URL <https://doi.org/10.1146%2Fannurev-conmatphys-031214-014726>.

- [133] Fabien Alet and Nicolas Laflorencie. Many-body localization: An introduction and selected topics. *Comptes Rendus Physique*, 19(6):498–525, sep 2018. doi: 10.1016/j.crhy.2018.03.003. URL <https://doi.org/10.1016%2Fj.crhy.2018.03.003>.
- [134] Dmitry A. Abanin, Ehud Altman, Immanuel Bloch, and Maksym Serbyn. Colloquium: Many-body localization, thermalization, and entanglement. *Reviews of Modern Physics*, 91(2), may 2019. doi: 10.1103/revmodphys.91.021001. URL <https://doi.org/10.1103%2Frevmodphys.91.021001>.
- [135] Jan Šuntajs, Janez Bonča, Tomaž Prosen, and Lev Vidmar. Quantum chaos challenges many-body localization. *Physical Review E*, 102(6), dec 2020. doi: 10.1103/physreve.102.062144. URL <https://doi.org/10.1103%2Fphysreve.102.062144>.
- [136] D.A. Abanin, J.H. Bardarson, G. De Tomasi, S. Gopalakrishnan, V. Khemani, S.A. Parameswaran, F. Pollmann, A.C. Potter, M. Serbyn, and R. Vasseur. Distinguishing localization from chaos: Challenges in finite-size systems. *Annals of Physics*, 427:168415, apr 2021. doi: 10.1016/j.aop.2021.168415. URL <https://doi.org/10.1016%2Fj.aop.2021.168415>.
- [137] Maksym Serbyn, Dmitry A. Abanin, and Zlatko Papić. Quantum many-body scars and weak breaking of ergodicity. *Nature Physics*, 17(6):675–685, may 2021. doi: 10.1038/s41567-021-01230-2. URL <https://doi.org/10.1038%2Fs41567-021-01230-2>.
- [138] Sanjay Moudgalya, B. Andrei Bernevig, and Nicolas Regnault. Quantum many-body scars and hilbert space fragmentation: A review of exact results, 2021. URL <https://arxiv.org/abs/2109.00548>.
- [139] Henning Labuhn, Daniel Barredo, Sylvain Ravets, Sylvain de Léséleuc, Tommaso Macrì, Thierry Lahaye, and Antoine Browaeys. Tunable two-dimensional arrays of single rydberg atoms for realizing quantum ising models. *Nature*, 534(7609):667–670, jun 2016. doi: 10.1038/nature18274. URL <https://doi.org/10.1038%2Fnature18274>.
- [140] Eric J. Heller. Bound-state eigenfunctions of classically chaotic hamiltonian systems: Scars of periodic orbits. *Phys. Rev. Lett.*, 53:1515–1518, Oct 1984. doi: 10.1103/PhysRevLett.53.1515. URL <https://link.aps.org/doi/10.1103/PhysRevLett.53.1515>.
- [141] Irene Papaefstathiou, Adam Smith, and Johannes Knolle. Disorder-free localization in a simple $U(1)$ lattice gauge theory. *Phys. Rev. B*, 102(16):165132, October 2020. doi: 10.1103/PhysRevB.102.165132.
- [142] Norbert Schuch, Michael M. Wolf, Frank Verstraete, and J. Ignacio Cirac. Entropy scaling and simulability by matrix product states. *Physical Review Letters*, 100(3), jan 2008. doi: 10.1103/physrevlett.100.030504. URL <https://doi.org/10.1103%2Fphysrevlett.100.030504>.
- [143] Y. Saad. Analysis of some krylov subspace approximations to the matrix exponential operator. *SIAM Journal on Numerical Analysis*, 29(1):209, 1992.
- [144] David J. Luitz, Nicolas Laflorencie, and Fabien Alet. Extended slow dynamical regime close to the many-body localization transition. *Phys. Rev. B*, 93:060201, Feb 2016. doi: 10.1103/PhysRevB.93.060201. URL <https://link.aps.org/doi/10.1103/PhysRevB.93.060201>.

Bibliography

- [145] Ingemar Bengtsson and Karol Zyczkowski. *Geometry of Quantum States: An Introduction to Quantum Entanglement*. Cambridge University Press, 2006. doi: 10.1017/CBO9780511535048.
- [146] Sandu Popescu, Anthony J. Short, and Andreas Winter. Entanglement and the foundations of statistical mechanics. *Nature Physics*, 2(11):754–758, oct 2006. doi: 10.1038/nphys444. URL <https://doi.org/10.1038/nphys444>.
- [147] Sheldon Goldstein, Joel L. Lebowitz, Roderich Tumulka, and Nino Zanghì. Canonical typicality. *Physical Review Letters*, 96(5), feb 2006. doi: 10.1103/physrevlett.96.050403. URL <https://doi.org/10.1103/physrevlett.96.050403>.
- [148] Robin Steinigeweg, Jochen Gemmer, and Wolfram Brenig. Spin and energy currents in integrable and nonintegrable spin- $\frac{1}{2}$ chains: A typicality approach to real-time autocorrelations. *Phys. Rev. B*, 91:104404, Mar 2015. doi: 10.1103/PhysRevB.91.104404. URL <https://link.aps.org/doi/10.1103/PhysRevB.91.104404>.
- [149] Tjark Heitmann, Jonas Richter, Dennis Schubert, and Robin Steinigeweg. Selected applications of typicality to real-time dynamics of quantum many-body systems. *Zeitschrift für Naturforschung A*, 75(5):421–432, apr 2020. doi: 10.1515/zna-2020-0010. URL <https://doi.org/10.1515/zna-2020-0010>.
- [150] Immanuel Bloch. Ultracold quantum gases in optical lattices. *Nature Physics*, 1(1): 23–30, 2005. ISSN 1745-2481. doi: 10.1038/nphys138. URL <https://doi.org/10.1038/nphys138>.
- [151] Immanuel Bloch. Introduction to cold atom experiments and optical lattices (online talk), 2018. URL <https://youtu.be/PSn10tbXhrg>.
- [152] Christian Gross and Waseem S. Bakr. Quantum gas microscopy for single atom and spin detection, 2020. URL <https://arxiv.org/abs/2010.15407>.
- [153] Waseem S. Bakr, Jonathon I. Gillen, Amy Peng, Simon Fölling, and Markus Greiner. A quantum gas microscope for detecting single atoms in a hubbard-regime optical lattice. *Nature*, 462(7269):74–77, nov 2009. doi: 10.1038/nature08482. URL <https://doi.org/10.1038/nature08482>.
- [154] Ulrich Schneider. *Interacting fermionic atoms in optical lattices - A quantum simulator for condensed matter physics*. PhD thesis, Mainz, 2011.
- [155] L. Boltzmann. *Lectures on Gas Theory*. Dover Books on Physics. Dover Publications, 1995. ISBN 9780486684550.
- [156] Emil J. Bergholtz, Masaaki Nakamura, and Juha Suorsa. Effective spin chains for fractional quantum hall states. *Physica E: Low-dimensional Systems and Nanostructures*, 43(3):755–760, 2011. ISSN 1386-9477. doi: <https://doi.org/10.1016/j.physe.2010.07.044>. URL <http://www.sciencedirect.com/science/article/pii/S1386947710004340>. NanoPHYS 09.
- [157] E. van Nieuwenburg, Y. Baum, and G. Refael. From Bloch oscillations to many-body localization in clean interacting systems. *PNAS*, 116(19):9269–9274, May 2019. ISSN 0027-8424, 1091-6490. doi: 10.1073/pnas.1819316116. URL <https://www.pnas.org/content/116/19/9269>.
- [158] S. Pai, M. Pretko, and R. M. Nandkishore. Localization in Fractonic Random Circuits. *Phys. Rev. X*, 9(2):021003, April 2019. doi: 10.1103/PhysRevX.9.021003. URL <https://link.aps.org/doi/10.1103/PhysRevX.9.021003>.

- [159] A general dipole conserving Hamiltonian is invariant under the transformation $S_n^\pm \rightarrow e^{\pm i\alpha \cdot n} S_n^\pm$ generated by the unitary $\exp(i\alpha \sum_n n S_n^z)$. Thus, for any spin representation, a local term $(S_{n_1}^+)^{d_1^+} \cdots (S_{n_k}^+)^{d_k^+} (S_{n_1}^-)^{d_1^-} \cdots (S_{n_k}^-)^{d_k^-}$ is dipole conserving if the following condition holds:

$$\sum_{n_i^+} d_i^+ n_i^+ - \sum_{n_i^-} d_i^- n_i^- = 0.$$
- [160] R. Resta. Quantum-Mechanical Position Operator in Extended Systems. *Physical Review Letters*, 80:1800–1803, March 1998. doi: 10.1103/PhysRevLett.80.1800.
- [161] Peter Reimann. Typicality for generalized microcanonical ensembles. *Phys. Rev. Lett.*, 99:160404, Oct 2007. doi: 10.1103/PhysRevLett.99.160404. URL <https://link.aps.org/doi/10.1103/PhysRevLett.99.160404>.
- [162] M. Michel Jochen Gemmer and Günter Mahler. *Quantum Thermodynamics: Emergence of Thermodynamic Behavior Within Composite Quantum Systems*. Springer, Berlin, Heidelberg, 2009. doi: 10.1017/CBO9780511813467.
- [163] Since $C_0^z(0) = 2/3$, $\sum_n \langle S_n^z(t) S_0^z(0) \rangle_{T=\infty}$ is conserved and the system is thermalizing and translational invariant, the initial value $2/3$ will be homogeneously distributed over the chain.
- [164] Linus Pauling. The nature of the chemical bond. application of results obtained from the quantum mechanics and from a theory of paramagnetic susceptibility to the structure of molecules. *Journal of the American Chemical Society*, 53(4):1367–1400, 1931. doi: 10.1021/ja01355a027. URL <https://doi.org/10.1021/ja01355a027>.
- [165] L. Onsager and M. Dupuis. The electric properties of ice(*). in *Rend. Sc. Int. Fis. "Enrico Fermi", Corso X, Varenna*, page pp. 294–315, 1959.
- [166] Sanjay Moudgalya and Olexei I. Motrunich. Hilbert space fragmentation and commutant algebras. *Physical Review X*, 12(1), mar 2022. doi: 10.1103/physrevx.12.011050. URL <https://doi.org/10.1103/physrevx.12.011050>.
- [167] We would like to thank Zlatko Papić for bringing this to our attention.
- [168] C. J. Turner, A. A. Michailidis, D. A. Abanin, M. Serbyn, and Z. Papić. Quantum scarred eigenstates in a rydberg atom chain: Entanglement, breakdown of thermalization, and stability to perturbations. *Phys. Rev. B*, 98:155134, Oct 2018. doi: 10.1103/PhysRevB.98.155134. URL <https://link.aps.org/doi/10.1103/PhysRevB.98.155134>.
- [169] Sanjay Moudgalya, B. Andrei Bernevig, and Nicolas Regnault. Quantum Many-body Scars in a Landau Level on a Thin Torus. *arXiv e-prints*, art. arXiv:1906.05292, Jun 2019.
- [170] M. Suzuki. Ergodicity, constants of motion, and bounds for susceptibilities. *Physica*, 51(2):277–291, 1971. ISSN 0031-8914. doi: [https://doi.org/10.1016/0031-8914\(71\)90226-6](https://doi.org/10.1016/0031-8914(71)90226-6). URL <http://www.sciencedirect.com/science/article/pii/0031891471902266>.
- [171] The Hamiltonian H_5 appearing in Fig. 4 is given by $H_5 = \sum_n [S_{n-2}^+ S_{n-1}^- S_{n+1}^- S_{n+2}^+ + H.c.]$.
- [172] S. Moudgalya, A. Prem, R. Nandkishore, N. Regnault, and B. A. Bernevig. Thermalization and its absence within Krylov subspaces of a constrained Hamiltonian, 2019.

Bibliography

- [173] We thank the anonymous referee for pointing out this observation to us.
- [174] Lea F. Santos and Marcos Rigol. Onset of quantum chaos in one-dimensional bosonic and fermionic systems and its relation to thermalization. *Phys. Rev. E*, 81:036206, Mar 2010. doi: 10.1103/PhysRevE.81.036206. URL <https://link.aps.org/doi/10.1103/PhysRevE.81.036206>.
- [175] S. Sorg, L. Vidmar, L. Pollet, and F. Heidrich-Meisner. Relaxation and thermalization in the one-dimensional bose-hubbard model: A case study for the interaction quantum quench from the atomic limit. *Phys. Rev. A*, 90:033606, Sep 2014. doi: 10.1103/PhysRevA.90.033606. URL <https://link.aps.org/doi/10.1103/PhysRevA.90.033606>.
- [176] Rubem Mondaini, Keith R. Fratus, Mark Srednicki, and Marcos Rigol. Eigenstate thermalization in the two-dimensional transverse field ising model. *Phys. Rev. E*, 93:032104, Mar 2016. doi: 10.1103/PhysRevE.93.032104. URL <https://link.aps.org/doi/10.1103/PhysRevE.93.032104>.
- [177] S. Moudgalya, S. Rachel, B. A. Bernevig, and N. Regnault. Exact excited states of nonintegrable models. *Phys. Rev. B*, 98(23):235155, December 2018. doi: 10.1103/PhysRevB.98.235155. URL <https://link.aps.org/doi/10.1103/PhysRevB.98.235155>.
- [178] Alan Morningstar, Vedika Khemani, and David A. Huse. Kinetically constrained freezing transition in a dipole-conserving system. *Physical Review B*, 101(21), Jun 2020. ISSN 2469-9969. doi: 10.1103/physrevb.101.214205. URL <http://dx.doi.org/10.1103/PhysRevB.101.214205>.
- [179] Yuji Nozawa and Kouhei Fukai. Explicit construction of local conserved quantities in the XYZ spin-1/2 chain. *Physical Review Letters*, 125(9), aug 2020. doi: 10.1103/physrevlett.125.090602. URL <https://doi.org/10.1103%2Fphysrevlett.125.090602>.
- [180] J. S. Bell. *La nouvelle cuisine*, pages 216–234. doi: 10.1142/9789812386540_0022. URL https://www.worldscientific.com/doi/abs/10.1142/9789812386540_0022.
- [181] V. Khemani, M. Hermele, and R. Nandkishore. Localization from Hilbert space shattering: From theory to physical realizations. *Phys. Rev. B*, 101(17):174204, May 2020. doi: 10.1103/PhysRevB.101.174204. URL <https://link.aps.org/doi/10.1103/PhysRevB.101.174204>.
- [182] John Z. Imbrie, Valentina Ros, and Antonello Scardicchio. Local integrals of motion in many-body localized systems. *Annalen der Physik*, 529(7):1600278, 2017. doi: 10.1002/andp.201600278. URL <https://onlinelibrary.wiley.com/doi/abs/10.1002/andp.201600278>.
- [183] D. A. Abanin, E. Altman, I. Bloch, and M. Serbyn. Colloquium : Many-body localization, thermalization, and entanglement. *Rev. Mod. Phys.*, 91(2):021001, May 2019. ISSN 0034-6861, 1539-0756. doi: 10.1103/RevModPhys.91.021001. URL <https://link.aps.org/doi/10.1103/RevModPhys.91.021001>.
- [184] Paul Fendley. Parafermionic edge zero modes in Z_n -invariant spin chains. *Journal of Statistical Mechanics: Theory and Experiment*, 2012(11):P11020, nov 2012. doi: 10.1088/1742-5468/2012/11/p11020. URL <https://doi.org/10.1088/1742-5468/2012/11/p11020>.

- [185] Paul Fendley. Strong zero modes and eigenstate phase transitions in the XYZ/interacting majorana chain. *Journal of Physics A: Mathematical and Theoretical*, 49(30):30LT01, jun 2016. doi: 10.1088/1751-8113/49/30/30lt01. URL <https://doi.org/10.1088%2F1751-8113%2F49%2F30%2F30lt01>.
- [186] Jason Alicea and Paul Fendley. Topological phases with parafermions: Theory and blueprints. *Annual Review of Condensed Matter Physics*, 7(1):119–139, 2016. doi: 10.1146/annurev-conmatphys-031115-011336. URL <https://doi.org/10.1146/annurev-conmatphys-031115-011336>.
- [187] Jack Kemp, Norman Y Yao, Christopher R Laumann, and Paul Fendley. Long coherence times for edge spins. *Journal of Statistical Mechanics: Theory and Experiment*, 2017(6):063105, jun 2017. doi: 10.1088/1742-5468/aa73f0. URL <https://doi.org/10.1088%2F1742-5468%2Faa73f0>.
- [188] Dominic V. Else, Paul Fendley, Jack Kemp, and Chetan Nayak. Prethermal strong zero modes and topological qubits. *Phys. Rev. X*, 7:041062, Dec 2017. doi: 10.1103/PhysRevX.7.041062. URL <https://link.aps.org/doi/10.1103/PhysRevX.7.041062>.
- [189] Loredana M. Vasiloiu, Federico Carollo, Matteo Marcuzzi, and Juan P. Garrahan. Strong zero modes in a class of generalized ising spin ladders with plaquette interactions. *Physical Review B*, 100(2), Jul 2019. ISSN 2469-9969. doi: 10.1103/physrevb.100.024309. URL <http://dx.doi.org/10.1103/PhysRevB.100.024309>.
- [190] David A. Huse, Rahul Nandkishore, Vadim Oganesyan, Arijeet Pal, and S. L. Sondhi. Localization-protected quantum order. *Phys. Rev. B*, 88:014206, Jul 2013. doi: 10.1103/PhysRevB.88.014206. URL <https://link.aps.org/doi/10.1103/PhysRevB.88.014206>.
- [191] Anushya Chandran, Vedika Khemani, C. R. Laumann, and S. L. Sondhi. Many-body localization and symmetry-protected topological order. *Phys. Rev. B*, 89:144201, Apr 2014. doi: 10.1103/PhysRevB.89.144201. URL <https://link.aps.org/doi/10.1103/PhysRevB.89.144201>.
- [192] Shu Zhang, Michael Karbach, Gerhard Müller, and Joachim Stolze. Charge and spin dynamics in the one-dimensional t-j_z and t-j models. *Phys. Rev. B*, 55:6491–6503, Mar 1997. doi: 10.1103/PhysRevB.55.6491. URL <https://link.aps.org/doi/10.1103/PhysRevB.55.6491>.
- [193] A. Bohrdt, D. Greif, E. Demler, M. Knap, and F. Grusdt. Angle-resolved photoemission spectroscopy with quantum gas microscopes. *Phys. Rev. B*, 97:125117, Mar 2018. doi: 10.1103/PhysRevB.97.125117. URL <https://link.aps.org/doi/10.1103/PhysRevB.97.125117>.
- [194] M. Kotrla. Energy spectrum of the hubbard model with $u=\infty$. *Physics Letters A*, 145(1):33–36, 1990. ISSN 0375-9601. doi: [https://doi.org/10.1016/0375-9601\(90\)90272-P](https://doi.org/10.1016/0375-9601(90)90272-P). URL <http://www.sciencedirect.com/science/article/pii/037596019090272P>.
- [195] C. D. Batista and G. Ortiz. Generalized jordan-wigner transformations. *Phys. Rev. Lett.*, 86:1082–1085, Feb 2001. doi: 10.1103/PhysRevLett.86.1082. URL <https://link.aps.org/doi/10.1103/PhysRevLett.86.1082>.

Bibliography

- [196] N. M. R. Peres, R. G. Dias, P. D. Sacramento, and J. M. P. Carmelo. Finite-temperature transport in finite-size Hubbard rings in the strong-coupling limit. *Phys. Rev. B*, 61:5169–5183, Feb 2000. doi: 10.1103/PhysRevB.61.5169. URL <https://link.aps.org/doi/10.1103/PhysRevB.61.5169>.
- [197] Marko Medenjak, Katja Klobas, and Tomaž Prosen. Diffusion in deterministic interacting lattice systems. *Phys. Rev. Lett.*, 119:110603, Sep 2017. doi: 10.1103/PhysRevLett.119.110603. URL <https://link.aps.org/doi/10.1103/PhysRevLett.119.110603>.
- [198] Katja Klobas, Marko Medenjak, and Tomaž Prosen. Exactly solvable deterministic lattice model of crossover between ballistic and diffusive transport. *Journal of Statistical Mechanics: Theory and Experiment*, 2018(12):123202, dec 2018. doi: 10.1088/1742-5468/aae853. URL <https://doi.org/10.1088/1742-5468/aae853>.
- [199] C. D. Batista and G. Ortiz. Quantum phase diagram of the $t - J_z$ chain model. *Phys. Rev. Lett.*, 85:4755–4758, Nov 2000. doi: 10.1103/PhysRevLett.85.4755. URL <https://link.aps.org/doi/10.1103/PhysRevLett.85.4755>.
- [200] Enej Ilievski, Marko Medenjak, and Tomaž Prosen. Quasilocal conserved operators in the isotropic Heisenberg spin-1/2 chain. *Phys. Rev. Lett.*, 115:120601, Sep 2015. doi: 10.1103/PhysRevLett.115.120601. URL <https://link.aps.org/doi/10.1103/PhysRevLett.115.120601>.
- [201] Lev Vidmar and Marcos Rigol. Generalized gibbs ensemble in integrable lattice models. *Journal of Statistical Mechanics: Theory and Experiment*, 2016(6):064007, jun 2016. doi: 10.1088/1742-5468/2016/06/064007. URL <https://doi.org/10.1088/1742-5468/2016/06/064007>.
- [202] Marcin Mierzejewski and Lev Vidmar. Eigenstate thermalization hypothesis and integrals of motion, 2019.
- [203] Tyler LeBlond, Krishnanand Mallayya, Lev Vidmar, and Marcos Rigol. Entanglement and matrix elements of observables in interacting integrable systems, 2019.
- [204] R. Mondaini, K. Mallayya, L. F. Santos, and M. Rigol. Comment on “Systematic Construction of Counterexamples to the Eigenstate Thermalization Hypothesis”. *Phys. Rev. Lett.*, 121(3):038901, July 2018. doi: 10.1103/PhysRevLett.121.038901. URL <https://link.aps.org/doi/10.1103/PhysRevLett.121.038901>.
- [205] Naoto Shiraishi and Takashi Mori. Shiraishi and mori reply. *Phys. Rev. Lett.*, 121:038902, Jul 2018. doi: 10.1103/PhysRevLett.121.038902. URL <https://link.aps.org/doi/10.1103/PhysRevLett.121.038902>.
- [206] J. P. Kestner, Bin Wang, Jay D. Sau, and S. Das Sarma. Prediction of a gapless topological haldane liquid phase in a one-dimensional cold polar molecular lattice. *Phys. Rev. B*, 83:174409, May 2011. doi: 10.1103/PhysRevB.83.174409. URL <https://link.aps.org/doi/10.1103/PhysRevB.83.174409>.
- [207] Thomas Scaffidi, Daniel E. Parker, and Romain Vasseur. Gapless symmetry-protected topological order. *Phys. Rev. X*, 7:041048, Nov 2017. doi: 10.1103/PhysRevX.7.041048. URL <https://link.aps.org/doi/10.1103/PhysRevX.7.041048>.
- [208] Ruben Verresen, Ryan Thorngren, Nick G. Jones, and Frank Pollmann. Gapless topological phases and symmetry-enriched quantum criticality. *arXiv e-prints*, art. arXiv:1905.06969, May 2019.

- [209] Ryan Thorngren, Ashvin Vishwanath, and Ruben Verresen. Intrinsically gapless topological phases. *Phys. Rev. B*, 104:075132, Aug 2021. doi: 10.1103/PhysRevB.104.075132. URL <https://link.aps.org/doi/10.1103/PhysRevB.104.075132>.
- [210] Johannes Zeiher, Rick van Bijnen, Peter Schauß, Sebastian Hild, Jae-yoon Choi, Thomas Pohl, Immanuel Bloch, and Christian Gross. Many-body interferometry of a rydberg-dressed spin lattice. *Nature Physics*, 12(12):1095–1099, Aug 2016. ISSN 1745-2481. doi: 10.1038/nphys3835. URL <http://dx.doi.org/10.1038/nphys3835>.
- [211] Johannes Zeiher, Jae-yoon Choi, Antonio Rubio-Abadal, Thomas Pohl, Rick van Bijnen, Immanuel Bloch, and Christian Gross. Coherent many-body spin dynamics in a long-range interacting ising chain. *Phys. Rev. X*, 7:041063, Dec 2017. doi: 10.1103/PhysRevX.7.041063. URL <https://link.aps.org/doi/10.1103/PhysRevX.7.041063>.
- [212] N. Henkel, R. Nath, and T. Pohl. Three-dimensional roton excitations and super-solid formation in rydberg-excited bose-einstein condensates. *Phys. Rev. Lett.*, 104:195302, May 2010. doi: 10.1103/PhysRevLett.104.195302. URL <https://link.aps.org/doi/10.1103/PhysRevLett.104.195302>.
- [213] Igor Lesanovsky. Many-body spin interactions and the ground state of a dense rydberg lattice gas. *Physical Review Letters*, 106(2), Jan 2011. ISSN 1079-7114. doi: 10.1103/physrevlett.106.025301. URL <http://dx.doi.org/10.1103/PhysRevLett.106.025301>.
- [214] T. M. Wintermantel, Y. Wang, G. Lochead, S. Shevate, G. K. Brennen, and S. Whitlock. Unitary and non-unitary quantum cellular automata with rydberg arrays, 2019.
- [215] Christopher L. Henley. Relaxation time for a dimer covering with height representation. *Journal of Statistical Physics*, 89(3-4):483–507, nov 1997. doi: 10.1007/bf02765532. URL <https://doi.org/10.1007%2Fbf02765532>.
- [216] Sanjay Moudgalya, Abhinav Prem, David A. Huse, and Amos Chan. Spectral statistics in constrained many-body quantum chaotic systems. *Physical Review Research*, 3(2), Jun 2021. ISSN 2643-1564. doi: 10.1103/physrevresearch.3.023176. URL <http://dx.doi.org/10.1103/PhysRevResearch.3.023176>.
- [217] F. D. M. Haldane. Nonlinear field theory of large-spin heisenberg antiferromagnets: Semiclassically quantized solitons of the one-dimensional easy-axis néel state. *Phys. Rev. Lett.*, 50:1153–1156, Apr 1983. doi: 10.1103/PhysRevLett.50.1153. URL <https://link.aps.org/doi/10.1103/PhysRevLett.50.1153>.
- [218] Tom Kennedy and Hal Tasaki. Hidden $z_2 \times z_2$ symmetry breaking in haldane-gap antiferromagnets. *Phys. Rev. B*, 45:304–307, Jan 1992. doi: 10.1103/PhysRevB.45.304. URL <https://link.aps.org/doi/10.1103/PhysRevB.45.304>.
- [219] Frank Pollmann, Erez Berg, Ari M. Turner, and Masaki Oshikawa. Symmetry protection of topological phases in one-dimensional quantum spin systems. *Phys. Rev. B*, 85:075125, Feb 2012. doi: 10.1103/PhysRevB.85.075125. URL <https://link.aps.org/doi/10.1103/PhysRevB.85.075125>.
- [220] In the case of open boundary conditions, the two additional terms $X_1 P_2$ and $X_{L-1} P_L$ were added to Eq. (3.26) in the analysis of Ref. [168] that we follow in this appendix.

Bibliography

- [221] F. Ritort and P. Sollich. Glassy dynamics of kinetically constrained models. *Advances in Physics*, 52(4):219–342, 2003. doi: 10.1080/0001873031000093582. URL <https://doi.org/10.1080/0001873031000093582>.
- [222] Juan P. Garrahan. Aspects of non-equilibrium in classical and quantum systems: Slow relaxation and glasses, dynamical large deviations, quantum non-ergodicity, and open quantum dynamics. *Physica A: Statistical Mechanics and its Applications*, 504:130–154, aug 2018. doi: 10.1016/j.physa.2017.12.149. URL <https://doi.org/10.1016%2Fj.physa.2017.12.149>.
- [223] Tibor Rakovszky, Frank Pollmann, and C. W. von Keyserlingk. Diffusive hydrodynamics of out-of-time-ordered correlators with charge conservation. *Phys. Rev. X*, 8:031058, Sep 2018. doi: 10.1103/PhysRevX.8.031058. URL <https://link.aps.org/doi/10.1103/PhysRevX.8.031058>.
- [224] P. W. Anderson. More is different. *Science*, 177(4047):393–396, 1972. doi: 10.1126/science.177.4047.393. URL <https://www.science.org/doi/abs/10.1126/science.177.4047.393>.
- [225] Michael Schechter and Thomas Iadecola. Weak ergodicity breaking and quantum many-body scars in spin-1 xy magnets, 2019.
- [226] DLMF. NIST Digital Library of Mathematical Functions. <http://dlmf.nist.gov/>, Release 1.1.2 of 2021-06-15. URL <http://dlmf.nist.gov/>. F. W. J. Olver, A. B. Olde Daalhuis, D. W. Lozier, B. I. Schneider, R. F. Boisvert, C. W. Clark, B. R. Miller, B. V. Saunders, H. S. Cohl, and M. A. McClain, eds.
- [227] Mark Raizen, Christophe Salomon, and Qian Niu. New light on quantum transport. *Physics Today*, 50(7):30–34, 1997. doi: 10.1063/1.881845. URL <https://doi.org/10.1063/1.881845>.
- [228] G.N. Watson. *A Treatise on the Theory of Bessel Functions*. Cambridge Mathematical Library. Cambridge University Press, 1995. ISBN 9780521483919. URL <https://books.google.es/books?id=Mlk3FrNoEVoC>.
- [229] Nicolò Defenu, Tobias Donner, Tommaso Macrì, Guido Pagano, Stefano Ruffo, and Andrea Trombettoni. Long-range interacting quantum systems, 2021. URL <https://arxiv.org/abs/2109.01063>.
- [230] C. Parra-Murillo and S. Wimberger. Manifold Approach for a Many-Body Wannier-Stark System: Localization and Chaos in Energy Space. *Acta Physica Polonica A*, 124, 01 2014. URL <http://dx.doi.org/10.12693/APhysPolA.124.1091>.
- [231] C. A. Parra-Murillo, J. Madroñero, and S. Wimberger. Two-band Bose-Hubbard model for many-body resonant tunneling in the Wannier-Stark system. *Phys. Rev. A*, 88:032119, Sep 2013. doi: 10.1103/PhysRevA.88.032119. URL <https://link.aps.org/doi/10.1103/PhysRevA.88.032119>.
- [232] A. Buchleitner and A. R. Kolovsky. Interaction-Induced Decoherence of Atomic Bloch Oscillations. *Phys. Rev. Lett.*, 91(25):253002, December 2003. doi: 10.1103/PhysRevLett.91.253002. URL <https://link.aps.org/doi/10.1103/PhysRevLett.91.253002>.
- [233] D. V. Else, W. W. Ho, and P. T. Dumitrescu. Long-Lived Interacting Phases of Matter Protected by Multiple Time-Translation Symmetries in Quasiperiodically Driven Systems. *Phys. Rev. X*, 10:021032, May 2020. doi: 10.1103/PhysRevX.10.021032. URL <https://link.aps.org/doi/10.1103/PhysRevX.10.021032>.

- [234] U. Schneider, L. Hackermüller, J. P. Ronzheimer, S. Will, S. Braun, T. Best, I. Bloch, E. Demler, S. Mandt, D. Rasch, and A. Rosch. Fermionic transport and out-of-equilibrium dynamics in a homogeneous Hubbard model with ultracold atoms. *Nature Physics*, 8(3):213–218, Jan 2012. ISSN 1745-2481. URL <http://dx.doi.org/10.1038/nphys2205>.
- [235] D. Abanin, W. De Roeck, W. W. Ho, and F. Huveneers. A Rigorous Theory of Many-Body Prethermalization for Periodically Driven and Closed Quantum Systems. *Commun. Math. Phys.*, 354(3):809–827, September 2017. ISSN 1432-0916. doi: 10.1007/s00220-017-2930-x. URL <https://doi.org/10.1007/s00220-017-2930-x>.
- [236] Jean-Yves Desaulès, Ana Hudomal, Christopher J. Turner, and Zlatko Papić. Proposal for realizing quantum scars in the tilted 1d fermi-hubbard model. *Physical Review Letters*, 126(21), may 2021. doi: 10.1103/physrevlett.126.210601. URL <https://doi.org/10.1103/PhysRevLett.126.210601>.
- [237] Florian Meinert, Manfred J. Mark, E. Kirilov, Katharina Lauber, Philipp Weinmann, Michael Gröbner, Andrew J. Daley, and H.-C. Nägerl. Observation of many-body dynamics in long-range tunneling after a quantum quench. *Science*, 344:1259 – 1262, 2014.
- [238] Subir Sachdev, K. Sengupta, and S. M. Girvin. Mott insulators in strong electric fields. *Physical Review B*, 66(7), aug 2002. doi: 10.1103/physrevb.66.075128. URL <https://doi.org/10.1103/PhysRevB.66.075128>.
- [239] Jonathan Simon, Waseem S. Bakr, Ruichao Ma, M. Eric Tai, Philipp M. Preiss, and Markus Greiner. Quantum simulation of antiferromagnetic spin chains in an optical lattice. *Nature*, 472(7343):307–312, apr 2011. doi: 10.1038/nature09994. URL <https://doi.org/10.1038/nature09994>.
- [240] F. Meinert, M. J. Mark, E. Kirilov, K. Lauber, P. Weinmann, A. J. Daley, and H.-C. Nägerl. Quantum quench in an atomic one-dimensional ising chain. *Physical Review Letters*, 111(5), Jul 2013. ISSN 1079-7114. doi: 10.1103/physrevlett.111.053003. URL <http://dx.doi.org/10.1103/PhysRevLett.111.053003>.
- [241] S. Bravyi, D. P. DiVincenzo, and D. Loss. Schrieffer–Wolff transformation for quantum many-body systems. *Annals of Physics*, 326(10):2793–2826, Oct 2011. ISSN 0003-4916. doi: 10.1016/j.aop.2011.06.004. URL <http://dx.doi.org/10.1016/j.aop.2011.06.004>.
- [242] C.-J. Lin and O. I. Motrunich. Explicit construction of quasiconserved local operator of translationally invariant nonintegrable quantum spin chain in prethermalization. *Phys. Rev. B*, 96(21):214301, Dec 2017. doi: 10.1103/physrevb.96.214301.
- [243] D. V. Else, B. Bauer, and C. Nayak. Prethermal Phases of Matter Protected by Time-Translation Symmetry. *Phys. Rev. X*, 7:011026, Mar 2017. doi: 10.1103/PhysRevX.7.011026. URL <https://link.aps.org/doi/10.1103/PhysRevX.7.011026>.
- [244] T. Kuwahara, T. Mori, and K. Saito. Floquet–Magnus theory and generic transient dynamics in periodically driven many-body quantum systems. *Annals of Physics*, 367:96–124, Apr 2016. ISSN 0003-4916. doi: 10.1016/j.aop.2016.01.012. URL <http://dx.doi.org/10.1016/j.aop.2016.01.012>.

Bibliography

- [245] Maciej Lewenstein, Anna Sanpera, and Verónica Ahufinger. *Ultracold Atoms in Optical Lattices: Simulating quantum many-body systems*. Oxford University Press, 2012. doi: 10.1093/acprof:oso/9780199573127.001.0001. URL <https://oxford.universitypressscholarship.com/10.1093/acprof:oso/9780199573127.001.0001/acprof-9780199573127>.
- [246] A. Eckardt and E. Anisimovas. High-frequency approximation for periodically driven quantum systems from a Floquet-space perspective. *New Journal of Physics*, 17(9):093039, sep 2015. doi: 10.1088/1367-2630/17/9/093039. URL <https://doi.org/10.1088%2F1367-2630%2F17%2F9%2F093039>.
- [247] M. Bukov, L. D’Alessio, and A. Polkovnikov. Universal high-frequency behavior of periodically driven systems: from dynamical stabilization to Floquet engineering. *Adv. Phys.*, 64(2):139–226, March 2015. ISSN 0001-8732. doi: 10.1080/00018732.2015.1055918. URL <https://doi.org/10.1080/00018732.2015.1055918>.
- [248] E. S. Mananga and T. Charpentier. Introduction of the Floquet-Magnus expansion in solid-state nuclear magnetic resonance spectroscopy. *The Journal of Chemical Physics*, 135(4):044109, 2011. URL <https://doi.org/10.1063/1.3610943>.
- [249] N. Goldman and J. Dalibard. Periodically Driven Quantum Systems: Effective Hamiltonians and Engineered Gauge Fields. *Phys. Rev. X*, 4(3):031027, August 2014. doi: 10.1103/PhysRevX.4.031027. URL <https://link.aps.org/doi/10.1103/PhysRevX.4.031027>.
- [250] T. Mikami, S. Kitamura, K. Yasuda, N. Tsuji, T. Oka, and H. Aoki. Brillouin-Wigner theory for high-frequency expansion in periodically driven systems: Application to Floquet topological insulators. *Phys. Rev. B*, 93:144307, Apr 2016. doi: 10.1103/PhysRevB.93.144307. URL <https://link.aps.org/doi/10.1103/PhysRevB.93.144307>.
- [251] S. R. Taylor, M. Schulz, F. Pollmann, and R. Moessner. Experimental probes of Stark many-body localization. *Phys. Rev. B*, 102(5):054206, August 2020. doi: 10.1103/PhysRevB.102.054206. URL <https://link.aps.org/doi/10.1103/PhysRevB.102.054206>.
- [252] Dominic V. Else, Bela Bauer, and Chetan Nayak. Prethermal phases of matter protected by time-translation symmetry. *Phys. Rev. X*, 7:011026, Mar 2017. doi: 10.1103/PhysRevX.7.011026. URL <https://link.aps.org/doi/10.1103/PhysRevX.7.011026>.
- [253] S. R. Taylor, M. Schulz, F. Pollmann, and R. Moessner. Experimental probes of Stark many-body localization. *Phys. Rev. B*, 102:054206, Aug 2020. doi: 10.1103/PhysRevB.102.054206. URL <https://link.aps.org/doi/10.1103/PhysRevB.102.054206>.
- [254] D. A. Abanin, W. De Roeck, W. W. Ho, and F. Huveneers. Effective Hamiltonians, prethermalization, and slow energy absorption in periodically driven many-body systems. *Phys. Rev. B*, 95:014112, Jan 2017. doi: 10.1103/PhysRevB.95.014112. URL <https://link.aps.org/doi/10.1103/PhysRevB.95.014112>.
- [255] R. Sensarma, D. Pekker, E. Altman, E. Demler, N. Strohmaier, D. Greif, R. Jördens, L. Tarruell, H. Moritz, and T. Esslinger. Lifetime of double occupancies in the Fermi-Hubbard model. *Phys. Rev. B*, 82:224302, Dec 2010. doi: 10.1103/PhysRevB.82.224302. URL <https://link.aps.org/doi/10.1103/PhysRevB.82.224302>.

- [256] D. A. Abanin, W. De Roeck, and F. Huveneers. Exponentially Slow Heating in Periodically Driven Many-Body Systems. *Phys. Rev. Lett.*, 115:256803, Dec 2015. doi: 10.1103/PhysRevLett.115.256803. URL <https://link.aps.org/doi/10.1103/PhysRevLett.115.256803>.
- [257] C. E. Soliverez. An effective Hamiltonian and time-independent perturbation theory. *Journal of Physics C: Solid State Physics*, 2(12):2161–2174, dec 1969. doi: 10.1088/0022-3719/2/12/301. URL <https://doi.org/10.1088%2F0022-3719%2F2%2F12%2F301>.
- [258] T. Kato. On the Convergence of the Perturbation Method. I. *Progress of Theoretical Physics*, 4(4):514–523, 12 1949. ISSN 0033-068X. doi: 10.1143/ptp/4.4.514. URL <https://doi.org/10.1143/ptp/4.4.514>.
- [259] D. Prato and P. W. Lambert. A note on Magnus formula. *The Journal of Chemical Physics*, 106(11):4640–4643, 1997. URL <https://doi.org/10.1063/1.473509>.
- [260] S. Moudgalya, A. Prem, R. Nandkishore, N. Regnault, and B. A. Bernevig. Thermalization and its absence within Krylov subspaces of a constrained Hamiltonian. *arXiv:1910.14048*, October 2019. URL <http://arxiv.org/abs/1910.14048>.
- [261] L. Vidmar and M. Rigol. Entanglement Entropy of Eigenstates of Quantum Chaotic Hamiltonians. *Phys. Rev. Lett.*, 119(22), Nov 2017. ISSN 1079-7114. URL <http://dx.doi.org/10.1103/PhysRevLett.119.220603>.
- [262] Sebastian Scherg. *Probing nonequilibrium dynamics in Fermi-Hubbard chains—from extensively-many to few conserved quantities*. PhD thesis, lmu, 2021.
- [263] Thomas Kohlert. Probing weak ergodicity breaking in the one-dimensional fermi-hubbard model, June 2021. URL <http://nbn-resolving.de/urn:nbn:de:bvb:19-282351>.
- [264] Constantine Shkedrov, Meny Menashes, Gal Ness, Anastasiya Vainbaum, Ehud Altman, and Yoav Sagi. Absence of heating in a uniform fermi gas created by periodic driving. *Physical Review X*, 12(1), mar 2022. doi: 10.1103/physrevx.12.011041. URL <https://doi.org/10.1103%2Fphysrevx.12.011041>.
- [265] S. Scherg, T. Kohlert, J. Herbrych, J. Stolpp, P. Bordia, U. Schneider, F. Heidrich-Meisner, I. Bloch, and M. Aidelsburger. Nonequilibrium Mass Transport in the 1D Fermi-Hubbard Model. *Phys. Rev. Lett.*, 121:130402, Sep 2018. doi: 10.1103/PhysRevLett.121.130402. URL <https://link.aps.org/doi/10.1103/PhysRevLett.121.130402>.
- [266] M. Gustavsson, E. Haller, M. J. Mark, J. G. Danzl, G. Rojas-Kopeinig, and H.-C. Nägerl. Control of Interaction-Induced Dephasing of Bloch Oscillations. *Phys. Rev. Lett.*, 100(8):080404, February 2008. doi: 10.1103/PhysRevLett.100.080404. URL <https://link.aps.org/doi/10.1103/PhysRevLett.100.080404>.
- [267] P. M. Preiss, R. Ma, M. E. Tai, A. Lukin, M. Rispoli, P. Zupancic, Y. Lahini, R. Islam, and M. Greiner. Strongly correlated quantum walks in optical lattices. *Science*, 347(6227):1229–1233, 2015. doi: 10.1126/science.1260364. URL <https://science.sciencemag.org/content/347/6227/1229>.
- [268] Guifré Vidal. Efficient classical simulation of slightly entangled quantum computations. *Phys. Rev. Lett.*, 91:147902, Oct 2003. doi: 10.1103/PhysRevLett.91.147902. URL <https://link.aps.org/doi/10.1103/PhysRevLett.91.147902>.

Bibliography

- [269] U. Schollwöck. The density-matrix renormalization group in the age of matrix product states. *Annals of Physics*, 326(1):96–192, 2011. ISSN 0003-4916. doi: <https://doi.org/10.1016/j.aop.2010.09.012>. URL <http://www.sciencedirect.com/science/article/pii/S0003491610001752>.
- [270] S. Paeckel, T. Köhler, A. Swoboda, S. R. Manmana, U. Schollwöck, and C. Hubig. Time-evolution methods for matrix-product states. *Annals of Physics*, 411:167998, 2019. ISSN 0003-4916. doi: <https://doi.org/10.1016/j.aop.2019.167998>. URL <http://www.sciencedirect.com/science/article/pii/S0003491619302532>.
- [271] J. Hauschild and F. Pollmann. Efficient numerical simulations with Tensor Networks: Tensor Network Python (TeNPy). *SciPost Phys. Lect. Notes*, page 5, 2018. doi: 10.21468/SciPostPhysLectNotes.5. URL <https://scipost.org/10.21468/SciPostPhysLectNotes.5>.
- [272] Bharath Hebbe Madhusudhana, Sebastian Scherg, Thomas Kohlert, Immanuel Bloch, and Monika Aidelsburger. Benchmarking a novel efficient numerical method for localized 1d fermi-hubbard systems on a quantum simulator. *PRX Quantum*, 2(4), nov 2021. doi: 10.1103/prxquantum.2.040325. URL <https://doi.org/10.1103/2Fprxquantum.2.040325>.
- [273] W. Morong, F. Liu, P. Becker, K. S. Collins, L. Feng, A. Kyprianidis, G. Pagano, T. You, A. V. Gorshkov, and C. Monroe. Observation of stark many-body localization without disorder. *Nature*, 599(7885):393–398, nov 2021. doi: 10.1038/s41586-021-03988-0. URL <https://doi.org/10.1038/2Fs41586-021-03988-0>.
- [274] Qiujiang Guo, Chen Cheng, Hekang Li, Shibo Xu, Pengfei Zhang, Zhen Wang, Chao Song, Wuxin Liu, Wenhui Ren, Hang Dong, Rubem Mondaini, and H. Wang. Stark Many-Body Localization on a Superconducting Quantum Processor. *Physical Review Letters*, 127(24):240502, December 2021. doi: 10.1103/PhysRevLett.127.240502.
- [275] Thivan Gunawardana and Berislav Buča. Dynamical l-bits in stark many-body localization, 2021. URL <https://arxiv.org/abs/2110.13135>.
- [276] Andreas Elben, Steven T. Flammia, Hsin-Yuan Huang, Richard Kueng, John Preskill, Benoît Vermersch, and Peter Zoller. The randomized measurement toolbox, 2022. URL <https://arxiv.org/abs/2203.11374>.
- [277] S. Pai and M. Pretko. Dynamical Scar States in Driven Fracton Systems. *Phys. Rev. Lett.*, 123(13):136401, September 2019. doi: 10.1103/PhysRevLett.123.136401. URL <https://link.aps.org/doi/10.1103/PhysRevLett.123.136401>.
- [278] H. Zhao, J. Vovrosh, F. Mintert, and J. Knolle. Quantum Many-Body Scars in Optical Lattices. *Phys. Rev. Lett.*, 124(16):160604, April 2020. doi: 10.1103/PhysRevLett.124.160604. URL <https://link.aps.org/doi/10.1103/PhysRevLett.124.160604>.
- [279] A. Kshetrimayum, J. Eisert, and D. M. Kennes. Stark time crystals: Symmetry breaking in space and time. *arXiv:2007.13820*, July 2020. URL <http://arxiv.org/abs/2007.13820>.
- [280] E. Bairey, G. Refael, and N. H. Lindner. Driving induced many-body localization. *Phys. Rev. B*, 96:020201, Jul 2017. doi: 10.1103/PhysRevB.96.020201. URL <https://link.aps.org/doi/10.1103/PhysRevB.96.020201>.

- [281] D. S. Bhakuni, R. Nehra, and A. Sharma. Drive-induced many-body localization and coherent destruction of Stark many-body localization. *Phys. Rev. B*, 102(2):024201, July 2020. doi: 10.1103/PhysRevB.102.024201. URL <https://link.aps.org/doi/10.1103/PhysRevB.102.024201>.
- [282] Elmer V. H. Doggen, Igor V. Gornyi, and Dmitry G. Polyakov. Many-body localization in a tilted potential in two dimensions. *Physical Review B*, 105(13), apr 2022. doi: 10.1103/physrevb.105.134204. URL <https://doi.org/10.1103%2Fphysrevb.105.134204>.
- [283] L.-N. Wu and A. Eckardt. Bath-Induced Decay of Stark Many-Body Localization. *Phys. Rev. Lett.*, 123(3):030602, July 2019. doi: 10.1103/PhysRevLett.123.030602. URL <https://link.aps.org/doi/10.1103/PhysRevLett.123.030602>.
- [284] B. Yang, H. Sun, R. Ott, H.-Y. Wang, T. V. Zache, J. C. Halimeh, Z.-S. Yuan, P. Hauke, and J.-W. Pan. Observation of gauge invariance in a 71-site Bose-Hubbard quantum simulator. *arXiv:2003.08945*, March 2020. URL <http://arxiv.org/abs/2003.08945>.
- [285] Yizhi You, Trithep Devakul, F. J. Burnell, and S. L. Sondhi. Subsystem symmetry protected topological order. *Physical Review B*, 98(3), Jul 2018. ISSN 2469-9969. doi: 10.1103/physrevb.98.035112. URL <http://dx.doi.org/10.1103/PhysRevB.98.035112>.
- [286] Zheng Zhou, Xue-Feng Zhang, Frank Pollmann, and Yizhi You. Fractal quantum phase transitions: Critical phenomena beyond renormalization, 2021.
- [287] Trithep Devakul, Yizhi You, F. J. Burnell, and S. L. Sondhi. Fractal Symmetric Phases of Matter. *SciPost Phys.*, 6:7, 2019. doi: 10.21468/SciPostPhys.6.1.007. URL <https://scipost.org/10.21468/SciPostPhys.6.1.007>.
- [288] Beni Yoshida. Exotic topological order in fractal spin liquids. *Physical Review B*, 88(12), Sep 2013. ISSN 1550-235X. doi: 10.1103/physrevb.88.125122. URL <http://dx.doi.org/10.1103/PhysRevB.88.125122>.
- [289] Pengfei Zhang. Subdiffusion in strongly tilted lattice systems. *Phys. Rev. Research*, 2:033129, Jul 2020. doi: 10.1103/PhysRevResearch.2.033129. URL <https://link.aps.org/doi/10.1103/PhysRevResearch.2.033129>.
- [290] A. Gromov, A. Lucas, and R. M. Nandkishore. Fracton hydrodynamics. *Phys. Rev. Research*, 2:033124, Jul 2020. doi: 10.1103/PhysRevResearch.2.033124. URL <https://link.aps.org/doi/10.1103/PhysRevResearch.2.033124>.
- [291] Jason Iaconis, Sagar Vijay, and Rahul Nandkishore. Anomalous subdiffusion from subsystem symmetries. *Physical Review B*, 100(21), Dec 2019. ISSN 2469-9969. doi: 10.1103/physrevb.100.214301. URL <http://dx.doi.org/10.1103/PhysRevB.100.214301>.
- [292] Jason Iaconis, Andrew Lucas, and Rahul Nandkishore. Multipole conservation laws and subdiffusion in any dimension. *Physical Review E*, 103(2), Feb 2021. ISSN 2470-0053. doi: 10.1103/physreve.103.022142. URL <http://dx.doi.org/10.1103/PhysRevE.103.022142>.
- [293] Paolo Glorioso, Jinkang Guo, Joaquin F. Rodriguez-Nieva, and Andrew Lucas. Breakdown of hydrodynamics below four dimensions in a fracton fluid, 2021. URL <https://arxiv.org/abs/2105.13365>.

Bibliography

- [294] Arun Paramekanti, Leon Balents, and Matthew P. A. Fisher. Ring exchange, the exciton bose liquid, and bosonization in two dimensions. *Phys. Rev. B*, 66:054526, Aug 2002. doi: 10.1103/PhysRevB.66.054526. URL <https://link.aps.org/doi/10.1103/PhysRevB.66.054526>.
- [295] Tiamhock Tay and Olexei I. Motrunich. Possible realization of the exciton bose liquid phase in a hard-core boson model with ring-only exchange interactions. *Phys. Rev. B*, 83:205107, May 2011. doi: 10.1103/PhysRevB.83.205107. URL <https://link.aps.org/doi/10.1103/PhysRevB.83.205107>.
- [296] Shouvik Sur and Kun Yang. Metallic state in bosonic systems with continuously degenerate dispersion minima. *Phys. Rev. B*, 100:024519, Jul 2019. doi: 10.1103/PhysRevB.100.024519. URL <https://link.aps.org/doi/10.1103/PhysRevB.100.024519>.
- [297] Yizhi You, Julian Bibo, Frank Pollmann, and Taylor L. Hughes. Fracton critical point in higher-order topological phase transition, 2020.
- [298] Ethan Lake, T. Senthil, and Ashvin Vishwanath. Bose-luttinger liquids. *Physical Review B*, 104(1), Jul 2021. ISSN 2469-9969. doi: 10.1103/physrevb.104.014517. URL <http://dx.doi.org/10.1103/PhysRevB.104.014517>.
- [299] Nathan Seiberg and Shu-Heng Shao. Exotic $u(1)$ symmetries, duality, and fractons in 3+1-dimensional quantum field theory. *SciPost Physics*, 9(4), Oct 2020. ISSN 2542-4653. doi: 10.21468/scipostphys.9.4.046. URL <http://dx.doi.org/10.21468/SciPostPhys.9.4.046>.
- [300] Pranay Gorantla, Ho Tat Lam, Nathan Seiberg, and Shu-Heng Shao. The low-energy limit of some exotic lattice theories and uv/ir mixing, 2021.
- [301] Yizhi You, Julian Bibo, Taylor L. Hughes, and Frank Pollmann. Fractonic critical point proximate to a higher-order topological insulator: How does uv blend with ir?, 2021.
- [302] Steven Roman. *Field theory*. Springer, 2006. doi: <https://doi.org/10.1007/0-387-27678-5>.
- [303] J. Konvalina and Valentin Matische. Palindrome-polynomials with roots on the unit circle. 2004.
- [304] Ivan Niven. *Irrational Numbers*. Mathematical Association of America, 1956. doi: 10.5948/9781614440116.
- [305] A. Gromov. Towards Classification of Fracton Phases: The Multipole Algebra. *Phys. Rev. X*, 9:031035, Aug 2019. doi: 10.1103/PhysRevX.9.031035. URL <https://link.aps.org/doi/10.1103/PhysRevX.9.031035>.
- [306] S. Mandt, A. Rapp, and A. Rosch. Interacting Fermionic Atoms in Optical Lattices Diffuse Symmetrically Upwards and Downwards in a Gravitational Potential. *Phys. Rev. Lett.*, 106:250602, Jun 2011. doi: 10.1103/PhysRevLett.106.250602. URL <https://link.aps.org/doi/10.1103/PhysRevLett.106.250602>.
- [307] J.-K. Yuan, S. A. Chen, and P. Ye. Fractonic superfluids. *Phys. Rev. Research*, 2:023267, Jun 2020. doi: 10.1103/PhysRevResearch.2.023267. URL <https://link.aps.org/doi/10.1103/PhysRevResearch.2.023267>.

- [308] Oliver Hart, Andrew Lucas, and Rahul Nandkishore. Hidden quasiconservation laws in fracton hydrodynamics. *Physical Review E*, 105(4), apr 2022. doi: 10.1103/physreve.105.044103. URL <https://doi.org/10.1103%2Fphysreve.105.044103>.
- [309] M. Abramowitz and I. A. Stegun. *Handbook of Mathematical Functions*. Dover Publications Inc., 1965.
- [310] Giuseppe De Tomasi. *Characterization of ergodicity breaking in disordered quantum systems*. PhD thesis, Technical University of Dresden, Germany, October 2018.
- [311] A. Weiße, G. Wellein, A. Alvermann, and H. Fehske. The kernel polynomial method. *Rev. Mod. Phys.*, 78:275–306, Mar 2006. doi: 10.1103/RevModPhys.78.275. URL <https://link.aps.org/doi/10.1103/RevModPhys.78.275>.
- [312] S. Bera, G. De Tomasi, F. Weiner, and F. Evers. Density Propagator for Many-Body Localization: Finite-Size Effects, Transient Subdiffusion, and Exponential Decay. *Phys. Rev. Lett.*, 118:196801, May 2017. doi: 10.1103/PhysRevLett.118.196801. URL <https://link.aps.org/doi/10.1103/PhysRevLett.118.196801>.
- [313] Ulrich Schollwöck. The density-matrix renormalization group in the age of matrix product states. *Annals of Physics*, 326(1):96–192, jan 2011. doi: 10.1016/j.aop.2010.09.012. URL <https://doi.org/10.1016%2Fj.aop.2010.09.012>.
- [314] Tibor Rakovszky, C. W. von Keyserlingk, and Frank Pollmann. Dissipation-assisted operator evolution method for capturing hydrodynamic transport. *Phys. Rev. B*, 105:075131, Feb 2022. doi: 10.1103/PhysRevB.105.075131. URL <https://link.aps.org/doi/10.1103/PhysRevB.105.075131>.
- [315] A. G. Burchards, J. Feldmeier, A. Schuckert, and M. Knap. Coupled Hydrodynamics in Dipole-Conserving Quantum Systems. *arXiv e-prints*, art. arXiv:2201.08852, January 2022.
- [316] H. van Beijeren. Transport properties of stochastic Lorentz models. *Rev. Mod. Phys.*, 54:195–234, Jan 1982. doi: 10.1103/RevModPhys.54.195. URL <https://link.aps.org/doi/10.1103/RevModPhys.54.195>.
- [317] Sagar Vijay and Wenjie Ji. Unpublished.
- [318] A. Morningstar, V. Khemani, and D. A. Huse. Kinetically constrained freezing transition in a dipole-conserving system. *Phys. Rev. B*, 101:214205, Jun 2020. doi: 10.1103/PhysRevB.101.214205. URL <https://link.aps.org/doi/10.1103/PhysRevB.101.214205>.
- [319] Thomas Kohlert, Sebastian Scherg, Xiao Li, Henrik P. Lüschen, Sankar Das Sarma, Immanuel Bloch, and Monika Aidelsburger. Observation of many-body localization in a one-dimensional system with a single-particle mobility edge. *Physical Review Letters*, 122(17), May 2019. ISSN 1079-7114. doi: 10.1103/physrevlett.122.170403. URL <http://dx.doi.org/10.1103/PhysRevLett.122.170403>.
- [320] M. E. J. Newman and Christopher Moore. Glassy dynamics and aging in an exactly solvable spin model. *Physical Review E*, 60(5):5068–5072, nov 1999. doi: 10.1103/physreve.60.5068. URL <https://doi.org/10.1103%2Fphysreve.60.5068>.
- [321] Trithep Devakul, Yizhi You, F. J. Burnell, and Shivaji Sondhi. Fractal symmetric phases of matter. *SciPost Physics*, 6(1), jan 2019. doi: 10.21468/scipostphys.6.1.007. URL <https://doi.org/10.21468%2Fscipostphys.6.1.007>.

Bibliography

- [322] Alexey Khudorozhkov, Apoorv Tiwari, Claudio Chamon, and Titus Neupert. Hilbert space fragmentation in a 2d quantum spin system with subsystem symmetries, 2021.
- [323] Russell Lyons and Yuval Peres. *Probability on Trees and Networks*, volume 42 of *Cambridge Series in Statistical and Probabilistic Mathematics*. Cambridge University Press, New York, 2016. ISBN 978-1-107-16015-6. doi: 10.1017/9781316672815. URL <http://dx.doi.org/10.1017/9781316672815>. Available at <https://rdlyons.pages.iu.edu/>.
- [324] James W. Miller. A matrix equation approach to solving recurrence relations in two-dimensional random walks. *Journal of Applied Probability*, 31(3):646–659, 1994. ISSN 00219002. URL <http://www.jstor.org/stable/3215145>.
- [325] Julius Lehmann, Pablo Sala, Frank Pollmann, and Tibor Rakovszky. Fragmentation-induced localization and boundary charges in dimensions two and above [to be published], 2022.
- [326] William Fulton. *Algebraic curves: an introduction to algebraic geometry (chapter 3)*. Addison-Wesley, 1989.
- [327] Pranay Gorantla, Ho Tat Lam, Nathan Seiberg, and Shu-Heng Shao. Global dipole symmetry, compact lifshitz theory, tensor gauge theory, and fractons, 2022. URL <https://arxiv.org/abs/2201.10589>.
- [328] Loïc Herviou, Jens H. Bardarson, and Nicolas Regnault. Many-body localization in a fragmented hilbert space. *Physical Review B*, 103(13), apr 2021. doi: 10.1103/physrevb.103.134207. URL <https://doi.org/10.1103/physrevb.103.134207>.
- [329] Federica M. Surace, Paolo P. Mazza, Giuliano Giudici, Alessio Lerose, Andrea Gambassi, and Marcello Dalmonte. Lattice Gauge Theories and String Dynamics in Rydberg Atom Quantum Simulators. *Physical Review X*, 10(2):021041, April 2020. doi: 10.1103/PhysRevX.10.021041.
- [330] Sanjay Moudgalya, B. Andrei Bernevig, and Nicolas Regnault. Quantum many-body scars and hilbert space fragmentation: A review of exact results, 2021. URL <https://arxiv.org/abs/2109.00548>.
- [331] Johannes Feldmeier and Michael Knap. Critically slow operator dynamics in constrained many-body systems. *Physical Review Letters*, 127(23), dec 2021. doi: 10.1103/physrevlett.127.235301. URL <https://doi.org/10.1103/physrevlett.127.235301>.
- [332] Oliver Hart, Andrew Lucas, and Rahul Nandkishore. Hidden quasi-conservation laws in fracton hydrodynamics, 2021.
- [333] Ruben Verresen, Nathanan Tantivasadakarn, and Ashvin Vishwanath. Efficiently preparing schrödinger’s cat, fractons and non-abelian topological order in quantum devices, 2021. URL <https://arxiv.org/abs/2112.03061>.
- [334] Yizhi You, F. J. Burnell, and Taylor L. Hughes. Multipolar topological field theories: Bridging higher order topological insulators and fractons. *Physical Review B*, 103(24), jun 2021. doi: 10.1103/physrevb.103.245128. URL <https://doi.org/10.1103/physrevb.103.245128>.
- [335] R B Stinchcombe. Ising model in a transverse field. i. basic theory. *Journal of Physics C: Solid State Physics*, 6(15):2459–2483, aug 1973. doi: 10.1088/0022-3719/6/15/009. URL <https://doi.org/10.1088/0022-3719/6/15/009>.

- [336] Serge Aubry and Gilles André. Analyticity breaking and anderson localization in incommensurate lattices. *Ann. Israel Phys. Soc*, 3(133):18, 1980.
- [337] Giacomo Roati, Chiara D’Errico, Leonardo Fallani, Marco Fattori, Chiara Fort, Matteo Zaccanti, Giovanni Modugno, Michele Modugno, and Massimo Inguscio. Anderson localization of a non-interacting bose–einstein condensate. *Nature*, 453(7197):895–898, jun 2008. doi: 10.1038/nature07071. URL <https://doi.org/10.1038%2Fnature07071>.
- [338] Henrik P. Lüschen, Sebastian Scherg, Thomas Kohlert, Michael Schreiber, Pranjal Bordia, Xiao Li, S. Das Sarma, and Immanuel Bloch. Single-particle mobility edge in a one-dimensional quasiperiodic optical lattice. *Phys. Rev. Lett.*, 120:160404, Apr 2018. doi: 10.1103/PhysRevLett.120.160404. URL <https://link.aps.org/doi/10.1103/PhysRevLett.120.160404>.
- [339] Shankar Iyer, Vadim Oganesyan, Gil Refael, and David A. Huse. Many-body localization in a quasiperiodic system. *Physical Review B*, 87(13), apr 2013. doi: 10.1103/physrevb.87.134202. URL <https://doi.org/10.1103%2Fphysrevb.87.134202>.
- [340] Vedika Khemani, D. N. Sheng, and David A. Huse. Two universality classes for the many-body localization transition. *Phys. Rev. Lett.*, 119:075702, Aug 2017. doi: 10.1103/PhysRevLett.119.075702. URL <https://link.aps.org/doi/10.1103/PhysRevLett.119.075702>.
- [341] Marko Žnidarič and Marko Ljubotina. Interaction instability of localization in quasiperiodic systems. *Proceedings of the National Academy of Sciences*, 115(18):4595–4600, apr 2018. doi: 10.1073/pnas.1800589115. URL <https://doi.org/10.1073%2Fpnas.1800589115>.
- [342] Daniel A. Roberts, Douglas Stanford, and Leonard Susskind. Localized shocks. *Journal of High Energy Physics*, 2015(3):51, Mar 2015. ISSN 1029-8479. doi: 10.1007/JHEP03(2015)051. URL [https://doi.org/10.1007/JHEP03\(2015\)051](https://doi.org/10.1007/JHEP03(2015)051).
- [343] C. W. von Keyserlingk, Tibor Rakovszky, Frank Pollmann, and S. L. Sondhi. Operator hydrodynamics, otocs, and entanglement growth in systems without conservation laws. *Phys. Rev. X*, 8:021013, Apr 2018. doi: 10.1103/PhysRevX.8.021013. URL <https://link.aps.org/doi/10.1103/PhysRevX.8.021013>.
- [344] Adam Nahum, Sagar Vijay, and Jeongwan Haah. Operator spreading in random unitary circuits. *Phys. Rev. X*, 8:021014, Apr 2018. doi: 10.1103/PhysRevX.8.021014. URL <https://link.aps.org/doi/10.1103/PhysRevX.8.021014>.
- [345] Tibor Rakovszky, Frank Pollmann, and C. W. von Keyserlingk. Diffusive hydrodynamics of out-of-time-ordered correlators with charge conservation. *Phys. Rev. X*, 8:031058, Sep 2018. doi: 10.1103/PhysRevX.8.031058. URL <https://link.aps.org/doi/10.1103/PhysRevX.8.031058>.
- [346] F. Verstraete, V. Murg, and J.I. Cirac. Matrix product states, projected entangled pair states, and variational renormalization group methods for quantum spin systems. *Advances in Physics*, 57(2):143–224, 2008. doi: 10.1080/14789940801912366. URL <https://doi.org/10.1080/14789940801912366>.
- [347] W. De Roeck and V. Verreet. Very slow heating for weakly driven quantum many-body systems. *arXiv:1911.01998*, November 2019. URL <http://arxiv.org/abs/1911.01998>.